

“The Optical Properties of Noble Metal Nanoclusters & Application in Bioimaging and Security”

by

Anurag Milind Chahande

10CC15J26002

A thesis submitted to the
Academy of Scientific & Innovative Research
for the award of the degree of
DOCTOR OF PHILOSOPHY

in
Sciences

Under the supervision of

Dr. R. Nandini Devi



CSIR- National Chemical Laboratory, Pune

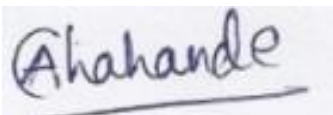


Academy of Scientific and Innovative Research
AcSIR Headquarters, CSIR-HRDC campus
Sector 19, Kamlā Nehru Nagar,
Ghaziabad, U.P. – 201002, India

January-2022

Certificate

This is to certify that the work incorporated in this Ph.D. thesis entitled, “*The Optical Properties Of Noble Metal Nanoclusters & Application In Bioimaging and Security*” submitted by Mr. Anurag Milind Chahande to the Academy of Scientific and Innovative Research (AcSIR), in partial fulfillment of the requirements for the award of the Degree of *Doctor of Philosophy in Science*, embodies original research work carried-out by the student. We, further certify that this work has not been submitted to any other University or Institution in part or full for the award of any degree or diploma. Research material(s) obtained from other source(s) and used in this research work has/have been duly acknowledged in the thesis. Image(s), illustration(s), figure(s), table(s) *etc.*, used in the thesis from other source(s), have also been duly cited and acknowledged.



Mr. Anurag M. Chahande

Research Student

Date: 05 /1/2022



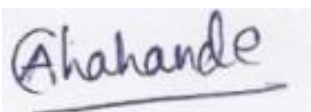
Dr. R. Nandini Devi

Research Supervisor

Date: 05 /1/2022

STATEMENTS OF ACADEMIC INTEGRITY

I Mr. Anurag Milind Chahande, a Ph.D. student of the Academy of Scientific and Innovative Research (AcSIR) with Registration No. 10CC15J26002 hereby undertake that, the thesis entitled “The Optical Properties Of Noble Metal Nanoclusters & Application In Bioimaging and Security” has been prepared by me and that the document reports original work carried out by me and is free of any plagiarism in compliance with the UGC Regulations on “*Promotion of Academic Integrity and Prevention of Plagiarism in Higher Educational Institutions (2018)*” and the CSIR Guidelines for “*Ethics in Research and in Governance (2020)*”.



Signature of the Student

Anurag M. Chahande

Date : 05 :/1/2022

Place : Pune

It is hereby certified that the work done by the student, under my/our supervision, is plagiarism-free in accordance with the UGC Regulations on “*Promotion of Academic Integrity and Prevention of Plagiarism in Higher Educational Institutions (2018)*” and the CSIR Guidelines for “*Ethics in Research and in Governance (2020)*”.



Signature of the Supervisor

Name : **Dr. R. Nandini Devi**

Date : 05/1/2022

Place : Pune

DEDICATION

This dissertation is dedicated to my dearest mother, grandmother and my beloved family members who constantly have been inspiring me in all that I do. Their constant love, trust, and support helped me to reach this stage of my life. Specially, to my beloved wife, Dimple for her love, encouragement, and constant support.

Further, I dedicate this dissertation to my doctoral advisor Dr. R. Nandini Devi, who have been encouraging me throughout my work and has taught me as much about life as chemistry.



Table of Contents

Contents

Acknowledgement:	i
Abbreviations:	iv
General remarks:	v
Synopsis Report:	vi
List of Figures:	xvi
List of Schemes and Table:	xxvii

Chapter-1

Introduction and Literature Survey

1.1. Ultra-small metal nanoclusters.....	3
1.2. Optical properties (UV-Visible absorption) of nanoparticles vs nanoclusters.....	4
1.3. Luminescence mechanism in noble metal nanoclusters.....	6
1.4. Metal quantum clusters synthesis.....	7
1.4.1. Thiol protecting ligands.....	8
1.4.2. Proteins, DNA oligonucleotides and Peptides as protecting ligands.....	10
1.4.3. Polymers.....	11
1.5. NIR emitting metal quantum clusters in bioimaging.....	11
1.6. Detection of bacteria with noble metal nanoclusters, specially by gold Nanoclusters.....	14
1.6.A. Label free detection of bacterial strains.....	14
1.6.B. Recognition of bacteria through molecular motifs	15
1.7. Noble metal nanoclusters in Anti-counterfeiting applications	19
1.8. Scope and objective of the thesis.....	22

Table of Contents

1.8.1.	What is known?.....	22
1.8.2.	What is not known?.....	23
1.9.	Thesis outline.....	23
	References.....	24

Chapter-2

Red Fluorescent Ultra-Small Gold Nanoclusters Functionalized with Signal Molecules to Probe Specificity in Quorum Sensing Receptors in Gram-Negative Bacteria

2.1.	Introduction.....	30
2.2.	Experimental section.....	32
2.2.1.	Synthesis of Au Nanoclusters and their conjugates used in bacterial cells detection.....	32
2.2.1.1.	Synthesis of Au Nanoclusters.....	32
2.2.1.2.	<i>N, N', N''</i> -tripropyl (11-mercaptoundecyl) ammonium chloride (RSH) ligand synthesis.....	32
2.2.1.3.	Synthesis of AuNC@OA@AHLs.....	33
2.2.1.4.	Bacterial cells culture used in quorum sensing studies.....	33
2.3.	Characterization techniques.....	34
2.4.	Results & Discussion.....	35
2.4.2.	CHARACTERIZATION.....	37
2.4.2.1.	¹ H NMR Spectroscopy.....	37
2.4.2.2.	FT-IR Spectroscopy.....	38
2.3.2.3.	Transmission Electron Microscopy to determine	

Table of Contents

the average diameter of AuNC@OA@AHL conjugates.....	41
2.3.2.4. Fluorescence Spectroscopy.....	42
2.4.2.5. Selective detection of the receptors of <i>E. coli</i> , <i>C. sakazakii</i> and <i>P. aeruginosa</i> through fluorescence microscopy.....	43
2.4.2.6. Specific interaction between lactone moiety of AHL and the receptors of bacterial strains.....	45
2.4.2.7. TEM analysis of the bacteria incubating with AuNC@OA@AHL.....	49
2.4.2.8. Statistical analysis to quantify AuNC present in gram-negative bacterial cells on the basis of fluorescence intensity.....	49
2.5. CONCLUSION.....	51
REFERENCES.....	52

Chapter-3

Enhanced emission from hetero atom doped red emitting water dispersible Au ultra-small nanoclusters and their multifaceted applications in imaging

3.1 Introduction.....	55
3.1.1 Experimental Section	56
3.2.1. Synthesis of Au Nanoclusters and Au ⁺¹ -SR complex.....	56
3.2.2. Synthesis of AuAg bimetallic nanoclusters.....	56
3.2.3. Preparation of AuAgNC-3@OA, AuAgNC-3@OA @AHLs conjugates.....	56

Table of Contents

3.2.4. Imaging.....	57
3.2.5. Regenerated silk fibroin (RSF) solution.....	57
3.2.6. Preparation of AuAgNC-3@RSF gel composite.....	58
3.2.7. Leaching studies to check the stability of AuAgNC-3@RSF gel composite.....	58
3.3. Characterization techniques.....	58
3.4. Results and Discussion.....	60
3.5. Conclusion.....	88
References.....	89

Chapter-4A

Ultra-small Au nanoclusters with tailored photoluminescence properties using modified thiol ligands: a theoretical and experimental demonstration

4A.1. Introduction.....	92
4A.2. Experimental Section.....	93
4A.2.1. Synthesis of <i>N, N', N''</i> -tripropyl (11-mercaptoundecyl) ammonium chloride.....	93
4A.2.2. Synthesis of <i>N, N', N''</i> -triethyl (11-mercaptoundecyl) ammonium chloride.....	92
4A.2.3. Synthesis of <i>N, N', N''</i> -tributyl (11-mercaptoundecyl) ammonium chloride.....	92
4A.2.4. Synthesis of <i>N</i> -(11-mercaptoundecyl)- <i>N, N'</i> -dimethylbenzenammonium Chloride.....	93
4A.2.5. Synthesis of Thiol-Stabilized Gold Nanoclusters.....	94
4A.3. Instruments for Characterization.....	94

Table of Contents

4A.4. Results and Discussion.....	96
4A.4.1. Structural Characterization of Thiol ligands.....	96
4A.4.1.1. NMR spectroscopy.....	96
4A.4.1.2. FTIR spectroscopy.....	98
4A.4.2. Structural Characterization of Au nanoclusters capped with different thiols...	100
4A.4.2.1. TEM for particle size distribution.....	100
4A.4.2.1. X-ray photoelectron spectroscopy (XPS).....	102
4A.4.3. Photophysical characterization of Au nanoclusters capped with different thiols.....	103
4A.4.3.1. UV–visible absorption spectroscopy.....	102
4A.4.3.1. Fluorescence spectroscopy.....	104
4A.4.3. DFT studies to correlate optical properties of different thiol capped AuNCs with experimental data.....	105
4A.5. Conclusion.....	106
References.....	107

Chapter-4B

Self-assembly of AuNCs capped with aromatic thiols and the thermal and solvent effect on its fluorescence

4B.1. Introduction.....	110
04B.2. Experimental Section.....	111
4B.2.1. Synthesis of <i>N</i> -(11-mercaptoundecyl)- <i>N</i> , <i>N'</i> -dimethylbenzenammonium	

Table of Contents

chloride.....	111
4B.2.2. Synthesis of AuNCs capped with <i>N</i> -(11-mercaptoundecyl)- <i>N</i> , <i>N</i> '- dimethylbenzenammonium chloride.....	111
4B.3. Instruments for Characterization.....	111
4B.4. Results and Discussion.....	112
4B.4.1. Structural Characterization of Au nanoclusters capped with <i>N</i> -(11- mercaptoundecyl)- <i>N</i> , <i>N</i> '-dimethylbenzenammonium chloride.....	113
4B.4.2. X-ray photoelectron spectroscopy (XPS).....	115
4B.4.3. Optical Characterization for Au nanoclusters capped with <i>N</i> -(11-mercaptoundecyl)- <i>N</i> , <i>N</i> '-dimethylbenzenammonium chloride.....	116
4B.4.3.1. UV–visible absorption spectroscopy.....	116
4B.4.3.2. Fluorescence spectroscopy.....	117
4B.4.3.2. Solvent dependent emission.....	119
4B.5. Conclusion.....	120
References.....	121

Chapter-5

Conclusion and Future perspective

5.1. Conclusion	124
5.2. Future perspective	125

Abstract for indexing.....	126
----------------------------	-----

List of Publications and Patents.....	127
---------------------------------------	-----

Table of Contents

List of posters.....	128
Copy of SCI Publications.....	129
Appendix-1.....	136
Appendix-2.....	143
Erratum.....	148

Many people have become acquainted with me, accompanied me, and supported me over the course of my studies. It's a great perk because I now have the opportunity to thank everybody of them personally.

It is a tremendous privilege for me to express my sincere gratitude to **Dr. R. Nandini Devi**, my instructor and research supervisor, for her superb supervision, persistent encouragement, and constructive criticism throughout my PhD research. I consider myself really fortunate to have had an advisor who not only taught me chemistry but also discipline and showed me innovative ways to reach my objectives. I genuinely appreciate the laboratory independence she provided for autonomous thinking, planning, and implementation of the project. I believe that the best way to express my gratitude to her is to contribute to the scientific community in the future.

Dr. Asmita Prabhune, Dr. Paresh L. Dhepe, and Dr. Kiran Kulkarni and Dr. Sarika M. Bhattacharyyamembers of my Doctoral Advisory Committee, deserve special thanks for their constant support, guidance, and ideas. Prof. Dr. Ashish Lele, Director, NCL, Dr. Ashwini K. Nangia (former director), Dr. Shubhangi Umbarkar, Head, Division of Catalysis and Inorganic Chemistry, and Dr. C. S. Gopinath (Former HoD, Division of Catalysis and Inorganic Chemistry) are all to thank for giving us this opportunity and all necessary infrastructure and facilities.

I'd like to express my gratitude to the NMR division's Dr. P. R. Rajamohanam, Dr. Udaya Kiran Marelli, Mr. Dinesh, Pramod, Satish, Minakshi, and Dipali. HRMS, Mrs. Santhakumari Dr. Santosh Babu Sukumaran from the Organic Chemistry division for Fluorescence and Lifetime experiments, Dr. Dhanashekar Shanmugan for maintaining our Fluorescence microscope, and Dr. Kiran Kulkarni from the Dept. Bio Chem CSIR-NCL for providing infrastructure for bacterial culture experiments for my research work. I am grateful to Mr. Gholap, Tushar, and Venkatesh for their assistance with HR-TEM and TEM experiments, as well as Dr. C.P. Vinod and Mr. S. S. Deo for XPS experiments. Mrs. Kohle, Mr. P.K. Purushothaman of the SAC office staff, and other NCL scientists for their motivation, ongoing encouragement, and support. Dr. K. Sreekumar (FTIR-experiments), Dr. S. K. Asha (ATIR-experiments), and Dr. Suresh Bhat (DLS measurements) from PALM building, CSIR-NCL, Pune, deserve special thanks. My sincere gratitude to Dr. C. S. Gopinath for permitting me to use their fluorescence instrument during my research. Dr.

Anuya Nisal provided me with silk fibroin for security application job, which I greatly appreciate.

Dr. **Sailaja Krishnamurty** and her student Ms. Asha Maibam from CSIR-Convergence NCL's Building were especially helpful in terms of conversations, advice, and collaborative effort for computational studies.

My sincere gratitude to **Dr. Asmita Pabhune** and her students, Dr. Amrita Patil, Sahana, and Swarali Hirlekar. My gratitude goes out to **Dr. Kiran Kulkarni** and his students, Disha and Sneha, for their continued assistance with bacterial culture and fluorescence imaging investigations.

All of my seniors, Dr. T. Rajesh, Dr. Anupam Samantha, Dr. Jijil, Dr. Ruchira Mukherji, and Dr. Soumya, as well as my closest lovable chechi, Dr. Leena George, deserve my heartfelt thanks. Dr. T. Shibin, Pavan, Dr. Sourik Mondal, Priyanka, Shunottara, Chinnu, Shubham, Jyoti Tekawadia, Jyoti Sharma, Deepali, Mohsin, Aathira, Meghana, Anjumol, Amruta, Neethu, Jyoti Tekawadia, Jyoti Sharma, Deepali, Mohsin, Aathira, Meghana, Anju. I'm also thankful to project trainee students Mohit, Sabna, Vineetha, Fessy, Akhil, and Dhaval for making the lab a wonderful place. Dr. Praveen Kumar, Dr. Venkannababu, Dr. Amar Yeware, Dr. Prabhanjan Giram, Dr. Vivek Wackchaure, Dr. Rahul Jagtap, and Dr. Goudappa Patil are among the mithra mandali with whom I spent a significant portion of my time at NCL. They've always been, and will continue to be, a source of inspiration for me. I always appreciate their presence, and they are a source of strength for me in a variety of situations. I am fortunate to have such a large family, which I received as a gift from NCL. I also want to express my gratitude to my high school and college pals. There are no words to express my gratitude to my valued friends in and outside of NCL who have assisted me at various stages of my career at NCL. I also thank my roommates Dr. Vikram Pandit, Kiran, Vinayak, Chandrashekhar for the cheerful environment in the room.

Personally, I am grateful to Dr. Avinash Kumbhar and Dr. Divya Ottur from the Department of Chemistry at Savitribai Phule Pune University for their helpful ideas.

This Ph.D. would not have been feasible without the support I received, and I would like to convey my gratitude to CSIR-UGC for awarding JRF and SRF. Special thanks to **Dr. R. Nandini Devi** and **Dr. Paresh L. Dhepe** for financially assisting me through a critical


*financial crisis following my arrival at CSIR-NCL during the Covid-19 time when I was without a fellowship, which enabled me to complete my table work successfully. My family has always been a source of inspiration and emotional support for me while I pursued my education; I used to thank the Almighty God for blessing me with such a lovely family. I'd want to take this occasion to express my thanks to my father, **Mr. Milind Chahande**, **Late.Mrs. Sangeeta Chahande (mother)**, **Late. Prabhabai Chahande (grandmother)**, **Late.Mr. Padmakar Lade (father-in-law)** and **Mrs. Sangeeta Lade (mother-in-law)** for their endless love, sacrifice, blessings, unwavering support, and encouragement, even when they had no idea what I was up to. I'd also like to thank my brother **Akshay** and brother-in-law **Litesh** for their help in times of need. I would want to express gratitude to **Mrs. Dimple Anurag Chahande (wife)** for her unwavering love and unwavering faith in me, that has lightened a heavy burden from my shoulders. I'd like to express my gratitude to the great scientific community, whose accomplishments serve as a continuous source of motivation for me. Above all, I thank God Almighty for His enormous blessings.*

With many thanks,

Anurag M. Chahande

<u>Units</u>	
°C	Degree centigrade
g	Gram
mg	Milligram
h	Hour (s)
Hz	Hertz
eV	Electron Volt
μL	Microlitre
mL	Millilitre
min	Minutes
MHz	Megahertz
mmol	Millimole
nM	Nanometre
ppm	Parts per million
mmole	Millimole
cm ⁻¹	Wavenumber
nm	Nanometer

- All reagents and solvents were purchased from commercial suppliers and used as such without any further purification. Starting materials were obtained from commercial suppliers or prepared using known procedures.
- All the organic thiol ligands reported in research work were characterized by their NMR spectra.
- NMR spectra were recorded on Bruker AV200 (200.13 MHz for ^1H NMR, AV 400 (400 MHz for ^1H NMR).
- Chemical shifts (δ) have been expressed in ppm units relative to CDCl_3 (d-Chloroform) as an internal standard.
- The following abbreviations were used for ^1H NMR: s = singlet, d = doublet, t = triplet, q = quartet, m = multiplet, brs = broad singlet.
- PTI QM40/400, Horiba flouromax-4 fluorescence instruments were used to acquire the fluorescence spectra.
- Thermo Scientific K-alpha+ spectrometer used for XPS spectroscopy experiments.
- TENSOR-27 BRUKER used for FTIR experiments.
- TF-20, FEI Tecnai transmission electron microscope and JEOL JEM-200 high resolution transmission electron microscope utilized for analysing ultra-small nanoclusters.
- Structures and IUPAC nomenclature were generated using ChemBioDraw Ultra 14.0 software.
- Zeiss Imager A2 fluorescent microscope with Rhodamine filters used for bioimaging.
- For Plotting graphs Origin software and for statistical analysis Graph Pad Prism software's were utilized.
- XPSPEAK 41 software were utilized for XPS fitting.

	Synopsis of the thesis to be submitted to the Academy of Scientific and Innovative Research for award of the degree of Doctor of philosophy in Chemical Science
Name of the Candidate	Mr. Anurag Milind Chahande
Enrollment No. and Date	Ph. D. in chemical Sciences (10CC15J26002); January, 2015
Title of the Thesis	"The Optical Properties Of Noble Metal Nanoclusters & Application In Bioimaging and Security"
Research Supervisor	Dr. R. Nandini Devi

1. Introduction: The present thesis describes the synthesis of Au nanoclusters with thiol ligand and their tuning of fluorescence established via hetero atom doping and ligand variation. Bacterial detection via fluorescent metal nanoclusters also established via surface ligand engineering and bioconjugation with biomolecules. These fluorescent nanoclusters also possess excellent stability under relevant circumstances, and water solubility, and also demonstrated their promising uses in bioimaging and security applications.

This proposed thesis is divided into four chapters. The opening chapter narrates the literature reports on various noble metal nanoclusters, their optical properties and applications in the field of bioimaging and security. The 2nd chapter addressed the gram-negative bacterial cell detection via surface functionalized ultra-small Au nanoclusters. The fluorescence in the red area shown by ultra-small gold nanoclusters (AuNCs) was used to better understand the quorum sensing phenomena in bacteria, which is regulated by signal molecules that are particular to different species. The signal molecules Acyl Homoserine Lactones (AHL) of varied carbon chain lengths, C-6, C-8, and C-12 without 3rd C modification, are subsequently functionalized on AuNCs to detect different types of gram-negative bacteria, such as *E. coli*, *Cronobacter sakazakii*, and *Pseudomonas aeruginosa*. This detection method was found to be rapid and detection has been

done within 2 hours.

The third chapter addressed the enhancement of photoluminescence properties of pristine Au nanoclusters via hetero atom doping (Ag here). A simple Anti-galvanic reduction (AGR) approach for synthesis of bimetallic Au-Ag nanoclusters were used by utilizing thiol as a capping agent, i.e., N, N', N'' Tripropyl (11-mercaptoundecyl) ammonium chloride, which has -SH on one end and +NR₄ on the other. It was found that, as Ag doping increases over AuNCs the emission in red region increases as well as quantum yield and decay life time also increased. Bimetallic bright red emitting AuAgNCs with excellent stability under relevant circumstances, and water solubility, have demonstrated promising uses in bioimaging and security applications.

4th chapter addressed the tailoring of photoluminescence of AuNCs via controlled nanoparticle ligand interface chemistry. N, N', N''-Trialkyl (11-mercaptoundecyl) ammonium chloride-based thiol ligands as capping agents used to create molecular gold nanoclusters with adjustable photoluminescence emission from 600 nm to 700 nm. Specific interface chemistry between gold nanoclusters of molecular range and functional groups of the quaternary ammonium head over N, N', N''-Trialkyl (11-mercaptoundecyl) ammonium chloride regulates the tunability in emission. The conclusion of the total study given in this thesis was described in Chapter 5. This chapter also discusses the thesis's future directions.

2.Statement of the problem :- Several atomically precise hydrophobic nanoclusters with high PL intensities have been discovered to date; nevertheless, their hydrophobic nature has hampered their use in chemical sensing, bio-imaging, bio-labeling, and biotherapy. Because of their (i) non-toxicity, (ii) good biocompatibility, (iii) potential anti-cancer activity, (iv) small size, (v) good photo-stability, (vi) strong luminescence, (vii) ability to enter cells easily, and (viii) ability to bear functional ligands, hydrophilic fluorescent nanoclusters are prominent candidates for biological applications. The effect on optical properties due to change in size by core and surface atoms present in nanoclusters are studied well but only possible for small size clusters (< 1nm). As size increases theoretical studies to correlate their optical properties with experimental observations became difficult due increase in the computational cost. Ligand engineering effect for hydrophilic ligands will affect the

fluorescence of nanoclusters studies are still going. Till now, the combined effect coming from metal nanocluster and the effect of capping ligand on the optical properties is not fully studied. This is the major challenge in big size nanoclusters (size~1nm to 2nm) capped with different hydrophilic ligands.

Hydrophilic thiolate capped nanoclusters should possess certain kind of functional group which could bind or interact specific biomolecule to target particular binding site. This will make them aqueous soluble as well as capable to target specific binding sites like in drug delivery or bacterial cell detection. Since, in bacterial cell detection the fluorescent probe should have emission in red or NIR region also detection of such bacterial cells should be accurate and rapid before causing disease inside host cells or organism. Deep understanding regarding specific bacterial cell detection in a small interval of time is needed.

3. Objectives:

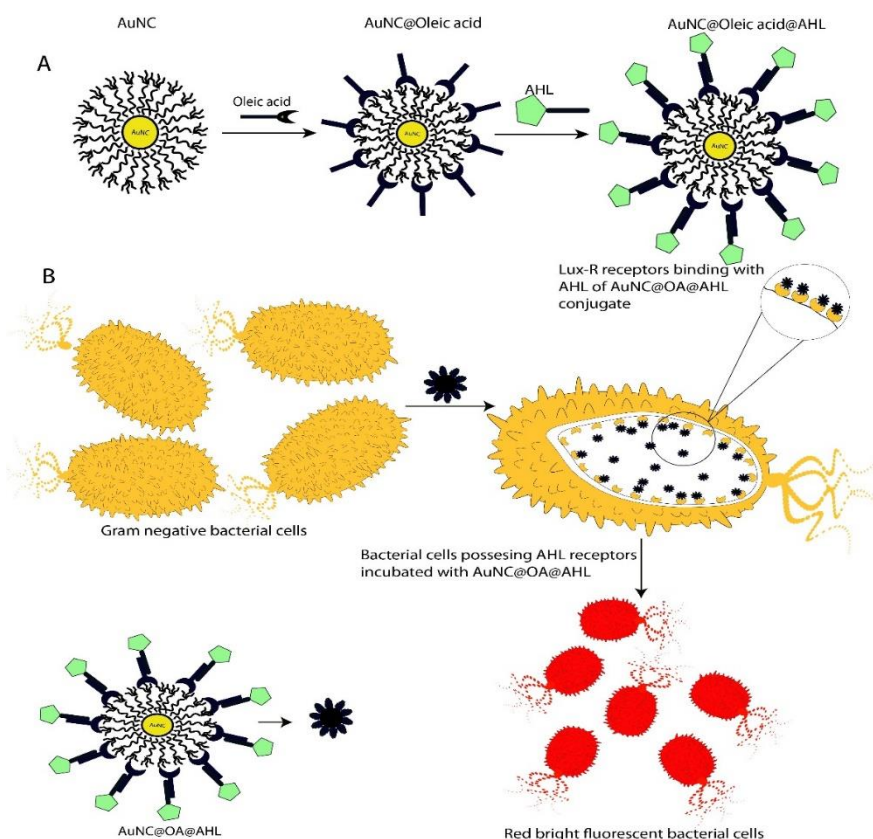
- ❑ To understand the mechanism of quorum sensing, we have focused on the question, whether different strains of gram-negative bacteria have specific affinity towards a particular AHL molecule
- ❑ To develop a method which should be rapid (detection in less than 2 h), with the potential of being able to detect bacteria much prior to the virulent quorate state
- ❑ To enhance the optical properties of AuNCs via hetero atom doping and apply them in various imaging applications
- ❑ To develop a surface engineered AuNCs via different thiol capping which could change their emission properties

4. Methodology and Result:

Chapter-1. *Red fluorescent ultra-small gold nanoclusters functionalized with signal molecules to probe specificity in quorum sensing receptors in gram-negative bacteria*

For researching quorum sensing behavior in bacteria, a red-emitting inorganic fluorescent Au nano-cluster-based probe has been designed.¹ This inorganic fluorescent probe is built up of

gold nanoclusters with acyl homoserine lactones (AHLs) of various carbon chain lengths on the surface.²



Scheme 1.1. Bacterial Cell incubated with fluorescent nanoprobes (A) Nanoprobe structure here AHL moiety deployed on the surface without disturbing amide and lactone moiety (B) Specific binding of AHL head groups from the AuNC@OA@AHL composites to receptor sites in Lux-R regulators within bacteria

The bioactive component of AHL (lactone moiety) stays intact after surface functionalization of AHLs over the Au nanocluster surface, allowing for natural activity as a pristine AHL molecule. This characteristic allows surface-functionalized Au nanoclusters to detect quorum sensing receptors in bacteria before they reach the maximum quorum state. Because of its simplicity, this method outperforms the biosensor targeting method. We may also analyse the change in selectivity and specificity of AHLs towards their target receptors within different

species of bacteria of the same strain using fluorescence microscopy research. *C. sakazakii* receptors are more selective for C-8 AHL than for C-6 AHL or C-12 AHL. *E. coli*

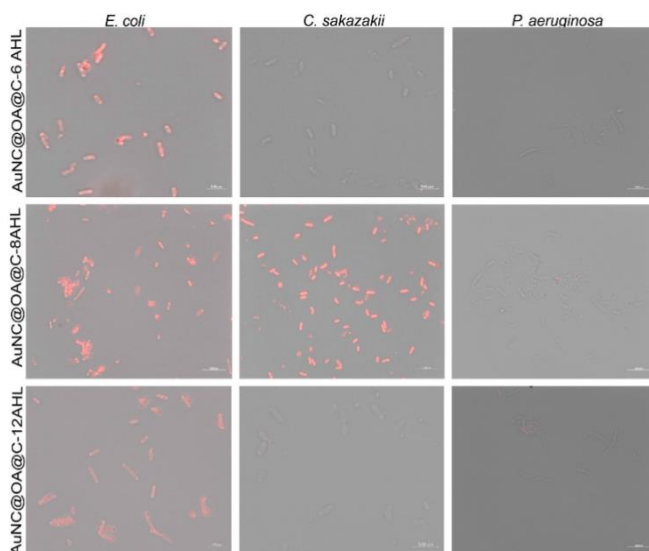
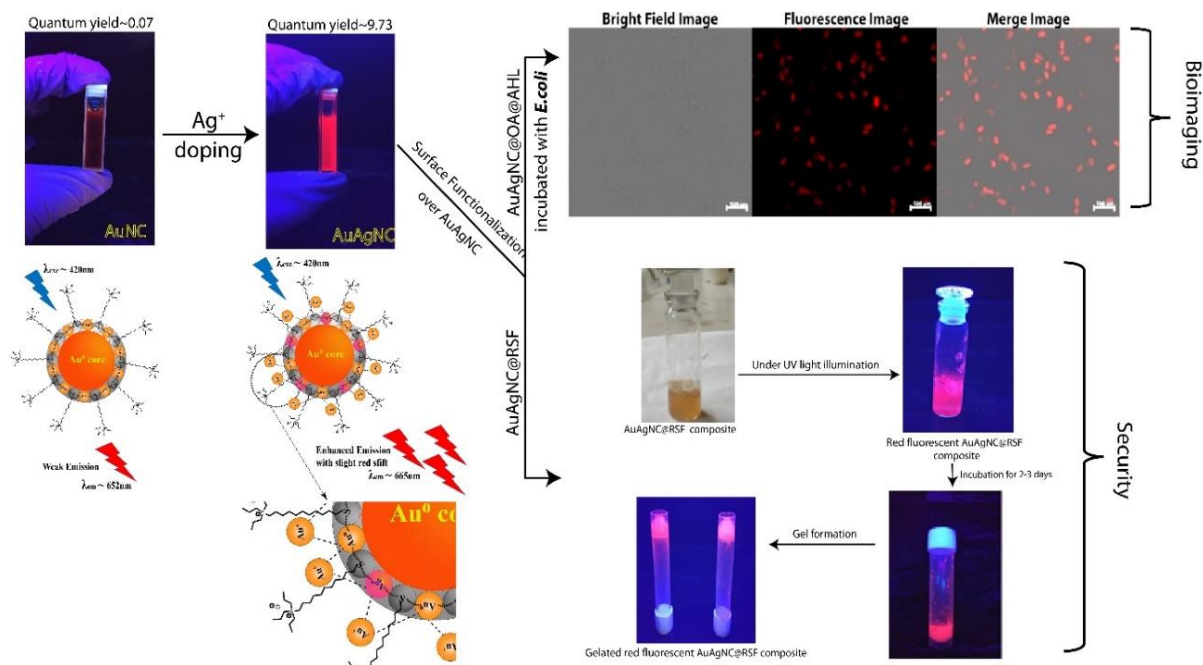


Fig. 1.1 Fluorescence microscopy images of (left column) *E. coli* incubated with AuNC@OA@C-6AHL (scale bar-500 μm), AuNC@OA@C-8AHL(scale bar-1000 μm), AuNC@OA@C-12AHL(scale bar-500 μm), (middle column) *Cronobacter sakazakii* incubated with AuNC@OA@C-6AHL(scale bar-500 μm), AuNC@OA@C-8AHL(scale bar-1000 μm), AuNC@OA@C-12AHL(scale bar-500 μm) and (right column) *Pseudomonas aeruginosa* incubated with AuNC@OA@C-6AHL(scale bar-1000 μm), AuNC@OA@C-8AHL(scale bar-1000 μm), AuNC@OA@C-12AHL(scale bar-1000 μm)

receptors interact with C-6 AHL, C-8 AHL, and C-12 AHL in a non-specific manner, whereas *P. aeruginosa* receptors do not interact with any of the three AHLs. Further research into the development of this technology will allow us to detect harmful bacteria selectively and understand their quorum sensitivities.

Chapter-2. Enhanced emission from hetero atom doped red emitting water dispersible Au ultra-small nanoclusters and their multifaceted applications in imaging

Due to their tunable photophysical and chemical properties, ultra-small nanoclusters have gotten a lot of attention in biolabeling, bioimaging, and security applications. The fluorescence of alloyed AuAg nanoclusters has recently been controlled using anti-galvanic replacement (AGR) in aqueous phase operations. Traditional capping ligands³ including glutathione, cysteine, and mercaptoundecanoic acid contain -SH as well as additional electron donor groups like -NH₂, -COOH, -OH, amide, and others, which can create a surface Ag⁺-thiolate complex after Ag doping on Au nanoclusters.^{4,5} Ag⁺-thiolate complexes also produce aggregate-induced emission, which improves fluorescence characteristics. For the first time, we show a simple AGR technique for synthesis of bimetallic Au-Ag nanoclusters by employing thiol as a capping agent, i.e., N, N', N'' tripropyl (11-mercaptoundecyl) ammonium chloride, which has -SH at one end and ⁺NR₄ at the other end and is incapable of forming M⁺-SR complexes. This study identified metallophillic interactions between Au⁺ and Au/Ag on the AuAg nanocluster surface as a new method for photoluminescence amplification.



Scheme.2.1. Ultrasmall-sized, red emitting AuAg bimetallic nanoclusters have been synthesized by a facile, AGR strategy, which further surface functionalized with AHLs and regenerated silk fibroin and utilized in multifaceted imaging applications.

This approach increased the red emission quantum yield of AuAgNC to 9.73 compared to pristine AuNC (Q.Y.~ 0.07), and these AuAgNC are utilized in bioimaging and security applications.

Chapter-3. *Ultra-small Au nanoclusters with tailored photoluminescence properties using modified thiol ligands: a theoretical and experimental demonstration*

Controlled nanoparticle ligand interface chemistry can be used to create Au nanoclusters with tailored photoluminescence. The present study uses N, N', N''-Trialkyl (11-mercaptoundecyl) ammonium chloride-based thiol ligands as capping agents to create molecular gold nanoclusters with tunable photoluminescence emission from 600 nm to 700 nm. Specific interface chemistry between gold nanoclusters of molecular range and functional groups of the quaternary ammonium head over N, N', N''-Trialkyl (11-mercaptoundecyl) ammonium chloride regulates the tunability within the red spectral region. The functional group specific electronic interactions at the interfaces steer the particle size of "molecular" Au nanoparticles characterized by the absence of surface plasmon resonance, according to a combined understanding obtained from transmission electron microscope studies and density functional theory-based studies. As a result, "molecular-Au clusters" with defined transition bands in the UV region were generated. The study clearly shows that bulkier functional groups reduce particle size through steric effects, resulting in tunable photoluminescence emission in the red spectral range.

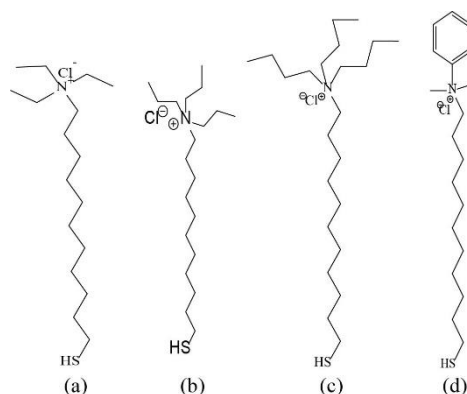


Fig.3.1. (a) *N,N',N''*-triethyl (11-mercaptoundecyl)ammonium chloride, (b) *N,N',N''*-tripropyl (11-mercaptoundecyl)ammonium chloride, (d) *N,N',N''*-tributyl (11-

mercaptoundecyl)ammonium chloride and (d) *N*-(11-mercaptoundecyl)-*N,N'*-dimethyl benzenammonium chloride.

Chapter-4:- This chapter presents the conclusion of the overall thesis and the possible area of research work in the field Au nanoclusters and their various future applications in the years to come.

5. Summary: Au nanoclusters surface functionalization or tagging of AHL signal molecules make them prone towards Lux-R receptor sensing. Because Au nanoclusters emitting in red region, signal to noise ratio is very less which is more advantageous for imaging. Lux-R receptors basically present in gram-negative bacteria. AHLs with different carbon chain length when tagged with Au nanoclusters showed selectivity towards gram negative bacterial cells. This method of detection can be used to detect such gram-negative bacteria much prior to their quorum state. Since fluorescence of Au nanoclusters can be tuned via hetero atom doping and ligand variation is also important. This will give enhanced optical properties for such tiny particles which can be used in various multifaceted imaging applications like bioimaging, drug delivery, sensing, security etc.

6. Future directions: The electrical and optical characteristics of colloidal systems are largely determined by the surface ligand. Several studies have found that ligands can have observable effects on their structure and properties. There is still a dearth of understanding of the interactions between NCs and protective ligands, as well as the impact of surface ligands in electrical and optical characteristics. We hypothesize that fluorescence can occur in either the NC core or the ligand and NC–ligand complex, implying that some of the fluorescence originates directly or indirectly from the ligands. More research is needed to fully understand such interactions.

Many unique applications of NCs for sensing, bioimaging, and chirality determination have been demonstrated in recent years. The parameters that influence their intracellular localization (in the cytoplasm, vesicles, or nucleus), uptake process, or even quantitative measurement, such as the size, shape, or ligand on the surface of clusters, have all been investigated. In vitro and in vivo investigations were recently used to study and validate the probe's features and multi-efficacy. In particular, Au/Ag NCs conjugated with a targeting ligand with high targeting

specificity and nuclear localization capability, low toxicity of multi-functional probe with tumor suppressing effect, and the tumor-targeted drug delivery nanocarrier all supported the potential of using NCs for early tumor diagnosis through tumor imaging and targeted therapy.

7. References:

- (1) Mukherji, R.; Samanta, A.; Illathvalappil, R.; Chowdhury, S.; Prabhune, A.; Devi, R. N. Selective Imaging of Quorum Sensing Receptors in Bacteria Using Fluorescent Au Nanocluster Probes Surface Functionalized with Signal Molecules. *ACS Appl. Mater. Interfaces* **2013**, *5* (24), 13076–13081. <https://doi.org/10.1021/am404093m>.
- (2) Chahande, A. M.; Lathigara, D.; Prabhune, A. A.; Devi, R. N. Red Fluorescent Ultra - Small Gold Nanoclusters Functionalized with Signal Molecules to Probe Specificity in Quorum Sensing Receptors in Gram - Negative Bacteria. *Arch. Microbiol.* **2021**, *203*, 4293–4301. <https://doi.org/10.1007/s00203-021-02338-y>.
- (3) Waterhouse, G. I. N.; Wang, Y.; Yin, H. Ultrasmall Au Nanoclusters for Biomedical and Biosensing Applications : A. *Talanta* **2019**, *200* (March), 432–442. <https://doi.org/10.1016/j.talanta.2019.03.068>.
- (4) Li, B.; Wang, X.; Shen, X.; Zhu, W.; Xu, L.; Zhou, X. Aggregation-Induced Emission from Gold Nanoclusters for Use as a Luminescence-Enhanced Nanosensor to Detect Trace Amounts of Silver Ions. *J. Colloid Interface Sci.* **2016**, *467*, 90–96. <https://doi.org/10.1016/j.jcis.2016.01.002>.
- (5) Luo, Z.; Yuan, X.; Yu, Y.; Zhang, Q.; Leong, D. T.; Lee, J. Y.; Xie, J. From Aggregation-Induced Emission of Au(I)-Thiolate Complexes to Ultrabright Au(0)@Au(I)-Thiolate Core-Shell Nanoclusters. *J. Am. Chem. Soc.* **2012**, *134* (40), 16662–16670. <https://doi.org/10.1021/ja306199p>.

List of Research Publications

(1) Dey.K, Kunjattu H.S., **Chahande A.M.**, Banerjee R.; Nanoparticle Size-Fractionation through Self-Standing Porous Covalent Organic Framework Films, **Angew. Chem.** **2020**,132 (3), 1177-1181

(2) **Chahande A.M.**, Lathigara D., Prabhune A.A., Devi R.N., Red fluorescent ultrasmall gold nanoclusters functionalized with signal molecules to probe specificity in quorum sensing receptors in gram - negative bacteria, **Arch. Microbiol.** **2021**,203 ,4293–4301.

<https://doi.org/10.1007/s00203-021-02338-y>.

(3) **Chahande A.M.**, Singh.S., Devi R.N., Enhanced red emission in water dispersible Au ultra-small nanoclusters by heteroatom doping and their multifaceted applications in imaging (Manuscript communicated)

(4) **Chahande A.M.**, Maibam.A.,Krishnamurthy S., Devi R.N., Ultra-small Au nanoclusters with tailored photoluminescence properties using modified thiol ligands: a computational and experimental demonstration (Manuscript under preparation)

Figure number	Figure Caption	Page number
Figure.1	Size comparisons of nanoclusters with nanoparticles and atoms	3
Figure.2	Evolution of band gaps and density of states (DOS) in bulk material, nanoparticles, and nanoclusters. (E_f : Fermi level) δ is the so-called Kubo gap. (Adapted from Ref.14)	4
Figure.3	Schematic representation of surface plasmon for a metal sphere, showing the displacement of electron cloud relative to nuclei. (Adapted from Ref.15)	5
Figure.4	(a)Change in the color of nanoparticles solution with the core diameter., (b) Surface plasmon peak shift and broadening with the change in the size of gold nanoparticle diameter. Adapted from Ref.16	5
Figure. 5	(a) Kohn-Sham orbital level diagram for Au ₂₅ clusters. (b) Peak assignment of absorption spectrum of Au ₂₅ clusters. (Adapted from Ref.17)	6
Figure.6	The galvanic replacement reaction process of synthesizing NIR Ag/Au alloy NCs. (Adapted from Ref.30)	9
Figure.7	Schematic of the formation of AuNCs in BSA solution under alkaline conditions. Adapted from Ref.25	10
Figure.8	Three-dimensional fluorescence confocal images of HeLa cells upon incubation with AuNCs (2.5 mMol/L, green) for 2 h: (a) without proteins and with 2.5 mMol/L (b) nHSA, (c) aHSA and (d) cHSA. Cell membranes were stained with Cell Mask Deep	12

	Red (red). The data are shown as sections in the x-y plane (upper left), x-z plane (lower left) and y-z plane (right). Scale bar, 10 mm. (Adapted from Ref. 50)	
Figure.9	(A) Fluorescence images of mice bearing an MDA-MB-45 tumour. Strong signal from AuNCs was observed in the tumour (marked by the red circle). The arrowheads indicated the tumour. (B) Ex vivo fluorescence image of the tumour tissue and the muscle tissue around the tumour from the mice used in A. (Adapted from Ref.52)	13
Figure.10	(A) Luminescent HSA-Au NCs as selective probes for <i>Staphylococcus aureus</i> and <i>MRSA</i> . (Adapted from Ref.53). (B) Schematic illustration of the working principle for the Cu ²⁺ mediated on-off-on Au NC-based fluorescent probe for rapid <i>Escherichia coli</i> detection. (Adapted from Ref.54). (C) Simplified scheme of pH controllable adherence of CP-GNC to <i>E. coli</i> cells. Specially, CP-GNC was fully attached to the cells at pH 5.2, whereas all the CP-GNC detached from the surface of <i>E. coli</i> cells at pH 7.4. (D) Bacterial cells can be efficiently labelled and form cell clusters using CP-GNC. (Adapted from Ref.55)	14
Figure.11	(A) Schematic illustration of the syntheses of AuAg NCs and photoluminescent quenching by <i>Acinetobacter baumannii</i> . (B) The fluorescence of Au/Ag NCs was selectively quenched by <i>A. baumannii</i> . The order numbers from 1 to 10 in turn represent the group in the presence of no bacteria (control), <i>Bacillus mycoides</i> , <i>Staphylococcus aureus</i> , methicillin-resistant <i>S. aureus</i> , <i>Candida albicans</i> , <i>P. aeruginosa</i> , <i>E. coli</i> , vancomycin-resistant <i>Enterococcus faecium</i> , <i>Saccharomyces cerevisiae</i> , and	16

	<p><i>A. baumannii</i>, respectively. (C) The concentration dependent quenching effect of <i>A. baumannii</i> toward AuAg NCs. Insets: Digital photos of AuAg NCs under UV illumination after treatment with different concentrations <i>A. baumannii</i>. (D) Relative fluorescence intensity (I_0/I) of AuAg NCs in contrast to the logarithm of the <i>A. baumannii</i> concentrations. (E) The transmission electron microscopy (TEM) micrographs of photoluminescent AuAg NCs treated with 1×10^5 CFU/mL <i>A. baumannii</i> demonstrate the bacteria induced agglomeration of NCs. (Adapted from Ref.57)</p>	
Figure.12	<p>(A) Interaction of the fluorescent probe with bacterial cells: structure of the probe with AHL signal molecules deployed on the surface with lactone and amide moieties intact (top) and specific binding of AHL head groups to receptor sites in Lux-R regulators within bacteria (bottom). (Adapted from Ref.58) (B) Visualization of mannose-protected Au NCs (25 nM) in the absence (left) and presence (right) of <i>E. coli</i> (2.5×10^8 CFU/mL) upon excitation under a hand-held UV lamp (365 nm). (Adapted from Ref.59) (C) Schematic diagram of the synthesis of the red fluorescent lysozyme-Au NCs and fluorescence enhancement detection of <i>E. coli</i>. (Adapted from ref.62)</p>	17
Figure.13	<p>(A) Schematic illustrations of (top) one-step preparation of AuNCs@Van and (bottom) determination of <i>S. aureus</i> in mixtures using the aptamer-coated magnetic beads and Au NCs@Van dual recognition strategy. (Adapted From Ref.65) (B) Illustration of the vancomycin and aptamer dual-recognition molecule-based FRET assay platform for <i>S. aureus</i>. (Adapted from Ref.64) (C) Illustration of the immunoassay of <i>E. coli</i></p>	18

	O157:H7 using AuNCs@CS nano capsules and Au NCs as labels. (Adapted from Ref.66)	
Figure.14	(a) The procedure for developing a golden silk synthesis approach. The photos also show pristine and golden silk under visible and UV light; (b-d) confocal fluorescence, DIC, and overlay images of a single pristine silk strand; (e-g) confocal fluorescent, DIC, and overlay images of a single golden silk strand. (Adapted from Ref.68)	20
Figure.15	Anti-counterfeiting golden silk or fabric (a, b) the pristine silk-based fabric in visible and UV light; (c, d) the golden fabric in visible and UV light; (e, f) the anticounterfeit label in visible and UV light, which was produced by needlework stitching golden silk on a pristine fabric. (Adapted from Ref.68)	21
Figure.16	Anti-counterfeit ink images of handwriting on several types of paper using as-prepared fluorescent Au NCs. Weighing paper, regular office paper, and Kraft paper, from left to right. (Adapted from Ref.69)	21
Figure.17	(A) A diagram of the stencil printing process used to print the QR code on a banknote. (B) BBOT chemical structure and absorption spectra. (C) A combination of NCs and BBOT was used to create a combined PL spectrum. Under UV light, photographs of (D) QR code-printed money and (E) data decryption using a smartphone. (Adapted from Ref.70)	22
Figure.2.1	¹ H NMR spectrum of 11-mercapto-N, N', N''-tripropylundecan-1-ammonium chloride ligand	37
Figure.2.2	FTIR spectra of ethanolic solution of oleic acid at pH= 7 and pH=9. At neutral pH -C=O stretch could be seen at 1710 cm ⁻¹	39

	shown by arrow which shows that H ⁺ of –COOH is bound. At pH=9, C=O stretch band shown by arrows appeared at 1651 cm ⁻¹ (symmetric stretch) and 1567 cm ⁻¹ (asymmetric stretch).	
Figure.2.3	FTIR spectra of (a) AuNC@OA@C-6AHL, (b)C-6AHL, (c)AuNC@OA@C-8AHL, (d) C-8 AHL, (e) AuNC@OA@C-12AHL and (f) C-12AHL	39
Figure.2.4	FTIR spectra of AuNC and AuNC@OA with (A) C-6 AHL and AuNC@OA@C-6AHL (B) C-8 AHL and AuNC@OA@C-8 AHL (C) C-12 AHL and AuNC@OA@C-12 AHL	40
Figure.2.5	TEM images of (A) Au nanoclusters (B) AuNC@OA@C-6AHL(C)AuNC@OA@C-8AHL (D) AuNC@OA@C-12AHL	41
Figure.2.6	Fluorescence spectra of Au nanoclusters and Au NC's composites (excitation wavelength at 420 nm)	42
Figure.2.7	Fluorescence spectra of Au nanoclusters at day 1 to 365 days (excitation wavelength at 420 nm)	43
Figure.2.8	Fluorescence microscopy images of (A)(left column) <i>E. coli</i> incubated with AuNC@OA@C-6AHL (scale bar-500μm), AuNC@OA@C-8AHL(scale bar-1000μm), AuNC@OA@C-12AHL(scale bar-500μm), (B)(middle column) <i>C. sakazakii</i> incubated with AuNC@OA@C-6AHL(scale bar-500μm), AuNC@OA@C-8AHL(scale bar-1000μm), AuNC@OA@C-12AHL(scale bar-500μm) & (C) (right column) <i>P. aeruginosa</i> incubated with AuNC@OA@C-6AHL(scale bar-1000μm), AuNC@OA@C-8AHL(scale bar-1000μm), AuNC@OA@C-12AHL(scale bar-1000μm)	44

Figure.2.9	Fluorescence microscopy images of (A) <i>E. coli</i> incubated with AuNC, (B) <i>E. coli</i> incubated with AuNC@OA (C) <i>E. coli</i> incubated with AuNC@C-6 AHL (D) <i>E. coli</i> incubated with AuNC@C-8 AHL (E) <i>E. coli</i> incubated with AuNC@C-12 AHL	45
Figure.2.10	Fluorescence microscopy images of <i>C. sakazakii</i> incubated with (A) AuNC (B) AuNC@OA (C) AuNC@C-6 AHL (D) AuNC@C-8 AHL (E) AuNC@C-12 AHL	47
Figure. 2.11	Fluorescence microscopy images of <i>P. aeruginosa</i> incubated with (A) AuNC, (B) AuNC@OA, (C) AuNC@C-6 AHL, (D) AuNC@C-8 AHL, (E) AuNC@C-12 AHL	48
Figure.2.12	TEM images taken for <i>Escherichia coli</i> when incubated with AuNC@OA@C-12AHL conjugates at various scales	49
Figure.2.13	Average fluorescence intensity of bacterial cells with different AuNC composites. AuNC was used as negative control (**p<0.01 and ***p< 0.001) (n=3).	50
Figure.3.1	HR-TEM images of AuAg nanoclusters and Au nanoclusters, (a & e) AuNC, (b & f) AuAgNC-1, (c and g) AuAgNC-2 and (d & h) AuAgNC-3. Particle size distribution histograms of (i) AuNC, (j) AuAgNC-1, (k) AuAgNC-2 and (l) AuAgNC-3. Top horizontal row (left to right) images are with scale bar 5nm and bottom row (left to right) images are with scale bar 2nm. (m, n and o) shows the HR-TEM images and particle size distribution of AgNCs.	62
Figure.3.2	HR-TEM images describing their crystalline nature with d-spacing analysis for all the nanoclusters i.e., (a) AuNC (scale bar 2 nm), (b) AuAgNC-1(scale bar 2 nm), (c) AuAgNC-2(scale bar	63

	2 nm), and (d) AuAgNC-3(scale bar 5 nm). Crystalline nature of nanoclusters is visible in the magnified images given in the insets.	
Figure.3.3	Elemental mapping through STEM-HAADF images of nanoclusters i.e., (a) AuAgNC-1, (b) AuAgNC-2, (c) AuAgNC-3. The dotted circles indicate the presence of Au and during EDS analysis	64
Figure.3.4	EDS through TEM giving wt% of Au and Ag in (a) AuAgNC-1, (b) AuAgNC-2, (c) AuAgNC-3	65
Figure.3.5	XPS spectrum showing (a) Au 4f core-level and (b) Ag 3d core-level binding energies for their respective pristine AuNC, and bimetallic AuAgNCs	66
Figure.3.6	XPS spectrum having Au 4f binding energies for bimetallic (a)pristine AuNC, (b) AuAgNC-1, (c) AuAgNC-2 and (d) AuAgNC-3. This also shows the effect of Ag doping and the presence of Au ⁺¹ over the bimetallic nanoclusters	68
Figure.3.7	XPS spectrum having Ag 3d binding energies for (a) pristine AgNC, (b) AuAgNC-1, (c) AuAgNC-2 and (d) AuAgNC-3	69
Figure.3.8	XPS spectrum having S 2p _{3/2} binding energies in pristine (a) AuNC, (b)AuAgNC-1, (c)AuAgNC-2, (d) AuAgNC-3 and (e) AgNC, (f) Au ⁺¹ -SR complex	70
Figure.3.9	(a) Absorption spectra and (b) Photoluminescence spectra for pristine AuNC and bimetallic AuAgNCs	71
Figure.3.10	Describing the PL stability in terms of c.p.s of (a)AuNC and bimetallic nanoclusters i.e., (b) AuAgNC-1, (c) AuAgNC-2 and (d) AuAgNC-3. The PL intensity are checked (excitation	73

	wavelength~420 nm) at different time scale from 1 st day to 30 th day	
Figure.3.11	Photoluminescence decay components of (a) pristine AuNC, (b) AuAgNC-1, (c) AuAgNC-2 and (d)AuAgNC-3	74
Figure.3.12	FTIR spectra of AuAgNC-3@OA and OA	78
Figure.3.13	FTIR spectra of (a) C-6 AHL, (b) AuAgNCs-3@OA @C-6AHL, (c) C-8AHL (d) AuAgNCs-3@OA @C-8AHL (e) C-12AHL (f) AuAgNCs-3@OA @C-12AHL	79
Figure.3.14	PL intensities after making AuAgNC-3 conjugates with oleic acid and AHLs	80
Figure.3.15	(a)Fluorescence microscopy images of <i>Escherichia coli</i> incubated AuAgNCs-3@OA@C-6AHL (top row and scale bar-500μm), (b) Average fluorescence intensity of bacterial cells with different AuAgNC-3 composites and comparison with the average fluorescence intensity of bacterial cells when incubated with AuNC and their composites, (c) STEM-HAADF elemental mapping image for <i>Escherichia coli</i> when incubated with AuAgNC-3@OA@C-6AHL	82
Figure.3.16	Fluorescence microscopy images of <i>Escherichia coli</i> incubated AuAgNCs-3@OA@C-6AHL (top row and scale bar-500μm), AuAgNCs-3@OA@C-8AHL (middle row and scale bar-500μm), AuAgNCs-3@OA@C-12AHL (bottom row and scale bar-500μm)	83
Figure.3.17	Average fluorescence intensity of bacterial cells with different AuAgNC-3 composites and comparison with the average	83

	fluorescence intensity of bacterial cells when incubated with AuNC and their composites	
Figure.3.18	Photoluminescence spectra of supernatant liquid solution collected after AuAgNC-3@RSF composite gel formation (excitation $\lambda=420\text{nm}$)	86
Figure.3.19	ATR spectra for untreated RSF solution, untreated RSF gel and AuAgNC-3 coated silk fibroin gel (RSF@AuAgNC-1) depicting non-covalent interaction with AuAgNC-3	87
Figure.3.20	Elemental analysis indicating leaching of (A) amount of Au and (B) amount of Ag metal at different time intervals from the AuAgNC-3@RSF composite.	88
Figure.3.21	An attempt to write letters (a) “CSIR” on Indian INR. 10 currency note (b) on glass slide with the help of AuAgNC-3@RSF gel composite	88
Figure.4A.1	^1H NMR of <i>N, N', N''</i> -tripropyl (11-mercaptoundecyl) ammonium chloride	96
Figure.4A.2	^1H NMR of <i>N, N', N''</i> -triethyl (11-mercaptoundecyl) ammonium chloride	97
Figure.4A.3	^1H NMR of <i>N, N', N''</i> -tributyl (11-mercaptoundecyl) ammonium chloride	97
Figure.4A.4	^1H NMR of <i>N</i> -(11-mercaptoundecyl)- <i>N, N'</i> -dimethylbenzenammonium chloride	98
Figure.4A.5	FT-IR spectrum of (a) <i>N, N', N''</i> -triethyl (11-mercaptoundecyl) ammonium chloride ligand (b) <i>N, N', N''</i> -tripropyl (11-mercaptoundecyl) ammonium chloride ligand, (c) <i>N, N', N''</i> -	98

	tributyl (11-mercaptoundecyl) ammonium chloride (d) N-(11-mercaptoundecyl)-N, N'-dimethylbenzenammonium chloride	
Figure.4A.6	Structures of (a) <i>N, N',N''</i> -triethyl (11-mercaptoundecyl) ammonium chloride, (b) <i>N,N',N''</i> -tripropyl (11-mercaptoundecyl) ammonium chloride, (d) <i>N,N',N''</i> -tributyl (11-mercaptoundecyl) ammonium chloride and (d) <i>N</i> -(11-mercaptoundecyl)- <i>N,N'</i> -dimethyl benzenammonium chloride	101
Figure.4A.7	Particle size distribution curves and respective TEM images of (a) AuNC-1 , (b) AuNC-2 , (c) AuNC-3 , (d) AuNC-4	101
Figure.4A.8	XPS spectrum shows the core energy levels i.e., $4f_{7/2}$ and $4f_{5/2}$ for (a) AuNC-1 , (b) AuNC-2 , (3) AuNC-3 and (d) AuNC-4	102
Figure.4A.9	Absorption spectra for AuNC-1 , AuNC-2 , AuNC-3 , and AuNC-4 shows discrete absorption bands denoted by arrows in the UV-Vis region	103
Figure.4A.10	PL spectra of all modified thiol capped Au nanoclusters excited at different wavelengths mentioned in Table.4.3	104
Figure.4B.1	Representative images during and after synthesis of <i>Au nanoclusters capped with N</i> -(11-mercaptoundecyl)- <i>N, N'</i> -dimethylbenzenammonium chloride	113
Figure.4B.2	TEM images of The AuNCs-dialyzed solution (Resolution~20nm). Yellow arrows around the self-assembled nanoclusters show aggregation effect	114
Figure.4B.3	HR-TEM images of AuNCs-supernatant solution of AuNCs (Resolution~10nm)	114

Figure.4B.4	XPS spectrum for (a) AuNCs-supernatant , (b) AuNCs-dialyzed	115
Figure.4B.5	Absorption spectrum for AuNCs-dialyzed , AuNCs-supernatant , AuNCs-colloid	116
Figure.4B.7	Fluorescence spectra of aqueous solution of AuNCs-dialyzed at various excitation wavelength. * Mark indicates 2 lambda wavelengths	117
Figure.4B.8	Fluorescence spectra of aqueous solution of AuNCs-dialyzed excited at (a) 380 nm and (b) 420 nm at different temperatures	117,118
Figure.4B.6	Solvent dependent fluorescence showed for AuNCs-dialyzed from stage-I to stage-III to show the regenerative emission characteristics for these nanoclusters. The correct tick label shows that red emission is present after organic solvent addition (stage-II).	119

Sr. number	Caption	Page number
Scheme.2.1	Scheme representing the synthesis of 11-mercapto-N, N', N''-tripropylundecan-1-ammonium chloride	33
Scheme.2.2	Bacterial cells incubated with fluorescent nanoprobe (A) Nanoprobe structure here AHL moiety deployed on the surface without disturbing amide and lactone moiety (B) Specific binding of AHL head groups from the AuNC@OA@AHL composites to receptor sites in Lux-R regulators within bacteria	36
Scheme 2.3	Structures of signal molecules with base Acyl homoserine skeleton. Cognate signal molecules synthesized by <i>C. sakazakii</i> and <i>P. aeruginosa</i> and those known to be detected by <i>E. coli</i> are given along with the ones used in this study	37
Table.2.1	Description of all important FTIR bands of AHLs and AuNC@OA@AHLs conjugates	41
Table.3.1	Variation in Ag ⁺¹ doping during AuAgNC synthesis with their elemental analysis	60
Table.3.2	Average d-spacings were calculated for 5 different particles from AuNCs, AuAgNCs and AgNCs and tabulated below	61
Table.3.3	Correlation between MP-AES analysis and EDS data for all the bimetallic AuAg nanoclusters	63
Scheme.3.1	Illustration of electron density redistribution from metal to metal on the nanocluster surface, surface metal atoms to Sulphur (thiolate) and metallophilic interactions between positive cation i.e., Au ⁺¹ and reduced metal (Au/Ag) on the nanocluster surface. Case-I and Case-II represents AuNCs and AgNCs, Case-III represents AuAgNC-1 and Case-IV represents- AuAgNC-2 and AuAgNC-3. Dotted lines show bonding between atoms	67
Table.3.4	Binding energies for Au ⁰ , Au ⁺¹ and Ag in pristine Au	68

	nanoclusters and bimetallic AuAgNC-1, AuAgNC-2 and AuAgNC-3	
Table.3.5	Absolute luminescence quantum yields and decay lifetimes of luminescent AuNCs and bimetallic AuAgNCs	73
Scheme.3.2	Illustration of the photoluminescence mechanism of red emission of AuNC and AuAg NCs via LMCTs and LMMCT	75
Table.3.6	Zeta potential values of pristine Au nanoclusters and bimetallic AuAgNC-1, AuAgNC-2, AuAgNC-3 nanoclusters	76
Scheme.3.3	Schematic way to present the structure of AuAgNCs and presence of metallophilic interactions between Au ⁺¹ --- Au/Ag on the surface of AuAgNCs	77
Scheme.3.4	Illustration of the mode of interaction of Au ⁺¹ species over AuAg bimetallic nanoclusters	77
Table.3.7	Describes the important stretching frequencies of lactone in AHL and AuAgNCs-3@OA @AHL conjugates	80
Table 3.8.	Abs. quantum yield (%) of surface functionalized AuAgNC and their composites	81
Table.3.9.	Zeta potential values of AuAgNC-3 and their surface functionalized composites	81
Scheme.3.5	(a) Illustration of Random coil of RSF transformation to β -sheets when incubated with aqueous solution of AuAgNC-3, (b) Fluorescence images of AuAgNC-3@RSF gel taken under FAR-UV illumination	84
Scheme.3.6	Illustration of mode of interaction between aqueous solution of AuAgNC-3 and RSF	85
Table.3.10	Comparative stretching frequencies (amide) of RSF solution, RSF gel and AuAgNC-3@RSF gel	87

Table.4A.1	Binding energies for core energy levels i.e., Au 4f _{7/2} and Au 4f _{5/2} in all Au nanoclusters	103
Table.4A.2.	Electronic transition band positions in the case of AuNC-1 , AuNC-2 , AuNC-3 , and AuNC-4	104
Table 4A.4	Comparison of the absorption spectra from UV-visible region with Mulliken charges and HOMO-LUMO energy gaps as obtained from DFT calculations	105

Chapter 1

Introduction and Literature Survey



Fluorescence biomedical imaging, which allows observation of the activity of specific organs or tissues, has become a significant tool for fundamental medical research analysis and medicinal interventions over the last ten years. Fluorescence biomedical imaging uses imaging agents that are excited into a higher energy state by light stimulation and then release light radiatively as they return to their ground (non-excited) state.^{1,2} Traditional optical imaging of living biological tissues is limited by the resolution and permeability of light in the tissue of interest³, with biofluorescence imaging and fluorescence detection providing viable ways for circumventing these limits⁴. Organic fluorescent dyes, carbon nanomaterials, quantum dots, and up-conversion nanomaterials are only a few of the bioimaging reagents that have been developed for biomedical applications.^{5,6,7} Organic fluorescent dyes are organic molecules that contain a mixture of conjugated systems, such as aromatic rings and heterocycles. Fluorescein and its derivatives have low temperature coefficients and high fluorescence quantum yields. They are, however, easily bleached, have tiny Stokes shifts, and are water insoluble, limiting their efficacy as imaging agents. Up-conversion materials with rare earth doped, such as NaY-F4:Yb,Er nanocrystals, can be stimulated in the near infrared (NIR) region (980 nm), where biological molecules do not adsorb, and thereafter emit at specific shorter wavelengths.⁸ The ability of NIR light to easily penetrate thick tissues is extremely desirable for biological imaging (avoiding tissue autofluorescence), promising an efficient and sustained luminescence signal at visible wavelengths. Rare earth-doped up-conversion nanoparticles or their metabolites, on the other hand, may be hazardous, limiting their usefulness in biomedical applications.⁹ Semiconductor quantum dots (QDs) like CdS and CdSe have size-dependent excitation and emission wavelengths with a very restricted emission wavelength range. Furthermore, unlike traditional organic fluorescent dyes, the emission wavelengths may be tuned by excitation with different wavelength lasers.⁸ However, because cadmium is hazardous, it is not practicable to use cadmium-based QDs in biomedical imaging.¹⁰

Anti-counterfeiting and security applications for determining authenticity are another rising application of fluorescence. Counterfeiting and forgery are important social issues that cause people to lose a lot of money every year and put their personal privacy and social stability at risk. It is crucial to build an anti-counterfeiting substance that is both inexpensive and non-toxic, as well as ultra-stable and ability to accomplish multiple anti-counterfeiting functions. Resistance to photobleaching and leaching, colourless in white light, high Stokes shift etc. are some of the desired properties for such materials. Most of the above-mentioned

fluorescent materials do not possess the desired qualities. Hence, designing new materials which fit the requirements is essential. In this context, noble metal nanoclusters (less than 2 nm in size) comprised of few atoms to hundreds of atoms (usually Ag or Au) have unique fluorescence features that make them useful for such applications.^{10,11} Larger nanoparticles (e.g., 5–10 nm) of the same noble metals lack these distinguishing fluorescence characteristics. The noble metal nanoclusters are created using protein, peptides, or small organic molecules as template or capping agents, which improves biocompatibility and enables for facile adjustment of surface properties for specific purposes. Irradiation stability, a large Stokes shift (excitation and emission maxima are well isolated), and size-dependent excitation and emission spectra allow the emission maximum to be varied from the visible to near infrared wavelength region are all properties that noble metal nanoclusters have that make them good fluorescent labels.¹² The fluorescence characteristics of Au nanoclusters have been the most intensively studied among noble metal nanoclusters.^{12,13}

1.1. Ultra-small metal nanoclusters

In recent years, metal nanoparticles and metal nanoclusters have attracted interest due to their size dependent physical and chemical properties and promising applications. Metal nanoclusters having size ≤ 2 nm are made up of ten to hundred atoms capped by strong electron donor ligands like phosphines, thiols, amines, selenides etc. Metal nanoclusters are generally designated with the formula, M_xL_y (x = number of metal atoms present in the core, y = ligands present on the surface of metal core). Because of the ultra-small size, their

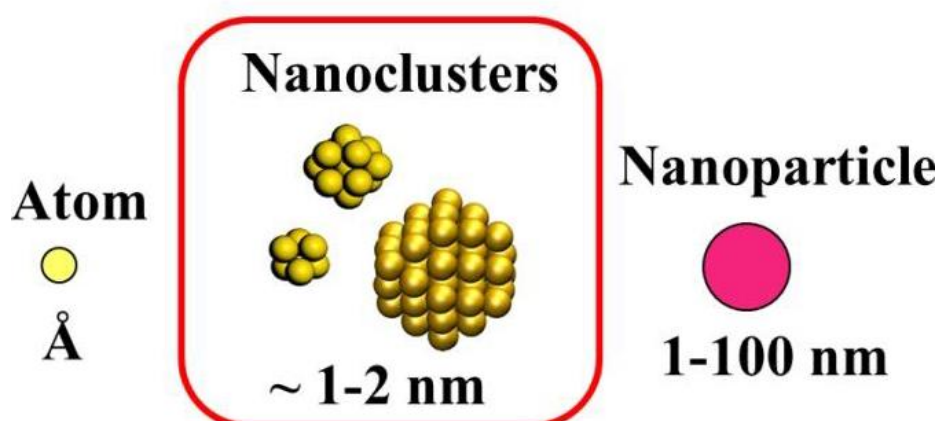


Figure.1. Size comparisons of nanoclusters with nanoparticles and atoms

photophysical properties differ from their bulk and nanoparticles counterparts. In the case of ultra-small metal nanoclusters, continuous/semi continuous density of energy states breaks into discrete energy levels which results in the unique molecule like properties, like HOMO-LUMO electronic transitions, quantized charging, intrinsic magnetism, optical activity, photoluminescence etc.¹⁴ Due to dimensions in between atoms and nanoparticles, ultra-small nanostructures form the missing link between atoms and nanoparticles. Hence, the structural and physio-chemical properties of nanoclusters are very important in order to understand the gradual emergence of various properties and crystal structures in solids.

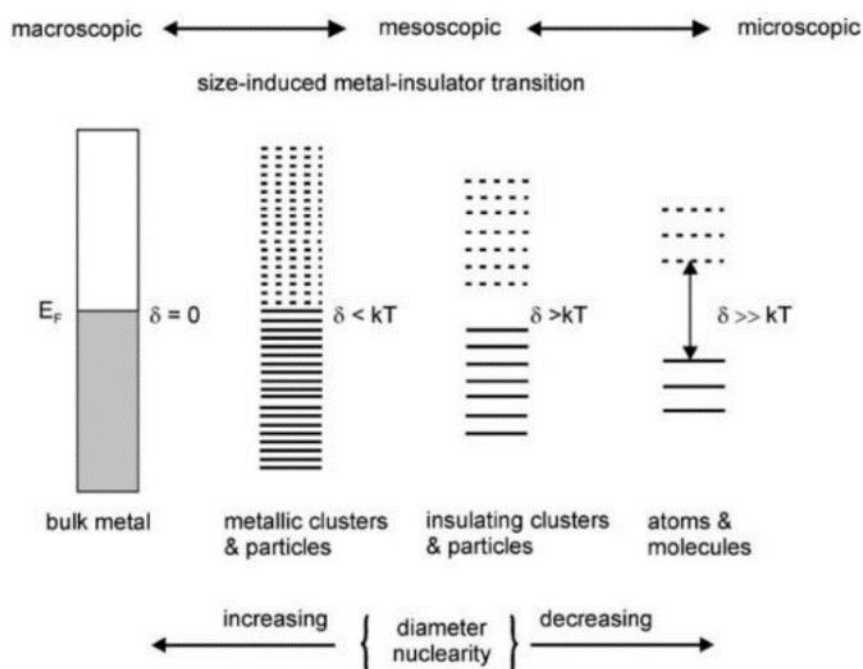


Figure.2. Evolution of band gaps and density of states (DOS) in bulk material, nanoparticles, and nanoclusters. (E_F : Fermi level) δ is the so-called Kubo gap. Adapted from Ref.14.

1.2. Optical properties (UV-Visible absorption) of nanoparticles vs nanoclusters

Interaction of light with metal particles gives rise to plasmon oscillation. This phenomenon involves the interaction of light with metal atoms leading to collective oscillation of surface excited electrons at the metal dielectric surface, known as surface plasmon resonance (SPR).

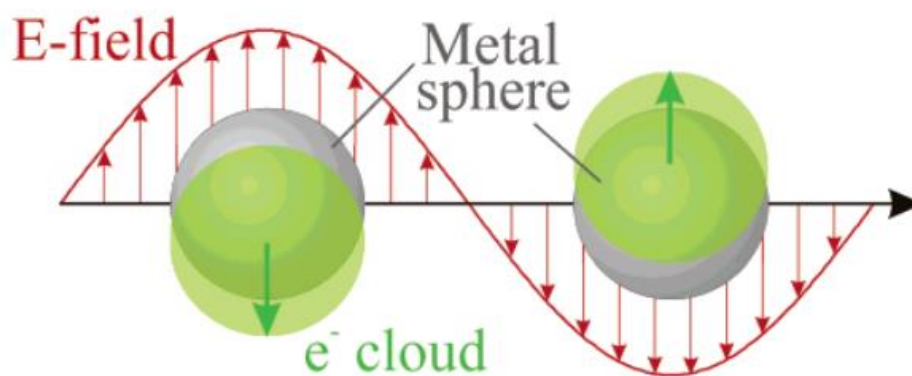


Figure.3. Schematic representation of surface plasmon for a metal sphere, showing the displacement of electron cloud relative to nuclei. Adapted from Ref.15.

SPR arises when the electron cloud is displaced from the nuclei, Coulomb interaction between electrons and nuclei produces a restoring force, causing the electron cloud to oscillate in relation to the nuclear frame- structure in figure 3.¹⁵ Noble metals, for the most part, have plasmon frequencies in the visible light area, allowing them to exhibit colours. Gold nanoparticles have a surface plasmon resonance band that ranges from 500nm to 570nm, depending on their spherical size. Ag, on the other hand, shows SPR band is between 430nm and 460nm. Also, as the size of the noble metal nanoparticles increases, resonance between the oscillating frequency from the conduction electrons and incident photons frequency is no longer homogenous. Retardation effect of the electromagnetic field across the nanoparticle can cause the broadening and shifting of the SPR peak wavelength as shown in figure.4 The SPR peak for Gold, Silver and other noble metals also depends upon the particle-particle interaction, the capping ligand surrounding the metal core, and also the

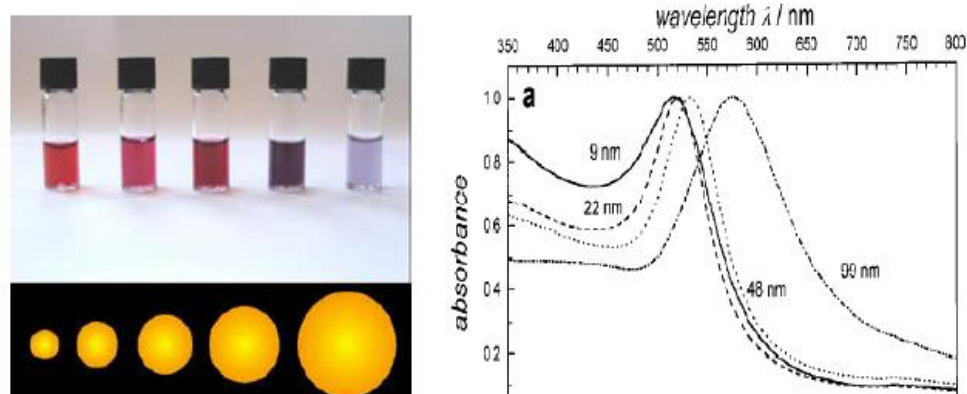


Figure. 4.(a). Change in the colour of nanoparticles solution with the core diameter., **(b)** Surface plasmon peak shift and broadening with the change in the size of gold nanoparticle diameter. Adapted from Ref.16.

dielectric medium of the nanoparticle. Mostly, we observe the SPR peaks for the noble metals having particle size ranges from 2nm to 100nm.¹⁶ When the size of the nanoparticles goes down below 2nm, the plasmon characters for the particle diminishes and quantum confinement gives rise to new discretization of energy.

The size of the core and total number of metal atoms situated on the surface of core of the clusters tunes the energy gap (HOMO-LUMO) between the energy states. However, until the crystal structure was examined, the concept of energy gap distribution and quantum confinement was unclear. In 2008, $\text{Au}_{25}(\text{SR})_{18}$ structure was obtained by Zhu and coworkers, where they correlated the crystal structure and optical properties. They found 3 types of absorption bands (i) HOMO-LUMO intra-band transition, (ii) HOMO orbitals (d-band) to LUMO inter-band transition and (iii) mixed types of transition (given in figure.5).¹⁷

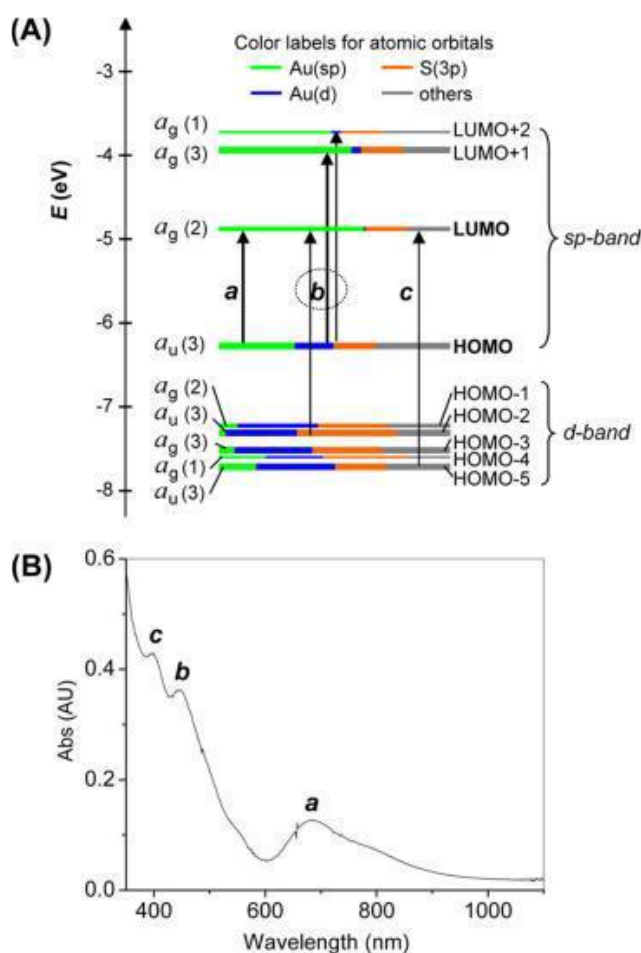


Figure.5. (a) Kohn-Sham orbital level diagram for Au_{25} clusters. (b) Peak assignment of absorption spectrum of Au_{25} clusters. Adapted from Ref.17.

1.3. Luminescence mechanism in noble metal nanoclusters

Mechanistic aspects of luminescence are mostly studied in Au nanoclusters among the metal clusters. The continuous energy levels (of particles) break down into multiple discrete energy states as particle sizes decrease below 2nm, which is comparable to the Fermi wavelength of electrons (1nm). Au nanoclusters also exhibit fluorescence in the visible to near-infrared region, which can be regulated by adjusting the number of Au atoms in the nanoclusters. Sakanaga et al. examined the fluorescence process of Au₂₅ clusters using density functional theory (DFT), looking at both the excitation and emission spectra as well as their temporal dependency.¹⁸ A fluorescence process was postulated based on the study of the electronic band structure, with the excitation peak at 1.8 eV and the emission peak at 2.8 eV, involving 5d→6sp and 6sp→5d transitions, respectively.

After this, an alternative theory was proposed to explain the fluorescence of Au nanoclusters depending upon the compositions. Nanoclusters made from noble metals like Au (size ≤ 2nm) consist of core Au⁰ atoms enveloped by a shell composed of Au⁺ ions. Wen et al. synthesized Au₂₅ clusters with bovine serum albumin (BSA) as a capping agent and examined its temperature dependent fluorescence.¹⁹ Two emission bands were observed: (i) Band -I attributed to 13 core Au⁰ atoms and (ii) Band-II arising from surface 6[-S-Au⁽⁺¹⁾-S-Au⁽⁺¹⁾-S-]chains. Xie's group confirmed that both Au⁰-based core and Au⁺¹-based shell were important for achieving the luminescence by studying the intermediates formed during Au nanocluster's evolution through ESI-MS of intermediates.²⁰ Prof. T. Pradeep and co-workers confirmed an Au₁₃ icosahedral core for Au₂₅(SR)₁₈ through X-ray crystal structure.²¹ Also, the outer shell of the clusters was made up of 12 Au and 18 SR groups. Time dependent DFT was used to model the electronic structures of Au nanoclusters, which suggested that three lowest occupied orbitals were from hybrid 6sp orbitals of Au and HOMO-I to HOMO-V mainly originates from 5d¹⁰ orbital of Au.

1.4. Metal quantum clusters synthesis

Generally, two routes are mostly followed for the synthesis of noble metal nanoclusters i.e. (a) "top-down" and (b) "bottom up". In "top-down" approach, bigger nanoparticles can be etched by strong capping ligands like thiols, peptides, proteins etc. to give smaller size (<2nm) metal nanoclusters. For a "bottom-up" synthesis approach, such synthesis is usually employed, where metal is first reduced and capped by reducing agents and then metal nanoaggregates are reduced to zero oxidation state to form the core of the metal nanoclusters.

Here, special templates can be used such as thiols and other biomolecules (such as DNA, peptides, proteins etc.), dendrimers and polymeric capping agents.

1.4.1. Thiol protecting ligands

n-Alkyl thiolates were used as capping agents because of the formation of well-known Au-S bonds. Generally, it was accepted that Au-S bond strength is similar to Au-Au bond strength, which means that thiolate ligand can modify the surface of the metal core surface i.e. Au-Au bonding and results into formation of Au-S bonds.²² Among all thiolates, Glutathione (GSH) is mostly used as a capping and reducing agent for the quantum clusters synthesis. In the typical procedure of synthesis, GSH first stabilizes Au^{+3} to Au^{+1} and then NaBH_4 reduces Au^{+1} -SR complex to $\text{Au}^0_x(\text{SR})_y$ clusters of various sizes depending upon the condition of the reaction. AuNCs capped with GSH display photostability, strong one and two photon emission and bio-compatibility.²³ Zhang et al. effectively synthesized AuNCs with a core size of 2.5nm at 90° C utilizing GSH as a reducing and capping agent.²⁴ GSH and a moderate reductant, such as tetra butyl ammonium borohydride (TBAB), may also be used to make water soluble Au nanoclusters, which have high fluorescence properties and minimal cytotoxicity²⁵. Recently Gao et al. synthesized AgNCs intra-cellularly by cancerous cells incubated with silver ions.²⁶ Wang and co-workers prepared water soluble Ag_2S nanoclusters, by using GSH as a scaffold and sulphur-hydrazine hydrate complex ($\text{S-N}_2\text{H}_4\cdot\text{H}_2\text{O}$) as S^{2-} source.²⁷ During Ag_2S synthesis, they discovered that photoluminescence characteristics may be adjusted by changing the ratio of Ag^{+1} : $\text{S-N}_2\text{H}_4\cdot\text{H}_2\text{O}$. Wang et al. also synthesized Au/Ag alloy nanoclusters, where AgNCs are synthesized first by using GSH (capping agent) and $\text{N}_2\text{H}_4\cdot 2\text{H}_2\text{O}$ (as a reducing agent).²⁸ Thus, in the aqueous solution of AgNC's, AuCl_4^- ions and GSH were added, to get the galvanic replacement reaction product. Because the standard reduction potential of the $\text{AuCl}_4^-/\text{Au}$ pair (0.99 volts versus S.H.E.) is larger than that of the Ag^+/Ag pair, a galvanic reaction occurred (0.80 volts vs S.H.E.).²⁹ The as synthesized Au/Ag alloy quantum clusters give NIR emission centered at 716 nm and the luminescence can be tuned by varying Au:Ag ratios.³⁰

Since, GSH is a mono-sulphur containing ligand, instead of GSH, Shang et al. synthesized AuNCs-DHLA where DHLA has two sulphur atoms, in a one-pot synthesis strategy.³¹ In this synthesis, Au salt gets first reduced by DHLA into Au^{+1} -DHLA complex and then reduced to Au^0 -DHLA nanostructures with long fluorescence lifetime (>100ns), which

makes them important markers in-cellular Fluorescence lifetime imaging (FLIM) applications.

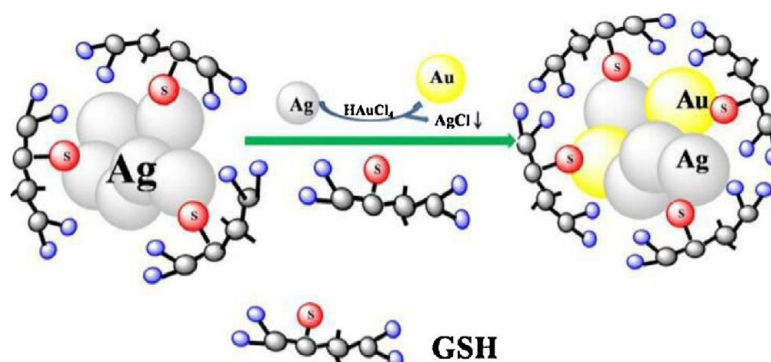


Figure.6. The galvanic replacement reaction process of synthesizing NIR Ag/Au alloy NCs. Adapted from Ref.30.

Afterwards, the same group has done same reaction by irradiating microwave to the reaction mixture, which further increases its quantum yield $\sim 0.6\%$ to 2.9% and shortened the period of reaction from several hours to few minutes.³² Nair and colleagues utilized the same technique to produce $\text{Au}_{18}(\text{LA})_{14}$ nanoclusters with a quantum yield of 10% by utilizing lipoic acid as a capping agent.³³ AuNC's formed with other thiols like mercapto-succinic acid (MSA), DHLA, troponin etc. have also been used as capping agents, which gives AuNCs emission maxima centered at 785nm (NIR emission) with quantum yield ranging from 3% to 4% .³⁴

In the above strategy of synthesis, the nanoclusters are prepared by bottom-up method via capping of metal ions through thiol followed by direct reduction with the help of reducing agents. Metal nanoclusters can also be prepared by etching larger metal nanoparticles with thiol ligands. $\text{Au}_{23}(\text{SG})_{18}$ (SG denotes glutathione) were prepared through the interfacial etching of $\text{Au}_{25}(\text{SG})_{18}$. For interfacial etching, a biphasic solvent system is used, for eg. toluene and water. The etching agent, octane thiol (OT) was added to toluene and the aqueous layer contained $\text{Au}_{25}(\text{SG})_{18}$. Etching occurs at the interface of the biphasic system and the resultant water soluble $\text{Au}_{23}(\text{SG})_{18}$ was found in the aqueous layer.³⁵ In a similar manner NIR emitting AgNCs were obtained where GSH was used as an etching agent and Ag nanoparticles protected by MSA acted as a precursor.³⁶ Lin et al. developed a procedure where AuNP's capped with DDAB (di dodecyl dimethyl ammonium bromide) were synthesized in organic layer.³⁷ Then AuNP's capped with DDAB were etched in organic

solvent by adding Au ions precursors (AuCl_3 or HAuCl_4) to give smaller size AuNCs@DDAB. This hydrophobic AuNCs@DDAB (present in organic solvent) undergo ligand exchange with DHLA and forms water soluble AuNCs@DHLA. The PL quantum yield of AuNCs@DHLA was later improved by the same team of researchers by thermal etching at 70°C , which increased the quantum yield to 7%.³⁷

1.4.2. Proteins, DNA oligonucleotides and Peptides as protecting ligands

Biomacromolecules such as peptides and proteins can also be used to synthesize NIR emitting noble metal quantum clusters. Aside from tiny peptide molecules, macromolecules have a lot of donor sites (such O, N, and S containing groups) that can reduce metals to zero oxidation state. This offers an excellent scaffold for producing metal nanoclusters³⁸⁻³⁷. Notably, Xie et al. first reported BSA (bovine serum albumin) as a better capping agent to form smaller size AuNCs@BSA with emission maximum at 640nm (figure.7).²⁰ Chen et al. also applied the same strategy for the formation of NIR emitting AuNCs@BSA under inert conditions.³⁹ Ratnakumari's group⁴⁰ was able to generate NIR emitting AuNCs@BSA by employing a different reducing agent, ascorbic acid, which was utilized for complete metal reduction and displays emission maximum at 670nm. After this, researchers have tried several macro biomolecules like transferrin family proteins⁴¹, trypsin¹⁵, insulin⁴² and ribonuclease⁴³

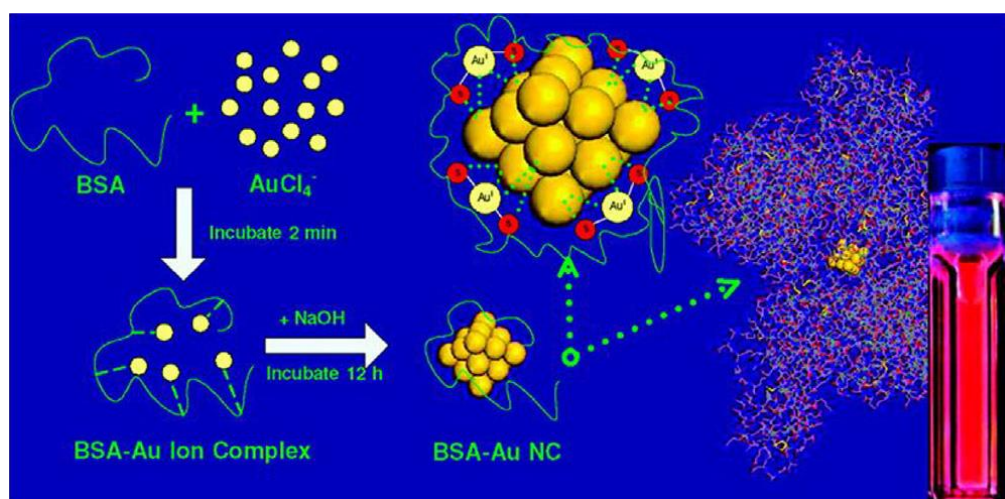


Figure. 7. Schematic of the formation of AuNCs in BSA solution under alkaline conditions. Adapted from Ref.25

as potential bio scaffolds in the synthesis of NIR emitting metal quantum clusters. Synthetically modified peptides can also have naturally occurring peptides and act as

bifunctional which can have the ability of biomineralization of metal ion and retain its activity towards substrate recognition.⁴⁴ In an important work, Gao et al.⁴⁴ developed a protocol for the biomineralization method to get AuNCs with the use of bifunctional CCYTAT peptide. CCYTAT peptide has two domains, one for biomineralization and another domain to target nuclei of the cell. AuNCs obtained from biomineralization by CCYTAT peptide has emission maximum centered at 677nm and quantum yield ~ 11%. Recently AuNCs gold nanoclusters capped by such peptide molecules have shown 70-fold increase in the QY which largely increases their application in bioimaging.⁴⁴ Interaction of metal cations with DNA enables these for further design and fabrication of various metal capped by DNA nanostructures.⁴⁴ Dickson group, firstly reported the application of ssDNA for the synthesis of five different metal cores containing AgNCs@ssDNA having tuneable fluorescence properties ranging from Visible to NIR.⁴⁴ By using four different DNA sequences as Ag nanoclusters template, Sharma et al. synthesized four different AgNCs where they emit at different wavelength with 50% increment in the QY.⁴⁵ It has been reported that Ag⁺¹ ion has greater affinity towards cytosine nitrogen bases than the other kind of nitrogen bases. On the basis of above synthesis procedure, Antoku group⁴⁶ reported NIR emitting AgNCs, where they used oligo-DNA made up of 12 to 24 cytosine bases. Wang group⁴⁷ used more advanced DNA template structures e.g. G-quadruplex, to synthesize AgNCs with 2-4 atoms whose emission maximum is at 680nm.

1.4.3. Polymers

Polymers are also used in the synthesis of metal nanoclusters. Their role is to sequester the metal ions from the solution. Polymers mostly have 2 domains, where one domain is involved in the nanocluster formation and another domain has certain functional groups or charged groups free for further biofunctionalization. Huang et al.⁴⁸ used one step reduction by NaBH₄ method for the synthesis of gold nanoclusters, by using multidentate templates as thio-ether terminated poly (methacrylic acid) (PTMP-PMAA), polydentate polymers etc. QY obtained was ~4.8% at an emission maximum of 660nm. In another report, HAuCl₄ was thermally reduced by thiolated PEG (poly ethylene glycol) (M.W.~1kDa) to synthesize fluorescent (PEG)-AuNP's in aqueous solution with emission maximum at 810nm.⁴⁹

1.5. NIR emitting metal quantum clusters in bioimaging

As discussed in previous sections, metal quantum clusters can show wide range in emission from Visible to NIR. However, NIR emitting metal nanoclusters, have attracted more interest owing to their low background autofluorescence and deeper tissue penetration properties. In 2012, Shang and coworkers³² explained the utilization of DHLA as capping agent for the synthesis of AuNCs. DHLA capped AuNC's was then incubated with HeLa cells, where an intracellular fluorescence quenching effect was observed after addition of Hg^{2+} ions. Afterwards the biological interaction of Human Serum Albumin (HSA) with AuNCs can be studied by modulating the surface charge of AuNCs.⁵⁰ Further, they used confocal microscopy to quantify the uptake and localization of AuNCs in the HeLa cells, they found difference in the uptake of AuNCs adsorbed HSA (figure.8)

Gao et al.⁵¹ synthesized AuNCs with bifunctional CCYTAT peptide which could target or sense the nucleus of 3 different cell lines including human cervical cancer cells (HeLa), normal cells human gastric mucosa cells (GES-I) and human embryonic lung fibroblast (MRC-5). Interestingly during imaging, they found uptake of AuNCs capped with CCYTAT more in the nucleus of HeLa cells compared to GES-I and MRC-5 cells. Ai and co-workers found that AgNCs formed with the G-quadruplex template have special binding affinity towards nucleolin over-expressed cancer cells,⁴⁷ which helps in the bioimaging of HeLa cells. Guevel et al.³⁶ employed AgNCs-GSH as an optical fluorescent probe (NIR emitting) for the imaging of epithelial cancer cells (A549 cells).

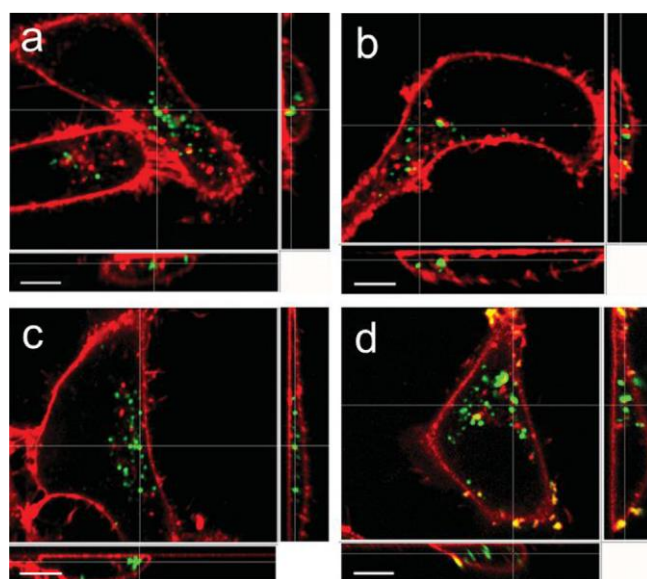


Figure.8. Three-dimensional fluorescence confocal images of HeLa cells upon incubation with AuNCs (2.5 mMol/L, green) for 2 h: (a) without proteins and with 2.5 mMol/L (b) nHSA, (c) aHSA and (d) cHSA. Cell membranes were stained with Cell Mask Deep Red

(red). The data are shown as sections in the x-y plane (upper left), x-z plane (lower left) and y-z plane (right). Scale bar, 10 nm. Adapted from Ref. 50.⁵⁰

It was found that AgNCs were taken up more in the vesicles of A549 cells and in the cytoplasm but absent in nucleus. In contrast, Wang et al.^{27,30} studied that Ag₂S and Au/Ag alloy clusters capped with GSH were not only distributed in the nucleus, as well as in the cytoplasm of MC3T3-EI cells and CAL-27 cells. Recently, many reports have focused on in-vivo tumour imaging done by fluorescent metal nanoclusters. Wu et al.⁵² firstly reported tumour imaging with the help of AuNCs-BSA. This AuNCs-BSA have high contrast and could be easily distinguishable from the background. With the help of enhanced permeability, ultrasmall AuNCs were able to be highly concentrated in the tumour areas (figure.9)

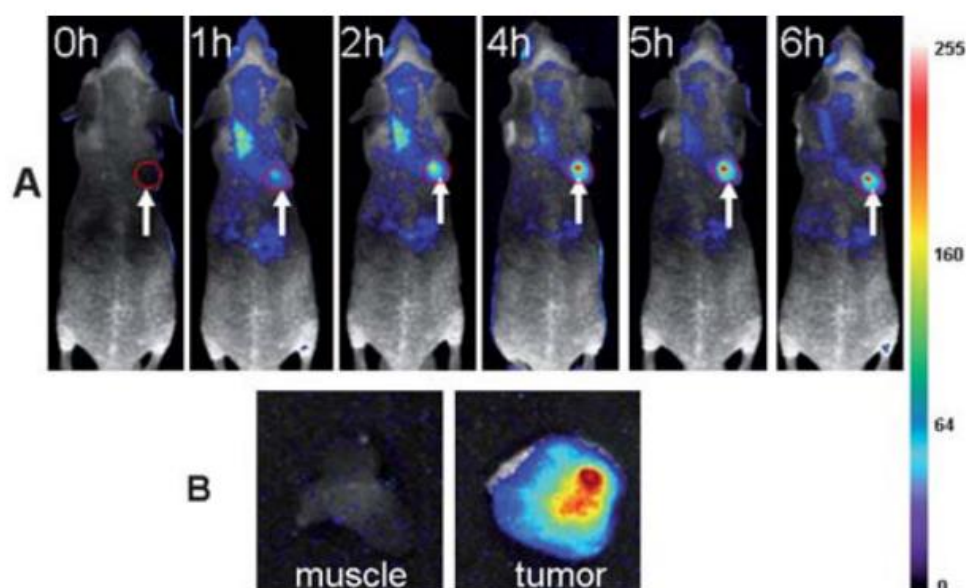


Figure.9. (A) Fluorescence images of mice bearing an MDA-MB-45 tumour. Strong signal from AuNCs was observed in the tumour (marked by the red circle). The arrowheads indicated the tumour. (B) Ex vivo fluorescence image of the tumour tissue and the muscle tissue around the tumour from the mice used in A. Adapted from Ref.52.⁵²

Sun et al. achieved bioimaging and ferritin receptor mediated targeting with the use of far-red emitting AuNCs. They show that AuNCs emits in far red region and is a good probe for targeting over expressed human Caco-cell 2 ferritin receptors as well as precise targeting to the kidney of entire nude mice. The renal clearance of AuNCs-GSH and AuNCs-PEG has been published for the in vivo NIR targeting of MCF-7 tumour bearing mice.^{24,25}

1.6. Detection of bacteria with noble metal nanoclusters, specially by gold nanoclusters

1.6.A. Label free detection of bacterial strains

Depending upon the fluorescence changes induced by bacterial cells, NIR emitting metal nanoclusters can be employed for the detection of bacteria without surface functionalization of metal nanoclusters. Chan et al.⁵³ found that human serum albumin (HSA) protected AuNC are selective towards the detection of *S. aureus* and methicillin resistant *S. aureus* (MRSA). HSA-AuNCs can have high affinity towards *S. aureus* and MRSA, resulting fluorescence enhancement (Figure.10a). Yan et al.⁵⁴ designed a luminescent on-off-on probe based on gold nanoclusters for fast and selective detection of *E. coli*, by sequestering the Cu^{2+} binding and redox pathway of *E. coli* to redeem the luminescence of Au nanoclusters from Cu-based quenching (from figure.10). This is a kind of selective and rapid detection of *E. coli* from the artificial contaminated water having trace amounts of bacterial cells (89CFU/mL) within thirty minutes. Liu et al.⁵⁵ developed a method of bacterial detection by the binding of AuNCs with the cell wall of bacterial cells having negative charge on their cell surface (in G-ve bacteria teichoic acid is present and in Gram positive bacteria phosphates are present in their structure).

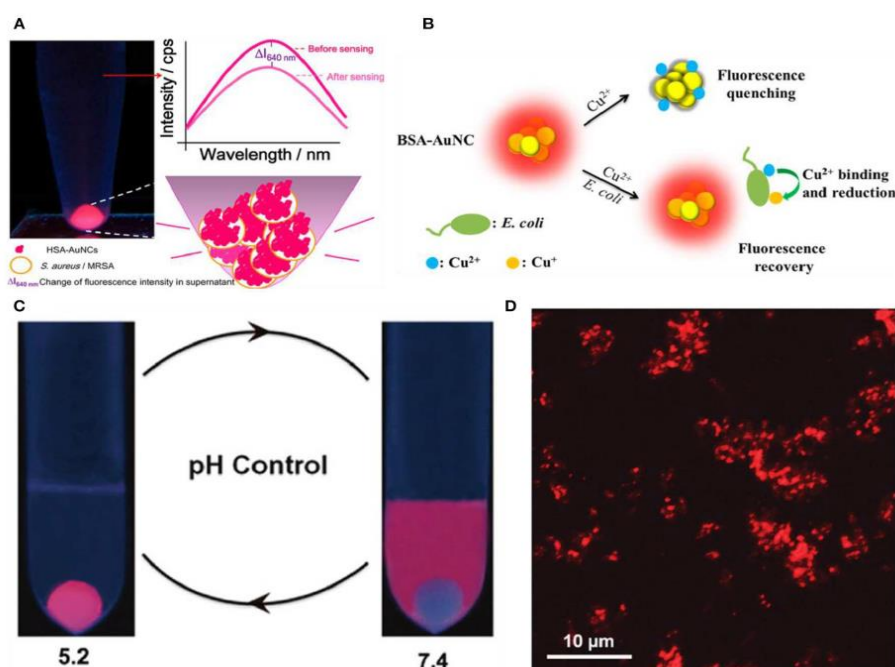


Figure.10. (A) Luminescent HSA-Au NCs as selective probes for *Staphylococcus aureus* and MRSA. Adapted from Ref.53.⁵³ (B) Schematic illustration of the working principle for the Cu^{2+} mediated on-off-on Au NC-based fluorescent probe for rapid *Escherichia coli*

detection. Adapted from Ref.54.⁵⁴ (C) Simplified scheme of pH controllable adherence of CP-GNC to *E. coli* cells. Specially, CP-GNC was fully attached to the cells at pH 5.2, whereas all the CP-GNC detached from the surface of *E. coli* cells at pH 7.4. (D) Bacterial cells can be efficiently labelled and form cell clusters using CP-GNC. Adapted from Ref.55.⁵⁵

In this protocol, BSA capped Au nanoclusters are firstly synthesized. BSA is an amphoteric ligand, which develops a charge on itself caused by environmental pH change. Since bacterial cells are negatively charged, the binding and release of BSA-AuNCs to the cell wall of bacteria depends upon the pH. From the confocal microscopy studies, it is clear that BSA-AuNCs were efficiently labelled with *E. coli* at pH~5.2 (figure 10d). In another work carried out by Pranantyo and coworkers,⁵⁶ it is explained that antimicrobial agent capped AuNCs also is an efficient candidate for bacterial cell detection, where the binding of fluorescent probes depends upon the pH. Recently Zeng et al.⁵⁷ found that the fluorescence properties of thiol capped AuNCs can be enhanced by Ag⁺¹ doping. The enhanced luminescence shown by Au/Ag alloy nanoclusters can be selectively and rapidly quenched by *A. baumannii* because of agglomeration of nanoclusters, which permits the label free detection of *A. baumannii* with a limit of detection~ 2.3×10^3 CFU/mL (in figure 11).

1.6.B. Recognition of bacteria through molecular motifs

The biggest drawback of label-free metal nanoclusters is that, the detection is generally non-selective and non-ideal. To improve the efficiency and selectivity of metal nanoclusters towards the bacterial strains, it is important to label metal nanoclusters with specific type of ligands. Mukherji et al.⁵⁸ decorated specific AHLs with different acyl chain (AHLs are autoinducers synthesized by gram negative bacteria) over the specially designed AuNCs that could sense the Lux-R homologues regulators in *E. coli*. Such decoration allows to differentiate *S. aureus* & *E. coli* with help of confocal microscopic studies (figure 12.A). It was found from confocal microscopic studies that the specially decorated AuNC only interacts with *E. coli* (Gram negative bacteria) and not *S. aureus*. Khlebstov et al.⁵⁹ used highly fluorescent BSA-capped AuNCs decorated with antiSAIgG (anti staphylococcal immunoglobulin) for the detection of *S. aureus* in bacterial mixture. According to Harris group⁶⁰, type-I fimbriae present on the surface of *Enterobacteriaceae* species for ex. *E. coli*, are considered to be responsive for the mannose and mannoside binding active sides.

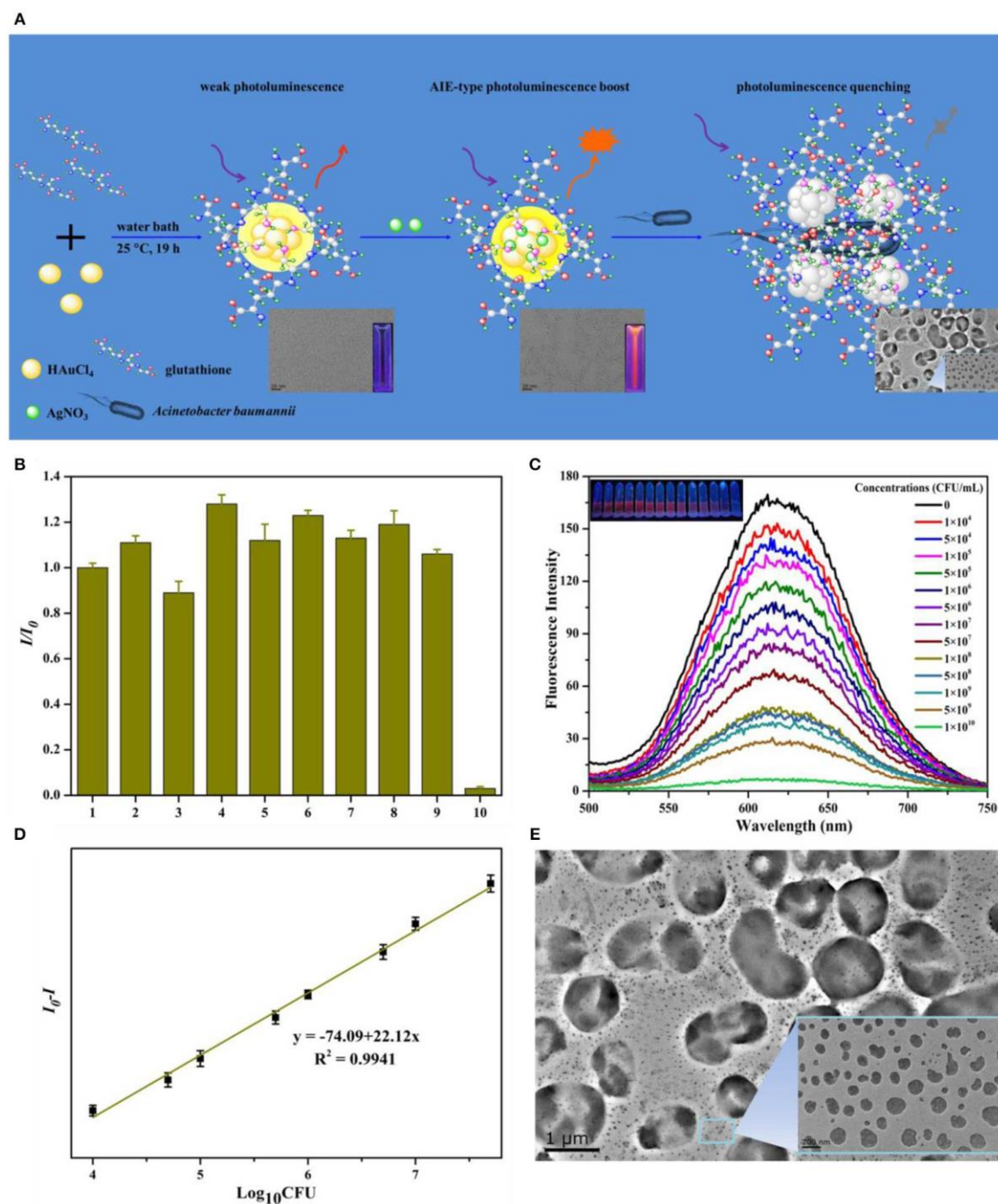


Figure.11. (A) Schematic illustration of the syntheses of AuAg NCs and photoluminescent quenching by *Acinetobacter baumannii*.⁵⁷ (B) The fluorescence of Au/Ag NCs was selectively quenched by *A. baumannii*. The order numbers from 1 to 10 in turn represent the group in the presence of no bacteria (control), *Bacillus mycoides*, *Staphylococcus aureus*, methicillin-resistant *S. aureus*, *Candida albicans*, *P. aeruginosa*, *E. coli*, vancomycin-resistant *Enterococcus faecium*, *Saccharomyces cerevisiae*, and *A. baumannii*, respectively. (C) The concentration dependent quenching effect of *A. baumannii* toward AuAg NCs.

Insets: Digital photos of AuAg NCs under UV illumination after treatment with different concentrations *A. baumannii*. (D) Relative fluorescence intensity (I_0/I) of AuAg NCs in contrast to the logarithm of the *A. baumannii* concentrations. (E) The transmission electron microscopy (TEM) micrographs of photoluminescent AuAg NCs treated with 1×10^5 CFU/mL *A. baumannii* demonstrate the bacteria induced agglomeration of NCs. Adapted from Ref.57.⁵⁷

From the family of FimA, FimH, FimG, and FimH, only FimH shows unique responsiveness toward the binding with mannose. Tseng et al.⁵⁹ developed a fluorescent probe-based approach for the special detection of *E. coli* by mannose etched AuNCs. Interaction between mannose etched AuNCs and FimH pili of *E. coli*, resulting in bright fluorescent bacterial cells (figure 12.b). According to Tseng et al.,⁵⁹ the fluorescence signals are directly proportional to the concentration of bacteria, by monitoring the fluorescence changes of gold nanoclusters allowed the *E. coli* detection with LOD~150 CFU/mL. Chan et al.⁶¹ synthesized mannose protected AuNCs by microwave irradiation during the reaction, which is capable of selective detection of *E. coli* J96 (an urinary tract infection isolate) by binding to FimH protein expressed over the type I pili.

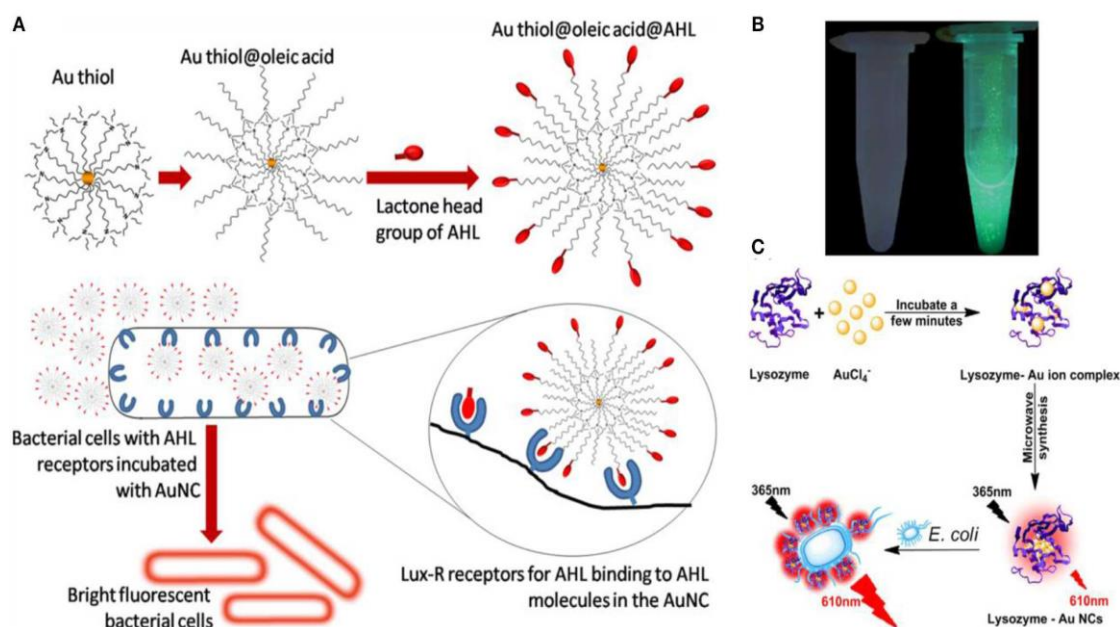


Figure.12. (A) Interaction of the fluorescent probe with bacterial cells: structure of the probe with AHL signal molecules deployed on the surface with lactone and amide moieties intact (top) and specific binding of AHL head groups to receptor sites in Lux-R regulators within bacteria (bottom). Adapted from Ref.58.⁵⁸ (B) Visualization of mannose-protected Au NCs (25 nM) in the absence (left) and presence (right) of *E. coli* (2.5×10^8 CFU/mL) upon

excitation under a hand-held UV lamp (365 nm). Adapted from Ref.59.⁵⁹ (C) Schematic diagram of the synthesis of the red fluorescent lysozyme-Au NCs and fluorescence enhancement detection of *E. coli*. Adapted from ref.62.⁶²

A similar method was employed for the specific detection of *Listeria monocytogenes* by Hossein-Nejad and coworkers.⁶¹ Lysozyme capped Au nanoclusters can also bind to the cell surface receptors on bacteria to recognize bacteria. Thus, lysozyme decorated AuNCs was used by Liu et al.⁶² for specific detection of *E. coli*. Based on specific recognition, when AuNCs decorated with lysozyme anchor on to the cell surface receptors of *E. coli*, it leads to a boost in the emission. Such kind of strategy can also be useful, if the AuNCs decorated with other recognition motifs, could also be used for selective detection of pathogenic microflora. The further development of AuNCs for the selective sensitivity towards bacteria

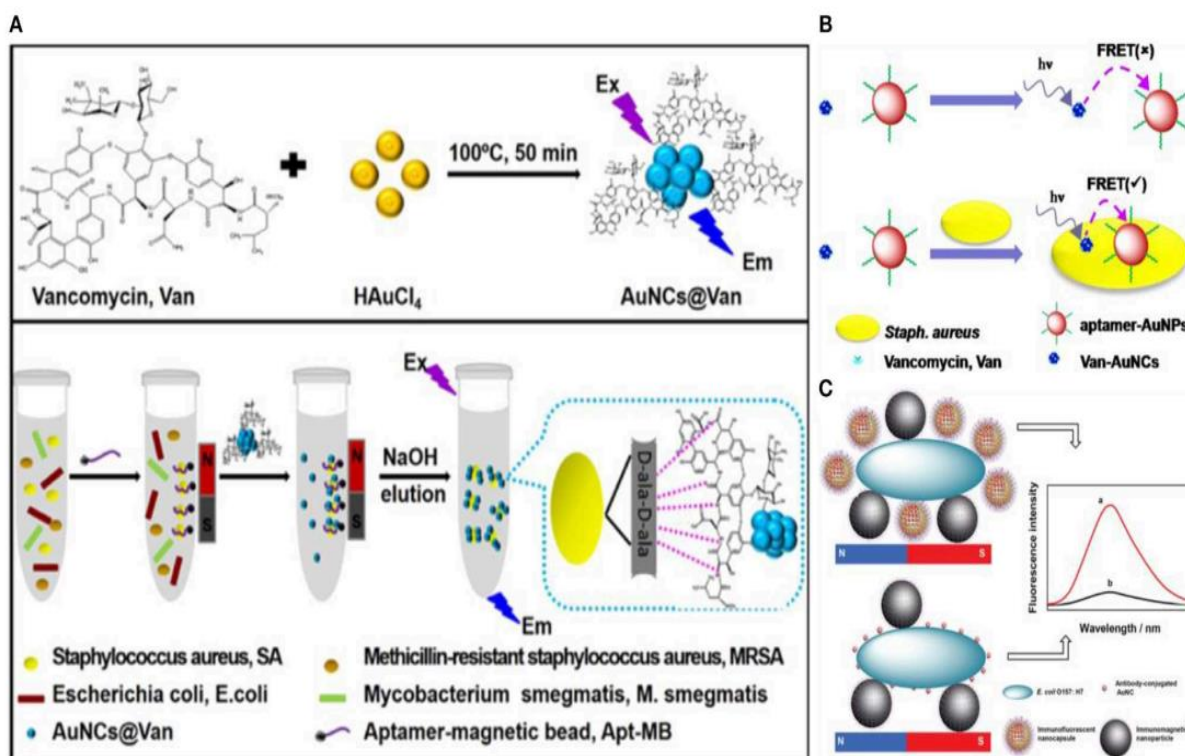


Figure.13. (A) Schematic illustrations of (top) one-step preparation of AuNCs@Van and (bottom) determination of *S. aureus* in mixtures using the aptamer-coated magnetic beads and Au NCs@Van dual recognition strategy. Adapted From Ref.65.⁶⁵ (B) Illustration of the vancomycin and aptamer dual-recognition molecule-based FRET assay platform for *S. aureus*. Adapted from Ref.64.⁶⁴ (C) Illustration of the immunoassay of *E. coli* O157:H7 using Au NCs@CS nano capsules and Au NCs as labels. Adapted from Ref.66.⁶⁶

can be improved via use of dual recognition probes. Song and co-workers involve DNA

aptamer and antibiotic based dual recognition probe, which enables the selective detection of *S. aureus* in the presence of high concentration of different bacterial strains (figure 13.A).⁶² Chen and co-workers⁶³ used aptamer decorated magnetic beads to capture *S. aureus* specifically. In another work, photoluminescence intensity based, vancomycin stabilized AuNCs were used for selective quantification of *S. aureus* with LOD~16 CFU/mL.^{63,64} Vancomycin has interaction with D-alanyl-D-alanine residues of N-acetylmuramic acid and N-acetylglucosamine which will make AuNCs to adhere on the surface of *S. aureus* in complex sample about 70 CFU/mL. Song et al. further developed the vancomycin and aptamer based dual recognition motif based on platform called as fluorescence resonance energy transfer (FRET) (figure 13.B).⁶⁵ Yu et al.⁶⁴ used AuNCs-vancomycin and aptamer modified-AuNPs as a energy donor and energy acceptor species respectively, within 30 minutes the FRET signal shows a linear variation with *S. aureus* concentration in the range from 20 CFU/mL to 108 CFU/mL with LOD ~ 10 CFU/mL. So, with the help of FRET strategy, selective sensing of bacterial cells from real samples has great application in the field of infectious diseases diagnosis and monitoring of environment. Cheng et al.⁶⁴ used nano-capsules with AuNCs capped with AuNCs capped with antibody confined with chitosan (AuNC@chitosan) and immune-magnetic nanoparticles for ultrasensitive recognition of *E. coli* O157:H7 (figure 13.C). After separation by magnetic fields, *E. coli* O157:H7 was attached to immunomagnetic nanoparticles, and AuNCs@chitosan coupled to bacteria was studied for fluorescence intensity. Xie et al.⁶⁴ mimicked the enzyme catalytic properties of gold nanoclusters which was utilized for colorimetric differentiation of pathogenic bacterial strains. A UV-assisted peroxidase like gold nanoclusters sensor combined with an aptamer selective towards *S. aureus* was developed. When *S. aureus* was tagged with this fluorescent probe, it starts the catalytic decomposition of H₂O₂ into reactive ·OH species (hydroxyl radicals). The substrate named 3,3',5,5'-tetramethyl benzidine (TMB) was continuously oxidized to blue product i.e., oxidized-TMB. This colorimetric sensor can easily differentiate *S. aureus* from *B. subtilis* and *E. coli* within half an hour with the LOD~4×10²CFU/mL.⁶⁷ This proves that, nano enzyme based AuNCs fluorescent probes have potential application in colorimetric detection of a specific bacteria.

1.7. Noble metal nanoclusters in Anti-counterfeiting applications

Silk is a wonderful natural material that has been utilized for many purposes. Depending on the desired use, the pristine silk may require some modification. The technological treatments used in the modification should not only be simple, quick, eco-friendly, and

inexpensive, but they should also be simple, quick, and ecologically friendly maintain the pure silk's characteristics. Zhang et al.⁶⁸ showed how nanotechnology may be used to make luminous silk and fabric. Through a redox reaction between protein-based silk and an Au salt precursor, the surface of the natural silk fiber is chemically coated with luminous gold nanoclusters (AuNCs) consisting of tens to hundreds of Au atoms. The resulting golden silk showed outstanding optical characteristics, including a reasonably long-wavelength fluorescence (red), a high QY (8%), a long fluorescence lifetime (322 ns), and strong photostability. Under UV light, the red fluorescent label used for anti-counterfeiting could be clearly identified from the backdrop when they needle worked some golden silk threads on a clean cloth.

Yan et al. developed BSA capped Au nanoclusters solution-based ink used to draw patterns **weighing paper, normal office paper and Kraft paper**.⁶⁹ Rival et al.⁷⁰ successfully shown the manufacture of nontoxic, cost-effective, dependable, and optically unclonable luminous security labels at room temperature. Stencil printing method were used to create such security labels, with near NIR-emitting precise AgNCs as the major component in ink (Fig.17). They also demonstrated the printing and viewing of a QR code on a mobile device utilizing a smartphone to exchange currencies.

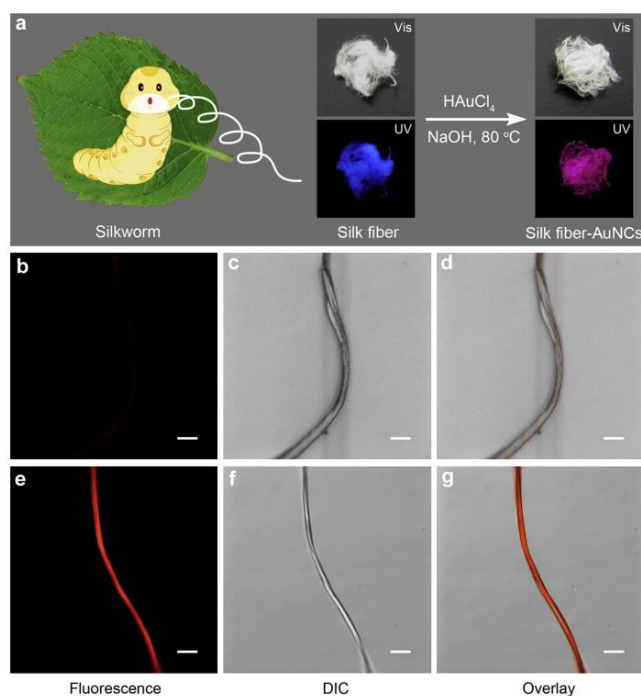


Figure.14 (a) The procedure for developing a golden silk synthesis approach. The photos also show pristine and golden silk under visible and UV light; (b-d) confocal fluorescence, DIC, and overlay images of a single pristine silk strand; (e-g) confocal fluorescent, DIC, and

overlay images of a single golden silk strand. Adapted from Ref.68.⁶⁸

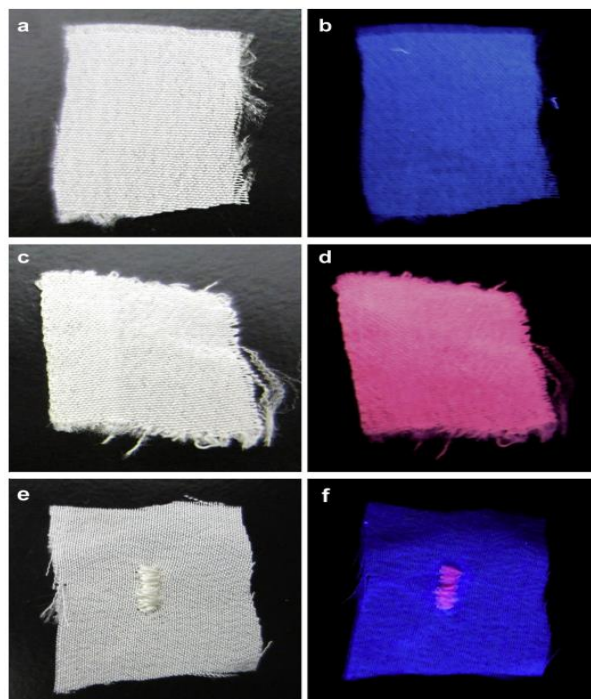


Figure.15. Anti-counterfeiting golden silk or fabric (a, b) the pristine silk-based fabric in visible and UV light; (c, d) the golden fabric in visible and UV light; (e, f) the anticounterfeit label in visible and UV light, which was produced by needlework stitching golden silk on a pristine fabric. Adapted from Ref.68.⁶⁸



Figure.16. Anti-counterfeit ink images of handwriting on several types of paper using as-prepared fluorescent Au NCs. Weighing paper, regular office paper, and Kraft paper, from left to right. Adapted from Ref.69.⁶⁹

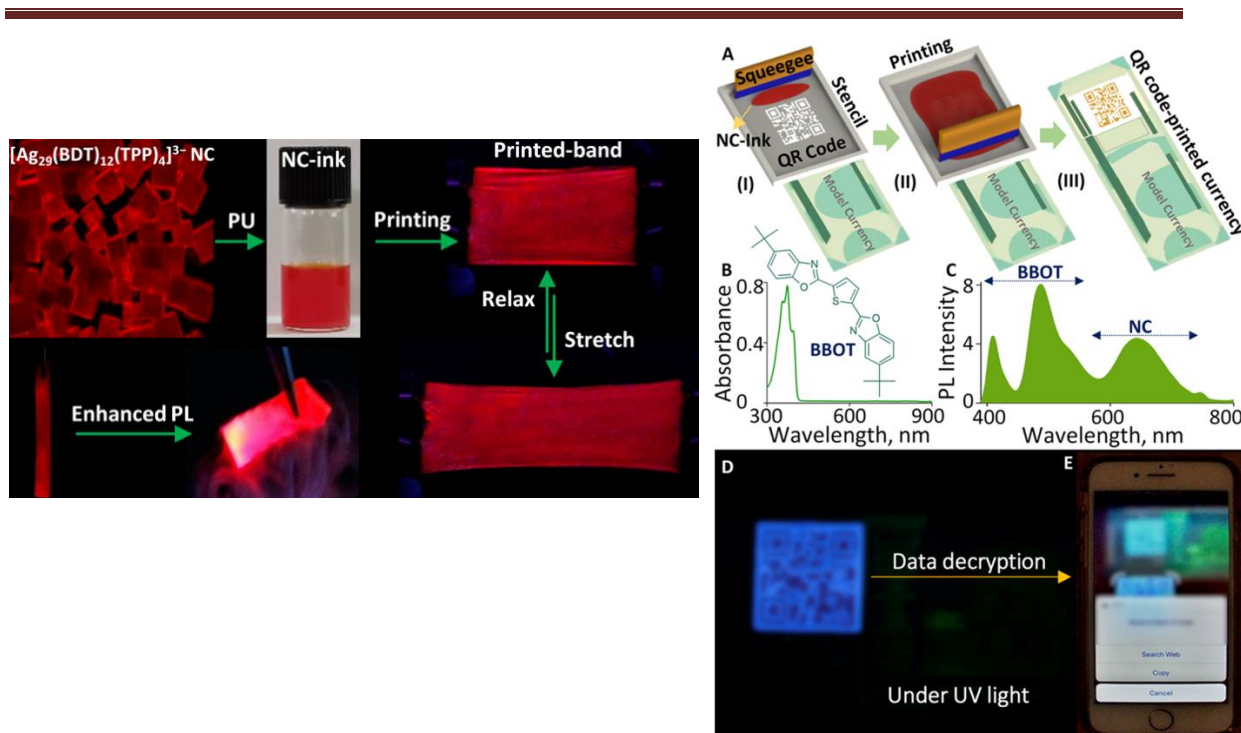


Figure.17. (A) A diagram of the stencil printing process used to print the QR code on a banknote. (B) BBOT chemical structure and absorption spectra. (C) A combination of NCs and BBOT was used to create a combined PL spectrum. Under UV light, photographs of (D) QR code-printed money and (E) data decryption using a smartphone. Adapted from Ref.70.⁷⁰

1.8. Scope and objective of the thesis

1.8.1. What is known?

Due to their unique sizes (bridging the gap between discrete atoms and plasmonic nanoparticles), atomically precise structures, interesting physicochemical characteristics, and prospective applications, the nanocluster concept has been steadily growing. Photoluminescence of noble metal nanoclusters were studied till now with respect to their particle size variation as well as by varying different capping agents and reaction conditions. Most studied metal nanoclusters are $\text{Au}_{25}(\text{SR})_{18}$ well known for their optical properties due to small size as well as ease of crystal formation which has led to unprecedented insights into the structures at this size regime. Also, with the help of DFT studies researchers are able to correlate the experimental data with theoretical data to check optical properties of such small nanoclusters. Tuning of fluorescence for Au nanoclusters is established via heteroatom doping and ligand variation. Bacterial detection via fluorescent metal nanoclusters is

also established via surface ligand engineering and bioconjugation with biomolecules.

1.8.2. What is not known?

(a) Several atomically precise hydrophobic nanoclusters with high PL intensities have been discovered to date; nevertheless, their hydrophobic nature has hampered their use in chemical sensing, bio-imaging, bio-labeling, and biotherapy. Because of their (i) non-toxicity, (ii) good biocompatibility, (iii) potential anti-cancer activity, (iv) small size, (v) good photo-stability, (vi) strong luminescence, (vii) ability to enter cells easily, and (viii) ability to bear functional ligands, hydrophilic fluorescent nanoclusters are prominent candidates for biological applications. The effect on optical properties due to change in size by core and surface atoms present in nanoclusters are studied well but only possible for small size clusters ($< 1\text{ nm}$). As size increases theoretical studies to correlate their optical properties with experimental observations became difficult due increase in the computational cost. Till now, the combined effect coming from metal nanocluster and the effect of capping ligand on the optical properties is not fully studied. This is the major challenge in big size nanoclusters (size~1nm to 2nm) capped with different hydrophilic ligands.

(b) Hydrophilic thiolate capped nanoclusters should possess certain kind of functional group which could bind or interact specific biomolecule to target particular binding site. This will make them water soluble as well as capable to target specific binding sites like in drug delivery or bacterial cell detection. Since, in bacterial cell detection the fluorescent probe should have emission in red or NIR region along with accurate and rapid detection of such bacterial cells before causing disease inside host cells or organism. Deep understanding regarding specific bacterial cell detection in a small interval of time is needed.

1.9. Thesis outline

Based on these observations, objectives of this work were set to (i) develop an fluorescent Au nanoclusters via specific surface functionalization with biomolecule like AHLs to sense the quorum sensing receptors present in gram-negative bacteria (ii) increase the fluorescence emission via hetero atom doping as well quantum yield to be used as improved optical probe in multifaceted imaging applications (iii) tune the optical properties of Au nanoclusters via surface-ligand engineering.

Chapter-2 addressed the gram-negative bacterial cell detection via surface functionalized

ultra-small Au nanoclusters. The fluorescence in the red area shown by ultra-small gold nanoclusters (AuNCs) was used to better understand the quorum sensing phenomena in bacteria, which is regulated by signal molecules that are particular to different species. The signal molecules Acyl Homoserine Lactones (AHLs) of varied carbon chain lengths, C-6, C-8, and C-12 without 3rd C modification, are subsequently functionalized on AuNCs to detect different types of gram-negative bacteria, such as *E. coli*, *Cronobacter sakazakii*, and *Pseudomonas aeruginosa*. This detection method was found to be rapid and detection has been done within 2 hours.

Chapter-3 addressed the enhancement of photoluminescence properties of pristine Au nanoclusters via hetero atom doping (Ag here). A simple Anti-galvanic reduction (AGR) approach for synthesis of bimetallic Au-Ag nanoclusters were used by utilizing thiol as a capping agent, i.e., *N, N', N''* tripropyl (11-mercaptoundecyl) ammonium chloride, which has -SH on one end and $^+NR_4$ on the other. It was found that, as Ag doping increases over AuNCs the emission in red region increases as well as quantum yield and decay life time also increased. Bimetallic bright red emitting AuAgNCs with excellent stability under relevant circumstances, and water solubility, have demonstrated promising uses in bioimaging and security applications.

Chapter-4 addressed the tailoring of photoluminescence of AuNCs via controlled nanoparticle ligand interface chemistry. *N, N', N''*-trialkyl (11-mercaptoundecyl) ammonium chloride-based thiol ligands as capping agents used to create molecular gold nanoclusters with adjustable photoluminescence emission from 600 nm to 700 nm. Specific interface chemistry between gold nanoclusters of molecular range and functional groups of the quaternary ammonium head over *N, N', N''*-trialkyl (11-mercaptoundecyl) ammonium chloride regulates the tunability in emission.

The conclusion of the total study given in this thesis was described in Chapter 5. This chapter also discusses the thesis's future directions.

References:

- 1 J. Sjollem, P. K. Sharma, R. J. B. Dijkstra, G. M. van Dam, H. C. van der Mei, A. F. Engelsman and H. J. Busscher, *Biomaterials*, 2010, **31**, 1984–1995.
- 2 Y. Yang, Q. Zhao, W. Feng and F. Li, *Chem. Rev.*, 2013, **113**, 192–270.
- 3 J. V. Frangioni, *Curr. Opin. Chem. Biol.*, 2003, **7**, 626–634.
- 4 X. Michalet, *Science (80-.)*, 2013, **307**, 538–545.

-
- 5 S. Xia, H. Yang, L. Duan, G. H. Gao and X. Zhang, *J. Polym. Res.*, 2016, **23**, 1–11.
 - 6 J. Lee, G. Hwang, Y. S. Hong and T. Sim, *Analyst*, 2015, **140**, 2864–2868.
 - 7 S. L. Raut, R. Fudala, R. Rich, R. A. Kokate, R. Chib, Z. Gryczynski and I. Gryczynski, *Nanoscale*, 2014, **6**, 2594–2597.
 - 8 M. Lin, Y. Zhao, S. Q. Wang, M. Liu, Z. F. Duan, Y. M. Chen, F. Li, F. Xu and T. J. Lu, *Biotechnol. Adv.*, 2012, **30**, 1551–1561.
 - 9 J. Li, X. Chang, X. Chen, Z. Gu, F. Zhao, Z. Chai and Y. Zhao, *Biotechnol. Adv.*, 2014, **32**, 727–743.
 - 10 L. Liu, G. Lin, F. Yin, W. C. Law and K. T. Yong, *J. Biomed. Mater. Res. - Part A*, 2016, **104**, 910–916.
 - 11 J. Zheng, P. R. Nicovich and R. M. Dickson, *Annu. Rev. Phys. Chem.*, 2007, **58**, 409–31.
 - 12 A. Mathew and T. Pradeep, *Part. Part. Syst. Character.*, 2014, **31**, 1017–1053.
 - 13 M. S. Devadas, J. Kim, E. Sinn, D. Lee, T. Goodson and G. Ramakrishna, *J. Phys. Chem. C*, 2010, **114**, 22417–22423.
 - 14 E. Roduner, *Chem. Soc. Rev.*, 2006, **35**, 583–592.
 - 15 K. L. Kelly, E. Coronado, L. L. Zhao and G. C. Schatz, *J. Phys. Chem. B*, 2003, **107**, 668–677.
 - 16 S. Link and M. A. El-sayed, *J. Phys. Chem. B*, 1999, **103**, 4212–4217.
 - 17 R. Jin, *Nanoscale*, 2010, **2**, 343–362.
 - 18 I. Sakanaga, M. Inada, T. Saitoh, H. Kawasaki, Y. Iwasaki, T. Yamada, I. Umezu and A. Sugimura, *Appl. Phys. Express*, 2011, **4**, 095001.
 - 19 X. Wen, P. Yu, Y. Toh and J. Tang, *J. Phys. Chem. C*, 2012, **116**, 11830–11836.
 - 20 J. Xie, Y. Zheng and J. Y. Ying, *J. Am. Chem. Soc.*, 2009, **131**, 888–889.
 - 21 K. R. Krishnadas, A. Ghosh, A. Baksi, G. Natarajan and T. Pradeep, *J. Am. Chem. Soc.*, 2016, **138**, 140–148.
 - 22 R. Jin, *Nanoscale*, 2010, **2**, 343–362.
 - 23 L. Polavarapu, M. Manna and Q. Xu, *Nanoscale*, 2011, **3**, 429–434.
 - 24 J. Liu, M. Yu, C. Zhou, S. Yang, X. Ning and J. Zheng, *J. Am. Chem. Soc.*, 2013, **135**, 4978–4981.
 - 25 Q. W. and D. C. C. Zhang, Z. Zhou, Q. Qian, G. Gao, C. Li, L. Feng, *J. Mater. Chem. B*, 2013, **1**, 5045–5053.
 - 26 S. Gao, D. Chen, Q. Li, J. Ye, H. Jiang, C. Amatore and X. Wang, *Sci. Rep.*, 2014, **4**,
-

-
- 4384.
- 27 C. Wang, Y. Wang, L. Xu, D. Zhang, M. Liu and X. Li, *Small*, 2012, **8**, 3137–3142.
- 28 C. Wang, L. Xu, X. Xu, H. Cheng, H. Sun, Q. Lin and C. Zhang, *J. Colloid Interface Sci.*, 2014, **416**, 274–279.
- 29 Y. Sun, Y. Xia and M. J. Science, *J. Am. Chem. Soc.*, 2004, **126**, 3892–3901.
- 30 C. Wang, L. Xu, X. Xu, H. Cheng, H. Sun, Q. Lin and C. Zhang, *J. Colloid Interface Sci.*, 2014, **416**, 274–279.
- 31 L. Shang, N. Azadfar, F. Stockmar, W. Send, V. Trouillet, M. Bruns, D. Gerthsen and G. U. Nienhaus, *sma*, 2011, **7**, 2614–2620.
- 32 L. Shang, L. Yang, F. Stockmar, R. Popescu, V. Trouillet, M. Bruns, D. Gerthsen and G. U. Nienhaus, *Nanoscale*, 2012, **4**, 4155–4160.
- 33 R. S. J. L. V. Nair, S. S. Nazeer, *ACS Nano*, 2015, **9**, 5825–5832.
- 34 J. Zhang, Y. Fu, C. V Conroy, Z. Tang, G. Li, R. Y. Zhao and G. Wang, *J. Phys. Chem. C*, 2012, **116**, 26561–26569.
- 35 M. A. H. Muhammed, P. K. Verma, S. K. Pal, R. C. A. Kumar, S. Paul, R. V. Omkumar and P. Thalappil, *Chem. - A Eur. J.*, 2009, **15**, 10110–10120.
- 36 X. Le Guével, C. Spies, N. Daum, G. Jung and M. Schneider, *nano r*, 2012, **5**, 379–387.
- 37 C. J. Lin, T. Yang, C. Lee, S. H. Huang, R. A. Sperling, M. Zanella, J. K. Li, J. Shen, H. Wang, K. H. Yeh, K. W. J. Parak and W. H. Chang, *ACS Nano*, 2009, **3**, 395–401.
- 38 L. Shang, S. Dong and G. U. Nienhaus, *Nano Today*, 2011, **6**, 401–418.
- 39 B. L. H. Chen, S. Li, *Nanoscale*, 2012, **4**, 6050–6064.
- 40 A. Retnakumari, S. Setua and D. Menon, *Nanotechnology*, 2010, **21**, 055103.
- 41 Y. Wang, J. T. Chen and X. P. Yan, *Anal. Chem.*, 2013, **85**, 2529–2535.
- 42 C. Liu, T. Liu, T. Hsieh, H. Liu, Y. Chen, C. Tsai, H. Chen, J. Lin, R. Hsu and T. Wang, *Small*, 2013, **9**, 2103–2110.
- 43 et al. Y. Kong, J. Chen, F. Gao, *Nanoscale*, 2013, **5**, 1009–1017.
- 44 et al. Q. Yuan, Y. Wang, L. Zhao, *Nanoscale*, 2016, **8**, 12095–12104.
- 45 J. Sharma, H. C. Yeh, H. Yoo, J. H. Werner and J. S. Martinez, *Chem. Commun.*, 2010, **46**, 3280–3282.
- 46 Y. Antoku, J. Hotta, H. Mizuno, R. M. Dickson and T. Vosch, *Photochem. Photobiol. Sci.*, 2010, **9**, 716–721.
- 47 J. Ai, W. Guo, B. Li, T. Li, D. Li and E. Wang, *Talanta*, 2012, **88**, 450–455.
-

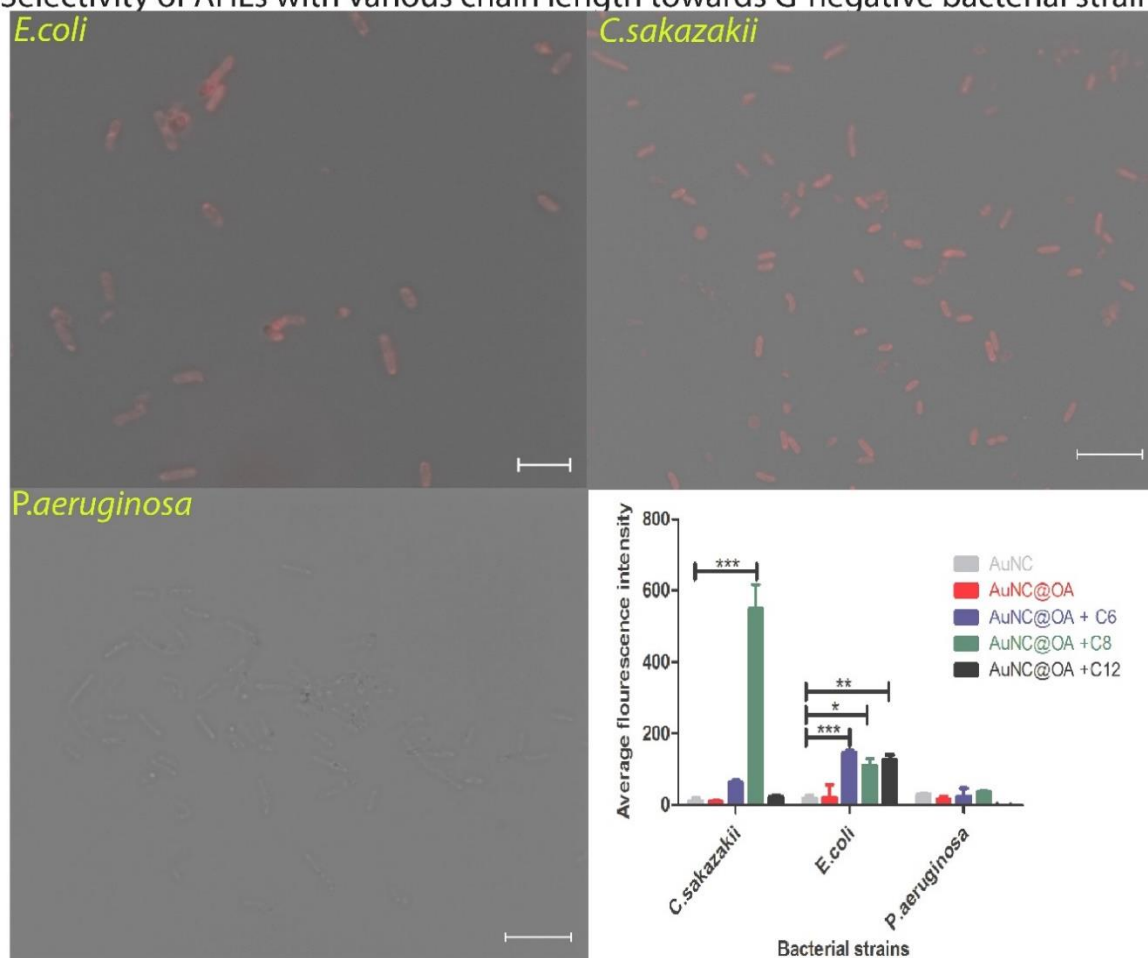
-
- 48 X. Huang, Y. Luo, Z. Li, B. Li, H. Zhang, L. Li, I. Majeed, P. Zou and B. Tan, *J. Phys. Chem. C*, 2011, **115**, 16753–16763.
- 49 J. Liu, M. Yu, X. Ning, C. Zhou, S. Yang and J. Zheng, *Angew. Chemie - Int. Ed.*, 2013, **52**, 12572–12576.
- 50 L. Shang, L. Yang, J. Seiter, M. Heinle, D. Gerthsen and G. U. Nienhaus, *Adv. Mater. Interfaces*, 2013, **1**, 1300079.
- 51 Y. Wang, Y. Cui, Y. Zhao, R. Liu, Z. Sun, W. Li and X. Gao, *Chem. Commun.*, 2012, **48**, 871–873.
- 52 X. Wu, X. He, K. Wang, C. Xie, B. Zhou and Z. Qing, *Nanoscale*, 2010, **2**, 2244–2249.
- 53 P. Chan and Y. Chen, *Anal. Chem.*, 2012, **84**, 8952–8956.
- 54 R. Yan, Z. Shou, J. Chen, H. Wu, Y. Zhao, L. Qiu, P. Jiang, X. Z. Mou, J. Wang and Y. Q. Li, *ACS Sustain. Chem. Eng.*, 2018, **6**, 4504–4509.
- 55 P. Liu, H. Wang, J. K. Hiltunen, Z. Chen and J. Shen, *Part. Part. Syst. Charact.*, 2015, **32**, 749–755.
- 56 D. Pranantyo, P. Liu, W. Zhong, E. Kang and M. B. Chan-park, *Biomacromolecules*, 2019, **20**, 2922–2933.
- 57 Y. Zheng, X. Wang and H. Jiang, *Sensors Actuators, B Chem.*, 2018, **277**, 388–393.
- 58 R. Mukherji, A. Samanta, R. Illathvalappil, S. Chowdhury, A. Prabhune and R. N. Devi, *ACS Appl. Mater. Interfaces*, 2013, **5**, 13076–13081.
- 59 Y. Tseng, H. Chang, C. Chen, C. Chen and C. Huang, *Biosens. Bioelectron.*, 2011, **27**, 95–100.
- 60 S. L. Harris, P. A. Spears, E. A. Havell, T. S. Hamrick, J. R. Horton, P. E. Orndorff, N. Carolina and N. Carolina, *J. Bacteriol.*, 2001, **183**, 4099–4102.
- 61 P. Chan, B. Ghosh, H. Lai, H. Peng, K. Kong, T. Mong and Y. Chen, *PLoS One*, 2013, **8**, e58064.
- 62 J. Liu, L. Lu, S. Xu and L. Wang, *Talanta*, 2014, **134**, 54–59.
- 63 B. Xing, C. Yu, K. Chow, P. Ho, D. Fu and B. Xu, *J. Am. Chem. Soc.*, 2002, **124**, 14846–14847.
- 64 H. J. Chung, T. Reiner, G. Budin, C. Min, M. Liong, D. Issadore, H. Lee and R. Weissleder, *ACS Nano*, 2011, **5**, 8834–8841.
- 65 M. Yu, H. Wang, F. Fu, L. Li, J. Li, G. Li, Y. Song, M. T. Swihart and E. Song, *Anal. Chem.*, 2017, **89**, 4085–4090.
-

-
- 66 et al. Cheng, C., Yang, L., Zhong, M., Deng, W., Tan, Y., Xie, Q., *Analyst*, 2018, **143**, 4067–4073.
- 67 X. Xie, F. Tan, A. Xu, K. Deng, Y. Zeng and H. Huang, *Sensors Actuators B. Chem.*, 2018, **279**, 289–297.
- 68 P. Zhang, J. Lan, Y. Wang, Z. Hong and C. Zhi, *Biomaterials*, 2015, **36**, 26–32.
- 69 L. Yan and Y. Yu, *NANO Br. Reports Rev*, 2019, **14**, 1–12.
- 70 J. V Rival, P. Mymoona, R. Vinoth, A. M. V. Mohan and E. S. Shibu, *ACS Appl. Mater. Interfaces*, 2021, **13**, 10583–10593.

Chapter-2

Red Fluorescent Ultra-Small Gold Nanoclusters Functionalized with Signal Molecules to Probe Specificity in Quorum Sensing Receptors in Gram-Negative Bacteria

Selectivity of AHLs with various chain length towards G-negative bacterial strains



2.1. INTRODUCTION

Quorum sensing is a mechanism in which many bacterial species coordinate their group activities by exchanging chemical signalling molecules. A variety of bacterial species use this phenomenon to synchronize their actions in order to operate as a multicellular organism.¹ Antibiotic resistance or multidrug resistance, surface attachment, swarming motility, virulence or biofilm development, sporulation, and other activities can all be coordinated through this system.^{2,3,4} Individual bacterial cells cannot exhibit such pathogenic traits, and they can only be triggered when the bacterial population is large enough to damage the host mechanism. Synthesizing specific chemical signal molecules known as autoinducers (AI) can control pathogenic traits. Oligopeptides and acyl homoserine lactones are autoinducers produced by both gram-positive and gram-negative bacteria (AHLs). These autoinducers are discriminatively sensed by their cognate receptor proteins, triggering a sequence of events that can be detrimental to the host organism.

Almost all Gram-negative bacteria use transcriptional agents, such as Lux-R receptor homologues, to detect acyl homoserine lactone signal molecules (AHLs) generated by their Lux-I type synthase homologues. The lactone ring is commonly attached to a long acyl carbon chain ranging from C-4 to C-18, with the third position in the chain either modified or unaltered by a carbonyl or hydroxyl group designated as oxo or OH. Modifications to the structure of AHL are known to provide a certain level of detection uniqueness to QS systems.⁵ Lux-R homologue proteins have two functional domains: a C-terminal DNA-binding domain and an N-terminal AHL-binding domain.⁶ Three tryptophan residues in the N-terminal polar group interact with the lactone moiety (from AHL) signal molecule to determine binding locations.^{7,8} AHL molecules have a hydrophobic acyl chain that can connect to the binding pocket in a variety of ways: shorter chain length AHLs are straight and point to the solvent, whereas longer chain length AHLs are folded and point to the inner leaflet of the cell membrane.⁹ Only a few studies have been done on gram-negative microfloral quorum sensing systems in terms of AHL specificity and selectivity in the direction of Lux-R type receptors. The only studied quorum sensing system is that of *P. aeruginosa*, which has three quorum sensing systems: PQS, Las-R receptor-Las-I synthase, Rhl-R receptor-Rhl-I synthase, and Las-R receptor-Las-I synthase.^{10,11} Las-I synthase can make 3-oxo-C-12AHL signal molecules that bind to Las-R receptors in a specific manner. This is also linked to phenotypes like pyocyanin production, motility, and iron uptake. Rhl-I

synthase produces N-butyryl-L-homoserine lactone, which binds to Rhl-R receptors and stimulates transcriptional factors that control phenotypic traits like virulence, exoenzyme synthesis, and biofilm formation. In addition to these QS systems, there is an orphan QscR receptor that lacks a cognate synthase. The third system uses 2-alkyl-4-quinolones, which are structurally unique from the cognate signal molecules in the other two systems.^{12,13} *E. coli* additionally includes orphan Sdi-A receptors that lack any AHL synthase and are thought to bind to AHL molecules with varied modified or unmodified chain lengths ranging from C-4 to C-12.^{14,15} Orphan Sdi-A receptors type quorum systems govern bacterial adherence and biofilm formation in *E. coli*. Until now, there have been few reports on *C. sakazakii*'s quorum sensing mechanism. AHLs with various C numbers and functionalities in the alkyl chain, like C-11AHL, N-(γ -ketocaroyl)-L-acyl homoserine lactone, C-14AHL, C-15AHL, 3-oxo-C-8AHL, C-8AHL and C-18AHL, have recently been isolated from biofilm forming *C. sakazakii* strains.¹⁶ Biochemical methods aid in the isolation of signal molecules from the quorum stage of the bacterial stage, which offers critical information on the signal molecules' binding mechanism with its cognate receptor. There are only a few reports that use fluorescence imaging to investigate the quorum sensing mechanism. For example, a fluorescent labelling agent for quorum sensing receptors named FLAQS was recently developed from Rhodamine-B and DDDA (dodecanedioic acid) to sense the wild type strain *Burkholderia cenocepacia* H111 CepR receptors.¹⁷ Inorganic-based luminous probes, on the other side, are more preferred for bioimaging due to their superior photostability and lower background fluorescence.¹⁸⁻²¹ Noble metal nanoclusters (thiolate capped, peptide capped, or protein capped) are also employed as fluorescence on-off-on²² and fluorescence off^{23,24,25} based sensors for the specific point of care detection of gram-negative and gram-positive bacteria. Using Au nanocluster based NIR light emitting luminescent probes, Mukherji et al. recently reported a method for distinguishing gram positive and gram-negative bacteria based on the orphan Sdi-A receptors of *E. coli*.²⁶ Investigation was done for various strains of gram-negative bacteria have a specific affinity for a particular AHL molecule in our quest to better understand the mechanism of quorum sensing. To answer this, specially designed fluorescent Au nanocluster conjugates to coat three AHL signal molecules were utilized without the 3rd C modification: N-hexanoyl-l-homoserine lactone (C-6), N-octanoyl-l-homoserine lactone (C-8) and N-dodecanoyl-homoserine lactone (C-12) and conducted fluorescence imaging studies with *E. coli*, *C. sakazakii* and *P. aeruginosa*. So, in this chapter we demonstrate the AHL molecules'

specificity towards particular bacterial species with the help of inorganic fluorescent Au Nanoclusters tagged with AHL. There are three major advantage of this method:-(i) Au nanocluster-based conjugate tagged with AHLs can be incubated with any pathogenic bacterial species at their ambient growth temperature, (ii) can detect bacterial species in less than 2 hours (rapid detection) much prior to the virulent quorate state, (iii) selective and cost-effective.

2.2. Experimental Section

2.2.1. Synthesis of Au Nanoclusters and their conjugates used in bacterial cells detection

2.2.1.1. Au nanoclusters synthesis:

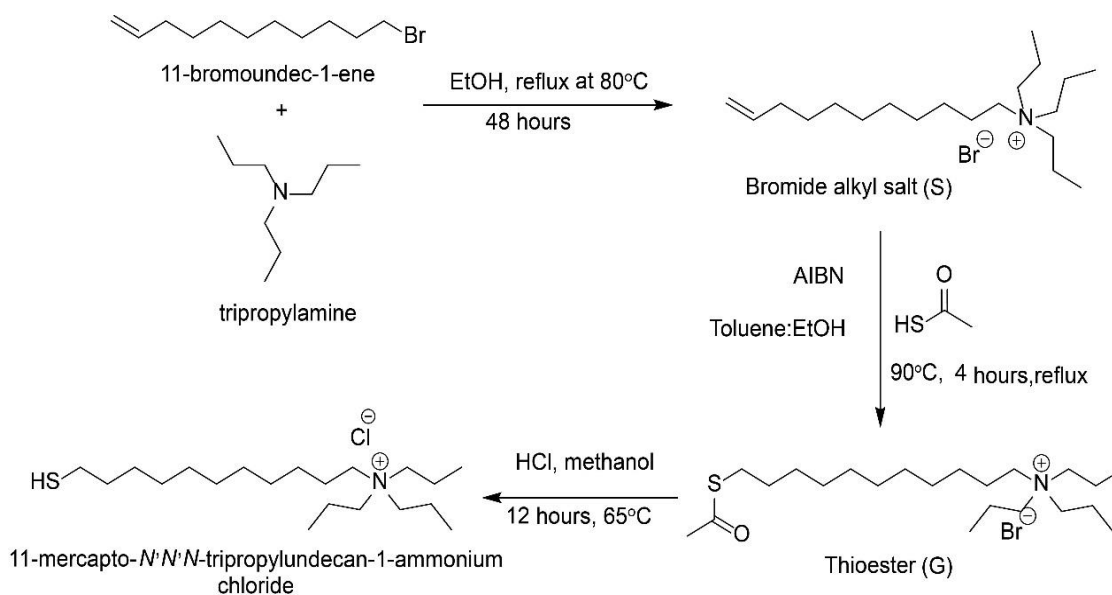
The method for making water dispersible Au NCs capped with *N, N', N''*-tripropyl (11-mercaptoundecyl) ammonium chloride has been reported elsewhere.²⁷ Firstly, 20 mL acetonitrile was mixed with 0.593 g (1.6 mmol) thiol ligand dissolved in 2 mL methanol. 8.5 mL of 10 mM stock solution (in CH₃CN) of HAuCl₄ (99.9%, Aldrich) was slowly (drop-wise) introduced to that mixture and stirred for the next 30 minutes. Then, under stirring, 100 μL of 1.58 M (stock in MeOH) NaBH₄ solution was added to the solution, changing the colour from colourless to pale yellow, showing the formation of Au nanoclusters. All the above synthesis steps were carried out at 0°C. Deionized water (30 mL) was then added and acetonitrile was removed through rotary evaporator. With the help of dialysis, the excess of thiol was removed and the remained Au NCs solution were stored at 4 °C. 2 mM was the final concentration of Au NCs solution estimated via elemental analysis.

2.2.1.2. *N, N', N''*-tripropyl (11-mercaptoundecyl) ammonium chloride (RSH) ligand synthesis

The ligand was produced by modifying recently reported methods. Scheme 2.1 shows the synthesis procedure. To begin, 5.4 g of 11-bromo-1-undecene (23 mmol) was added to 10.2 g of tripropylamine (71 mmol) in ethanol (40 mL) and rapidly agitated for 48 h at 80 °C under reflux. The solvent was evaporated in vacuo, leaving the bright yellow bromide unsaturated alkyl salt behind (**S**).

Bromide unsaturated alkyl salt (**S**) was purified using non-polar hexane (100 mL) and sonicating three times (with yield of 93%). After dissolving 19.0 mmol **S** in a 1:1

combination of toluene and ethanol (total volume 40 mL), 10.0 mmol AIBN and 80 mmol thioacetic acid were added. For the following 4 h, the mixture was vigorously stirred under reflux. In vacuo, the solvents were reduced, yielding a dark yellow thioester (**G**). This thioester was purified by sonicating three times with 100 mL of a 9:1 combination of hexane and ethyl acetate. **G** was vigorously agitated in 40 mL of methanol with 2mL of conc. HCl acid for the following 12 h under reflux.



Scheme.2.1. Scheme representing the synthesis of 11-mercapto-*N, N', N''*-tripropylundecan-1-ammonium chloride.

The solvent was then removed under vacuum resulting in thiol. Thiol was purified by washing (3 times) with 100 mL of hexane: ethyl acetate (9:1 mixture) under sonication (yield: 80 %).

2.2.1.3. Synthesis of Au NC@OA@AHLs

To the above gold nanocluster solution (1mL), 12 μL of oleic acid stock (0.05 M) in methanol was added and agitated for 2 hours. C-6AHL (14.7 μL), C-8AHL (17 μL), and C-12AHL (20.8 μL) were added to the AuNC@OA mixed solution with 500 μL of ethanol and agitated for yet another 2 hours to obtain final AuNC@OA@AHL conjugate.

2.2.1.4. Bacterial cells culture used in quorum sensing studies

C. sakazakii ATCC12868, *E. coli* ATCC8739, and *P. aeruginosa* NCIB 6571 were the bacteria employed in this investigation. Bacterial cells were cultivated in LB medium at the

optimum temperature to reach log phase (10⁶ cells/mL), then harvested and washed in 1X PBS. After that, the cells were resuspended in 1X PBS and gently shaken for 2 h with 100 μ L AuNC@OA@AHL conjugates. The concentrations of Au and AHL were 0.13 μ moles and 0.024 μ moles, respectively, when Au and AHL were introduced to 1 mL of 1X PBS containing bacterial cells. Cells were pelleted after incubation, washed in 1X PBS, and resuspended in fresh PBS to ensure that any unbound fluorescent clusters did not interfere with imaging.

2.3. Characterization techniques

2.3.1. Transmission electron microscopy

A TF-20-FEI Tecnai transmission electron microscope operating at 200 kV was used to examine the size of clusters and their conjugates. Drop casting the sample solution onto a carbon coated mesh 200 grid and air drying the samples were used to prepare the samples. The grid of AuNC conjugates incubated bacteria was prepared using the same procedure.

2.3.2. Fluorescence spectroscopy

The PTI QM-40 fluorescence instrument has been used to acquire the fluorescence spectra. The emission of the sample solution was collected using a 3.5 mL quartz cuvette with a 10 mm path length. Throughout the experiments, the emission-band width stayed unchanged at 5 nm.

2.3.3. Fourier-Transform IR spectroscopy

SENSOR-27 BRUKER instrument has been used to acquire FTIR spectra in % Transmittance mode. All of the specimens were prepared using KBr as a standard matrix.

2.3.5. Microscopy and image analysis:

The slides were prepared with a 50 percent glycerol mounting media for imaging. The sample solution and mounting media were drop casted onto a plain J. Melvin glass slide (size 75mm x 25mm) and stacked using Sigma-Aldrich cover glasses (size- 22mm x 22mm). Within 3-4 h of preparation, sample slides were analysed using a Zeiss Imager A2 fluorescent microscope with Rhodamine filters (transmission wavelength 660nm-750nm) and a HXP 120V source lamp (excitation range 350nm-700nm) (Carl Zeiss. Inc, Germany). Zen 2.3 lite software has been used to capture and analyse the images.

2.3.6. Inductively Coupled Plasma Spectroscopy

Spectro Arcos, FHS-12 Inductively coupled plasma atomic emission spectrometer was used to analyse the elements in the Au nanocluster solution (ICP-AES). Standard solutions were used to calibrate the system. To remove the organic ligand, 1 mL of Au nanocluster solution was dried at 100°C and subsequently calcined at 350°C for 8 h. After calcination, the residue was treated in 1 mL of aqua regia, and the volume of the final solution was increased to 10 mL using Millipore water. This diluted 10 mL solution was used directly for ICP-AES elemental analysis.

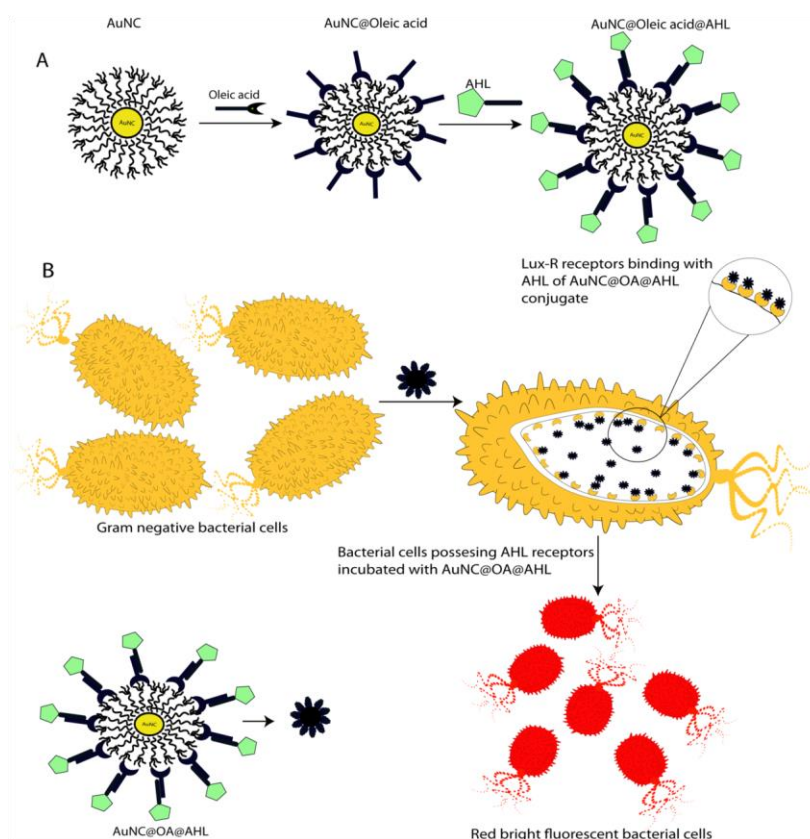
2.3.7. NMR Spectroscopy

¹H NMR were collected in Bruker 400 MHz NMR spectrometer and 10mg samples were prepared by dissolving in 0.5mL of CDCl₃.

2.4. Results & Discussion

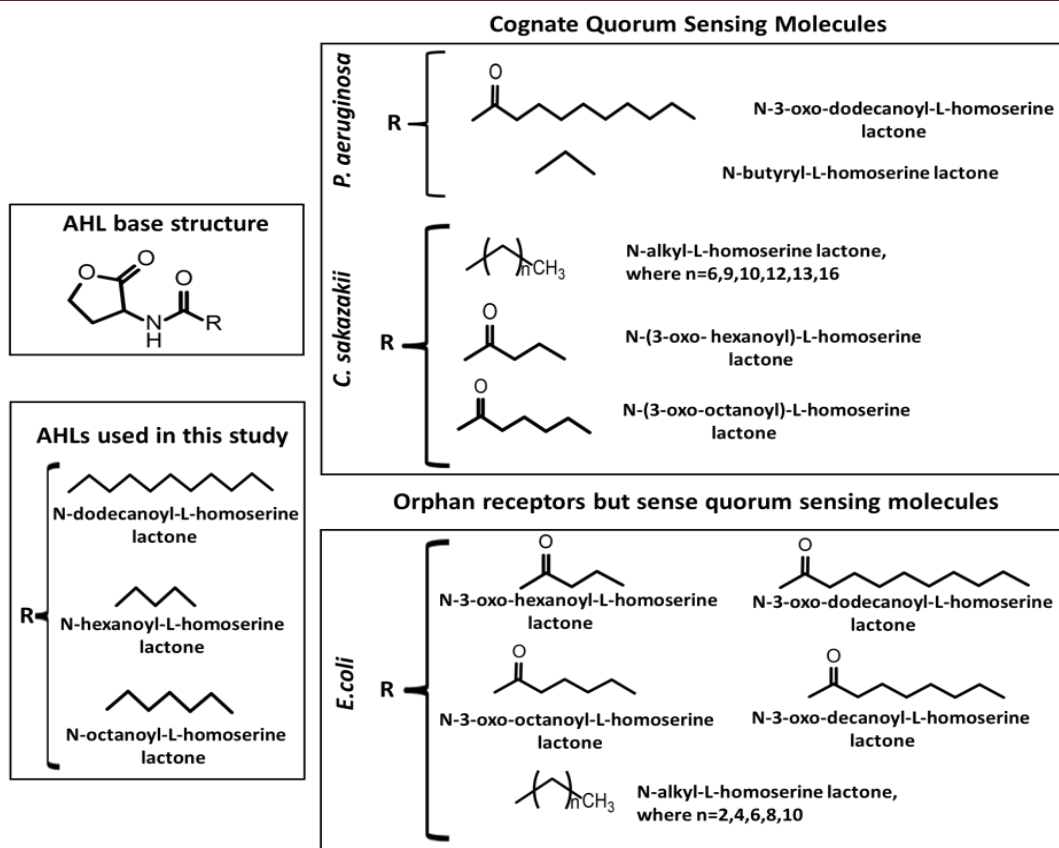
2.4.1. Strategy developed for the early detection of quorum sensing receptors in pathogenic bacteria

Goal of this work is to use the AHL-receptor (namely Lux-R) interaction to better understand gram-negative bacteria's quorum sensing responses. NIR emitting Au nanoclusters-based probes surface functionalized with AHL molecules have already been used to establish that the AHL-Lux-R interaction is independent of the virulent stage and hence useful in the early phases of bacterial development.²⁶ Quantum size Au clusters (less than 2 nm in diameter) that emit red light are excellent candidates for bioimaging since they have a low signal-to-noise ratio. The quantum confinement effects in these sub-2-nm Au NCs lead to discrete and size-dependent electronic transitions, which are exhibited as photophysical features including luminescence. We have synthesized Au NCs ligated with thiol ligand named as *N, N', N''*-tri propyl(11-mercaptoundecyl) ammonium chloride with broad emission in the red spectral region as reported elsewhere.²⁷ As a capping agent, this thiol ligand has a positively charged quaternary ammonium (⁺NR₄) head on one end and a negatively charged thiol ligand on the other end to provide water dispersibility (medium for biological systems). AHLs which are used in this study are synthesized by gram-negative bacterial cells and consist of carbon chains (hydrophobic part) with varying lengths like C-6, C-8 and C-12;



Scheme 2.2. Bacterial cells incubated with fluorescent nanoprobe (A) Nanoprobe structure here AHL moiety deployed on the surface without disturbing amide and lactone moiety (B) Specific binding of AHL head groups from the AuNC@OA@AHL composites to receptor sites in Lux-R regulators within bacteria.

their framework is given in Scheme 2.2 and also contains lactone head group, which binds through H-bonding with the N-terminal amino acids of the Lux-R receptors. OA (oleic acid) were used to facilitate electrostatic interaction between the positively charged quaternary ammonium ($^+NR_4$) head containing thiol capped Au NCs and hydrophobic interaction with AHL. We used OA (oleic acid) as a connecting component in our research so that the hydrophobic contact between its long 18 carbon chain and the carbon chains of AHLs would aid in the formation of a balanced conjugate. We assume that the lactone moiety is free to bind to Lux-R receptor homologues in this way (Scheme 2.2). The interactions between distinct functional moieties were investigated using FTIR spectroscopy to examine the conjugate framework building at individual points.



Scheme 2.3. Structures of signal molecules with base Acyl homoserine skeleton. Cognate signal molecules synthesized by *C. sakazakii* and *P. aeruginosa* and those known to be detected by *E. coli* are given along with the ones used in this study.

2.4.2. CHARACTERIZATION

2.4.2.1. ¹H NMR Spectroscopy

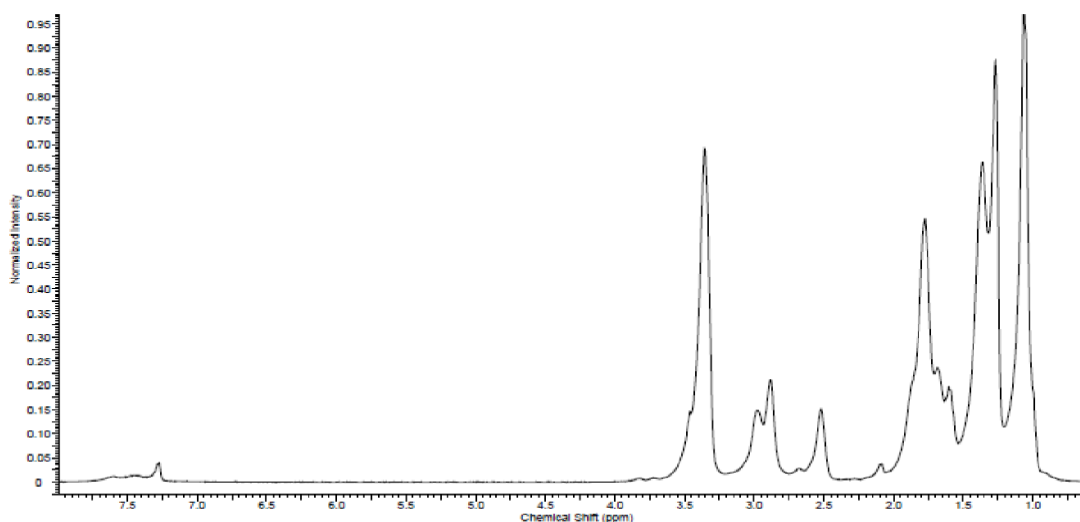


Figure.2.1. ^1H NMR spectrum of 11-mercapto-N, N', N''-tripropylundecan-1-ammonium chloride ligand.

11-mercapto-N, N', N''-tripropylundecan-1-ammonium chloride ligand was characterized by ^1H NMR [Fig. 2.1]. ^1H NMR (400 MHz, CDCl_3): δ 1.07 (t, $J = 7$ Hz, 9 H, $\text{CH}_3\text{CH}_2\text{CH}_2\text{N}^+$), δ 1.20- 1.39 (m, 14 H, $-\text{CH}_2$), δ 1.58-1.64 (m, 2 H, $\text{HS}-\text{CH}_2\text{CH}_2$), δ 1.66-1.84 (bm, 6 H, $\text{CH}_3\text{CH}_2\text{CH}_2\text{N}^+$), δ 1.86-1.91 (m, 2 H, $\text{CH}_2\text{CH}_2\text{N}^+$), δ 2.51-2.55 (m, 2 H, $\text{HS}-\text{CH}_2$), δ 2.90-3.01 (bm, 2 H, CH_2N^+), δ 3.34-3.40 (m, 6 H, $\text{CH}_3\text{CH}_2\text{CH}_2\text{N}^+$).

2.4.2.2. FT-IR Spectroscopy

Electrostatic attraction between the $-\text{COO}^-$ group and the $^+\text{NR}_4$ head group of gold nanocluster is proven by correlate the stretching frequency of $\text{C}=\text{O}$ of AuNC@OA composite with original OA (oleic acid). Previously is it proven that $\text{C}=\text{O}$ stretch of carboxylic acid from OA which is quoted in 1710 cm^{-1} in original sample fades in bound states with R_4N^+ of ligand with rise of bands near 1640 cm^{-1} & 1540 cm^{-1} analogous to symmetric and asymmetric $-\text{COO}$ vibrations.^{28,29} A very weak band at 1524 cm^{-1} corresponding to asymmetric $-\text{COO}$ stretch and strong intense band at 1631 cm^{-1} corresponding to symmetric stretch are observed in Figure 2.2. This is a desirable composition because the $^+\text{NR}_4$ groups of Au NCs interact with the $-\text{COO}^-$ moiety of OA (oleic acid), extending the hydrophobic carbon chain on the periphery. FTIR analysis of oleic acid at neutral pH and $\text{pH}=9$ confirms this, $\text{C}=\text{O}$ stretch is given at 1710 cm^{-1} at $\text{pH}=7$, indicating that H^+ of $-\text{COOH}$ is bound. At $\text{pH}=9$, the $\text{C}=\text{O}$ stretch band appears at 1651 cm^{-1} for symmetric stretch and 1567 cm^{-1} for asymmetric stretch. We find a boost in the intensity of asymmetric COO stretch (1635 cm^{-1}) after introducing oleic acid to the Au NC, suggesting the possibility of monodentate interaction. At 1284 cm^{-1} , the peak for $\text{C}-\text{O}$ stretching vibration of the carboxylic group of Oleic acid was found. At 2888 cm^{-1} and 2936 cm^{-1} , possible symmetric and asymmetric $-\text{CH}_2$ stretching vibrations were detected. When the three AHLs, C-6AHL, C-8AHL, and C-12AHL, are introduced to the AuNC@OA composite solution, the modifications in the biological lactone component with $\text{C}=\text{O}$ (strong) stretch, lactone $\text{C}=\text{O}$ stretch, $\text{N}-\text{H}$ (weak), $\text{O}-\text{CO}$ vibrations, and $\text{O}-\text{CH}_2$ vibrations are preserved.³⁰

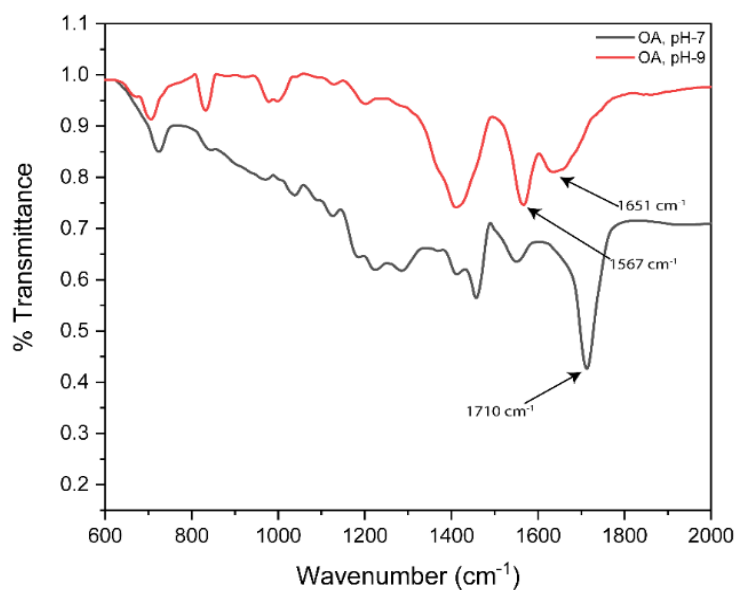


Figure 2.2. FTIR spectra of ethanolic solution of oleic acid at pH= 7 and pH=9. At neutral pH -C=O stretch could be seen at 1710 cm^{-1} shown by arrow which shows that H^+ of -COOH is bound. At pH=9, C=O stretch band shown by arrows appeared at 1651 cm^{-1} (symmetric stretch) and 1567 cm^{-1} (asymmetric stretch).

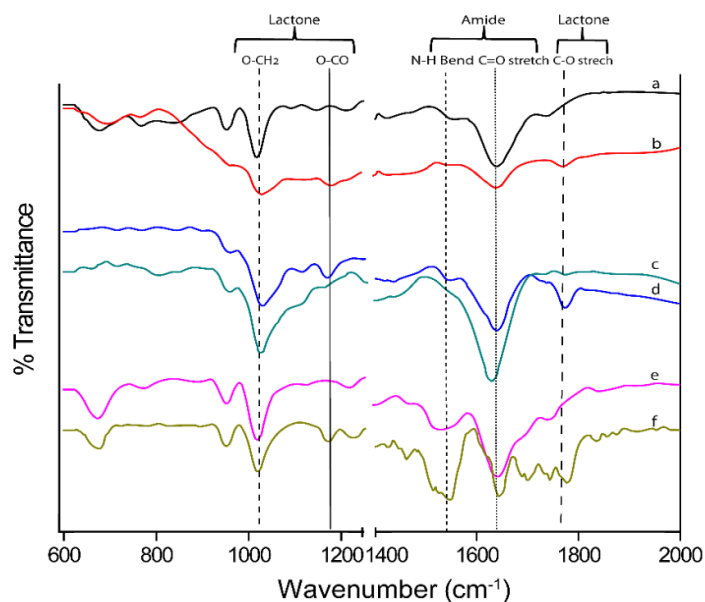


Figure.2.3. FTIR spectra of (a) AuNC@OA@C-6AHL, (b)C-6AHL, (c)AuNC@OA@C-8AHL, (d) C-8 AHL, (e) AuNC@OA@C-12AHL and (f) C-12AHL.

Table 2.1 compiles all of this data. From the above FTIR data, it can be concluded that AuNC@OA@AHL composite is of appropriate framework with the AHL having free lactone head lie outside the composite and remained free to interact with the pathogenic bacterial receptors.

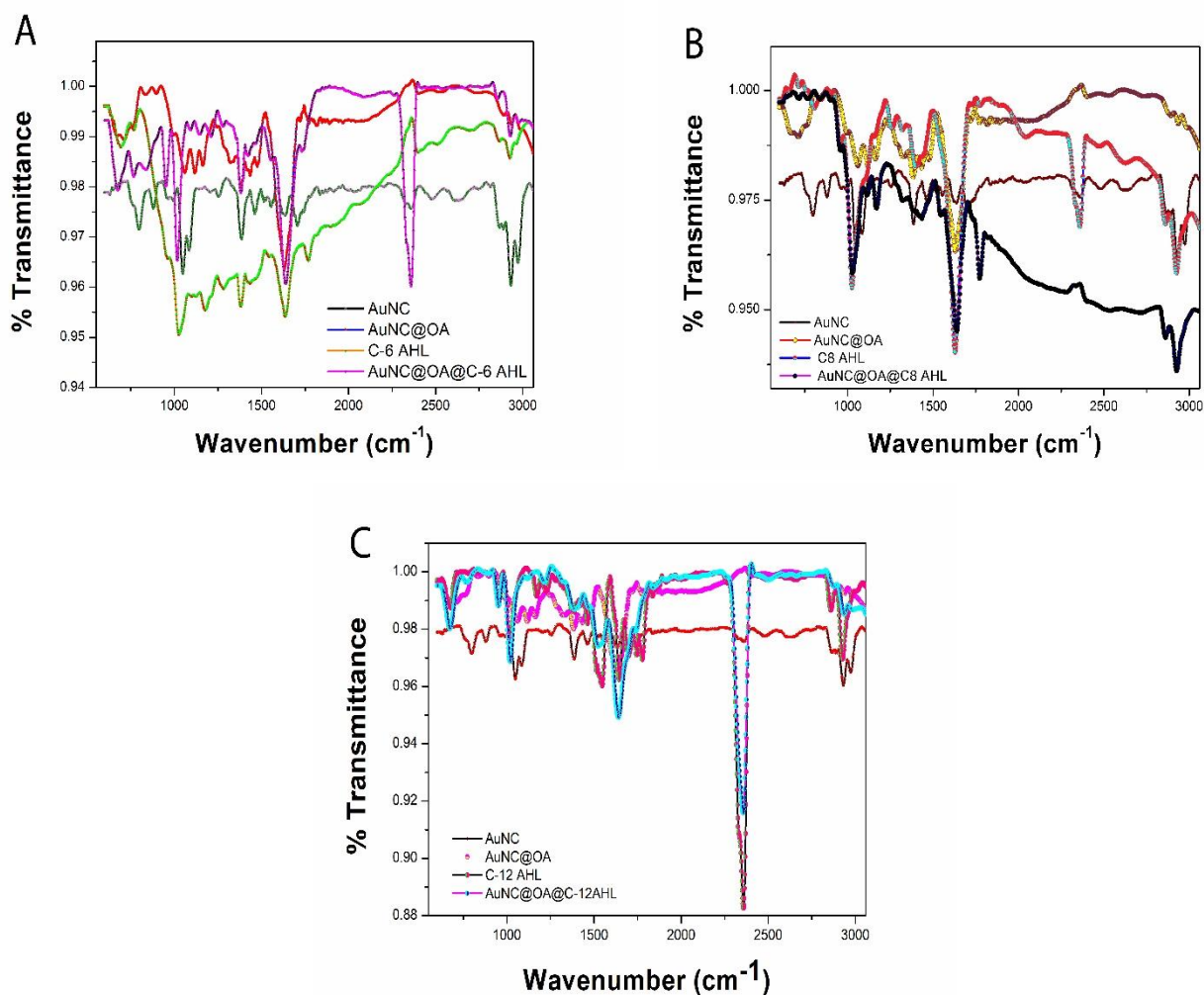


Figure.2.4. FTIR spectra of AuNC and AuNC@OA with (A) C-6 AHL and AuNC@OA@C-6AHL (B) C-8 AHL and AuNC@OA@C-8 AHL (C) C-12 AHL and AuNC@OA@C-12 AHL.

Table 2.1. Description of all important FTIR bands of AHLs and AuNC@OA@AHLs conjugates.

Vibrations	C-6 AHL	C-8 AHL	C-12 AHL	AuNC@OA@C-6 AHL	AuNC@OA@C-8 AHL	AuNC@OA@C-12 AHL
Amide C=O	1637 cm^{-1}	1636 cm^{-1}	1643 cm^{-1}	1641 cm^{-1}	1631 cm^{-1}	1639 cm^{-1}
Amide N-H bend	1543 cm^{-1}	1543 cm^{-1}	1546 cm^{-1}	1540 cm^{-1}	1539 cm^{-1}	1545 cm^{-1}
Lactone C=O	1770 cm^{-1}	1774 cm^{-1}	1742 cm^{-1}	1773 cm^{-1}	1173 cm^{-1}	1741 cm^{-1}
Lactone O-CO	1024 cm^{-1}	1028 cm^{-1}	1019 cm^{-1}	1021 cm^{-1}	1023 cm^{-1}	1018 cm^{-1}
Lactone O-CH ₂	1176 cm^{-1}	1167 cm^{-1}	1170 cm^{-1}	1179 cm^{-1}	1161 cm^{-1}	1165 cm^{-1}

2.3.2.3. Transmission Electron Microscopy to determine the average diameter of AuNC@OA@AHL conjugates

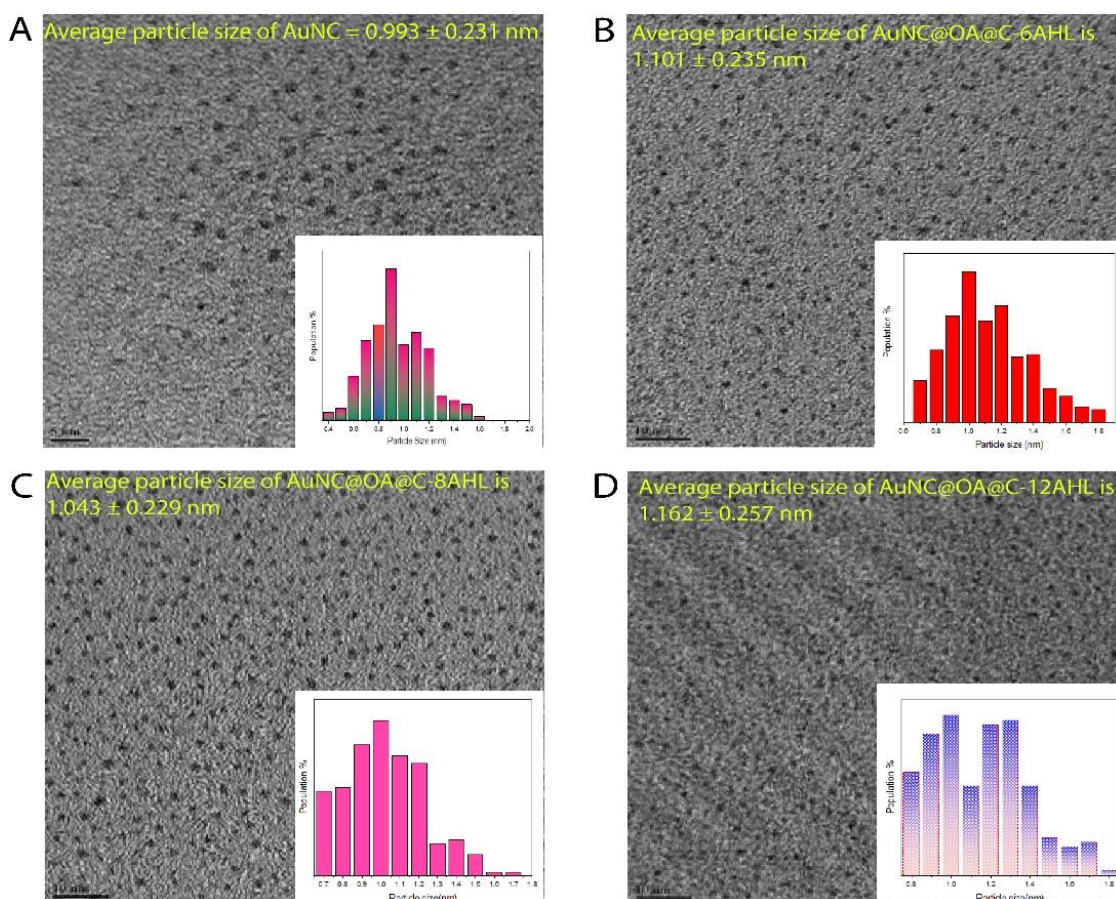


Figure.2.5. TEM images of (A) Au nanoclusters (B) AuNC@OA@C-6AHL(C)AuNC@OA@C-8AHL (D) AuNC@OA@C-12AHL.

After surface functionalization with AHLs, the average particle size of ultra-small Au NCs (0.993 ± 0.231 nm) was not affected (size of AuNC@OA@C-6AHL conjugate is 1.101 ± 0.235 nm, size of AuNC@OA@C-8AHL conjugate is 1.043 ± 0.229 nm, size of AuNC@OA@C-12AHL conjugate is 1.162 ± 0.257 nm), according to TEM images. Figure 2.5 illustrates TEM images.

2.3.2.4. Fluorescence Spectroscopy

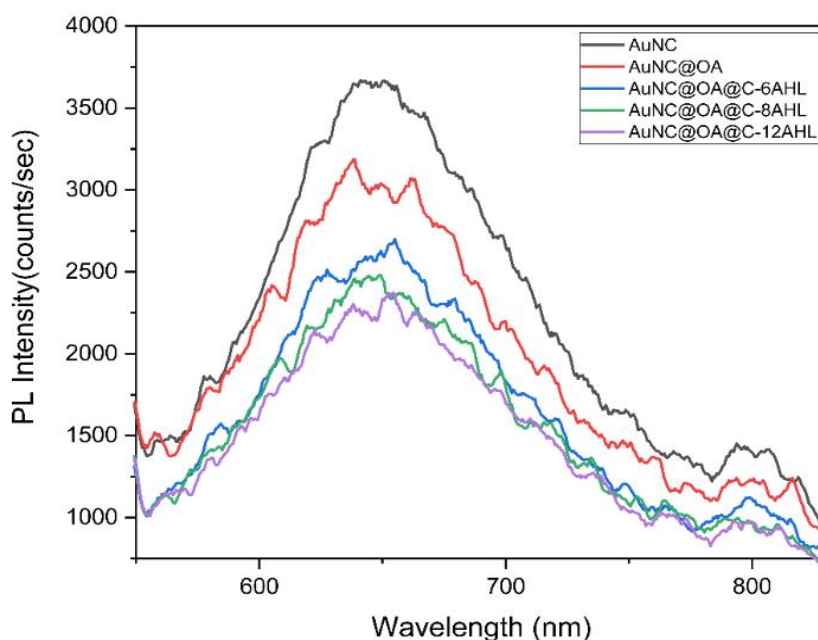


Figure.2.6. Fluorescence spectra of Au nanoclusters and Au NC's composites (excitation wavelength at 420 nm).

Fluorescence spectra of pristine Au NCs (excitation=420 nm) and their composites were recorded to elucidate whether any interaction happened after surface functionalization over AuNCs. The emission from Au nanoclusters and their composites are found to be identical, according to this study (in figure 2.6). As expected, the conjugate's fluorescence intensity decreases. In addition, for all conjugates, we found no change in emission. Because it is within the statistical error, minor differences in emission intensity among the conjugate probes (seen in Figure.2.6) are ignored.

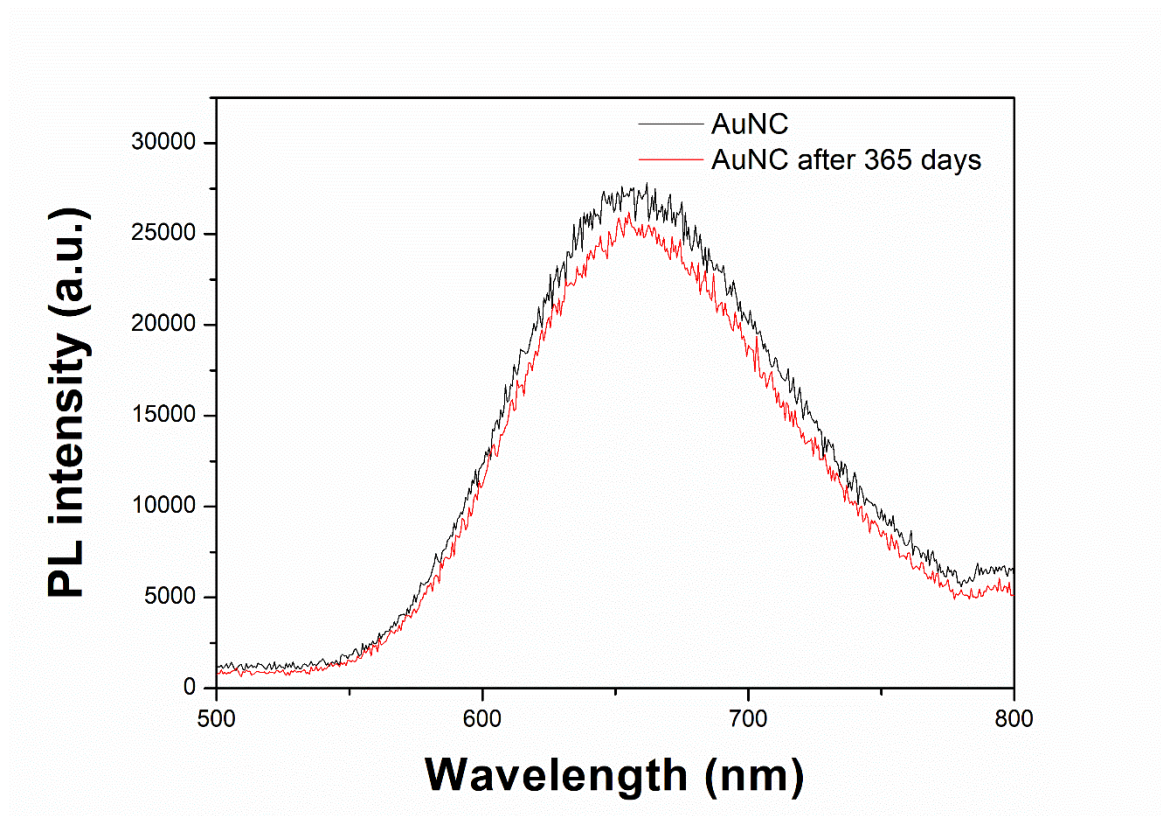


Figure.2.7. Fluorescence spectra of Au nanoclusters at day 1 to 365 days (excitation wavelength at 420 nm).

The photostability of AuNCs after its synthesis also checked (showed in Fig.2.7) at different time intervals as at 1 day and after 365 days. It was found that, these nanoclusters are quite stable after 1 year also, which makes them an excellent candidate as a fluorescent probe in bioimaging.

2.4.2.5. Selective detection of the receptors of *E. coli*, *C. sakazakii* and *P. aeruginosa* through fluorescence microscopy

For the quorum sensing experiments, *E. coli*, *C. sakazakii*, and *P. aeruginosa* as three representative gram-negative bacteria were used. After incubation with the AuNC@OA@AHLs conjugates, bacterial samples were imaged under a fluorescence microscope with a 100 X oil immersion lens (at continuous exposure duration) (with all the three AHLs). During the studies, the concentrations of Au NCs solution (1.3 mM in 1.5 mL of AuNC@OA@AHLs stock), OA (0.4 mM in 1.5 mL of AuNC@OA@AHLs stock), and

AHL (0.2 mM in 1.5 mL of AuNC@OA@AHLs stock) were kept constant in all three AuNC@OA@AHLs. To compute the inconstancy, the bioimaging studies were carried out

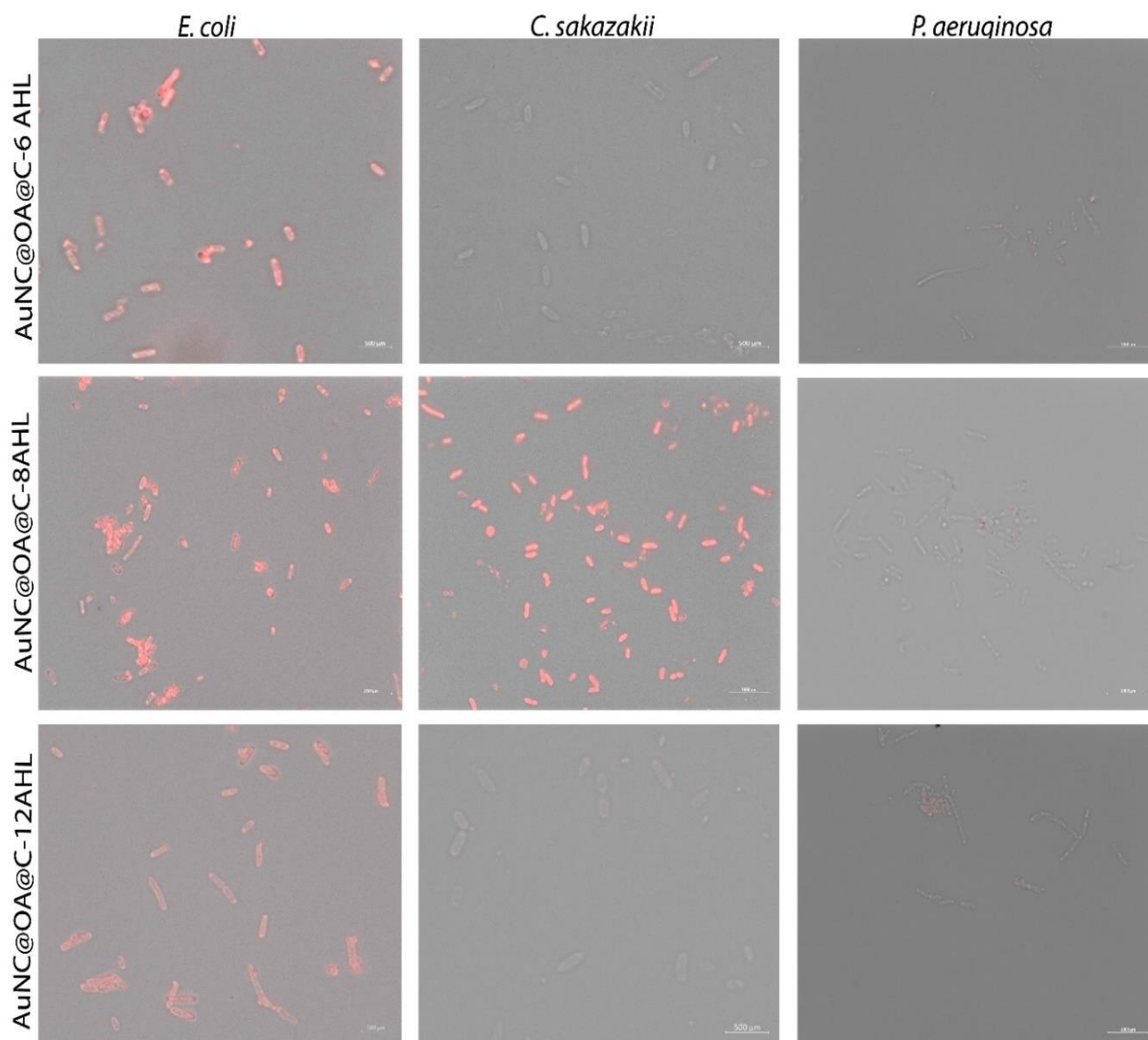


Figure.2.8. Fluorescence microscopy images of (A)(left column) *E. coli* incubated with AuNC@OA@C-6AHL (scale bar-500 μ m), AuNC@OA@C-8AHL(scale bar-1000 μ m), AuNC@OA@C-12AHL(scale bar-500 μ m), (B)(middle column) *C. sakazakii* incubated with AuNC@OA@C-6AHL(scale bar-500 μ m), AuNC@OA@C-8AHL(scale bar-1000 μ m), AuNC@OA@C-12AHL(scale bar-500 μ m) & (C) (right column) *P. aeruginosa* incubated with AuNC@OA@C-6AHL(scale bar-1000 μ m), AuNC@OA@C-8AHL(scale bar-1000 μ m), AuNC@OA@C-12AHL(scale bar-1000 μ m).

in three sets. Representative fluorescence microscopy images of *E. coli*, *C. sakazakii*, and *P. aeruginosa* incubated in conjugates containing C-6AHL, C-8AHL, and C-12AHL are shown in Figure 2.8. When *E. coli* is incubated with AuNC@OA@AHL composites containing all

three AHL molecules, red emission occurs (with carbon chain length of C-6, C-8, C-12). Fluorescence is only observed in *C. sakazakii* when the AuNC@OA@C-8AHL conjugate is used. *P. aeruginosa*, on the other hand, does not emit red emission when incubated with AuNC@OA@C-6AHL, AuNC@OA@C-8AHL, or AuNC@OA@C-12AHL. Because gram-negative bacteria secrete acyl homoserine lactone molecules, the AuNC@OA@AHL conjugate should only interact with the receptors of *E. coli*, *C. sakazakii*, and *P. aeruginosa*. These findings reveal the AuNC@OA@AHL conjugates' native specificity for interacting selectively with strains that have AHL receptors, as well as the effectiveness with which inorganic fluorescent probes made up of AuNC@OA@AHL conjugates cross bacterial cell walls to interact with their receptors in the cytoplasm.

2.4.2.6. Specific interaction between lactone moiety of AHL and the receptors of bacterial strains

The bacterial cells were stained with intermediate structures such as AuNC@AHL, AuNC@OA, and AuNCs to further analyse our assumption of the fluorescent probe conjugates framework and manner of interaction. All three of the aforementioned composites were made in such a way that the concentrations of AuNCs, acyl homoserine lactone, and oleic acid were similar to those of the AuNC@OA@AHL conjugates. There may be an electrostatic contact between the quaternary ammonium head of the thiol ligand capped gold nanoclusters and the lactone head of AHLs when *E. coli*, *C. sakazakii*, and *P. aeruginosa* are stained with AuNC@AHL composite. We expect the lactone moiety of AHL to be available for binding to receptors in this case. Even without AHL, fluorescent AuNC@OA (oleic acid across the surface of AuNC makes the clusters hydrophobic) and AuNC can approach the binding receptor site at random without the signal molecule. When *E. coli*, *C. sakazakii*, and *P. aeruginosa* were stained with AuNC, AuNC@OA, AuNC@AHL (shown in Figures 2.9, 2.10 and 2.11), no red emission was observed, confirming the significance of the proposed fluorescent probe structure. As a result of the foregoing analysis, it is obvious that the AuNC@OA@AHL fluorescent probe is the only framework capable of sensing the Lux-R homologues of gram-negative bacterial cells.

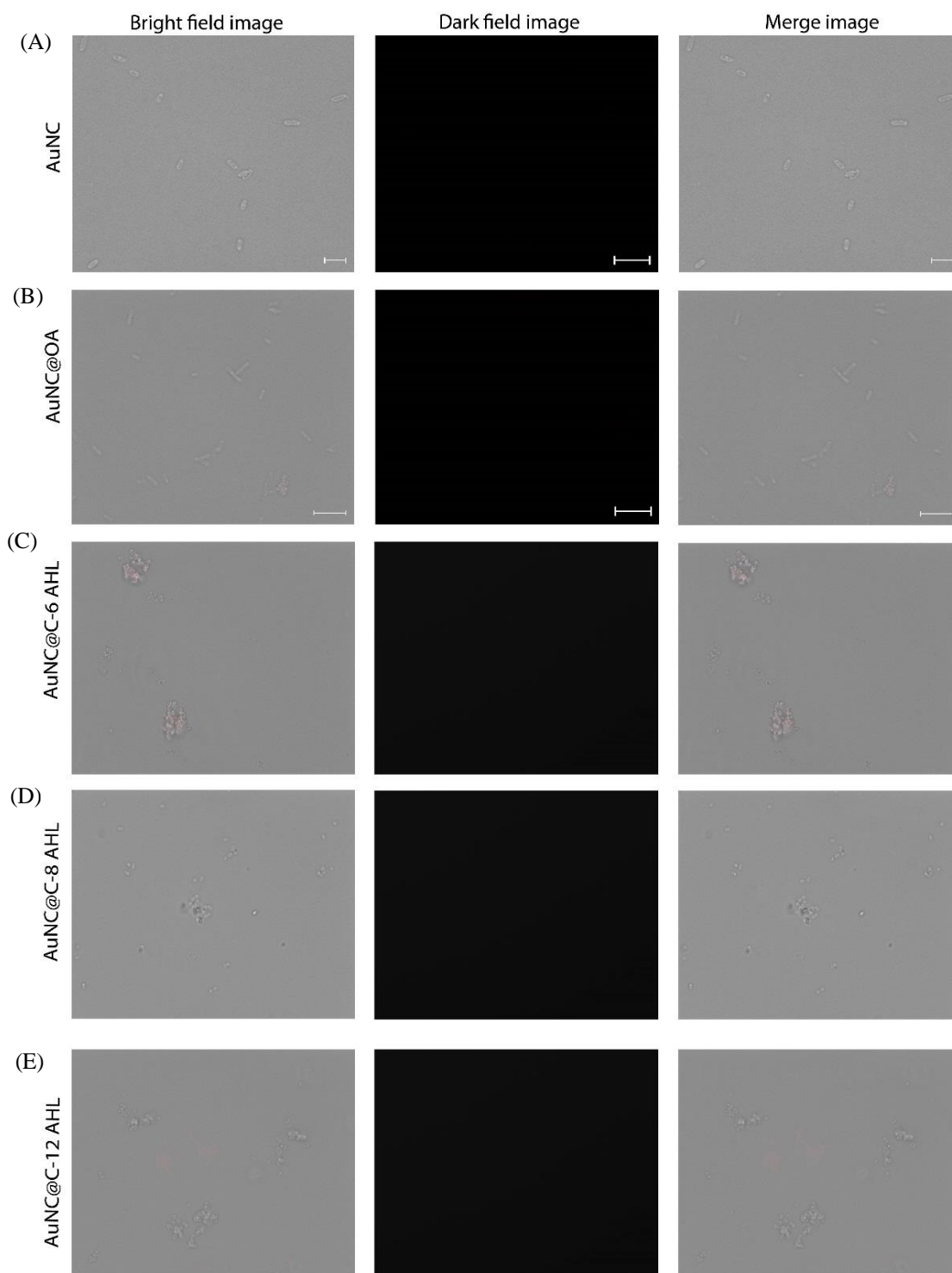


Figure.2.9. Fluorescence microscopy images of (A) *E. coli* incubated with AuNC, (B) *E. coli* incubated with AuNC@OA (C) *E. coli* incubated with AuNC@C-6 AHL (D) *E. coli* incubated with AuNC@C-8 AHL (E) *E. coli* incubated with AuNC@C-12 AHL.

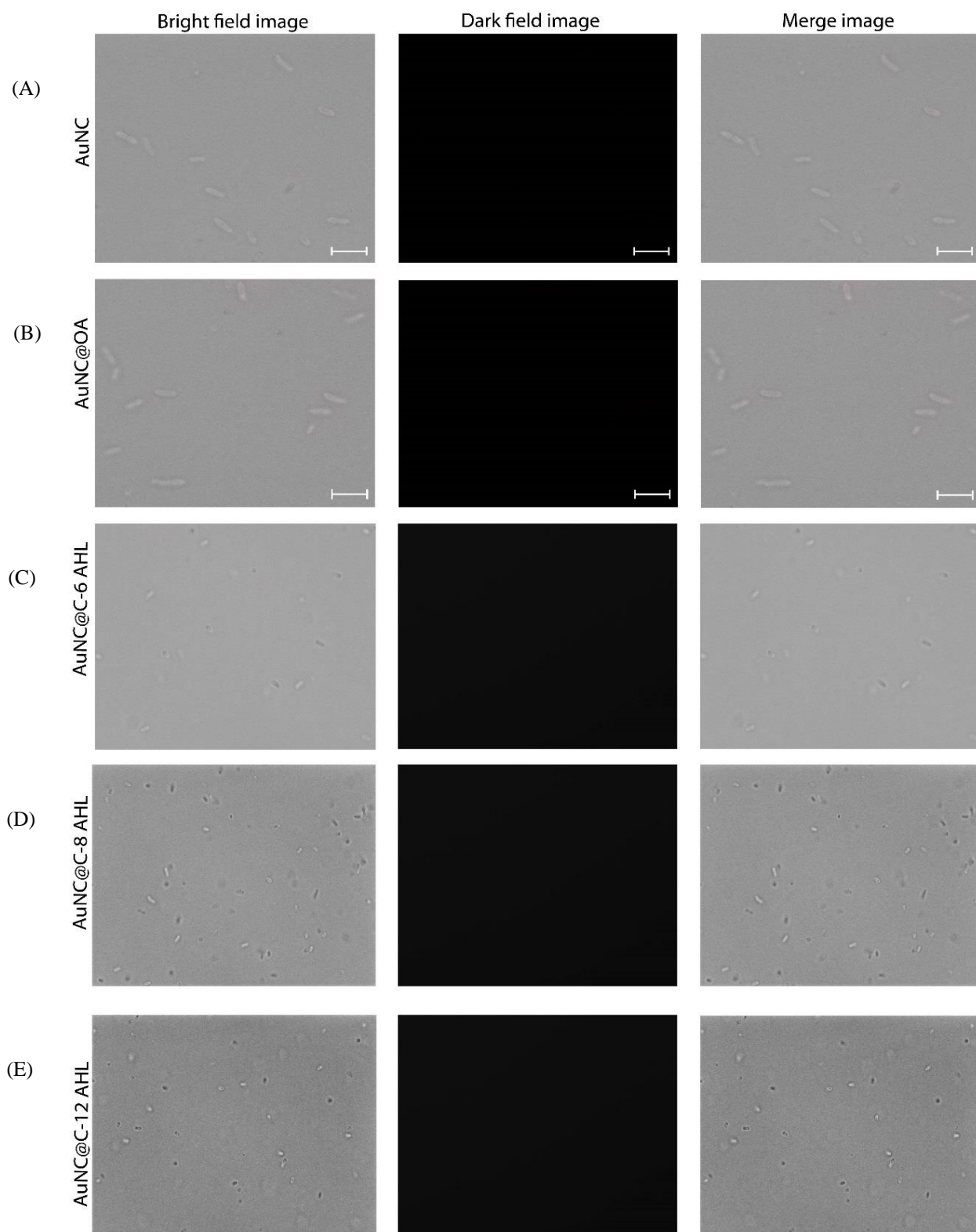


Figure.2.10. Fluorescence microscopy images of *C. sakazakii* incubated with (A) AuNC (B) AuNC@OA (C) AuNC@C-6 AHL (D) AuNC@C-8 AHL (E) AuNC@C-12 AHL.

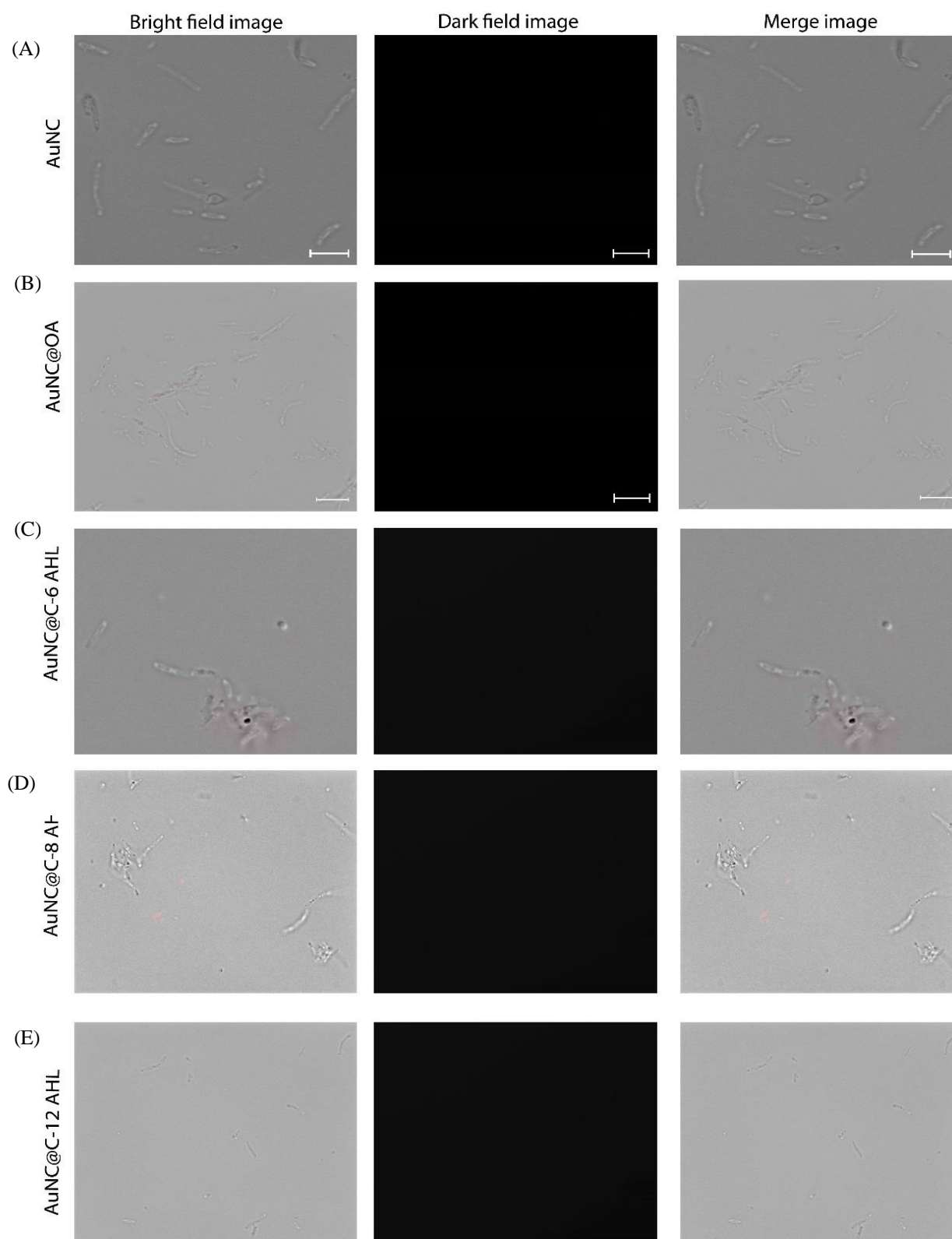


Figure.2.11. Fluorescence microscopy images of *P. aeruginosa* incubated with (A) AuNC, (B) AuNC@OA, (C) AuNC@C-6 AHL, (D) AuNC@C-8 AHL, (E) AuNC@C-12 AHL.

2.4.2.7. TEM analysis of the bacteria incubating with AuNC@OA@AHL

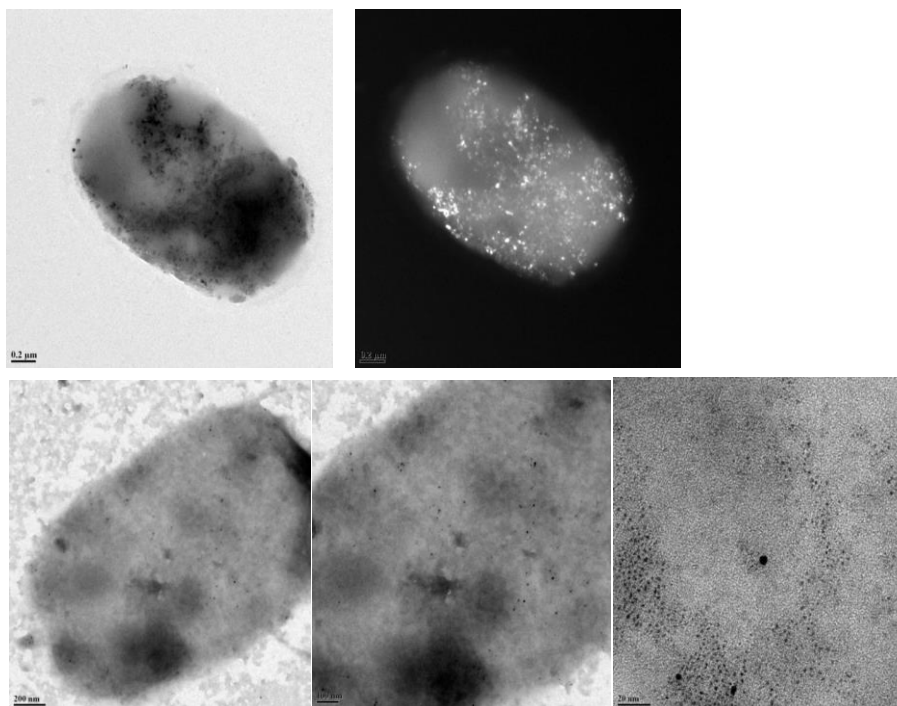


Figure.2.12. TEM images taken for *Escherichia coli* when incubated with AuNC@OA@C-12AHL conjugates at various scales.

After incubation with the conjugate, TEM examination of the bacteria reveals the presence of Au particles within the cell wall, as illustrated in figure 2.12.

2.4.2.8. Statistical analysis to quantify AuNC present in gram-negative bacterial cells on the basis of fluorescence intensity

Following the quorum sensing experiments, a statistical analysis of the fluorescence intensities was carried out to distinguish the quantity of AuNC present in the bacteria and quantify the differences in conjugate uptake by the three gram-negative bacterial strains. Fluorescence intensities from three distinct zones of images with the same number of cells (average 15 cells per image for each experiment) were calculated using Zeiss 2.3 lite software. To evaluate the AuNC@OA@AHL conjugate's selectivity towards the pathogen's unique quorum sensing receptors, we selected three photos for each strain (on average 15 to 20 bacterial cells per image) cultured independently with three different bacteria. The selectivity and specificity of AuNC@OA@AHL composites against pathogen quorum sensing receptors were then determined using statistical analysis. The data reported here was derived from three different studies (n=3). GraphPad Prism 5 was used to compare data sets

using two-way ANOVA. $**p < 0.01$ and $***p < 0.001$ (given in figure 2.13) were regarded statistically significant probability values.

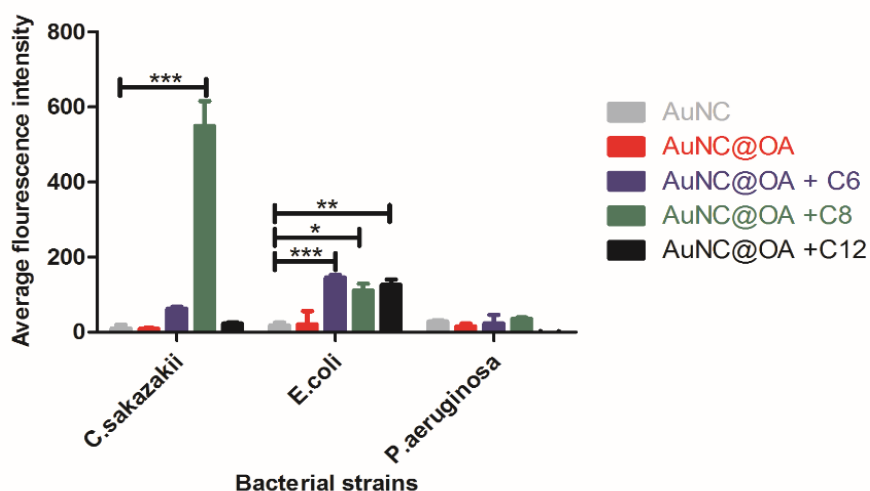


Figure.2.13. Average fluorescence intensity of bacterial cells with different AuNC composites. AuNC was used as negative control ($**p < 0.01$ and $***p < 0.001$) ($n=3$).

The fluorescence intensities were found to be directly proportional to the concentration of AuNC@OA@AHLs fluorescent probes inside the bacterial cell, as well as their interaction with Lux-R type receptors. Small variations in emission intensity among the conjugate probes (shown in Fig. 2.13) is not considered since it is within the statistical error. When compared to AuNC@OA@C-6AHL and AuNC@OA@C-12AHL, the fluorescent AuNC@OA@C-8AHL probe shows red emission with the greatest fluorescence intensity in the case of *C. sakazakii*, indicating excellent specificity. *E. coli*, on the other hand, gives no preference to any of the AuNC@OA@AHL conjugates and emits red with all of them at equal intensities, albeit less than *C. sakazakii*. It is concluded that AHLs have no specific selectivity for *E. coli* Lux-R type receptors. *P. aeruginosa*, on the other hand, shows minimal interaction with any of the conjugates studied. The selectivity and specificity of AuNC@OA@C-8AHL towards *C. sakazakii* is the most evident among *E. coli*, *C. sakazakii*, and *P. aeruginosa*, according to average intensities estimation.

In quorum sensing, signal selectivity is a key feature that may be used to identify bacteria or target antibacterial activity. LuxR homologue receptors are selective to AHLs generated by cognate synthases, despite the fact that most AHLs have a similar molecular framework. Signal promiscuity by LuxR homologue receptors is also acknowledged, like in the instance

of *C. violaceum*, which is implied to have evolved for inter-species communication. The interaction between LuxR homologue receptors and AHLs of various frameworks, which is based on crystal structures of the receptors coupled to cognate autoinducers, might be the source of signal selectivity. It is widely known that Sdi-A receptors can detect AHLs from both modified and unmodified acyl chains at concentrations ranging from nM to μ M. This non-specificity was also seen in our tests using the C chain length of AHLs in *E. coli*. In the case of *P. aeruginosa*, however, the signalling process is more complicated. The LasR cognate modified 3-oxo-C12 AHL is reported to be the most common AHL for *P. aeruginosa*, and it is required at high quantities in the absence of las-B promoters. Purified LasR exhibits good binding to 3-oxo-C12 AHL and to a lesser extent 3-oxo-C10 AHL, but no affinity for other AHLs, as previously described. Some studies also established that the preference shown by LasR towards 3-oxo substituted AHLs which is further dependent upon H-bonding of the polar groups which stabilizes the LasR-AHL binding. Orphan QscR has a worse signal selectivity than LasR, owing to a bigger ligand binding site and a distinct H-bonding architecture.³¹ However, because QscR is activated later than LasR, its activity may not be seen in the early phases. As a result, it is likely that the bacteria do not even detect the concentrations employed here for unaltered AHLs. Due to the lack of such detailed investigations in the instance of *C. sakazakii*, to comment more on the inherent structural characteristics that may have emerged in the selectivity to C-8AHL is prevented. However, this application might be aimed towards a signal selectivity in *C. sakazakii*, which would require further mechanistic insights.

2.5. CONCLUSION

Hence, an NIR emitting inorganic Au nanocluster-based fluorescent probe was created to better understand gram-negative bacteria's quorum sensing behaviour. This inorganic fluorescent probe is made up of gold nanoclusters that have been surface functionalized with various length AHLs (acyl homoserine lactones). The bioactive portion of AHL (lactone moiety) stays intact after surface functionalization of AHLs over the surface of Au nanocluster, allowing for natural activity as a pure AHL molecule. This feature allows the surface functionalized Au nanoclusters to detect quorum sensing receptors in bacteria before they achieve the havoc quorum state.

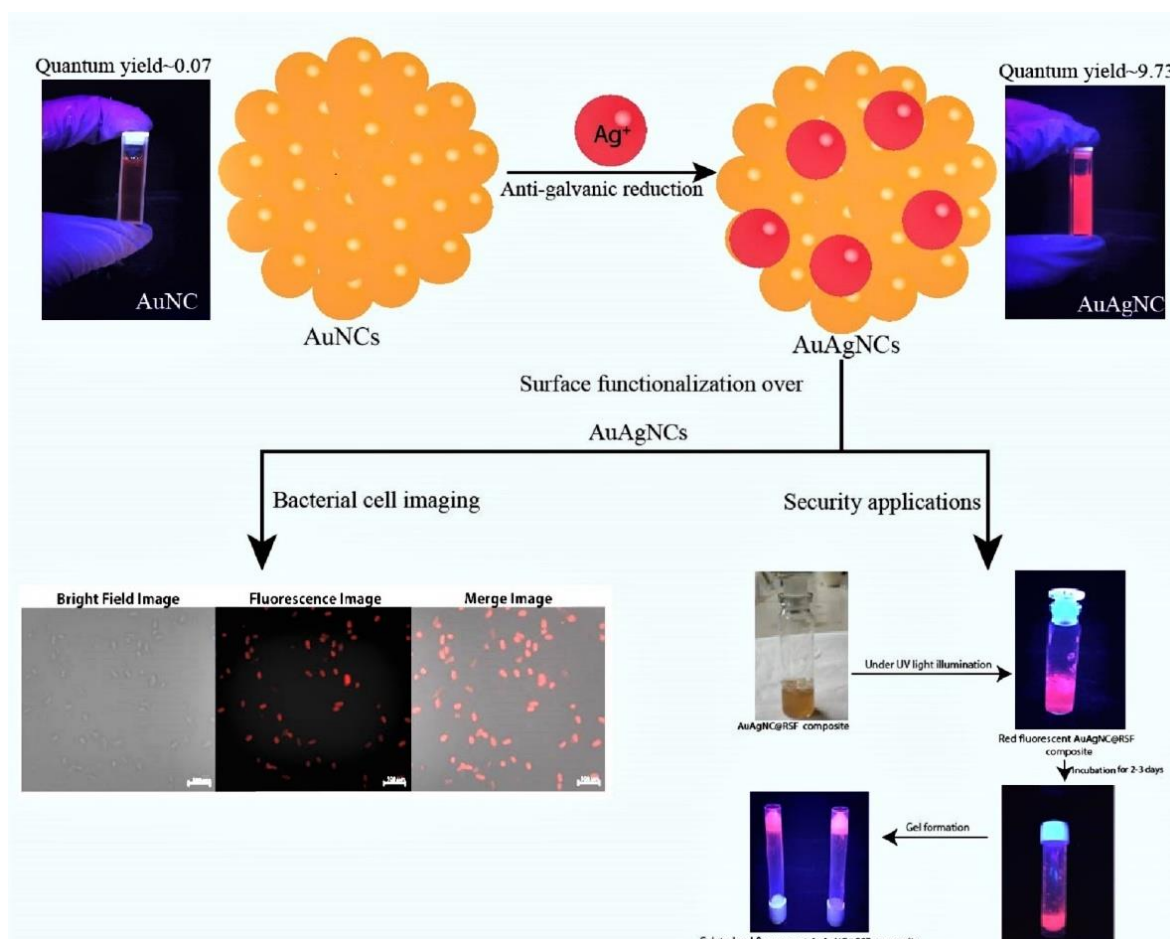
2.7. References:

- 1 C. M. Waters and B. L. Bassler, *Annu. Rev. Cell Dev. Biol.*, 2005, **21**, 319–46.
- 2 M. B. Miller and B. L. Bassler, 2001, **12**, 48.
- 3 Mickae Boyer & Florence Wisniewski-Dye, *FEMS Microbiol. Ecol.*, 2009, **70**, 1–19.
- 4 S. T. Rutherford and B. L. Bassler, *Cold Spring Harb. Perspect. Med.*, 2012, **2**.
- 5 J. A. Ahmer, Brian M.M. and Soares, *Curr. Opin. Microbiol.*, 2011, **14**, 188–193.
- 6 M. Y. Galperin and M. Y. Galperin, *J. Bacteriol.*, 2006, **188**, 4169–4182.
- 7 M. Y. Galperin, A. N. Nikolskaya and E. V Koonin, *FEMS Microbiol. Lett.*, 2001, **203**, 11–21.
- 8 C. Fuqua and E. P. Greenberg, *Nat. Rev. Mol. Cell Biol.*, 2002, **3**, 685–695.
- 9 Z. Li and S. K. Nair, *Protein Sci.*, 2012, **21**, 1403–1417.
- 10 R. Chen, E. Déziel, M. C. Groleau, A. L. Schaefer and E. P. Greenberg, *Proc. Natl. Acad. Sci. U. S. A.*, 2019, **116**, 7021–7026.
- 11 D. Kušar, K. Šrampf, P. Isaković, L. Kalšek, J. Hosseini, I. Zdovc, T. Kotnik, M. Vengušt and G. Tavčar-Kalcher, *BMC Vet. Res.*, 2016, **12**, 1–11.
- 12 K. Papenfort and B. L. Bassler, *Nat. Rev. Microbiol.*, 2016, **14**, 576–588.
- 13 J. Lee and L. Zhang, *Protein Cell*, 2015, **6**, 26–41.
- 14 J. L. Dyszel, J. A. Soares, M. C. Swearingen, A. Lindsay, J. N. Smith and B. M. M. Ahmer, *PLoS One*, , DOI:10.1371/journal.pone.0008946.
- 15 J. A. Soares and B. M. M. Ahmer, *Curr. Opin. Microbiol.*, 2011, **14**, 188–193.
- 16 N. Singh, A. Patil, A. A. Prabhune, M. Raghav and G. Goel, *Virulence*, 2017, **8**, 275–281.
- 17 K. Gademann, *Chem. Eur. J*, 2013, **19**, 9766–9770.
- 18 L. Zhang and E. Wang, *Nano Today*, 2014, **9**, 132–157.
- 19 Y. Tao, M. Li, J. Ren and X. Qu, *Chem. Soc. Rev.*, 2015, **44**, 8636–8663.
- 20 A. Mathew and T. Pradeep, *Part. Part. Syst. Character.*, 2014, **31**, 1017–1053.
- 21 Y. Zheng, L. Lai, W. Liu, H. Jiang and X. Wang, *Adv. Colloid Interface Sci.* , 2017,

-
- 242, 1-16.
- 22 R. Yan, Z. Shou, J. Chen, H. Wu, Y. Zhao, L. Qiu, P. Jiang, X. Z. Mou, J. Wang and Y. Q. Li, *ACS Sustain. Chem. Eng.*, 2018, **6**, 4504–4509.
- 23 P. H. Chan and Y. C. Chen, *Anal. Chem.*, 2012, **84**, 8952–8956.
- 24 H. Ji, L. Wu, F. Pu, J. Ren and X. Qu, *Adv. Healthc. Mater.*, 2018, **7**, 1–6.
- 25 Y. Zheng, X. Wang and H. Jiang, *Sens. Actuators B Chem.*, 2018, **277**, 388–393.
- 26 R. Mukherji, A. Samanta, R. Illathvalappil, S. Chowdhury, A. Prabhune and R. N. Devi, *ACS Appl. Mater. Interfaces*, 2013, **5**, 13076–13081.
- 27 A. Samanta, B. B. Dhar and R. N. Devi, *J. Phys. Chem. C*, 2012, **116**, 1748–1754.
- 28 J. J. Nájera and A. B. Horn, *Phys. Chem. Chem. Phys.*, 2009, **11**, 483–494.
- 29 L. Zhang, R. He and H. C. Gu, *Appl. Surf. Sci.*, 2006, **253**, 2611–2617.
- 30 H. Sheng, F. Wang, C. Gu, R. Stedtfeld, Y. Bian, G. Liu, W. Wu and X. Jiang, *RSC Adv.*, 2018, **8**, 9364–9374.
- 31 C. Ha, S. J. Park, S. J. Im, S. J. Park and J. H. Lee, *Mol. Cells*, 2012, **33**, 53–59.

Chapter-3

Enhanced emission from hetero atom doped red emitting water dispersible Au ultra-small nanoclusters and their multifaceted applications in imaging



3.1. INTRODUCTION

Even though red emitting AuNCs have been shown to have potential in a variety of applications, low emission intensity remains a concern. As a result, a variety of strategies are used to tune the photoluminescence of AuNCs, with many of the above-mentioned parameters influencing emission properties being targeted, such as (a) solvent induced etching¹, (b) ligand induced etching², (c) hetero atom doping³, and (d) co-reduction method⁴ (one pot synthesis). Heteroatom doping is one of these that has recently received a lot of attention. Changes in the synthesis techniques have recently been used to replace one or more Au atoms with noble metals (such as Ag, Pd, Cu, and others) in order to further modify the photophysical and photochemical properties of AuNCs.^{5,6,7} Anti-galvanic replacement (AGR) has been reported as the most exceptional way for modifying the fluorescence properties of metal nanoclusters by heteroatom doping.⁸

In the case of Ag doping in Au nanoclusters, AGR entails the reduction of metal ions with a lower electrochemical potential (more reactive) by less reactive noble metals. The anti-galvanic reduction approach, in which water soluble Au⁰@Au⁺¹ GSH core shell nanoclusters were doped with Ag⁺¹ ion, significantly boosted the aggregation-induced emission of Au⁺¹-SG.³ In this context, AuNCs were already synthesized showing emission in a broad range of red spectral region.⁹ The ligand was created with an ammonium functionalized free end and a covalent link with Au. As a result, the clusters are highly water dispersible and compatible with biological systems and other uses. With this system, however, just 3% quantum yield could be produced.¹⁰ In this chapter, by using the AGR approach, improvement in the fluorescence emission of functionalized alkyl thiolate-based AuNCs is shown. With a small red shift (10-15 nm) in the boosted emission and improved QY, very brilliant bimetallic AuAgNCs are synthesized.

The improved PL intensity and quantum yield of AuAgNCs are utilized in bioimaging of quorum sensing receptors in gram- negative bacteria (*E. coli* in this case) as well as integrating in silk fibroins, demonstrating the materials versatility and utility. The contact of an imaging probe with the target substrate is one of the most significant requirements. Structural versatility is thus critical, as is the potential to functionalize the probe to permit interaction with multiple substrates. The AuNCs are developed with cationic head groups that allow for electrostatic interaction with substrates with anionic functional groups. It also allows to change the hydrophobicity of the material by adding functionalities for improved

interaction. The cluster probes stable contact with bacteria as well as silk fibroin through various functionalisation's illustrates its multifaceted applications. One of the most important criteria of an imaging probe, is its interaction with the target substrate. Bacterial interaction is aided by the addition of signal molecules (known as autoinducers) after the hydrophobicity has been adjusted. On gram- negative bacterial cell walls, signal molecules interact with homologous receptor proteins (LuxR-type homologues). Direct electrostatic interaction with electron rich functional groups is used in the instance of regenerated silk fibroin (RSF). The production of fluorescent regenerated silk fibroin (RSF) via genetic alteration, chemical modification, and physical adsorption was recently described by researchers.¹¹ These techniques, however, still confront significant costs and difficulties scaling up robust and long-lasting fluorescence on RSF. We show a straightforward approach for making stable fluorescent RSF without any additives by post-treatment, resulting in a gel that may be utilized as a fluorescent ink or spun into fibres. AuAgNC composites have a lot of potential for imaging and security applications.

3.2. Experimental Section

3.2.1. Synthesis of Au Nanoclusters and Au⁺¹-SR complex

The procedure for the synthesis of Au nanoclusters is given in the previous chapter. For the synthesis of Au⁺¹-SR -complex, same method was used but avoiding NaBH₄ reduction step.

3.2.2. Synthesis of AuAg bimetallic nanoclusters

To avoid light exposure, the Au nanocluster solution was placed in a 100 mL round bottom flask and covered with foil from the outside. At room temperature (26°C), varying concentrations of Ag⁺ ion (AgNO₃ 99.99 %, Merck) were added to this solution with a steady stirring rate of 300 rpm for 30 minutes. The solution was dialyzed with DI water for 3 days in the dark after the reaction. The final volume was adjusted to 14.112 mL after dialysis and kept at 4 °C for further analysis.

3.2.3. Preparation of AuAgNC-3@OA, AuAgNC-3@OA @AHLs conjugates

2 mL of the aforesaid AuAgNC-3 nanocluster solution (2 moles) was added to 0.012 mL (0.6 moles) of oleic acid stock (0.05 M) in MeOH and agitated for 2 h. From 0.2 mM stock of N-hexanoyl-L-homoserine lactone (C-6AHL), N-octanoyl-L-homoserine lactone (C-8AHL) & N-dodecanoyl-L-homoserine lactone (C-12AHL) solutions, 14.7 μL of N-

hexanoyl-L-homoserine lactone (0.37 μ moles), 17 μ L of N-octanoyl-L-homoserine lactone (0.37 μ moles) and 20.8 μ L of N-dodecanoyl-L-homoserine lactone (0.36 μ moles) with 500 μ L of EtOH were added to the mixture of AuAgNC-3@OA solution and stirred again for 2 h to obtain the final conjugate AuAgNC-3@OA@AHL. Same concentrations of AuAgNC-3 and oleic acid were used to synthesize intermediate composites, AuAgNC-3 @AHL and AuAgNC-3 @OA.

3.2.4. Imaging

Escherichia coli ATCC8739 was the bacterial strain employed in this study. Bacteria cells were cultivated in LB medium at optimal temperature until log phase, i.e., 10^6 cells/mL, before being removed and washed in 1X PBS. After that, the cells were resuspended in 1X PBS and gently shaken for 2 hours with 200 μ L AuAgNC-3@OA@AHL conjugates. Au and AHL concentrations were estimated to be (0.13moles) and (0.024moles) respectively when added to 1 mL of 1X PBS containing bacterial cells. Cells were pelleted after incubation, washed in 1X PBS, and resuspended in fresh PBS to ensure that any unbound fluorescent clusters did not interfere with imaging. The slides were prepared with a 50 percent glycerol mounting media for imaging. The sample solution and mounting media were drop cast onto a J. Melvin plain glass slide (75mm x 25mm) and stacked using sterile Sigma-Aldrich cover glasses (size- 22mm x 22mm). Sample slides were then analysed within 3-4 h of preparation using Zeiss Imager A2 fluorescence microscope using Rhodamine filters (transmission wavelength 660nm-750nm) with HXP 120V (excitation range 350nm-700nm) as a source lamp (Carl Zeiss. Inc, Germany). Images were captured and analysed with the help of Zen 2.3 lite software and Image J software respectively.

3.2.5. Regenerated silk fibroin (RSF) solution

The regenerated silk fibroin was provided by Dr. Anuya Nisal (PAML, CSIR-NCL) by adopting the following method. Bombyx mori cocoons were used to make RSF solution (obtained from Central Sericulture Research and Training Institute, Mysore, India). To extract sericin from the silk, the cocoons were first boiled repeatedly for 30 minutes in a sodium bicarbonate (0.05 w/v percent) solution. The extracted mass of silk fibroin was dissolved in 9.3 M lithium bromide (Sigma Aldrich) solution and incubated at 60°C for the following 4 hours. The excess LiBr was then removed using dialysis for 48 hours, with water changes every 8 hours. The dialyzed regenerated silk fibroin solution had a final

concentration of 5% (w/v). This concentration was estimated by weighing the residual solid after RSF powder was dried at 60°C under vacuum. By diluting the 5 percent solution with deionized water, a regenerated silk solution with a concentration of 3 percent (w/v) was created. The RSF solution's final pH was measured to be 6.9 ± 0.2 .

3.2.6. Preparation of AuAgNC-3@RSF gel composite

30 mg of dry RSF powder was placed in a 10 mL vial, followed by 1 mL of AuAgNC-3 stock solution (Au~0.95mM, Ag~0.06mM) in same vial. After that, the liquid solution was maintained for around 2 to 3 days to age. During this time, RSF began to gel, forming an AuAgNC-3@RSF composite.

3.2.7. Leaching studies to check the stability of AuAgNC-3@RSF gel composite

After 30 minutes, 3 mL of buffer solution (ranging from pH 4 to 10) was added to the vial of AuAgNC-3@RSF gelled composite, and this 3 mL of buffer solution was collected with a syringe. Fresh 3 mL of buffer solution (same pH) was added to the same vial, incubated for 2 h, and the buffer solution was collected. This procedure was repeated for 12 h and 24 h.

3.3. Characterization techniques

3.3.1. Transmission electron microscopy

The clusters and conjugates were observed using a TF-20, FEI Tecnai transmission electron microscope operating at 200 kV. Drop casting and air drying the sample solution over a carbon coated mesh 200 grid were used to create the samples. The grid of incubated bacteria was prepared using the same manner.

3.3.2. High resolution transmission electron microscopy

The nanoclusters and conjugates were observed using a JEOL JEM-200 high resolution transmission electron microscope operating at 200 kV, as well as d-spacing calculations and STEM-HAADF imaging also been done.

3.3.3. X-ray photoelectron spectroscopy (XPS)

Thermo Scientific K-alpha+ spectrometer with an energy of 1486.6 eV was used to perform X-ray photoelectron spectroscopy (XPS) observations employing micro-focused and monochromatic Al K radiation. Binding energies were calibrated to the C 1s peak at 284.8 eV after samples were loaded onto silicon wafers and dried at room temperature for analysis. Using XPS peak41 software and a Shirley type background, the XPS peaks profile of individual core levels of elements was fitted.

3.3.4. Fluorescence spectroscopy

A Horiba flouromax-4 fluorescence instrument was used to acquire the fluorescence spectra. Sample solutions (1×10^{-4} M) were placed in a 3.5 mL quartz cuvette with a 10 mm route length for this purpose. The integrating sphere method was used to determine absolute quantum yield, with DI water as the reference solvent and a slit width of 2 nm.

3.3.5. Time-correlated single photon counting (TCSPC) studies

Using a spectrofluorometer (Horiba Scientific) and a 443 nm LED excitation source, photoluminescence lifetimes were determined using time-correlated single photon counting (TCSPC). The characteristics of triexponential fit was judged by fitting parameters such that χ^2 values were maintained ~ 1.2 .

3.3.6. Fourier-Transform IR spectroscopy

The TENSOR-27 BRUKER device was used to acquire FTIR spectra. The standard matrix for making samples was KBr. A 25 μ L sample solution was completely mixed with 100 mg of KBr powder (99.9%, Aldrich), ground well, dried, and formed into a pellet, which was then used to acquire FTIR spectra.

3.3.7. Microwave Plasma Atomic Emission Spectrometry (MP-AES):

On an Agilent 4200, the elemental analysis of nanocluster aqueous solution was performed using inductively coupled plasma atomic emission spectroscopy (MP-AES). For calibration, standard solutions were employed. To remove the organic ligand, 1 mL nanocluster aqueous solution was dried at 100°C for 10 min and calcined at 350°C for 8 h. The residue was dissolved in 1 mL aqua regia and diluted with 15 mL Millipore water. Further elemental analysis was performed using this diluted 15 mL solution.

3.4. Results and Discussion

Gold is less reactive than silver according to the electrochemical potential series, and it is anticipated that Ag metal can reduce Au^{+3} ions, but the reduction of Ag^{+1} by Au metal is difficult in ambient conditions, according to the galvanic theory. However, Au particles in the size regime of ultra-small nanoclusters are suggested to be more amenable to oxidation because of their smaller average diameter and high surface energy.¹² In such reactions, Ag^{+1} ion gets reduced and replaces an Au atom from the nanoclusters, which is known as

Table.3.1. Variation in Ag^{+1} doping during AuAgNC synthesis with their elemental analysis.

Nanocluster	Number of Au^0 moles ($\times 10^{-5}$)	Number of Ag^{+1} moles ($\times 10^{-6}$)	Au^0 : Ag^{+1}	Metal-concentration(mM) by MP-AES analysis	
				Au	Ag
AuNC	1.064	-	1:0	2	0
AuAgNC-1	2.125	3.502	6:1	2	0.03
AuAgNC-2	1.064	3.502	3:1	1	0.03
AuAgNC-3	1.064	7.0125	1.5:1	0.95	0.06

anti-galvanic displacement or reduction reaction. Following this method, AuAg bimetallic nanoclusters were synthesized by varying the mole ratios of Au^0 : Ag^{+1} as 1:0, 6:1, 3:1 and 1.5:1 as given in Table.3.1. However, as observed by elemental analysis by MP-AES (shown in Table.3.1), incorporation of Ag was 10 order less than expected from the concentration of Ag^{+1} added. The core size and structure of AuAg nanoclusters and Au nanoclusters were evaluated using HR-TEM. The average diameters of AuAgNC-1, AuAgNC-2, AuAgNC-3, and AuNC spherical particles were found to be 1.143 ± 0.20 nm, 1.28 ± 0.24 nm, 1.33 ± 0.25 nm, and 0.99 ± 0.23 nm, respectively. A total of 300 particles were examined in order to get the histogram (Fig.3.1). The presence of well-defined lattice planes and facets (Fig.3.2) indicates that AuNCs and bimetallic AuAgNCs have a high order of crystallinity. The cubic FCC crystal structure of Au and Ag is identical, with significant d-spacing values of 0.23 nm and 0.20 nm, respectively, corresponding to the (111) and (200) planes.¹³ The average d-spacing values (Table.3.2) for five separate particles from AuNC, AuAgNCs, and AgNC

were determined, and it was discovered that AuAgNCs d(111) and d(200) are more similar to the (111) and (200) planes of AuNCs and AgNCs, respectively.

Table.3.2. Average d-spacings were calculated for 5 different particles from AuNCs, AuAgNCs and AgNCs and tabulated below.

Nanoclusters	(111) plane d-spacing (nm)	(200) plane d-spacing (nm)
AuNC	0.2328±0.0027	0.2043±0.0026
AuAgNC-1	0.2331±0.0019	0.2050±0.0020
AuAgNC-2	0.2330±0.0012	0.2066±0.0021
AuAgNC-3	0.2331±0.0029	0.2043±0.0030
AgNC	0.2339±0.0026	0.2012±0.0017

This suggests that Ag gets incorporated into AuNCs on a nanoscale level. The presence of Ag in the Au NCs is also confirmed by element mapping using the HAADF-STEM approach (Fig.3.3). The synthesis of bimetallic is also confirmed by TEM-EDS analysis (Fig.3.4), with Au:Ag concentrations comparable to those found by MP-AES (Table.3.3).

The incorporation of Ag in AuNCs is expected to result in changes in electron density distribution on both atoms, and a thorough understanding of this was sought from oxidation state alterations of Au and Ag discovered by XPS. The Au 4f and Ag 3d core-level XPS spectra are shown in Fig.3.5(a) and (b), with the Au⁰ and Ag⁰ peak positions indicated (detailed deconvolution and fitting of different peaks are shown in Fig.3.6 and Fig.3.7).

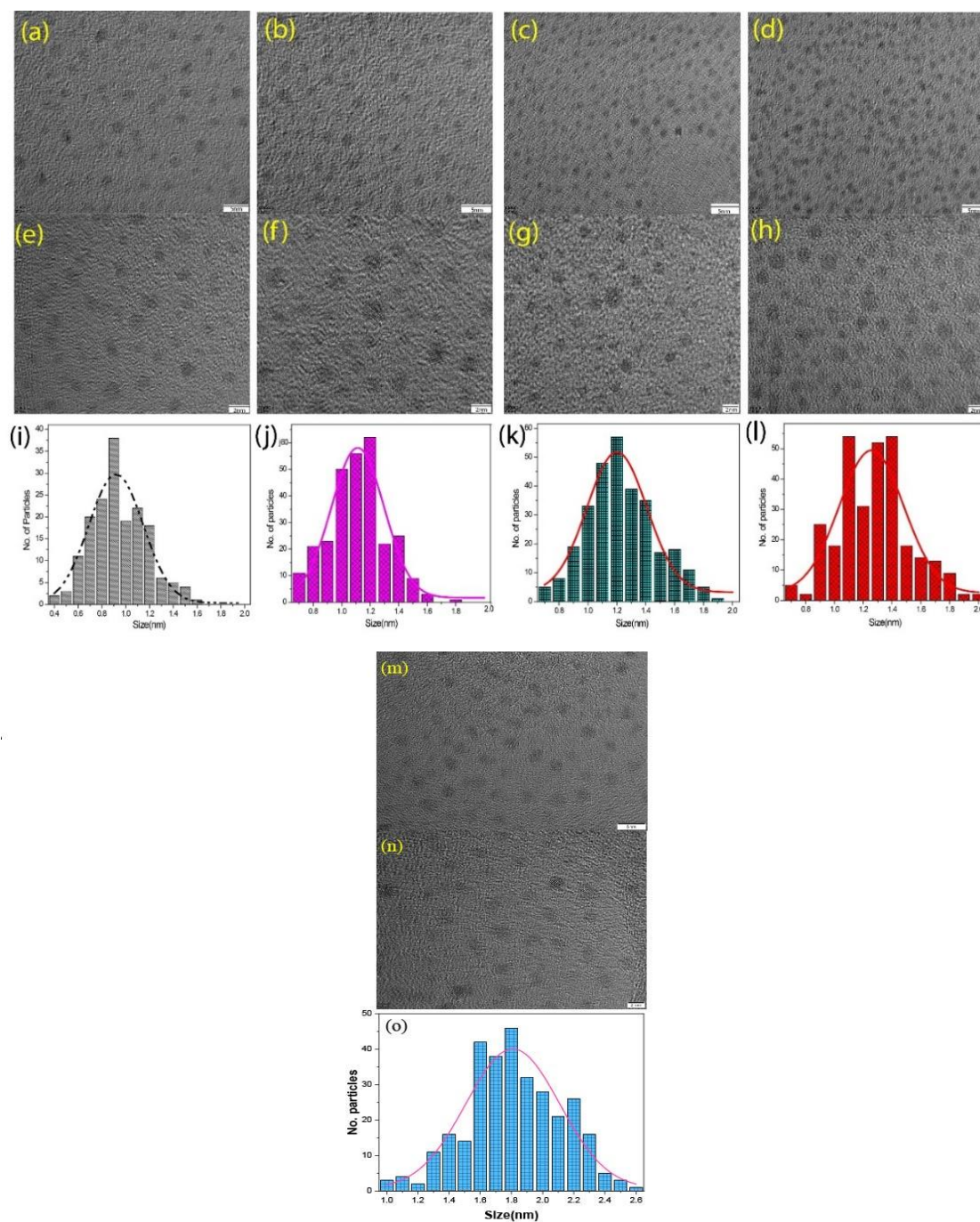


Fig.3.1.HR-TEM images of AuAg nanoclusters and Au nanoclusters, (a & e) AuNC, (b & f) AuAgNC-1, (c and g) AuAgNC-2 and (d & h) AuAgNC-3. Particle size distribution histograms of (i) AuNC, (j) AuAgNC-1, (k) AuAgNC-2 and (l) AuAgNC-3. Top horizontal row (left to right) images are with scale bar 5nm and bottom row (left to right) images are with scale bar 2nm. (m, n and o) shows the HR-TEM images and particle size distribution of AgNCs.

Table.3.3. Correlation between MP-AES analysis and EDS data for all the bimetallic AuAg nanoclusters.

Nanoclusters	Metal- concentration(mM) by MP-AES analysis		Metal wt % by EDAX analysis		Au:Ag ratio by MP-AES analysis	Au:Ag ratio by EDAX
	Au	Ag	Au	Ag		
AuAgNC-1	2	0.03	98.71	1.45	66.67:1	68.11:1
AuAgNC-2	1	0.03	97.25	2.75	33.33:1	35.36:1
AuAgNC-3	0.95	0.06	94.58	5.91	15.83:1	16:1

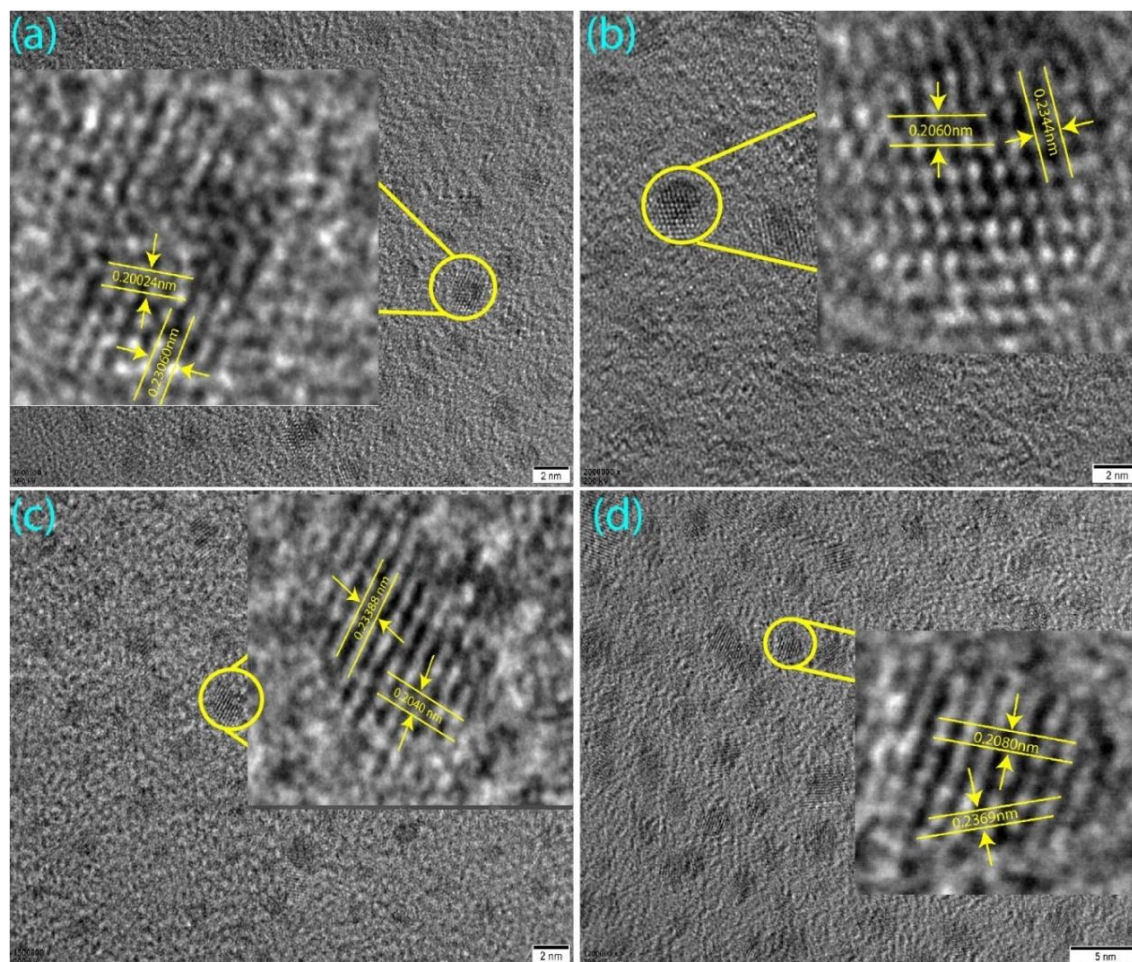


Fig.3.2. HR-TEM images describing their crystalline nature with d-spacing analysis for all the nanoclusters i.e., (a) AuNC (scale bar 2 nm), (b) AuAgNC-1(scale bar 2 nm), (c) AuAgNC-2(scale bar 2 nm). and (d) AuAgNC-3(scale bar 5 nm). Crystalline nature of nanoclusters is visible in the magnified images given in the insets.

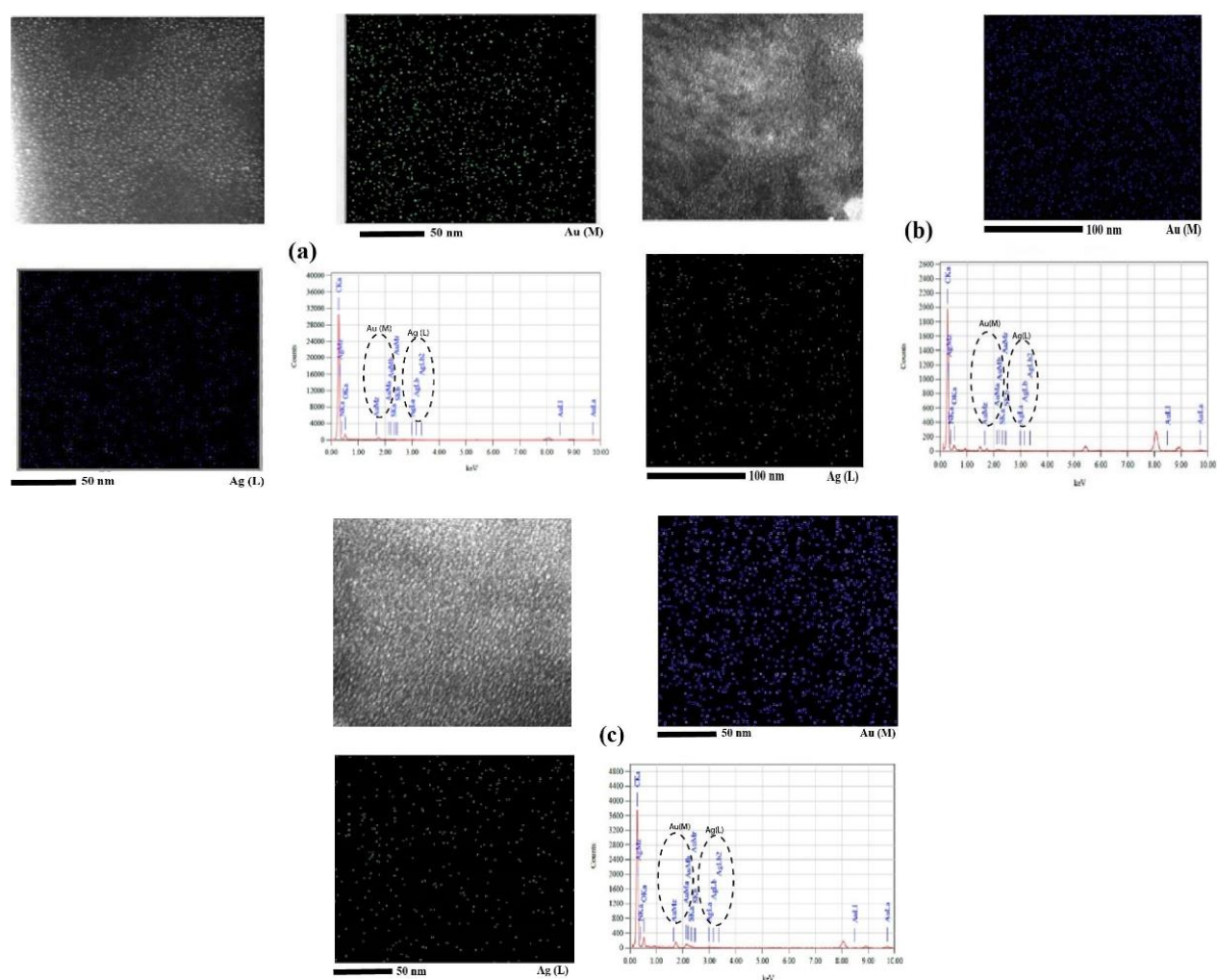


Fig.3.3. Elemental mapping through STEM-HAADF images of nanoclusters i.e., (a) AuAgNC-1, (b) AuAgNC-2, (c) AuAgNC-3. The dotted circles indicate the presence of Au and during EDS analysis.

The change in binding energies (B.E.) of thiol S $2p_{3/2}$ core energy levels before and after Ag^{+1} doping onto Au nanoclusters is shown in Fig.3.8. The XP spectra of S $2p_{3/2}$ from Au^{+1} -SR complex, synthesized without the reduction step, is also considered to understand the interaction between thiolate sulphur and Au^{+1} , as shown in Fig.3.8. The peak positions and concentrations of the various species identified are listed in Table 3.4. In Scheme.3.1., we attempted to depict the possible electron redistributions in these nanoclusters schematically.

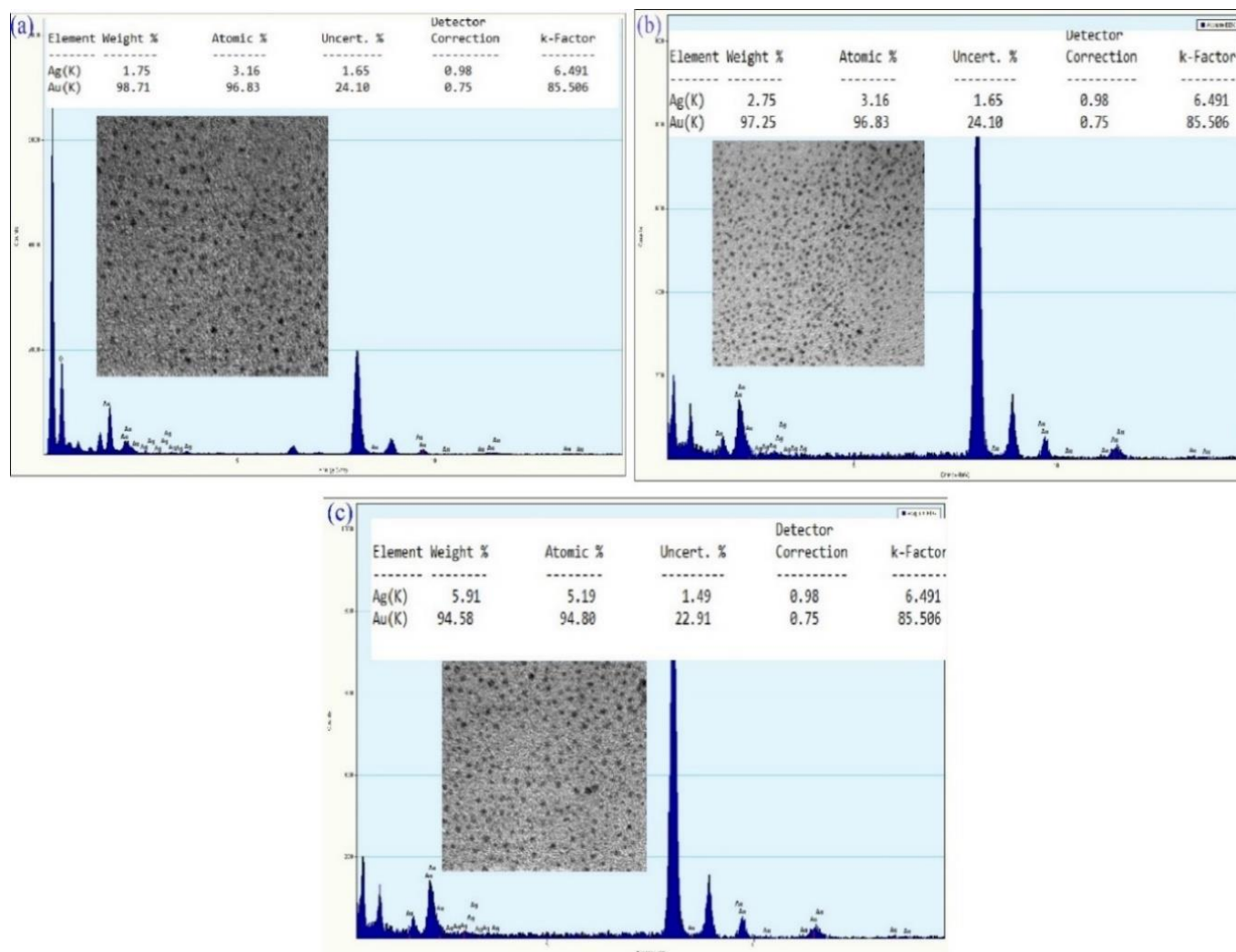


Fig.3.4. EDS through TEM giving wt% of Au and Ag in (a) AuAgNC-1, (b) AuAgNC-2, (c) AuAgNC-3.

In the case of pristine gold nanoclusters, B.E. of Au⁰ 4f_{7/2} and 4f_{5/2} energy levels were detected at 84.8 eV and 88.5 eV, respectively, at higher binding energies than bulk metallic Au, as expected due to the nano size effect.¹⁴ In Au nanoclusters (Case-I, Scheme.3.1) no Au⁺¹ species were detected, indicating that these nanoclusters only contain fully reduced Au atoms. At 162.99 eV, the B.E. of S 2p_{3/2} thiolate in AuNCs was observed. The core energy level 3d_{5/2} of Ag was found at 368.3 eV in AgNCs (Case-II in Scheme.3.1), and the B.E. of S 2p_{3/2} of thiolate was measured at 162.32 eV. Because the electronegativity difference (EN) between Au and S is smaller than the difference between Ag and S (EN of S, Au, and Ag are 2.58, 2.4, and 1.93, respectively), electron transfer from Ag surface atoms to S is preferred over electron transfer from Au to S. In comparison to undoped Au and Ag NCs, the core binding energy levels of Au 4f_{7/2} and Ag 3d_{5/2} in Ag doped AuNCs were moved

towards lower binding energies. With less Ag doping, this shift was more prominent in AuAgNC-1 clusters. In general, a tiny amount of Ag electron density donation to Au (Ag: less electronegative atom, $X_{Ag}=1.93$ to Au: more electronegative atom, $X_{Au}=2.4$) is thought to cause a negative shift in the Au 4f binding energies.^{15,16} This should result in an electron deficiency on Ag, resulting in higher B.E. values in Ag 3d XP spectra, but we see the opposite. Negishi et al. observed similar contradicting Ag 3d B.E. behavior in $Au_{25-x}Ag_x$ clusters¹⁵, which was explained by Au-Ag charge redistribution, which balanced the electron density removed from Au by thiolate ligands, resulting in Au 4f binding energies comparable to Au nanoclusters.¹⁷

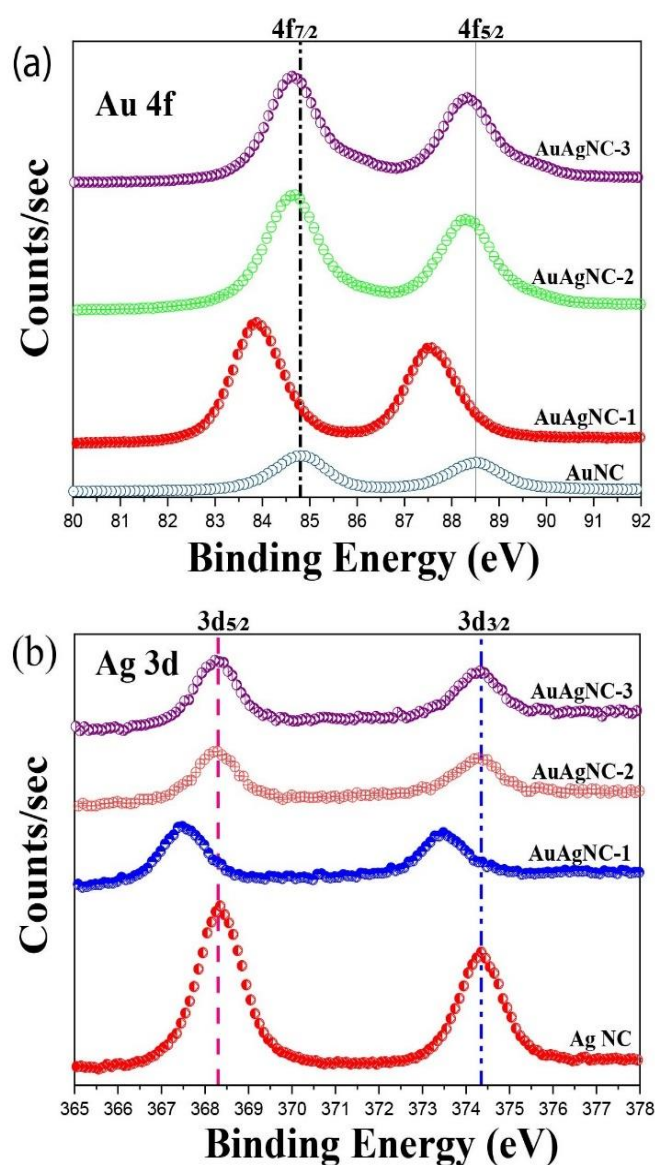
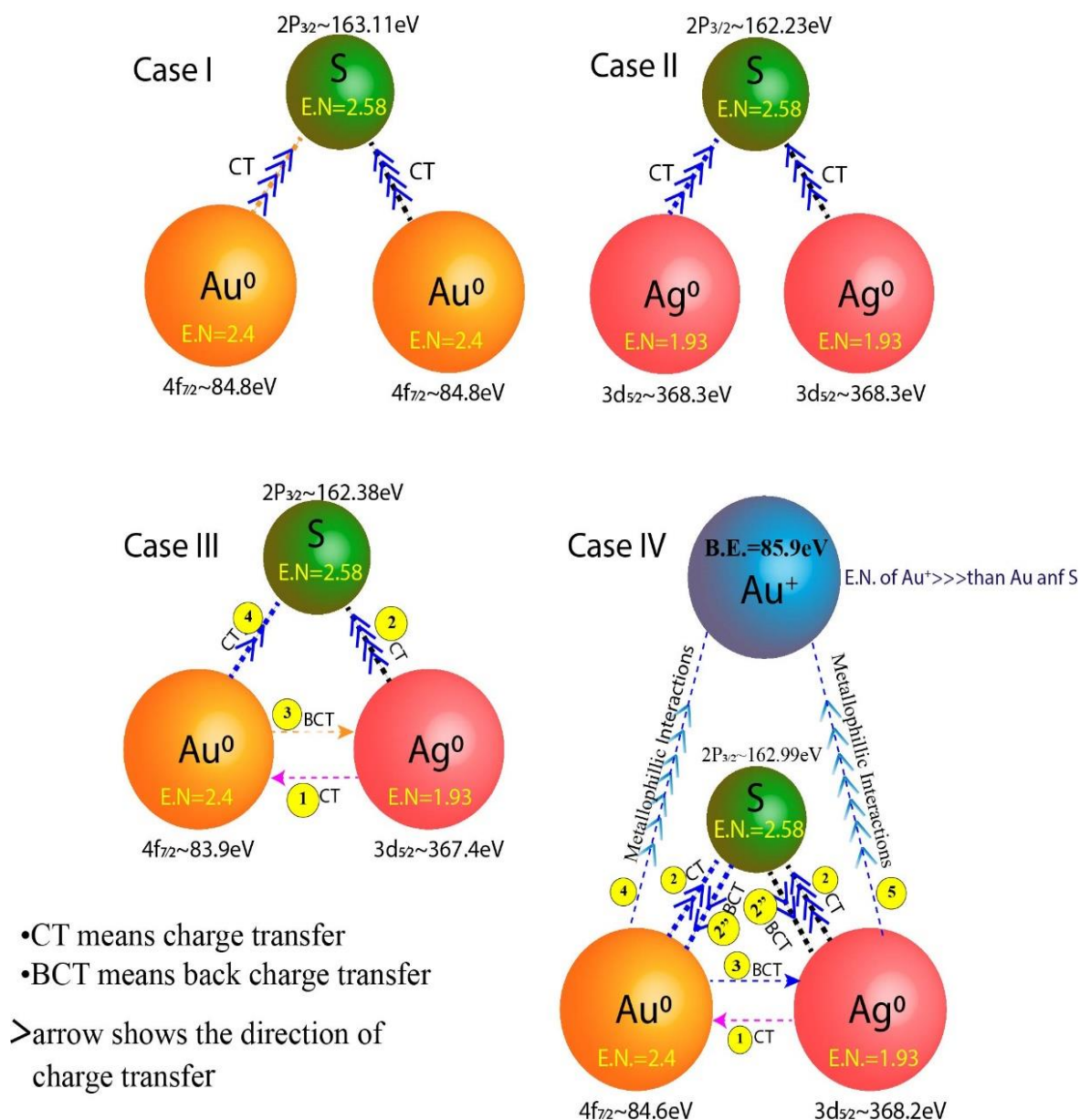


Fig.3.5. XPS spectrum showing (a) Au 4f core-level and (b) Ag 3d core-level binding energies for their respective pristine AuNC, and bimetallic AuAgNCs.



Scheme.3.1. Illustration of electron density redistribution from metal to metal on the nanocluster surface, surface metal atoms to Sulphur (thiolate) and metallophilic interactions between positive cation i.e., Au⁺¹ and reduced metal (Au/Ag) on the nanocluster surface. Case-I and Case-II represents AuNCs and AgNCs, Case-III represents AuAgNC-1 and Case-IV represents- AuAgNC-2 and AuAgNC-3. Dotted lines show bonding between atoms.

Table.3.4. Binding energies for Au⁰, Au⁺ and Ag in pristine Au nanoclusters and bimetallic AuAgNC-1, AuAgNC-2 and AuAgNC-3.

Sample name	Au 4f _{7/2}	Au 4f _{5/2}	Au ⁺	XPS Peak area ratio Au 4f _{7/2} / Au ⁺	Ag 3d _{5/2}	Particle diameter (nm) from HR-TEM
AuNC	84.8eV	88.50eV	not detected	Au ⁺ species not detected	-	0.99±0.23
AuAgNC-1	83.9eV	87.5eV	not detected	Au ⁺ species not detected	367.4eV	1.143±0.20
AuAgNC-2	84.6eV	88.2eV	85.9eV	7.73:1	368.2eV	1.28±0.24
AuAgNC-3	84.6eV	88.3eV	85.9eV	6.3:1	368.1eV	1.33±0.25
AgNC	-	-	-	-	368.3eV	1.80±0.32

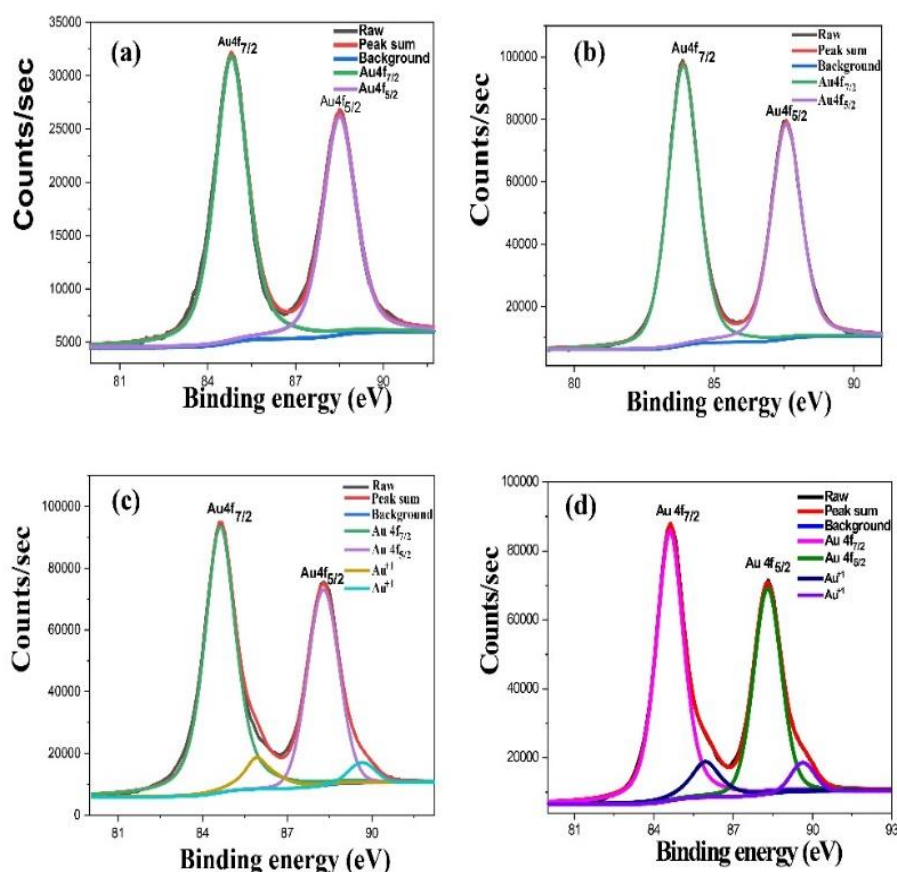


Fig.3.6. XPS spectrum having Au 4f binding energies for bimetallic (a)pristine AuNC, (b) AuAgNC-1, (c) AuAgNC-2 and (d) AuAgNC-3. This also shows the effect of Ag doping and the presence of Au⁺ over the bimetallic nanoclusters.

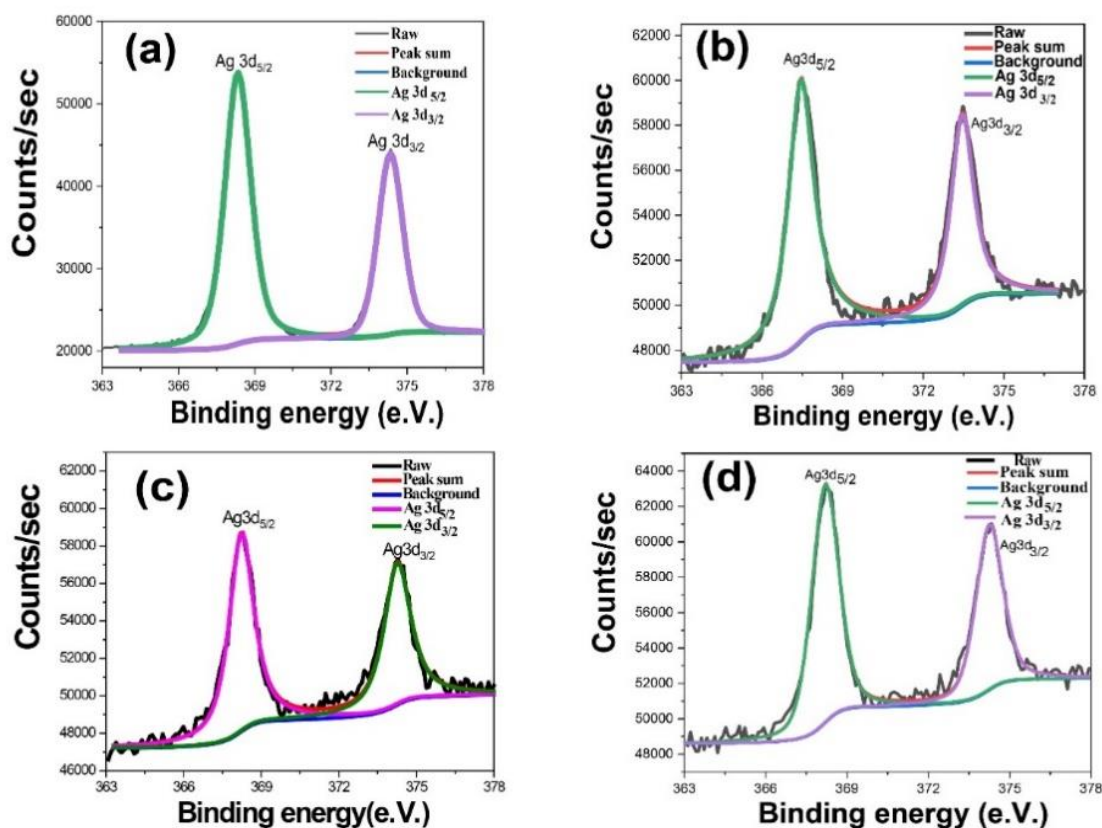


Fig. 3.7. XPS spectrum having Ag 3d binding energies for (a) pristine AgNC, (b) AuAgNC-1, (c) AuAgNC-2 and (d) AuAgNC-3.

Another notable difference between AuAgNC-1 and the other two doped nanoclusters is that at 85.9 eV, Au^+ species could be detected in AuAgNC-2 and AuAgNC-3, but not in AuAgNC-1. Case-III (Scheme.3.1) explains how the charge redistribution event in AuAgNC-1 occurs. As previously stated, Ag ($X_{\text{Ag}} = 1.93$) has a proclivity to give its electron density to Au ($X_{\text{Au}} = 2.4$), which is referred to as charge transfer (CT-1). Because of the electronegativity difference, S is more tightly bound to Ag than Au, making Ag more electron deficient. Charge redistribution could occur as a result of reverse charge transfer (BCT-3) from Au to Ag. In AuAgNC-1, the S $2p_{3/2}$ core level binding energy is around 162.38 eV. Au^+ is thought to interact metallophilically with both Au and Ag surface atoms in AuAgNC-2 and AuAgNC-3 (Case-IV in Scheme.3.1). The similar mechanism is observed here, specifically, electron redistribution between surface Au and Ag atoms. The Au $4f_{7/2}$ and Ag $3d_{5/2}$ core levels are at higher B.E., i.e., 84.6 eV and 362.2 eV, respectively, due to metallophilic interactions between Au^+ and Au/Ag (shown by metallophilic interaction-4

and 5). Surface Au and Ag atoms (bonded with thiolates) get more partial positive character as a consequence of these metallophilic interactions, which could be the basis for charge sharing from thiolate sulphur towards these electron deficient Au and Ag atoms (indicated as BCT-2"). This raises the B.E. of the $2p_{3/2}$ core level of thiolate sulphur to 162.99 eV. When the S $2p_{3/2}$ (162.99 eV) of AuAgNC-2 and AuAgNC-3 is compared to the S $2p_{3/2}$ (163.75 eV) of Au^{I} -SR complex (Fig.3.8), it is clear that there was no probable interaction

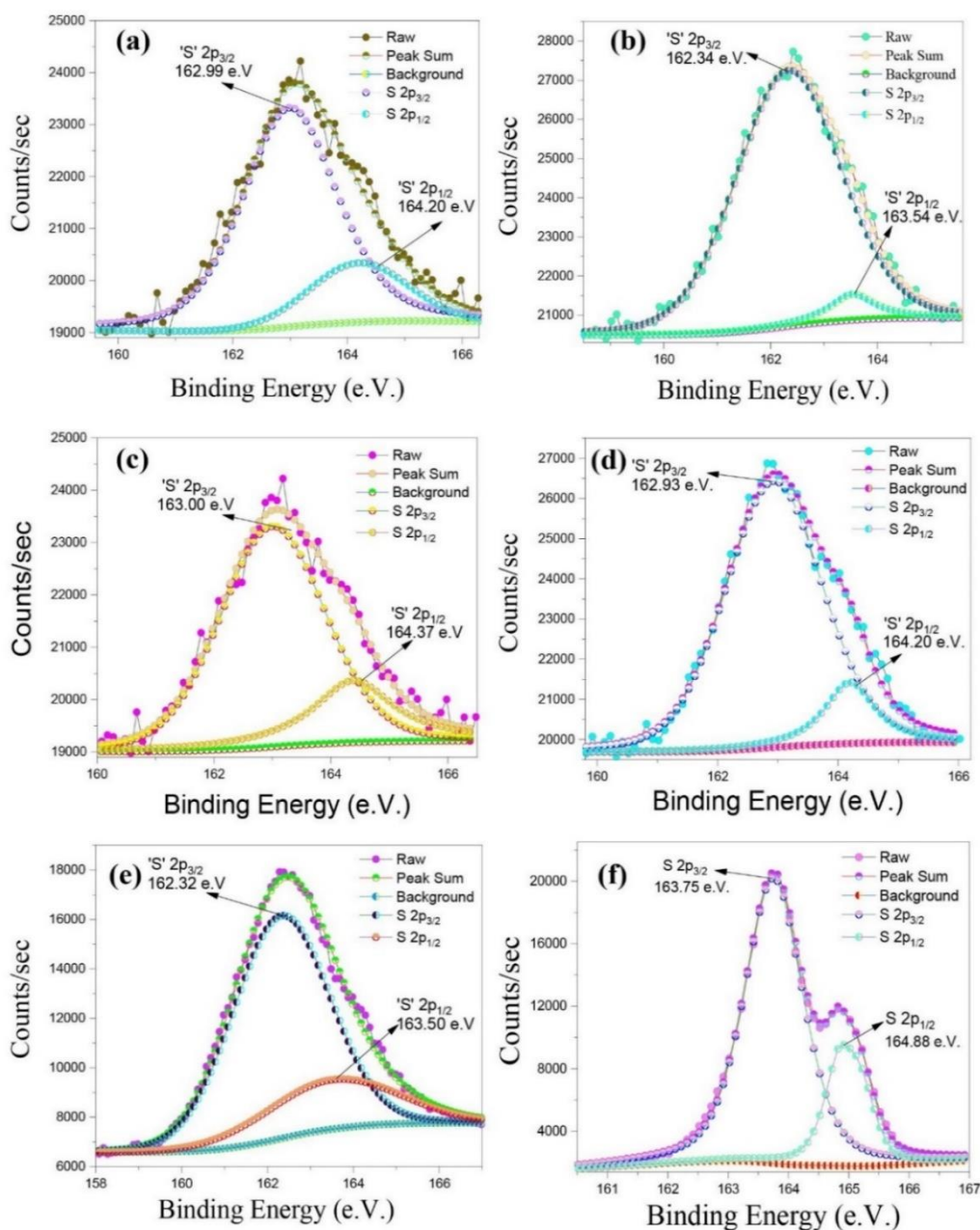


Fig. 3.8. XPS spectrum having S $2p_{3/2}$ binding energies in pristine (a) AuNC, (b) AuAgNC-1, (c) AuAgNC-2, (d) AuAgNC-3 and (e) AgNC, (f) Au^{I} -SR complex.

between thiolate sulphur and Au^{+1} in AuAgNC-2 and AuAgNC-3. Thus, in the case of AuAgNCs, the overall shifting of the Au $4f_{7/2}$ and Ag $3d_{5/2}$ binding energies could be explained by a combination of (a) electron charge transfer from surface Au/Ag atoms towards surface linked thiolates, (b) the presence of Au^{+1} species over the nanocluster surface, and (c) Au-Ag charge redistribution.

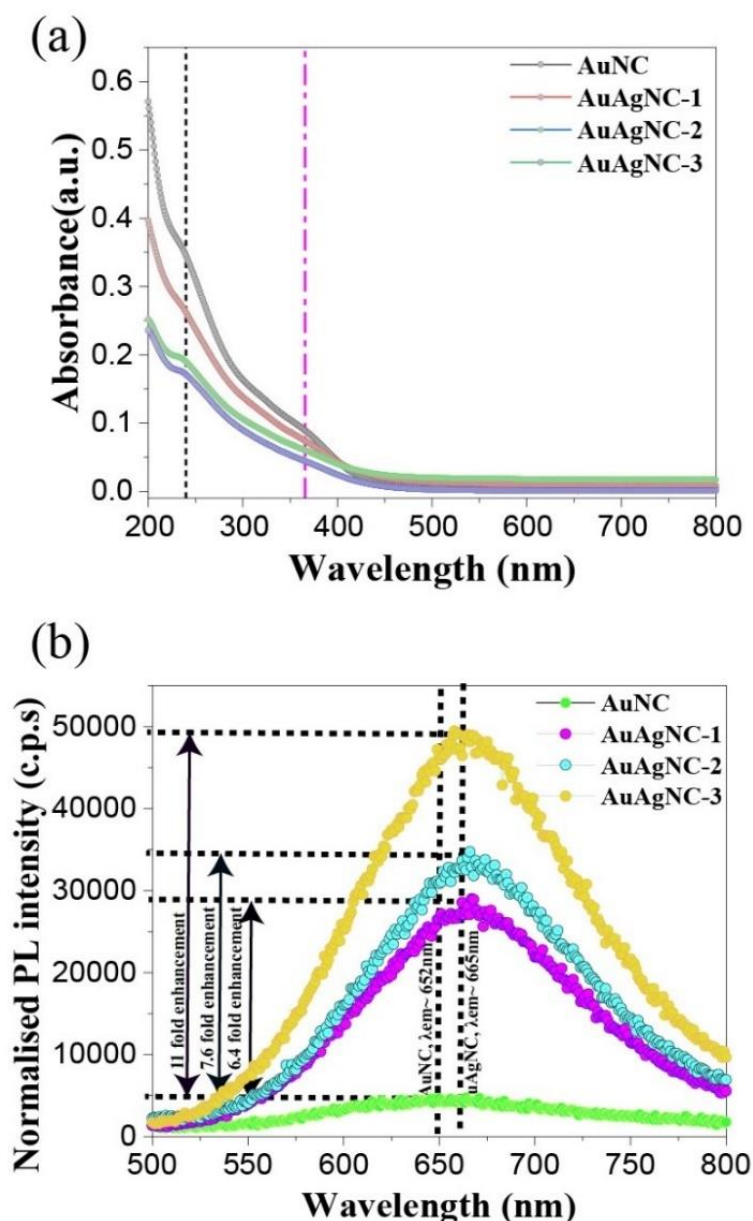


Fig.3.9. (a) Absorption spectra and (b) Photoluminescence spectra for pristine AuNC and bimetallic AuAgNCs.

UV-visible absorption spectroscopy has also been used to examine the optical and electronic characteristics of the clusters. Surface plasmon band characteristic peaks are strongly

influenced by the shape and size of metal nanoparticles.^{18,19} Surface plasmon resonance (SPR) bands are apparent in Ag and Au metal nanoparticles with diameters greater than 2 nm. This characteristic is absent in ultra-small nanoclusters, which exhibit molecule-like behavior in the UV region as discrete absorption bands (shown in Fig.3.9). In our investigation, pristine Au NC and bimetallic AuAg nanoclusters lacked any SPR bands, confirming the nanoclusters' ultra-small size. Peak characteristics at 240 nm and 366 nm are attributed to d-sp and sp-sp electronic transitions in pristine Au nanoclusters.²⁰

In the UV-visible spectrum, Ag doping into Au nanoclusters results in a small blue shift of shoulder peaks. Because the Au atoms in the core of Au nanoclusters provide them the molecule-like properties, the optical properties of pristine Au nanoclusters are maintained after silver doping, implying that the Au atoms are replaced from the surface. As expected, Ag doping increases the red emission of the nanoclusters, which is found to be proportional to the Ag concentration (Fig. 3.9). When excited at 420 nm, the fluorescence spectra of aqueous AuNC solution reveals a broad emission peak maximum at 652 nm. After Ag doping in gold nanoclusters, it was discovered that AuAgNC-3 had the highest PL intensity augmentation (11-fold), with emission maximum at 665 nm, slightly red shifted when compared to the pristine Au nanocluster.

When compared to pristine Au nanoclusters, the PL intensity of bimetallic AuAgNC-2 and AuAgNC-1 nanoclusters increased by 7.6 and 6.4 times, respectively. AuAgNC-2 and AuAgNC-1 emission maxima were found to be similar to AuAgNC-3, i.e., 665nm. It was found that as-synthesized luminous pristine AuNC and other bimetallic nanoclusters, such as AuAgNC-1, AuAgNC-2, and AuAgNC-3, are extremely stable (details in Fig.3.10), with no apparent change in luminescence spectra after 30 days at 4°C. Table 3.5 shows the absolute quantum yield of bimetallic AuAg nanoclusters in comparison to pristine AuNC. In the case of bimetallic nanoclusters, the clusters with the highest concentration of Ag had the highest absolute quantum yield, and as the doping concentration increases, the PL intensity and absolute quantum yield also increases.

Fluorescence lifetimes were measured to learn more about the clarification for this rise in Ag doped Au NCs. After irradiation at 443 nm, the lifetime was determined by fitting the fluorescence decay curve with triexponential fitting (see Fig.3.11) and monitoring at 652 nm (for AuNC) and 665 nm (for AuAgNCs).

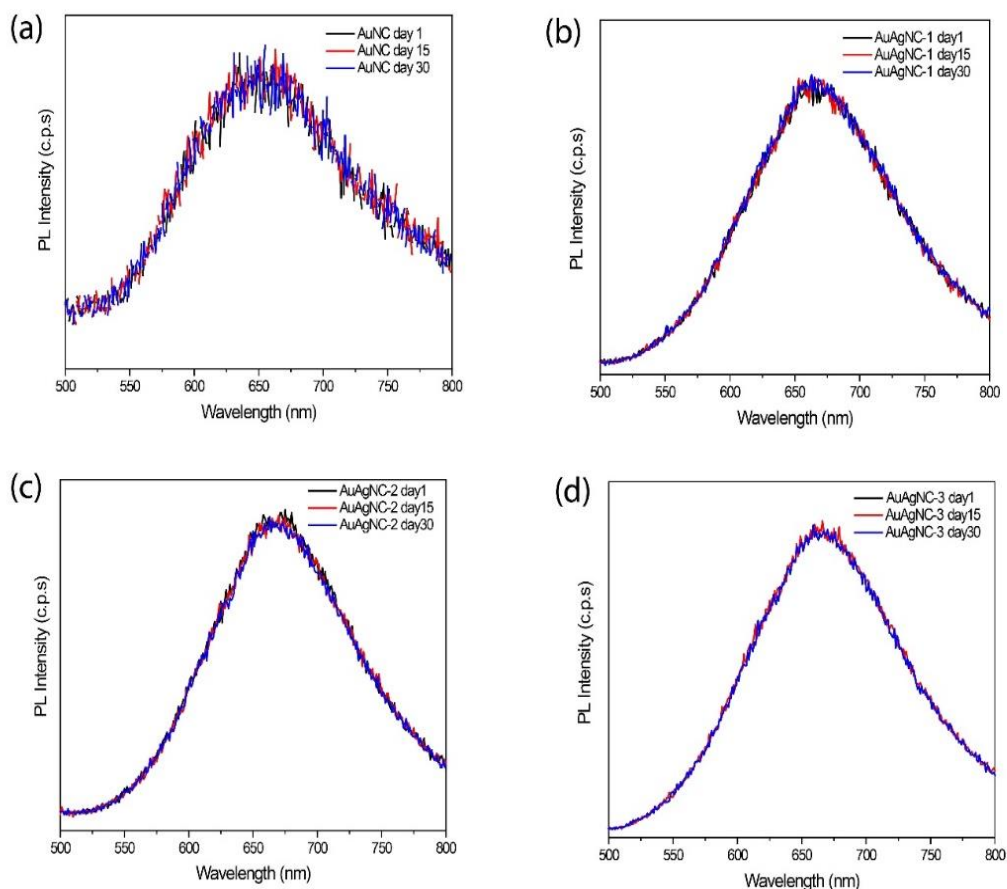


Fig.3.10. Describing the PL stability in terms of c.p.s of (a)AuNC and bimetallic nanoclusters i.e., (b) AuAgNC-1, (c) AuAgNC-2 and (d) AuAgNC-3. The PL intensity are checked (excitation wavelength~420 nm) at different time scale from 1st day to 30th day.

Table.3.5. Absolute luminescence quantum yields and decay lifetimes of luminescent AuNCs and bimetallic AuAgNCs.

Sample	Excitatio n Wavelen gth(nm)	Emission Wavelen gth(nm)	Emission Quantum yield (%)	τ_1 (sec)	A_1	τ_2 (sec)	A_2	τ_3 (sec)	A_3
AuNC	420	652	0.07	6.9×10^{-7}	52.74	1×10^{-7}	23.91	2.1×10^{-6}	23.35
AuAgNC-1	420	665	1.48	9×10^{-7}	50.37	2.6×10^{-6}	32.97	1.5×10^{-7}	16.66
AuAgNC-2	420	665	2.73	1.9×10^{-6}	60.03	4.7×10^{-7}	32.88	5.7×10^{-8}	7.06
AuAgNC-3	420	665	9.73	2.3×10^{-6}	59.59	5.4×10^{-7}	32.76	6.8×10^{-8}	7.65

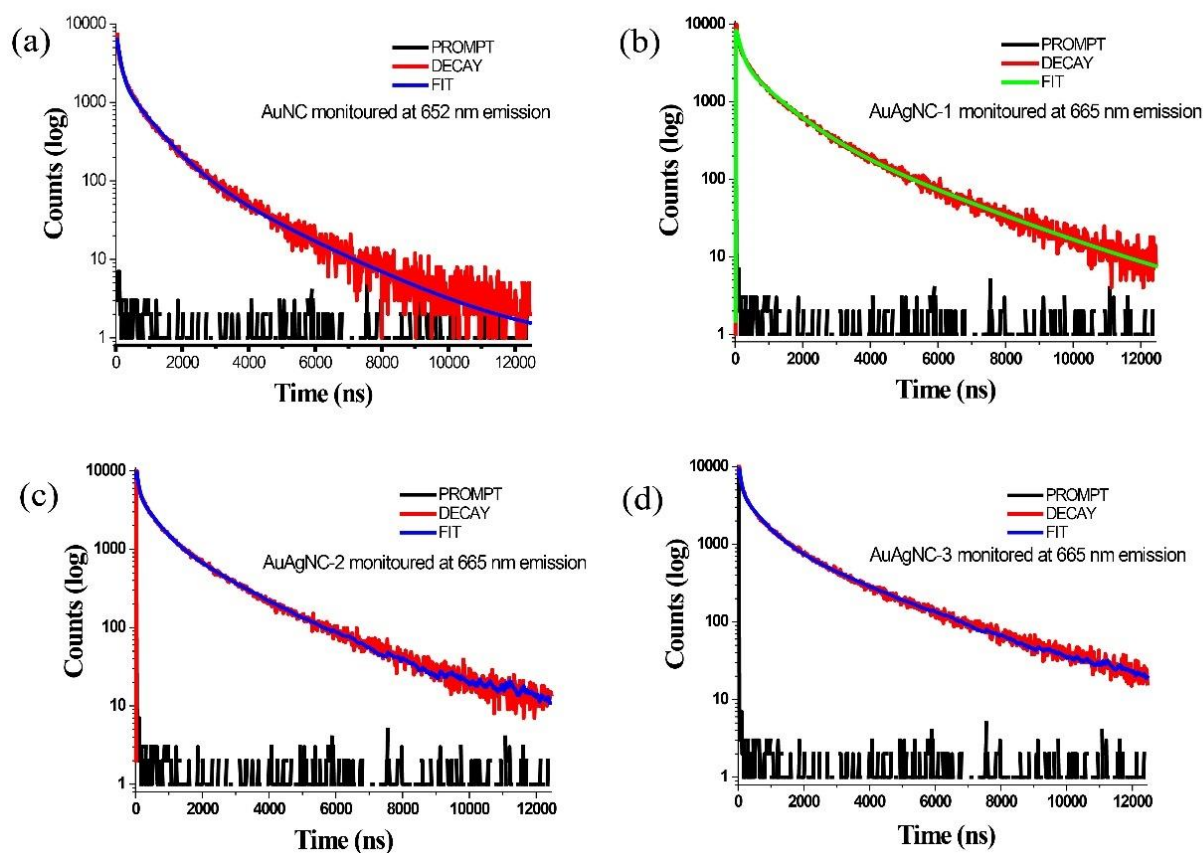
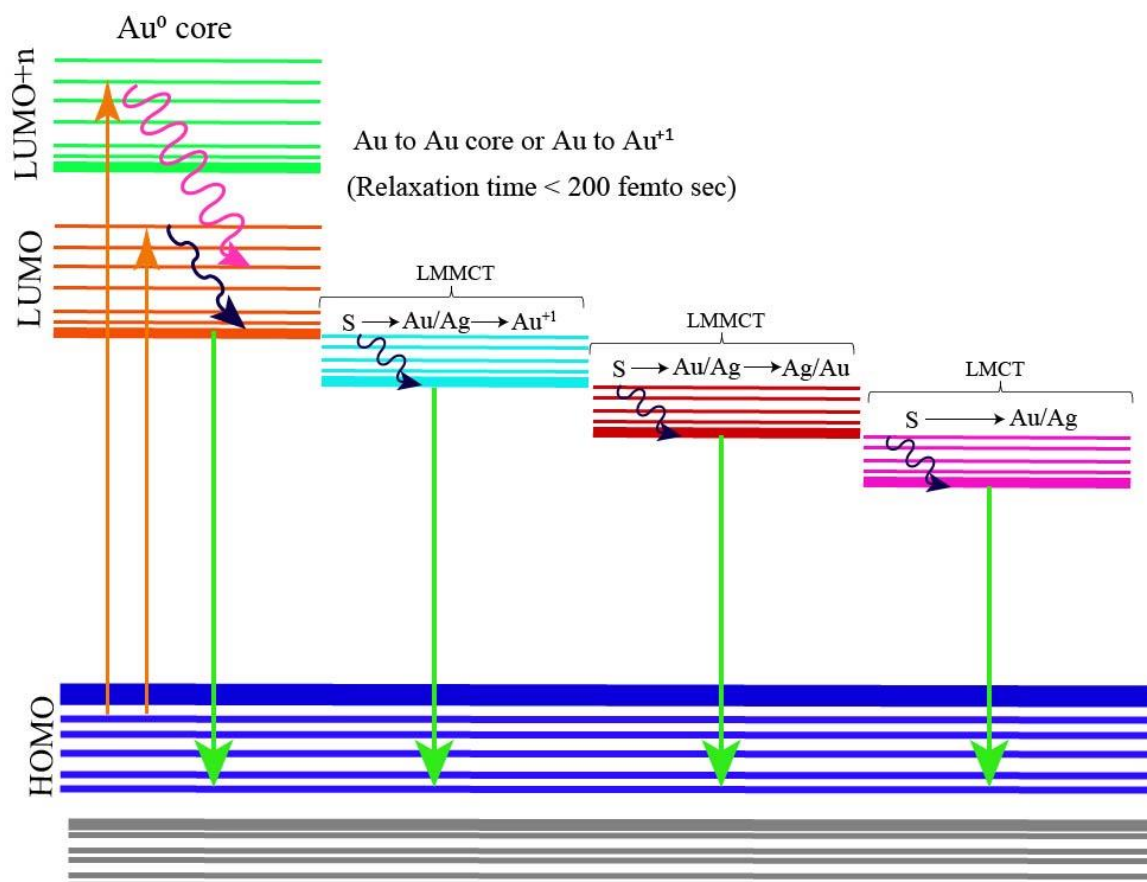


Fig.3.11. Photoluminescence decay components of (a) pristine AuNC, (b) AuAgNC-1, (c) AuAgNC-2 and (d) AuAgNC-3.

The lifetime investigations yielded detailed parameters, which are listed in Table 3.5. In AuNC, the component with 6.9×10^{-7} sec was found to be the greatest contributor. 9×10^{-7} sec is the primary contributor in AuAgNC-1, which acts almost identically to pristine Au clusters. More Ag doping over AuNCs resulted in a greater increase in the extended life time contribution. With a μ sec lifetime, AuAgNC-2 and AuAgNC-3 have the most decay components, 1.9×10^{-6} sec and 2.3×10^{-6} sec, respectively, with a nearly 60% contribution. This suggests that the emission of pure Au nanoclusters is distinct from the majority of longer lifetime decay components for AuAgNCs at 665 nm. This could be attributed to newly created metal-centered triplet states via ligand to metal charge transfer (LMCT) and

ligand to metal-metal charge transfer (LMMCT), where the triplet states could be present in the gap between both the HOMO and LUMO given by AuNC after Ag doping.²¹



Scheme.3.2. Illustration of the photoluminescence mechanism of red emission of AuNC and AuAg NCs via LMCTs and LMMCT

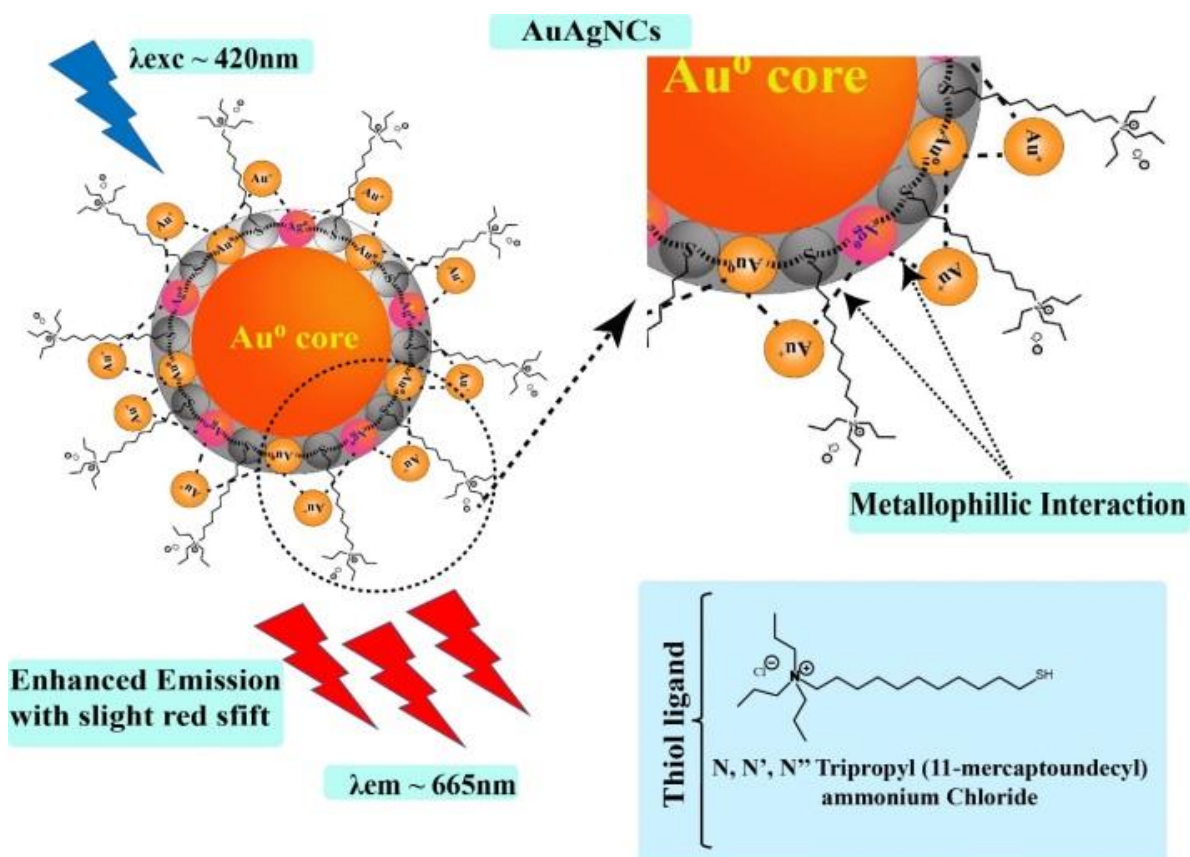
The two probable charge transfer paths in bimetallic AuAgNCs, S to Au-Ag and S to Au-Au, are responsible for their prolonged decay period, according to Chen et al.²² On this foundation, we suggest a mechanism that demonstrates the formation of three metal-centered triplet states: LMMCT-I (S to Au/Ag to Au/Ag), LMMCT-II (S to Au/Ag to Au⁺¹), and LMCT (S to Au/Ag). For AuAgNCs, LMMCT-I and LMMCT-II are totally dependent on Ag doping and the metallophilic interaction between Au⁺¹ and Au/Ag (surface atoms). AuAgNC-2 and AuAgNC-3 had longer decay times (in micro seconds) than AuNC, which could be attributed to the mechanism of metallophilic interaction between Au⁺¹ species and Au/Ag present on the surface of bimetallic nanoclusters (shown in Scheme.3.2). The charge created at the AuAgNC & AuNC interaction in aqueous solution is determined using the zeta potential method. The quaternary ammonium head on the capping thiolate ligand renders the nanoclusters' surface positively charged.

Table.3.6. Zeta potential values of pristine Au nanoclusters and bimetallic AuAgNC-1, AuAgNC-2, AuAgNC-3 nanoclusters.

Nanoclusters	Zeta potential (10 cycles per run) in mV
AuNC	+ 31.54
AuAgNC-1	+33.13
AuAgNC-2	+ 37.69
AuAgNC-3	+ 41.35

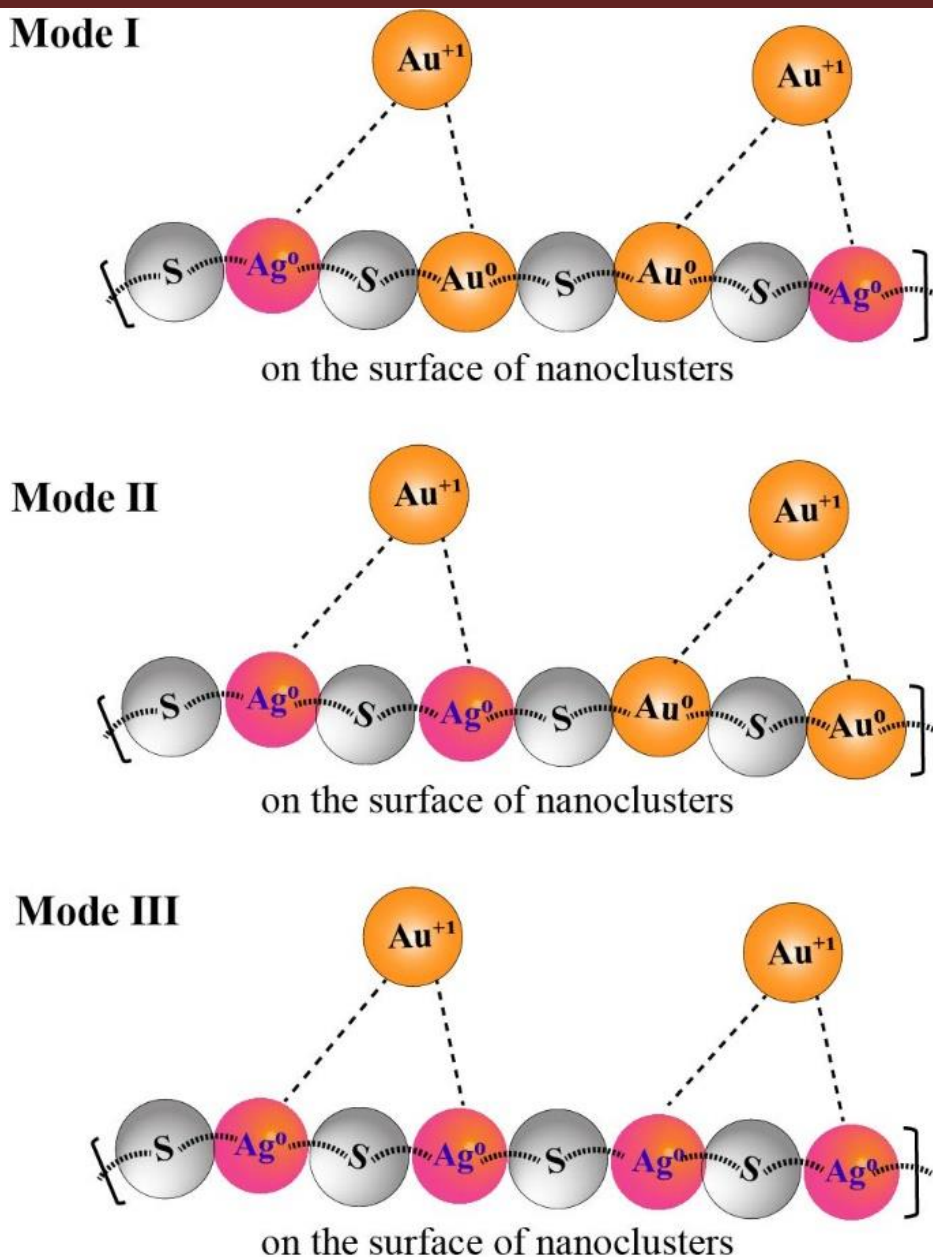
The zeta potential values of AuNC and the three AuAgNCs were in the range of + 30 mV to +42 mV (Table.3.6), indicating high stability in aqueous solution. XPS analysis confirms the presence of Au⁺¹ over the surface of bimetallic nanoclusters by increasing surface charge (Table.3.6) as Ag concentration increases. Based on the findings, a metallophillic interaction between Au⁺¹ and Au/Ag surface atoms is postulated as a mechanism for the improved emission, as shown in Scheme. 3.3. On the [-S-Au⁰-S-] bimetallic nanoclusters surface, three forms of Ag bindings (shown in Scheme.3.4) and metallophillic interactions such as Ag⁰-Au⁺¹-Au⁰ or Au⁰-Au⁺¹-Au⁰ or Ag⁰ -Au⁺¹-Ag⁰ are possible. The increased fluorescence emission intensity in Ag doped AuNCs encouraged for imaging applications, where AuAgNC-3 nanoclusters of maximum intensity was used as a fluorescent probe. The advantages of these clusters are their water dispersibility and end group functionality, therefore bacterial bioimaging and AuAgNC addition into silk fibroin as prospective applications due to their very different modes of interaction and functionalization needs.

The use of clusters as probes for bacterial imaging was based on the concept of bacterial quorum sensing, as detailed elsewhere.⁹ In a nutshell, quorum sensing is a phenomenon in which cells communicate with one another by exchanging chemical signal molecules (known as auto inducers) in order to coordinate activities such biofilm formation, surface attachment, multidrug resistance, and sporulation.²³ Acyl Homoserine Lactones (AHLs), which have cyclic lactone head groups that engage with the receptor protein (Lux-R homologous) by H- bonding and alkyl chains of variable C numbers, are autoinducers released by Gram-negative bacteria (from C-4 to C-18). Lux-R homologous receptors can detect AHLs produced by Lux-I homologues cognate proteins.



Scheme.3.3. Schematic way to present the structure of AuAgNCs and presence of metallophillic interactions between Au^{+1} --- Au/Ag on the surface of AuAgNCs.

We have exploited this selective interaction by labelling the clusters with AHL, which allows them to bind with receptors in gram-negative bacteria. To avoid interactions between the ligand's ammonium, head groups and the lactones of AHL molecules, oleic acid was utilized as a bridging group that binds to the clusters by electrostatic interaction ($R_4N^+ \cdots OOCR^-$) and to the acyl chain of AHL via hydrophobic interaction. FTIR spectroscopy was used for checking the conjugation of OA and AHLs over the surface of AuAgNC-3. For bioimaging purpose, we tagged the biomolecule i.e., AHL with AuAgNCs-3 in such a way that AHL should retain its activity to sense the Lux-R receptors in gram-negative bacterial cells. To tag AuAgNCs-1 with AHL we used oleic acid as a bridging ligand here which can bind AuAgNCs-3 via electrostatic interaction (thiol containing $R_4N^+ \cdots OOCR^-$ of oleic acid), also binds with acyl chain of AHL via hydrophobic interaction. All such above interactions as well as the capability of lactone functionality of AHL to sense the Lux-R receptors could be analysed through FTIR analysis.



Scheme.3.4. Illustration of the mode of interaction of Au^{+1} species over AuAg bimetallic nanoclusters.

In this way, we anticipate that the lactone group is free to interact with the Lux-R receptor. Electrostatic interaction between the COO^- of oleic acid and the R_4N^+ of Au Ag NCs is validated by comparing the $\text{C}=\text{O}$ stretching frequency of AuAgNCs-3@OA composite with pristine oleic acid. It is already established that carboxylic acid $\text{C}=\text{O}$ stretch which is observed in 1710 cm^{-1} in pristine sample disappears in bound states with R_4N^+ of ligand with appearance of bands near 1640 cm^{-1} and 1540 cm^{-1} corresponding to symmetric and asymmetric $-\text{COO}$ vibrations. A very weak band at 1520 cm^{-1} corresponding to asymmetric

-COO stretch and strong intense band at 1637 cm^{-1} corresponding to symmetric stretch are observed. This implies a desirable configuration, in which R_4N^+ groups of AuAgNCs-3 interact with COO^- group of oleic acid thereby deploying the hydrophobic carbon chain on the outside. After addition of oleic acid to the AuAgNCs-3, we recognize increase in the intensity of asymmetric COO stretch (1637 cm^{-1}) indicating the probability of a monodentate

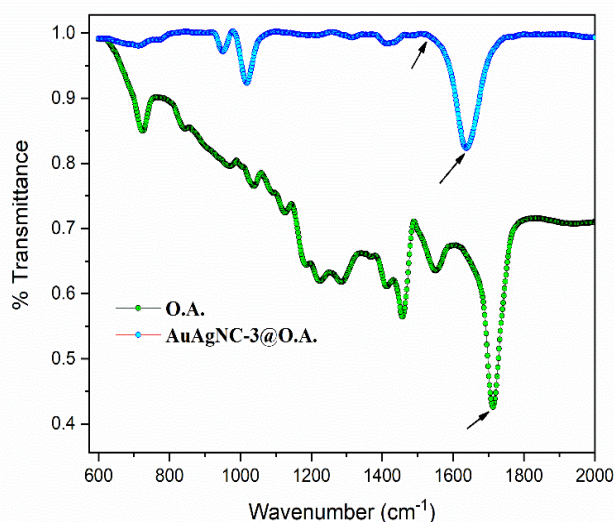


Fig.3.12. FTIR spectra of AuAgNC-3@OA and OA.

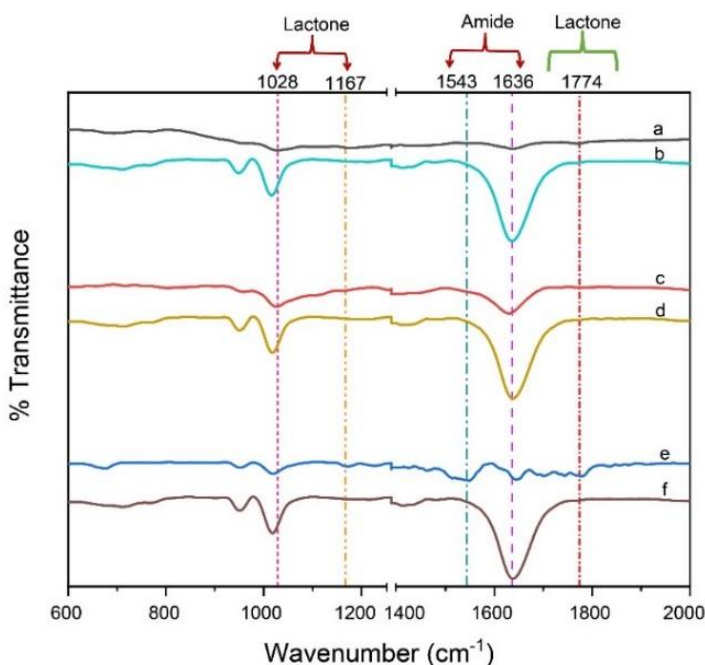


Fig.3.13. FTIR spectra of (a) C-6 AHL, (b) AuAgNCs-3@OA @C-6AHL, (c) C-8AHL (d) AuAgNCs-3@OA @C-8AHL (e) C-12AHL (f) AuAgNCs-3@OA @C-12AHL.

interaction. Peak at 1284 cm^{-1} is attributed to C-O stretching vibration of carboxylic group of oleic acid. Also peaks at 2853 cm^{-1} and 2924 cm^{-1} are the possible symmetric and asymmetric $-\text{CH}_2$ stretching vibrations. The important stretching frequencies for AHLs and AuAgNCs-3@OA @AHLs are given in below figure. When C-6AHL, C-8AHL and C-12AHL are added to the AuAgNCs-3@OA composite solution, the changes in the C=O (strong) stretch, N-H (weak), lactone C=O stretch, O-CO vibrations and O-CH₂ vibrations are retained. From the above FTIR data, we can tentatively conclude that AuAgNCs-3@OA @AHL composite is of appropriate structure with free lactone head of the AHL present outside the composite and free to interact with the bacterial receptors.

Table.3.7. Describes the important stretching frequencies of lactone in AHL and AuAgNCs-3@OA @AHL conjugates.

Vibrations (cm^{-1})	C-6 AHL	C-8 AHL	C-12 AHL	AuAgNCs-3 @OA @ C- 6AHL	AuAgNCs-3 @OA @ C-8 AHL	AuAgNCs-3 @OA @ C-12 AHL
Amide C=O	1635	1636	1643	1634	1628	1638
Amide N-H Bend	1543	1543	1546	1542	1542	1546
Lactone C=O	1770	1774	1778	1769	1774	1774
Lactone O-CO	1024	1024	1017	1016	1018	1017
Lactone O-CH ₂	1176	1167	1170	1174	1167	1169

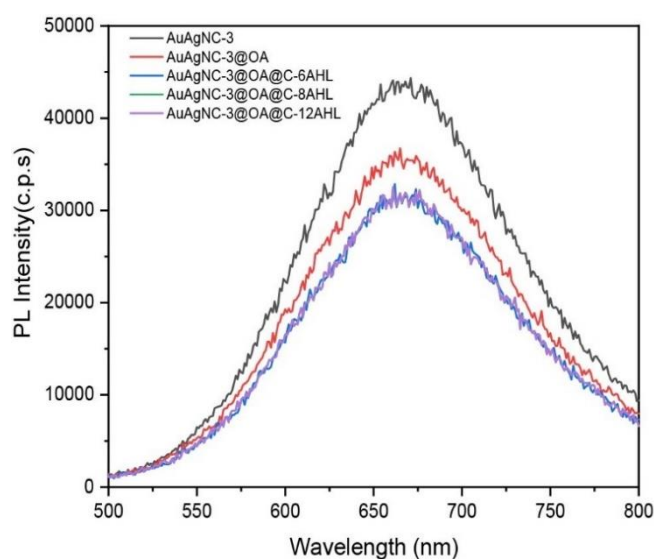


Fig.3.14. PL intensities after making AuAgNC-3 conjugates with oleic acid and AHLs.

When compared to pristine AuAgNC-3 clusters, the emission intensities of these conjugates decrease, as expected. The PL intensities of all AuAgNCs-3 conjugates correlate with the absolute quantum yield values (shown Fig. 3.14 & Table.3.8).

Table 3.8. Abs. quantum yield (%) of surface functionalized AuAgNC and their composites.

Sample name	Excitation wavelength(nm)	Emission wavelength(nm)	Abs. Quantum Yield (%)
AuAgNC-3	420	665	9.18
AuAgNC-3@OA	420	665	5.73
AuAgNC-3@OA@C-6AHL	420	665	3.38
AuAgNC-3@OA@C-8AHL	420	665	3.90
AuAgNC-3@OA@C-12AHL	420	665	3.88

Table.3.9. Zeta potential values of AuAgNC-3 and their surface functionalized composites.

Conjugates	Zeta potential (10 cycles per run) in mV
AuAgNC-3	+ 41.35
AuAgNC-3@OA	+ 40.01
AuAgNC-3@OA@C-6AHL	+39.73
AuAgNC-3@OA@C-8AHL	+ 37.02
AuAgNC-3@OA@C-12AHL	+ 36.16

Zeta potential values for AuAgNC-3 and their surface functionalized conjugates in solution suggests that they have quite good stability in the solution (Table 3.9). It was seen that after surface functionalization over bimetallic nanoclusters, there is small decrease in the zeta potential which is due to increase in the hydrophobicity over the surface of nanoclusters. For the imaging studies, we chose a Gram-negative bacterium, *Escherichia coli*, and examined its interaction with three different AHL molecules, namely N-hexanoyl-L-homoserine lactone (C-6AHL), N-octanoyl-L-homoserine lactone (C-8AHL), and N-dodecanoyl-L-homoserine lactone (C-12AHL). The conjugates, AuAgNC-3@OA@AHLs, were incubated with the bacterial sample and viewed under a fluorescence microscope using a 100 X oil immersion lens and a constant exposure time. In all of the studies, the concentrations of AuAgNC-3, oleic acid, and AHL were the same. To examine variability, the trials were repeated three times.

When incubated with AuAgNC-3@OA@AHLs composites containing all three AHL molecules, *Escherichia coli* produces red emission (seen in Fig.3.15a) (with carbon chain length of C-6, C-8 and C-12). When compared to pristine cluster conjugates, the bimetallic cluster conjugate showed a 10-fold increase in emission intensity (Fig. 3.15b and Fig. 3.16 & 3.17). After incubation with the conjugate, TEM analysis of the bacteria reveals the presence of Au particles within the cell wall (Fig.3.15c).

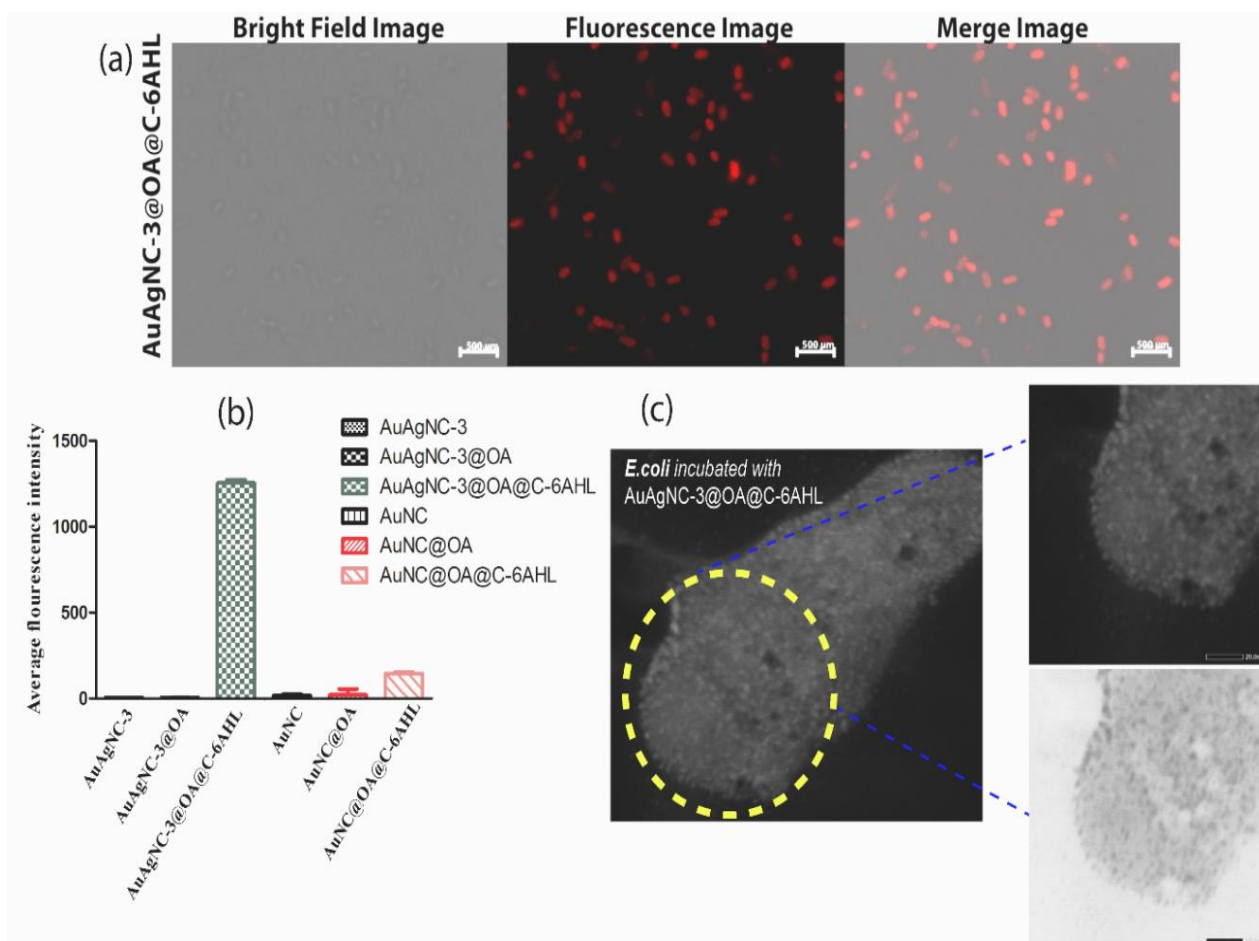


Fig.3.15. (a) Fluorescence microscopy images of *Escherichia coli* incubated AuAgNCs-3@OA@C-6AHL (top row and scale bar-500μm), (b) Average fluorescence intensity of bacterial cells with different AuAgNC-3 composites and comparison with the average fluorescence intensity of bacterial cells when incubated with AuNC and their composites, (c) STEM-HAADF elemental mapping image for *Escherichia coli* when incubated with AuAgNC-3@OA@C-6AHL.

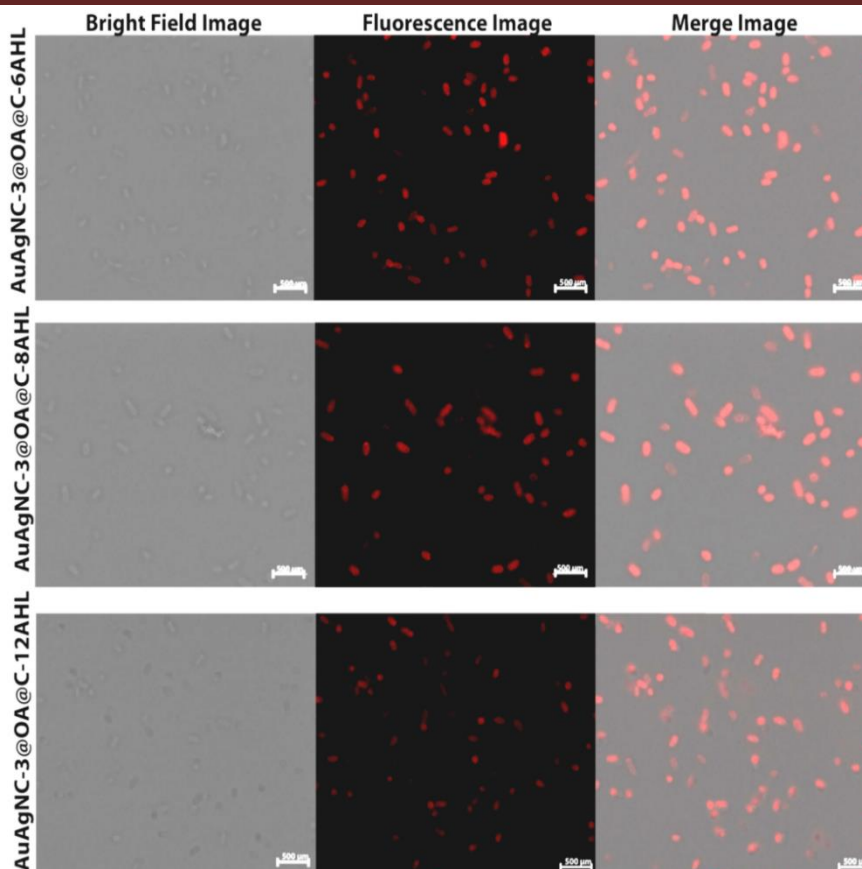


Fig.3.16. Fluorescence microscopy images of *Escherichia coli* incubated AuAgNCs-3@OA@C-6AHL (top row and scale bar-500μm), AuAgNCs-3@OA@C-8AHL (middle row and scale bar-500μm), AuAgNCs-3@OA@C-12AHL (bottom row and scale bar-500μm).

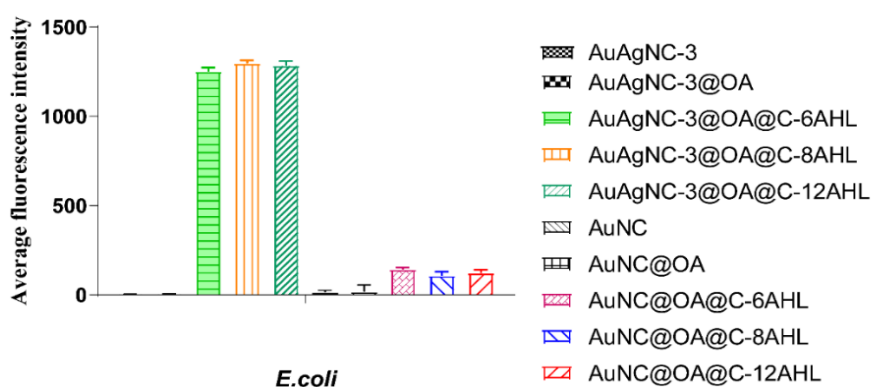
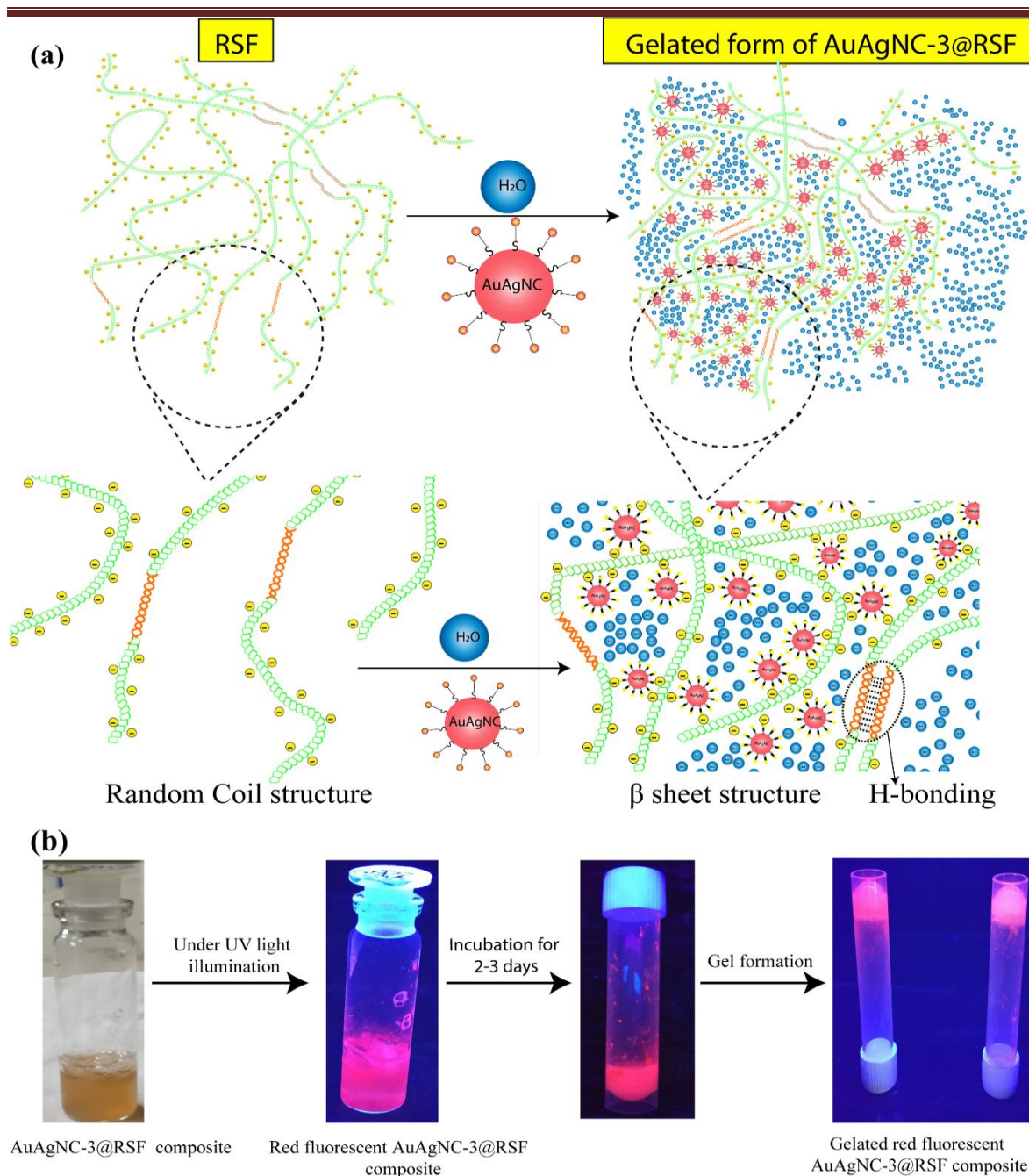


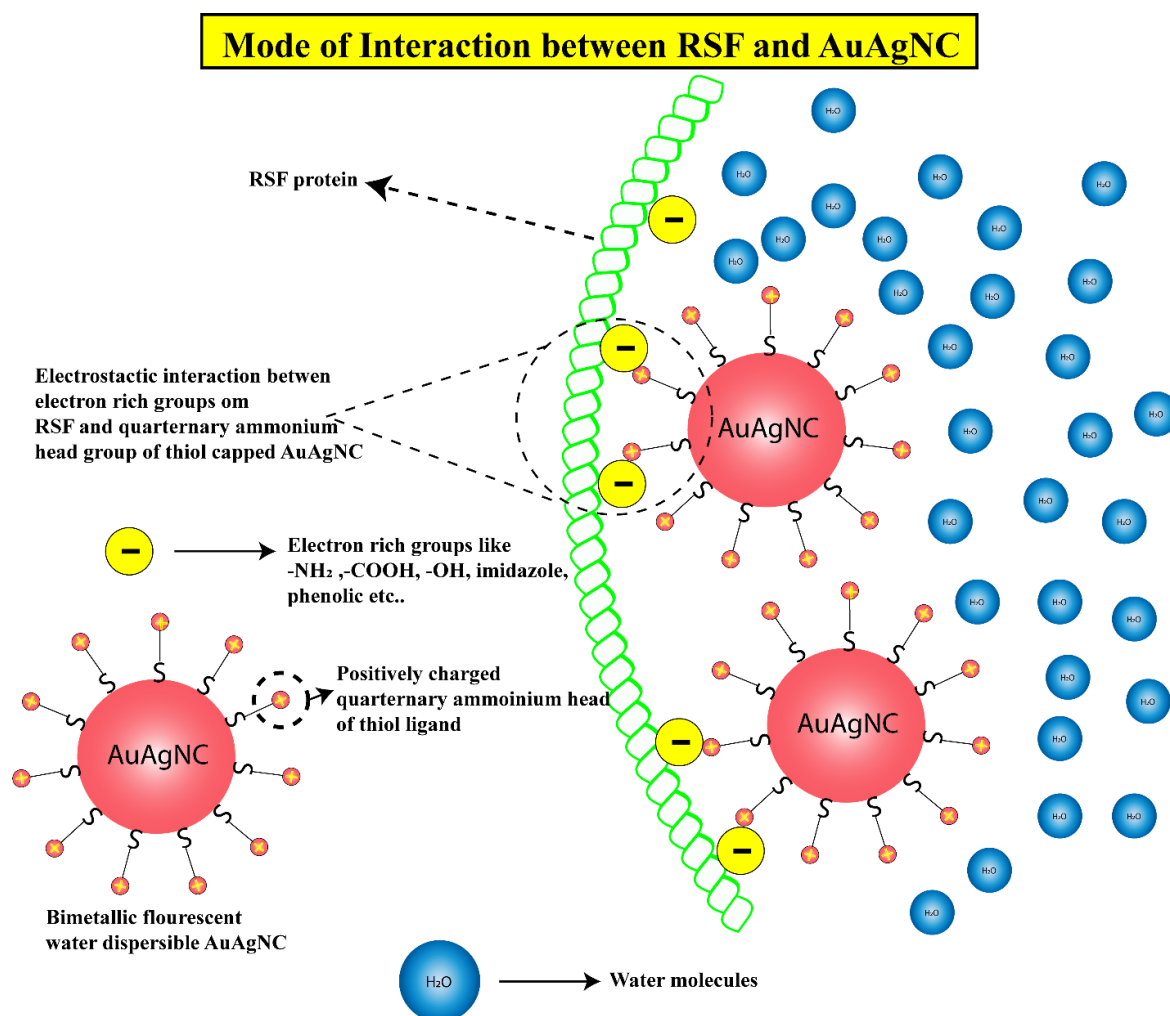
Fig.3.17. Average fluorescence intensity of bacterial cells with different AuAgNC-3 composites and comparison with the average fluorescence intensity of bacterial cells when incubated with AuNC and their composites.



Scheme.3.5.(a) Illustration of Random coil of RSF transformation to β -sheets when incubated with aqueous solution of AuAgNC-3, (b) Fluorescence images of AuAgNC-3@RSF gel taken under FAR-UV illumination.

The AuAgNC-3 nanoclusters were decorated on silk fibroin to further explore their potential in security applications. We used direct electrostatic interaction between the $^+NR_4$ of the thiol ligand of the clusters and electron donor atoms from the regenerated silk fibroin, such as $-COOH$, $-OH$, $-NH_2$, amide groups, and so on. In Scheme.3.5b, we show how we prepared an AuAgNC-3@RSF gel, and the method of interaction between AuAgNC-3 and RSF is proposed to be completely electrostatic (as shown in Scheme.3.6). Following the formation

of the AuAgNC-3@RSF composite gel, a transparent supernatant liquid was collected, which contained only minor traces ($\sim 10^{-4}$ ppm) of Au and Ag as determined by MP-AES; additionally, no emission (shown in Fig.3.18) was observed in the supernatant liquid, indicating that metal cluster leaching had not occurred. The ATIR spectra of RSF solution (3wt%) revealed peaks at 1648 cm^{-1} for amide-I (C=O stretch), 1549 cm^{-1} for amide-II (N-H plane bending), and 1247 cm^{-1} for amide-III (C-N stretch) of silk-I secondary structure (Fig. 3.19).²⁴



Scheme.3.6. Illustration of mode of interaction between aqueous solution of AuAgNC-3 and RSF.

The β -sheet structure of silk fibroin formation after gelation is responsible for the change of amide-I from 1650 cm^{-1} to 1621 cm^{-1} (RSF gel) and 1623 cm^{-1} (AuAgNC-3@RSF gel).

In Table.3.10, the essential stretching frequencies for RSF solution, RSF gel, and AuAgNC-3@RSF gel are listed.

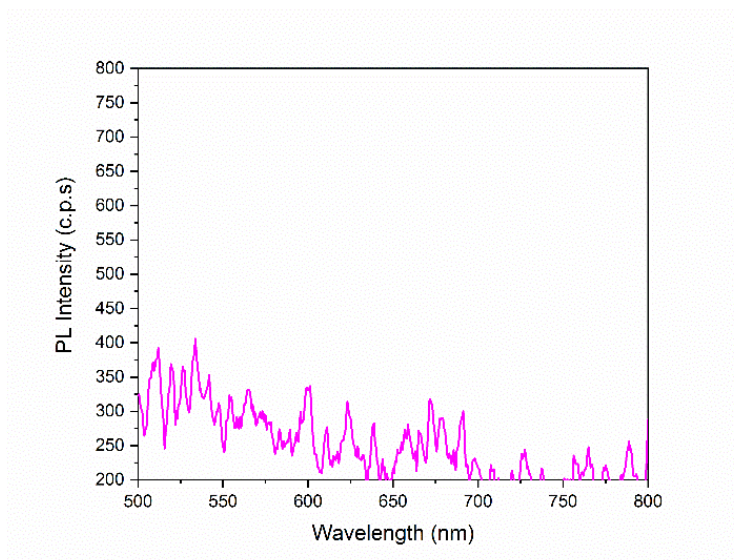


Fig.3.18. Photoluminescence spectra of supernatant liquid solution collected after AuAgNC-3@RSF composite gel formation (excitation $\lambda=420\text{nm}$).

On anchoring the clusters, the stretching frequencies of essential functional groups from AuAgNC-3@RSF composite gel revealed no structural deformation and the β -sheet structure was not affected, indicating a purely electrostatic connection. To test the stability of interactions between RSF and AuAgNC-3 (showed in Fig.3.20), the gel form of AuAgNC-3@RSF composite was treated with 3mL of buffer solutions ranging in pH from 4 to 10 and incubated at room temperature for varied time durations (30 min, 2 h, 12 h, 24 h). The content of Au and Ag in the supernatant liquid was determined by MP-AES. Leaching was found to be modest (on the range of 10^{-3} ppm) in general, with pH=7 exhibiting excellent stability. Additionally, the gel's potential for printing on surfaces such as paper (currency note) and glass were evaluated (Fig.3.21) and appears to be highly promising. For more advanced uses, the fibroin gel can be spun into threads.

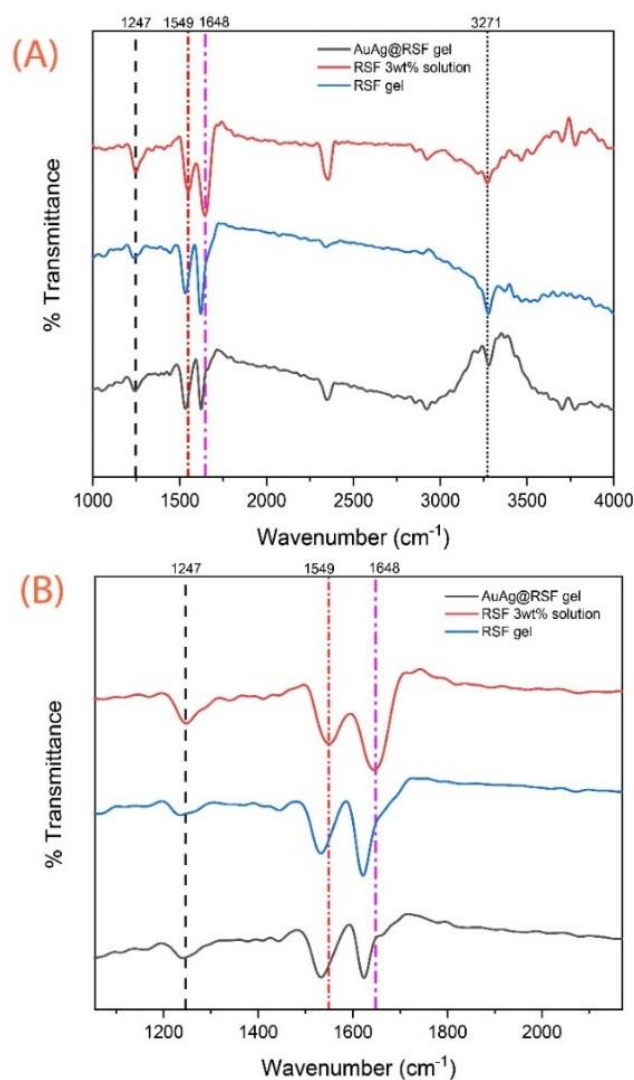


Fig.3.19. ATR spectra for untreated RSF solution, untreated RSF gel and AuAgNC-3 coated silk fibroin gel (RSF@ AuAgNC-1) depicting non-covalent interaction with AuAgNC-3.

Table.3.10. Comparative stretching frequencies (amide) of RSF solution, RSF gel and AuAgNC-3@RSF gel.

Sample	amide I (C=O)	amide II (N-H)	amide III(C-N)
RSF (3wt%) solution	1648 cm ⁻¹	1549 cm ⁻¹	1247 cm ⁻¹
RSF gel	1621 cm ⁻¹	1531 cm ⁻¹	1236 cm ⁻¹
AuAgNC-3@RSF gel	1623 cm ⁻¹	1532 cm ⁻¹	1240 cm ⁻¹

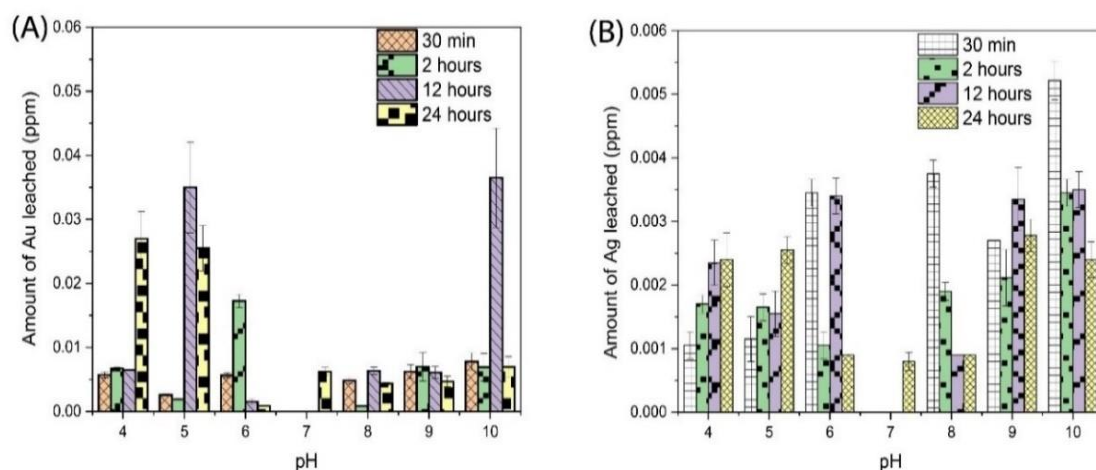


Fig.3.20 Elemental analysis indicating leaching of (A) amount of Au and (B) amount of Ag metal at different time intervals from the AuAgNC-3@RSF composite.

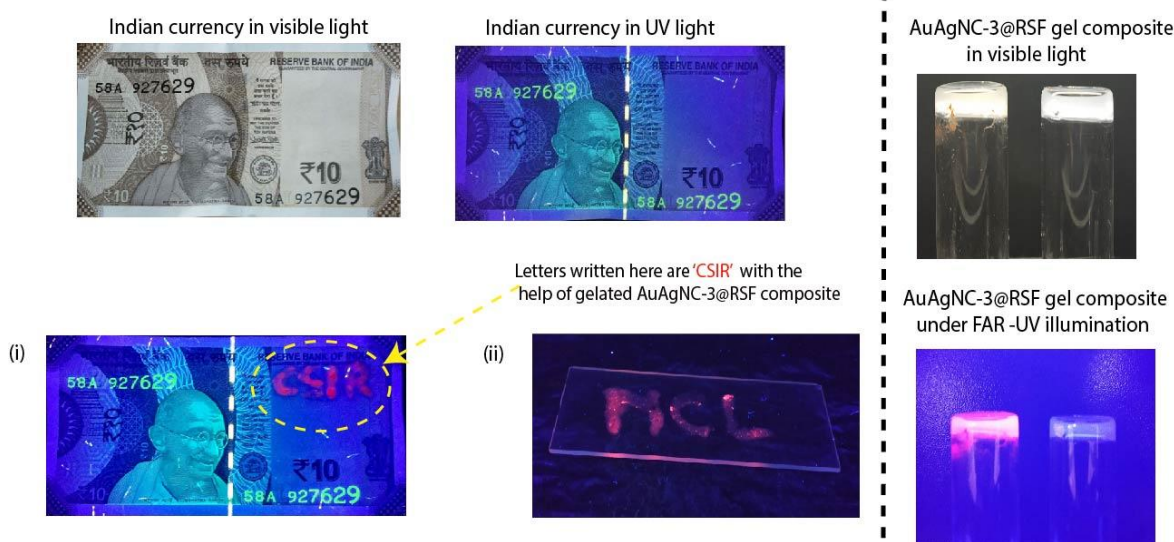


Fig.3.21. An attempt to write letters (a) “CSIR” on Indian INR.10 currency note (b) on glass slide with the help of AuAgNC-3@RSF gel composite.

3.5. Conclusion

In conclusion, very bright red luminescent bimetallic AuAg nanoclusters with an average diameter of less than 2nm using an anti-galvanic reduction method has been synthesized. AuAgNCs are crystalline and bimetallic, according to HR-TEM analysis. For AuAgNCs, XPS studies reveal the presence of two separate oxidation states for Au, namely Au⁰ and Au⁺¹, as well as one oxidation state for Ag, namely Ag⁰. It was also proven using XPS that as Ag⁺ doping rises, the population of Au⁺¹ over AuAgNCs increases as well. UV-visible absorption spectra revealed that Ag doping has no effect on core level transitions, indicating

that Ag is deposited on the AuNC surface rather than in the core via the anti-galvanic reduction technique. Ag doping also enhances PL emission and quantum yield and life time measurements indicates an emission mechanism by the different metal centered triplet states via LMCT and LMMCT which gives longer life time (in μ sec) for AuAgNCs. Over AuAgNCs, the improvement in optical characteristics (PL emission and Quantum yield) was shown to be dependent on Au^{+1} concentration. Because of its emission in the near-infrared region, high stability under relevant conditions, and water solubility, bright red bimetallic AuAgNCs have demonstrated prospective applications in bioimaging in this study.

References: -

- 1 Z. Luo, X. Yuan, Y. Yu, Q. Zhang, D. T. Leong, J. Y. Lee and J. Xie, *J. Am. Chem. Soc.*, 2012, **134**, 16662–16670.
- 2 H. Duan and S. Nie, *J. Am. Chem. Soc.*, 2007, **129**, 2412–2413.
- 3 Z. Wang, Z. Zhu, C. Zhao, Q. Yao, X. Li, H. Liu, F. Du, X. Yuan and J. Xie, *Chem. - An Asian J.*, 2019, **14**, 765–769.
- 4 J. Sun, H. Wu and Y. Jin, *Nanoscale*, 2014, **6**, 5449–5457.
- 5 B. Paramanik and A. Patra, *J. Mater. Chem. C*, 2014, **2**, 3005–3012.
- 6 Q. Huifeng and B. Ellen, *Acta Phys. Chim. Sin.*, 2011, **27**, 513–519.
- 7 Y. Negishi, K. Munakata, W. Ohgake and K. Nobusada, *J. Phys. Chem. Lett.*, 2012, **3**, 2209–2214.
- 8 Z. Wu, *Angew. Chemie - Int. Ed.*, 2012, **51**, 2934–2938.
- 9 A. M. Chahande, D. Lathigara, A. A. Prabhune and R. N. Devi, *Arch. Microbiol.*, 2021, **203**, 4293–4301.
- 10 R. Mukherji, A. Samanta, R. Illathvalappil, S. Chowdhury and A. Prabhune, *ACS Appl. Mater. Interfaces*, 2013, **5**, 13076–13081.
- 11 O. J. Lee, T. Sultan, H. Hong, Y. J. Lee, J. S. Lee, H. Lee, S. H. Kim and C. H. Park, *Front. Mater.*, 2020, **7**, 1–12.
- 12 S. Pramanik, A. Saha and P. S. Devi, *RSC Adv.*, 2015, **5**, 33946–33954.

-
- 13 M. B. Cortie and A. M. McDonagh, *Chem. Rev.*, 2011, **111**, 3713–3735.
 - 14 A. Bzowski, M. Kuhn, T. K. Sham, J. A. Rodriguez and J. Hrbek, *Phys. Rev. B*, 1999, **59**, 13379–13393.
 - 15 Y. Negishi, T. Iwai and M. Ide, *Chem. Commun.*, 2010, **46**, 4713–4715.
 - 16 J. F. Weaver and G. B. Hoflund, *Chem. Mater.*, 1994, **6**, 1693–1699.
 - 17 D. R. Kau, D. Alfonso, C. Matranga, H. Qian and R. Jin, *J. Phys. Chem. C*, 2013, **117**, 7914–7923.
 - 18 D. E. Mustafa, T. Yang, Z. Xuan, S. Chen, H. Tu and A. Zhang, *Plasmonics*, 2010, **5**, 221–231.
 - 19 S. K. Lim, K. J. Chung, C. K. Kim, D. W. Shin, Y. H. Kim and C. S. Yoon, *J. Appl. Phys.*, , DOI:10.1063/1.2106019.
 - 20 R. Jin, *Nanoscale*, 2010, **2**, 343–362.
 - 21 Z. Wang, Z. Zhu, C. Zhao, Q. Yao, X. Li, H. Liu, F. Du, X. Yuan and J. Xie, *Chem. - An Asian J.*, 2019, **14**, 765–769.
 - 22 J. Chen, L. Liu, H. Liu, Y. Li, J. Wang, X. Mu, F. Xu, T. Liu and X. D. Zhang, *J. Innov. Opt. Health Sci.*, 2020, **13**, 1–13.
 - 23 C. M. Waters and B. L. Bassler, *Annu. Rev. Cell Dev. Biol.*, 2005, **21**, 319–346.
 - 24 A. Matsumoto, J. Chen, A. L. Collette, U. J. Kim, G. H. Altman, P. Cebe and D. L. Kaplan, *J. Phys. Chem. B*, 2006, **110**, 21630–21638.

Chapter-4A

Ultra-small Au nanoclusters with tailored photoluminescence properties using modified thiol ligands: a theoretical and experimental demonstration

4A.1. Introduction

Despite the fact that a variety of fluorescent nanoclusters have been developed, the majority of them have low PL quantum yields.¹ Recent research has concentrated on tailoring the fluorescent features of Au nanoclusters, such as PL intensity and emission wavelength, the two most important fluorescence properties.² In one such demonstration, the para-, meta-, or ortho-nature of the stiff backbone of the capped methyl benzenethiol ligand was used to link optical properties to the structure of atomically precise Au nanoclusters like Au₁₃₀(p-MBT)₅₀, Au₁₀₄(m-MBT)₄₁, and Au₄₀(o-MBT)₂₄.³ The careful interplay of electronic and steric interactions between Au nanoclusters and aromatic thiol ligands guides such precise nanoclusters. The rigid backbone of the capped ligand provides a structural barrier, reducing the ability of the para-position groups in the benzene rings of thiol ligands to donate electrons, yielding Au₁₃₀(p-MBT)₅₀ and Au₁₃₃(p-TBBT)₅₂.^{4,5} It is more difficult to control the emission wavelengths of nanoclusters than it is to control the PL intensity. Fluorescent nanoclusters can produce red light (wavelengths larger than 600 nm) or other colours, such as blue or green.⁶ The emission wavelength was found to decrease as the number of atoms in the metallic kernel of the nanocluster increased.⁷ Changing the structure of Au nanoclusters led by the choice of thiol ligands may also be used to modify the fluorescence emission wavelength and intensity.⁸

The reversible structural changes from FCC to non-FCC affected the fluorescence of such nanoclusters.⁸ PPh₃ ligands were recently changed with various bidentate phosphine ligands in Ag₂₉(SSR)₁₂(PPh₃)₄, resulting in a range of Ag₂₉ nanoclusters with diverse surface topologies.⁹ The PL intensities of these nanoclusters were found to be exactly related to the length of the carbon chain in bidentate phosphine ligands. Surface ligand engineering on atomically precise Au₃₆(SR)₂₄ nanoclusters improved optical and luminescent properties by changing the R groups to thiol.¹⁰

In the studies mentioned above, surface-protecting ligands were found to have a significant impact on the structures and properties of the underlying metal nanoclusters. Furthermore, intrinsic structure, metal composition, hydrophilic property, surface charge, environment, and other factors can all influence fluorescence.¹¹ Combining experimental and computational research revealed the photoluminescence process for modifying the emission spectra of Au nanoclusters when ligands vary. According to Halawa et al. increasing the number of polar ligands on AuNCs increases the luminescence intensity.¹² There are just a

few papers in the literature that demonstrate the mechanism of photoluminescence by correlating experimental and theoretical data. One of the causes for increased photoluminescence and quantum yield in AuNCs, according to Wu et al., is electron donation from the ligand to the Au-core.¹³ It was discovered that adjusting electron donation from ligands to Au-core can also improve photoluminescence in AuNCs.

With insights from DFT and TD-DFT calculations, Aikens et al. have made significant contributions to interpreting the photoluminescence of Au₂₅(SR)₁₈⁻ nanoparticles.^{14,15} In this chapter, a ligand-engineering technique is applied to explore the origin of photoluminescence of Au NCs with *N, N', N''*-trialkyl (11-mercaptoundecyl) ammonium chloride, by altering the -R group over the quaternary ammonium head of the thiol ligand. According to our findings, the charge donating and accepting capacity of thiolate ligands plays a critical role in increasing and modifying photoluminescence emission wavelength. These findings are also supported by DFT studies that looked at varied alkyl chain lengths in ligands.

4A.2. Experimental Section

4A.2.1. Synthesis of *N, N', N''*-tripropyl (11-mercaptoundecyl) ammonium chloride

Synthesis procedure for this ligand is mentioned in Chapter-2 (experimental section).

4A.2.2. Synthesis of *N, N', N''*-triethyl (11-mercaptoundecyl) ammonium chloride

11-bromo-1-undecene (5.4 g, 23 mmol) was added to triethylamine (10.2 g, 71 mmol) in ethanol (40 mL) and agitated for two days at 80 °C under reflux. After purifying the bromide salt with n-hexane three or four times, AIBN (10.0 mmol) and thioacetic acid (80 mmol) were added to a solution in a toluene:ethanol (1:1 ratio) and heated (90 °C) for next 4 h to form thioesters. Purified thioesters are obtained by washing with n-hexane:ethyl acetate (9:1 v/v). Purified thioesters were mixed with 2 mL of concentrated hydrochloric acid in 40 mL of methanol and refluxed for 12 h. The thiol was generated when the solvent was reduced in vacuo. It was purified three times using a 9:1 n-hexane:ethyl acetate (100 mL) mixture under sonication. (Yield: 82.15%)

4A.2.3. Synthesis of *N, N', N''*-tributyl (11-mercaptoundecyl) ammonium chloride

To make bromide salt, 11-bromo-1-undecene (5.4 g, 23 mmol) was mixed with tributylamine (10.2 g, 71 mmol) in ethanol (40 mL) for two days at 80 °C under reflux.

AIBN (10.0 mmol) and thioacetic acid (80 mmol) were added to a solution in a 1:1 toluene:ethanol ratio and heated (90 °C) for next 4 h to produce thioesters after purifying the bromide salt with n-hexane three to four times under sonication. Purified thioesters are produced by washing with a 9:1 v/v mixture of n-hexane and ethyl acetate. Purified thioesters are combined with conc. 2 mL hydrochloric acid in 40 mL methanol and refluxed for 12 h to produce thiol, which is recovered after the solvent is removed in vacuo. It was purified three times with a 9:1 v/v mixture of n-hexane and ethyl acetate and sonication. (Yield: 83%)

4A.2.4. Synthesis of *N*-(11-mercaptoundecyl)-*N*, *N'*-dimethylbenzenammonium chloride

The bromide salt was made by mixing 11-bromo-1-undecene (5.4 g, 23 mmol) with *N*, *N*-dimethyl aniline (10.2 g, 71 mmol) in ethanol (40 mL) and agitating it for two days at 80 °C under reflux. AIBN (10.0 mmol) and thioacetic acid (80 mmol) were added to a solution in a 1:1 toluene:ethanol ratio and heated (90 °C) for next 4 h to form thioesters after purifying the bromide salt with n-hexane three to four times under sonication. Purified thioesters are obtained by washing with n-hexane:ethyl acetate (9:1 v/v). Purified thioesters are mixed with 2 mL hydrochloric acid in 40 mL methanol and refluxed for 12 h to produce thiol, which is recovered in vacuo after the solvent is removed. With a 100 mL mixture of (9:1 v/v mixture) n-hexane: ethyl acetate (9:1 v/v mixture) and sonication, it was purified three times. (Yield: 84%)

4A.2.5. Synthesis of Thiol-Stabilized Gold Nanoclusters

A 20 mL acetonitrile stock solution of H₂AuCl₄ in acetonitrile was mixed with an 8.5 mL stock solution of H₂AuCl₄ in acetonitrile (10 mM). A dosage of thiol (0.593 g, 1.6 mmol) in 2 mL methanol was given to this combination. The mixture was stirred for 30 min. After adding a NaBH₄ solution (100 μL, 1.58 M) in methanol, stirring was continued for 45 min. 30 mL of water was added to the gold nanocluster solution. Acetonitrile was removed in vacuo. Using cellulose membrane dialysis, aqueous gold nanocluster solution was purified (Aldrich, pore size 12 kDa). The final solution had a concentration of 2 mM, according to elemental analysis.

4A.3. Instruments for Characterization

4A.3.1. Transmission electron microscopy

A TF-20 FEI Tecnai transmission electron microscope operating at 200 kV was used to view the clusters. The samples were made by drop casting and air drying the sample solution over a carbon coated mesh 200 grid. In the same way, the grid of incubated bacteria was created.

4A.3.2. X-ray photoelectron spectroscopy (XPS)

X-ray photoelectron spectroscopy (XPS) observations using micro-focused and monochromatic Al K radiation were performed using Thermo Scientific's K-alpha+ spectrometer with an energy of 1486.6 eV. After samples were placed onto silicon wafers and dried at room temperature for measurement, binding energies were calibrated to the C 1s peak at 284.8 eV. The XPS peaks profile of individual core amounts of elements were fitted using XPS peak41 software and a Shirley type background.

4A.3.3. Fluorescence spectroscopy

The fluorescence spectra were collected using a Horiba flouromax-4 fluorimeter. For this, sample solutions (1×10^{-4} M) were put in a 3.5 mL quartz cuvette with a 10 mm route length. The absolute quantum yield was determined using the integrating sphere method with DI water as the reference solvent and a slit width of 2 nm.

4A.3.4. Fourier-Transform IR spectroscopy

FTIR spectra were collected using the TENSOR-27 BRUKER instrument. KBr was the typical matrix for creating samples. A 25 μ L sample solution was thoroughly mixed with 100 mg of KBr powder (99.9%, Aldrich), ground well, dried, and shaped into a pellet, which was then utilised to get FTIR spectra.

4A.3.5. UV-Visible absorption spectroscopy

The measurements were carried out using a quartz cell with a 10 mm path length (capacity 3.5 mL) and methanol as the solvent in an Agilent Cary 5000 series UV-vis-NIR spectrophotometer.

4A.3.6. NMR spectroscopy

The ^1H NMR spectra of organic linkers in DMSO with tiny quantities of deuterated chloroform (CDCl_3) as an internal standard were recorded using Bruker 200 and 400 MHz NMR spectrophotometers. Using an appropriate deuterated solvent, samples for ^1H NMR studies were prepared by dissolving 10-15 mg of material in a 5mm diameter NMR tube.

4A.3.6. Computational Details

Computational studies were carried out by Miss. Ashakiran Maibam under the guidance of Dr. Sailaja Krishnamurthy, Physical and Materials Chemistry Division, CSIR-National Chemical Laboratory, Pune. All details are given in Appendix 2.

4A.4. Results and Discussion

4A.4.1. Structural Characterization of Thiol ligands

4A.4.1.1. NMR spectroscopy

Since, the quaternary ammonium modified with different alkyl and aromatic groups on thiol ligands were analysed through NMR spectroscopy.

N, N', N''-tripropyl (11-mercaptoundecyl) ammonium chloride, ^1H NMR (400 MHz, CDCl_3), $\text{C}_{20}\text{H}_{44}\text{ClNS}$: δ 1.07 (t, $J = 7$ Hz, 9 H, $\text{CH}_3\text{CH}_2\text{CH}_2\text{N}^+$), δ 1.20-1.39 (m, 14 H, - CH_2), δ 1.58-1.64 (m, 2 H, HS- CH_2CH_2), δ 1.66-1.84 (bm, 6 H, $\text{CH}_3\text{CH}_2\text{CH}_2\text{N}^+$), δ 1.86-1.91 (m, 2 H, $\text{CH}_2\text{CH}_2\text{N}^+$), δ 2.51-2.55 (m, 2 H, HS- CH_2), δ 2.90-3.01 (bm, 2 H, CH_2N^+), δ 3.34-3.40 (m, 6 H, $\text{CH}_3\text{CH}_2\text{CH}_2\text{N}^+$).

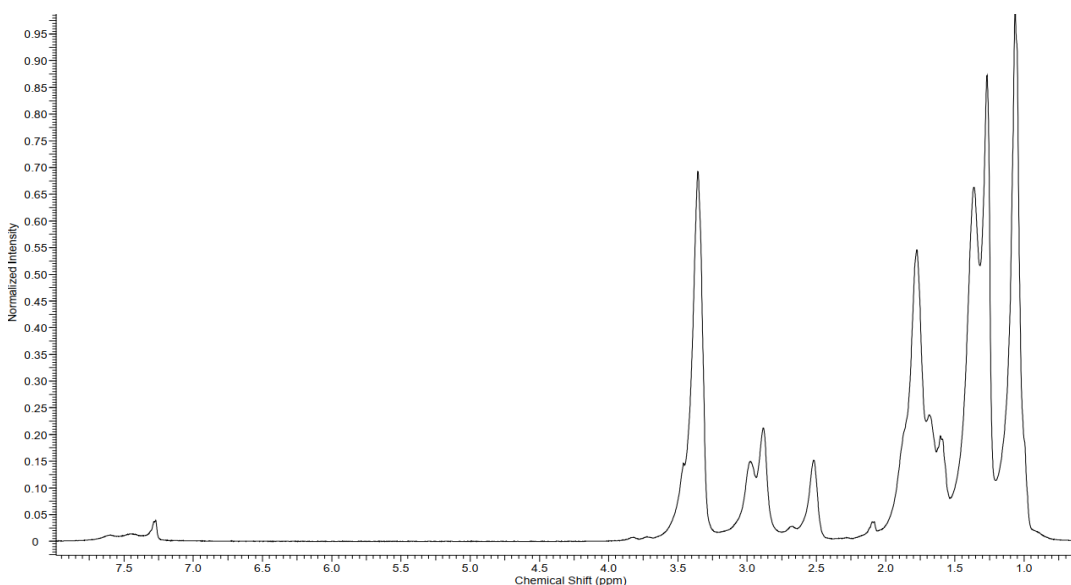


Fig.4A.1. ^1H NMR of *N, N', N''*-tripropyl (11-mercaptoundecyl) ammonium chloride.

***N,N',N''*-triethyl (11-mercaptoundecyl)ammonium chloride**, ^1H NMR(200 MHz, CDCl_3) $\text{C}_{17}\text{H}_{38}\text{ClNS}$:- (δ values in ppm) 1.28 [br.s., 9H, $\text{CH}_3\text{-CH}_2\text{-CH}_2\text{-N}^+$] ,1.35 to 1.48 [m,14H, $\text{HS-CH}_2\text{-CH}_2\text{-(CH}_2\text{)}_7$] , 1.53 to 1.63 [m,2H, $\text{HS-CH}_2\text{-CH}_2$] , 1.69 [s,2H,- CH_2 - CH_2 - $\text{N}^+(\text{Ethyl})_3$] , 2.48 to 2.59 [q, $J=7.47$ Hz, 2H,- $\text{CH}_2\text{-SH}$] , 3.23 to 3.32 [m, 2H, - CH_2 - $\text{N}^+(\text{Ethyl})_3$] 3.46 to 3.59 [m, $J=7.33\text{Hz}$,6H, $\text{N}^+ \text{-CH}_2\text{-CH}_3$].

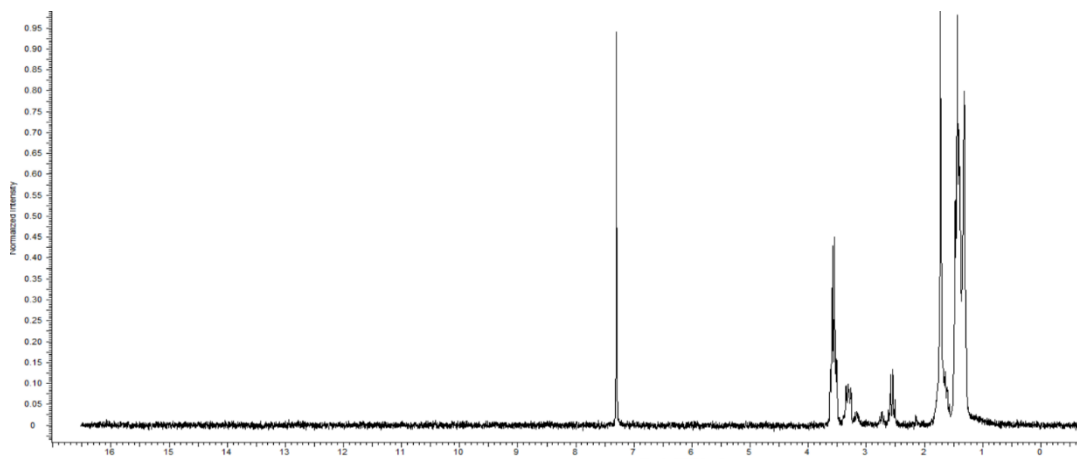


Fig.4A.2. ^1H NMR of *N, N', N''*-triethyl (11-mercaptoundecyl) ammonium chloride.

***N,N',N''*-tributyl (11-mercaptoundecyl)ammonium chloride**, ^1H NMR(200 MHz, CDCl_3), $\text{C}_{23}\text{H}_{50}\text{ClNS}$:- (δ values in ppm) 0.90 to 1.10 [m, 9H, $\text{CH}_3\text{-CH}_2\text{-CH}_2\text{-CH}_2\text{-N}^+$] ,1.29 [br.s,6H, $\text{N}^+ \text{-CH}_2\text{-CH}_2\text{-CH}_2\text{-CH}_3$], 1.35 to 1.53 [m,12H, $\text{HS-CH}_2\text{-CH}_2\text{-CH}_2\text{-(CH}_2\text{)}_6\text{-}$] , 1.59 to 1.73 [m,8H, $\text{HS-CH}_2\text{-CH}_2\text{-CH}_2\text{-}$ & $\text{N}^+ \text{-CH}_2\text{-CH}_2\text{-CH}_2\text{-CH}_3$] , 1.77 to 1.88 [m,4H,- $\text{(CH}_2\text{)}_2\text{-CH}_2\text{-SH}$] , 2.48 to 2.58 [q, $J=7.37$ Hz, 2H, - $\text{CH}_2\text{-SH}$] , 2.93 to 3.05 [m, 2H, - CH_2 - $\text{N}^+(\text{Butyl})_3$] 3.31 to 3.46 [m,6H, $\text{N}^+ \text{-CH}_2\text{-CH}_2\text{-CH}_2\text{-CH}_3$].

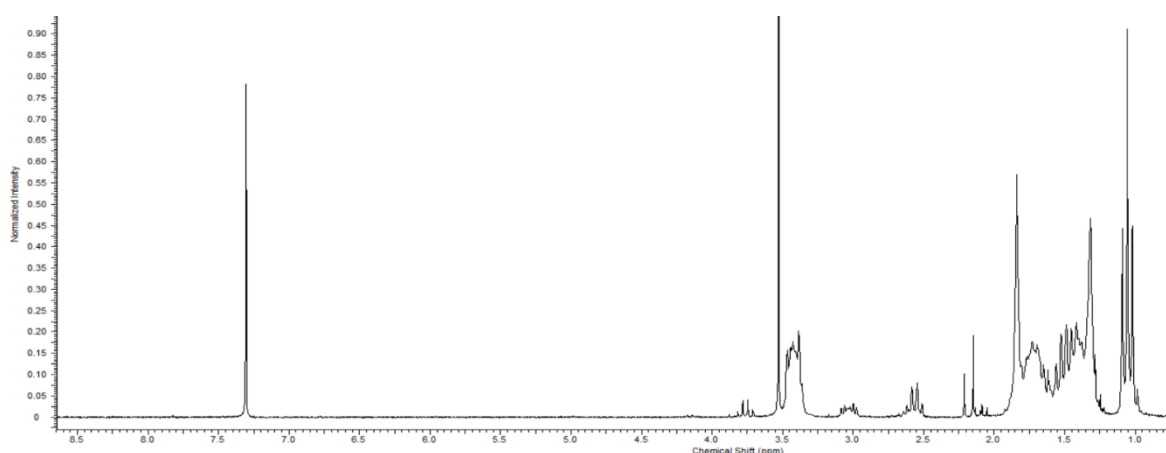


Fig.4.3. ^1H NMR of *N, N', N''*-tributyl (11-mercaptoundecyl) ammonium chloride.

***N*-(11-mercaptoundecyl)-*N, N'*-dimethylbenzenammonium chloride**, ^1H NMR (400 MHz, CDCl_3), $\text{C}_{19}\text{H}_{34}\text{ClNS}$:- (δ values in ppm) 1.10 to 1.27 [m, 12H, - $\text{(CH}_2\text{)}_6\text{-CH}_2\text{-SH}$]

, 1.27 to 1.39 [m, 4H, N^+ -CH₂-CH₂-(CH₂)₂-], 1.48 to 1.69 [m, 2H, N^+ -CH₂-CH₂-], 2.49 [q, 8H, $J=7.28$ Hz, HS-CH₂-], 3.13 to 3.25 [m, 2H, N^+ -CH₂-(CH₂)₁₀-SH], 3.83 to 4.13 [m, 6H, CH₃- N^+ -CH₃], 7.50 to 7.59 [m, 2H(benzene ring), meta to N^+], 7.63 to 7.66 [d, 1H(benzene ring), para to N^+], 7.77 to 7.89 [m, 2H(benzene ring), ortho to N^+].

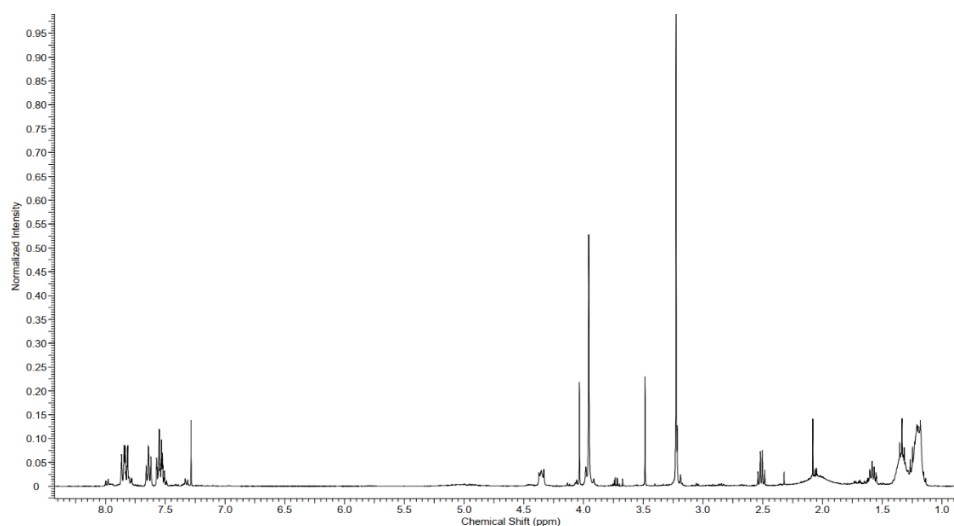


Fig.4A.4. ¹H NMR of *N*-(11-mercaptoundecyl)-*N,N'*-dimethylbenzenammonium chloride.

4A.4.1.2. FTIR spectroscopy

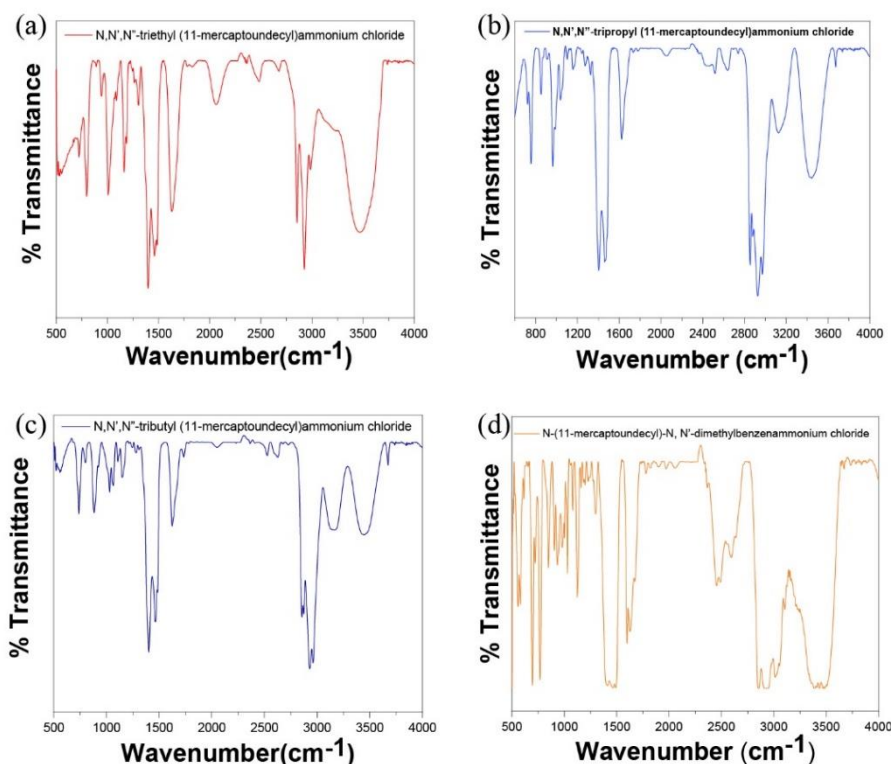


Fig.4A.5. FT-IR spectrum of (a) *N,N',N''*-triethyl (11-mercaptoundecyl) ammonium chloride ligand (b) *N,N',N''*-tripropyl (11-mercaptoundecyl) ammonium chloride ligand,

(c) *N, N', N''*-tributyl (11-mercaptoundecyl) ammonium chloride (d) *N*-(11-mercaptoundecyl)-*N, N'*-dimethylbenzenammonium chloride.

***N, N', N''*-triethyl (11-mercaptoundecyl) ammonium chloride** was characterized by FTIR spectroscopy. IR in cm^{-1} (KBr): 3474, 3122, 2982, 2925, 2855, 2680, 2484, 2357, 2062, 1625, 1460, 1400, 1303, 1266, 1187, 1161, 1090, 1006, 942, 892, 792, 722. Figure 4A.5(a) shows the vibrational frequencies of the *N, N', N''*-triethyl (11-mercaptoundecyl) ammonium chloride molecule in the C–H stretching region. The C-H stretching modes in the 2700-3100 cm^{-1} range are the most prominent features in the FT-IR spectra of long alkane chain thiol. The asymmetric and symmetric CH_2 stretching modes produce the two prominent peaks at 2927 and 2853 cm^{-1} . The asymmetric C-H vibration stretching frequencies of the CH_3 group are represented at 2984 cm^{-1} and symmetric C-H vibration stretching frequencies of the CH_3 group are merged with CH_2 symmetric stretching vibrations respectively. The stretching frequency of the S-H bond is indicated by a peak position of roughly 2678 cm^{-1} , confirming the thiol formation. Aliphatic carbon attached to N^+ shows C-N stretch around 1264 cm^{-1} .

***N, N', N''*-tripropyl (11-mercaptoundecyl) ammonium chloride** was characterized by FTIR- spectroscopy [Fig 4A.5(b)]. IR in cm^{-1} (KBr): 3438, 3123, 2970, 2927, 2879, 2853, 2638, 2518, 2418, 2058, 1781, 1738, 1623, 1465, 1405, 1326, 1272, 1157, 1104, 1040, 984, 963, 909, 851, 759, 720. The S-H stretching vibration found at around 2635 cm^{-1} shows the formation of thiol ligand. The symmetric and asymmetric stretching vibrations of CH_2 groups were found at 2852 and 2927 cm^{-1} respectively. Aliphatic C-N stretch shows around 1273 cm^{-1} . The asymmetric & symmetric vibration stretching frequencies of the CH_3 group are designated by two peaks at 2970 and 2879 cm^{-1} , respectively.

***N, N', N''*-tributyl (11-mercaptoundecyl) ammonium chloride** was characterized by FTIR- spectroscopy [Fig 4A.5(c)]. IR(KBr): 3446, 3153, 2962, 2929, 2873, 2856, 2626, 2526, 2052, 1736, 1625, 1467, 1402, 1281, 1246, 1216, 1151, 1108, 1065, 1030, 883, 801, 738. The synthesis of thiol ligand confirmed through the S-H stretching vibration at roughly denoted at 2627 cm^{-1} . At 2856 and 2936 cm^{-1} , respectively, the symmetric and asymmetric stretching vibrations of CH_2 groups were observed. The peak around 1273 cm^{-1} attributed to aliphatic C-N stretch. Two peaks at 2960 and 2873 cm^{-1} , respectively, denote the asymmetric and symmetric vibration stretching frequencies of the CH_3 group.

N-(11-mercaptoundecyl)-*N*, *N'*-dimethylbenzenammonium chloride was characterized by FTIR- spectroscopy [Fig 4A.5(d)]. IR (KBr): 3483, 3449, 3389, 3104, 3014, 2930, 2854, 2637, 2593, 2490, 2454, 2056, 1971, 1897, 1819, 1779, 1671, 1628, 1597, 1493, 1462, 1408, 1297, 1227, 1244, 1228, 1198, 1184, 1162, 1124, 1080, 1029, 1002, 979, 933, 903, 848, 768, 722, 695, 616, 580, 557. C-N stretching vibration between aromatic carbon and N⁺ observed at 1297 cm⁻¹. Two CH₃ groups attached to N⁺ possess C-H symmetric and asymmetric stretch around 2854 and 2930 cm⁻¹ respectively. C-H stretching vibrations from the aromatic ring denoted at 3014 cm⁻¹. C-H symmetric bending and asymmetric bending frequencies (from two CH₃ groups attached to N⁺) were observed around 1462 and 1493 cm⁻¹ respectively. S-H stretching band observed around 2637 cm⁻¹. C-H symmetric and asymmetric stretching vibration frequencies from eleven CH₂ groups in between S and N⁺ were found to be merged with symmetric and asymmetric stretching vibrations from two CH₃ groups attached to N⁺. The C-N stretch from the aliphatic carbons attached to N⁺ were observed at 1274 cm⁻¹.

4A.4.2. Structural Characterization of Au nanoclusters capped with different thiols

4A.4.2.1. TEM for particle size distribution

To produce photoluminescent AuNCs, we employed a bottom-up approach, first treating the gold precursor with suitable ligands, then reducing the gold. Among the various ligands known for stabilising AuNCs, thiol-based ligands provide improved colloidal stability. The positive charged quaternary ammonium head of the thiol ligand were modified in this study by replacing tertiary amine groups with tri ethyl amine, tri propyl amine, tri butyl amine, and *N,N'*- dimethyl aniline. Figure 4A.6 shows the structures and names of these modified thiols. Au⁺³ ions were initially reduced to Au⁺¹ with ligated thiol in slow stirring in a typical technique for the manufacture of AuNCs. Then, using a powerful reducing agent like NaBH₄, Au⁺¹ was reduced to Au⁰, leading in ultra-small nanoclusters. All of the preceding stages are performed at 0 °C with slow stirring. **AuNC-1**, **AuNC-2**, **AuNC-3**, and **AuNC-4** are made by employing four distinct modified thiols: *N*, *N'*, *N''*-triethyl (11-mercaptoundecyl) ammonium chloride, *N,N',N''*-tripropyl (11-mercaptoundecyl)ammonium chloride, *N,N',N''*-tributyl (11-mercaptoundecyl) and *N*-(11-mercaptoundecyl)-*N,N'*-dimethyl benzenammonium chloride. The particle size distribution of these Au nanocluster solutions was then determined using TEM.

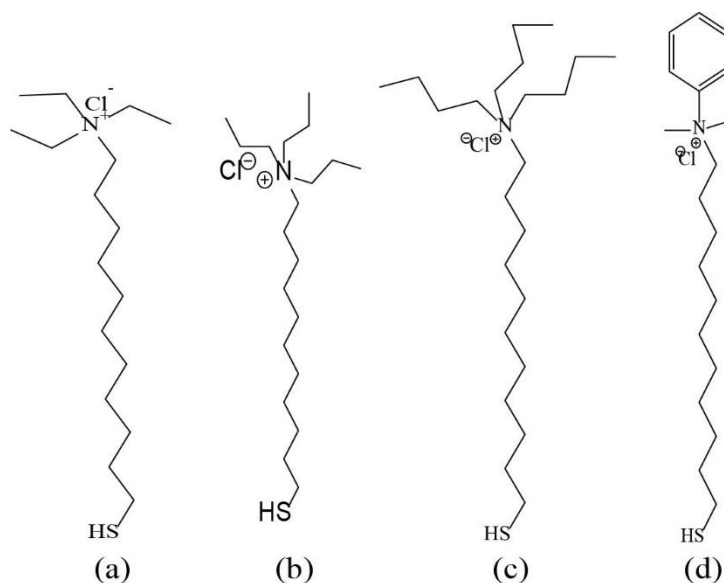


Fig.4A.6. Structures of (a) *N,N',N''*-triethyl (11-mercaptoundecyl) ammonium chloride, (b) *N,N',N''*-tripropyl (11-mercaptoundecyl) ammonium chloride, (c) *N,N',N''*-tributyl (11-mercaptoundecyl) ammonium chloride and (d) *N*-(11-mercaptoundecyl)-*N,N'*-dimethyl benzenammonium chloride.

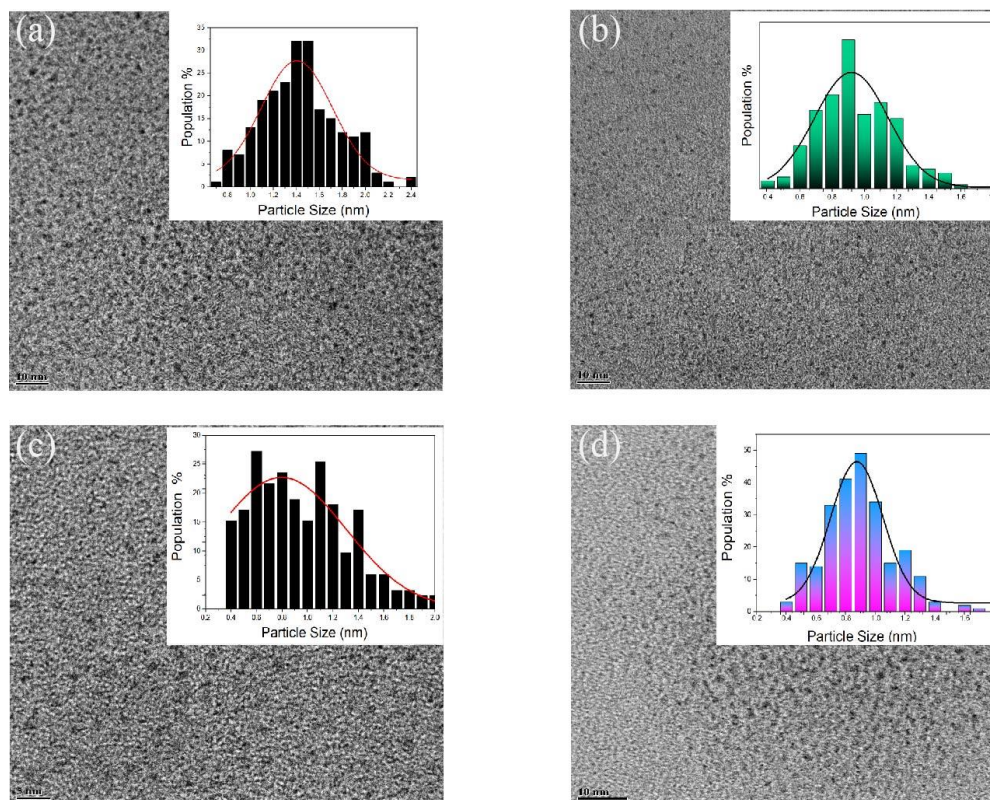


Fig.4A.7. Particle size distribution curves and respective TEM images of (a) AuNC-1, (b) AuNC-2, (c) AuNC-3, (d) AuNC-4

According to Fig.4A.7, the particle sizes of AuNC-1, AuNC-2, AuNC-3, and AuNC-4 are 1.460 ± 0.32 nm, 0.990 ± 0.23 nm, 0.95 ± 0.32 nm, and 0.920 ± 0.26 nm, respectively. The

particle sizes of AuNCs were discovered to be dependent on the hydrophobicity, i.e., the length of the alkyl chain or the hydrophobic character of the quaternary ammonium head of the thiol ligand, as determined by TEM images. The particle size reduces as the hydrophobicity of the thiol ligand over the quaternary ammonium head increases. The hydrophobicity of nanoclusters surfaces is arranged as follows: **AuNC-1** < **AuNC-2** < **AuNC-3** < **AuNC-4**.

4A.4.2.1. X-ray photoelectron spectroscopy (XPS)

XPS analysis was used to determine the oxidation state of Au nanoclusters with all thiol ligands. In all Au nanoclusters, Au was found to be completely reduced. The binding energies of **AuNC-1**, **AuNC-2**, **AuNC-3**, and **AuNC-4** in Au $4f_{7/2}$ were found to be 84.35 eV, 84.81 eV, 84.90 eV, and 84.89 eV, respectively. The core energy level, i.e., Au $4f_{7/2}$ binding energy, increases as particle size decreases.¹⁶ In the current scenario, a similar pattern has been noticed. Table.4A.1 and Figure.4A.8 shows the binding energies of all Au nanoclusters, which are $4f_{7/2}$ and $4f_{5/2}$.

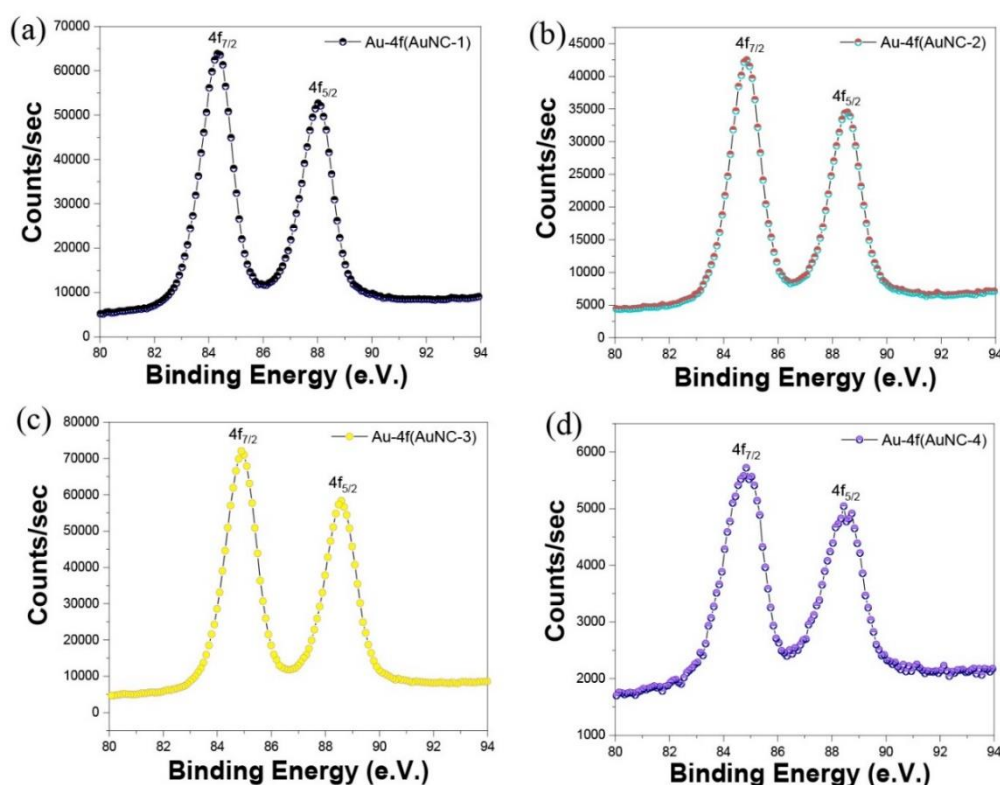


Fig.4A.8. XPS spectrum shows the core energy levels i.e., $4f_{7/2}$ and $4f_{5/2}$ for (a)**AuNC-1**, (b)**AuNC-2**, (3) **AuNC-3** and (d) **AuNC-4**.

Table.4A.1. Binding energies for core energy levels i.e., Au 4f_{7/2} and Au 4f_{5/2} in all Au nanoclusters.

Core level	AuNC-1	AuNC-2	AuNC-3	AuNC-4
Au 4f _{7/2}	84.35 eV	84.81 eV	84.90 eV	84.89 eV
Au 4f _{5/2}	88.00 eV	88.53 eV	88.58 eV	88.55 eV

4A.4.3. Photophysical characterization of Au nanoclusters capped with different thiols

4A.4.3.1. UV–visible absorption spectroscopy

The optical and electronic properties of the clusters were also examined using UV–visible absorption spectroscopy. The form and size of metal nanoparticles have an important influence on the peak positions of surface plasmon bands. In Au metal nanoparticles larger than 2 nm, surface plasmon resonance (SPR) bands can be detected.¹⁷ This feature is absent in ultra-small nanoclusters, which have discrete absorption bands in the UV region and shows molecule like transitions.

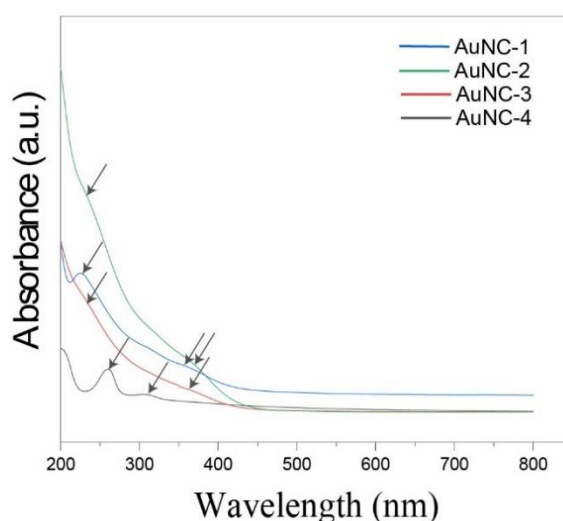


Fig.4A.9. Absorption spectra for **AuNC-1**, **AuNC-2**, **AuNC-3**, and **AuNC-4** shows discrete absorption bands denoted by arrows in the UV-Vis region.

Figure 4A.9. shows that there were no SPR bands in **AuNC-1**, **AuNC-2**, **AuNC-3**, and **AuNC-4** also indicating the nanoclusters are in the ultra-small regime (size ≤ 2 nm). The quantum confinement effect is caused by the ultra-small size of these nanoclusters. As a result, nanoclusters act like a single molecule and exhibit HOMO-LUMO electronic transitions, as demonstrated by the UV-Vis absorption spectra shown above. The

absorption peak characteristics represented by arrows in Fig.4A.9. vary from 225 nm to 370 nm and are attributed to d-sp and sp-sp electronic transitions in general for **AuNC-1**, **AuNC-2**, **AuNC-3**, and **AuNC-4**.

Table.4A.2. Electronic transition band positions in the case of **AuNC-1**, **AuNC-2**, **AuNC-3**, and **AuNC-4**.

Transitions Bands	AuNC-1	AuNC-2	AuNC-3	AuNC-4
d-sp	226 nm	240 nm	239 nm	260 nm
sp-sp	368 nm	366 nm	367 nm	310 nm

4A.4.3.1. Fluorescence spectroscopy

Photoluminescence is the most critical characteristic of these ultra-small quantum clusters. The quantum confinement effect is responsible for the excitation and emission features of fluorescent metal nanoclusters, which is further influenced by particle size and the interaction between metal and ligand.

Table.4A.3. Excitation and Emission max. wavelength for all modified thiol capped Au nanoclusters.

Nanocluster	Excitation Wavelength (nm)	Emission Max.(nm)
AuNC-1	420nm	662nm
AuNC-2	420nm	650nm
AuNC-3	420nm	632nm
AuNC-4	380nm	670nm

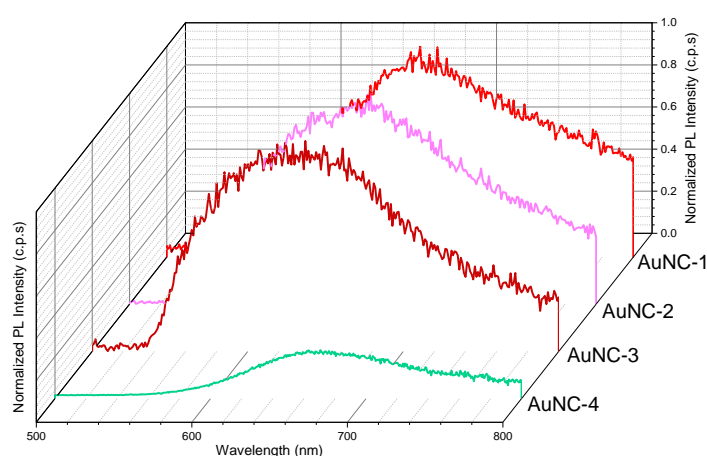


Fig.4A.10. PL spectra of all modified thiol capped Au nanoclusters excited at different wavelengths mentioned in Table.4A.3.

4A.4.3. DFT studies to correlate optical properties of different thiol capped AuNCs with experimental data

All the computational details are given in Appendix-2.

Table 4A.4. Comparison of the absorption spectra from UV-visible region with Mulliken charges and HOMO-LUMO energy gaps as obtained from DFT calculations.

AuNCs	Transition bands	Δq_{avg} of R' (Mulliken charge)	Δq_{avg} of N (Mulliken charge)	DFT-HOMO-LUMO energy gap
AuNC-1	226 nm	-0.27	-0.09	1.15 eV
AuNC-2	240 nm	-0.26	-0.09	1.15 eV
AuNC-3	239 nm	-0.26	-0.11	1.15 eV
AuNC-4	260 nm	-0.09	-0.17	1.06 eV

For computational studies on the above AuNCs, we consider the $\text{Au}_{25}(\text{SC}_5\text{H}_{11})_{18}\text{NH}_3^+$ nanocluster and substitute the ammonium head with *N*, *N'*, *N''*-triethyl ammonium for **AuNC-1**, *N*, *N'*, *N''*-tripropyl ammonium for **AuNC-2**, *N*, *N'*, *N''*-tributyl ammonium for **AuNC-3** and *N*, *N'*-dimethyl benzenammonium for **AuNC-4** respectively. Studies showed that as the *N*, *N'*, *N''* substitution on the mercapto ligands changes from triethyl to dimethyl benzene, the average size of the AuNCs decreases. The size of the AuNCs formed by the self-assembly of the ammonium mercapto ligand is dependent on the torsional hindrance among the substituents on the ammonium moiety; the larger tributyl and dimethyl benzene substituents pose a higher steric hindrance on the ammonium centre than the smaller triethyl substituent. As a result, mercapto capped AuNCs with larger substituents and higher steric hindrance on the ammonium head are found to be smaller than those with substituents that have less steric hindrance on the ammonium head. The average Mulliken charges on the *N*, *N'*, *N''* substituents and N-atom of the ammonium head of **AuNC-1**, **AuNC-2**, **AuNC-3**, and **AuNC-4**, as well as their HOMO-LUMO energy gaps, are summarized in Table 4.4. When compared to the other three *N*, *N'*, *N''* trialkyl AuNCs with aliphatic R' groups, the aromatic benzene moiety on **AuNC-4** is found to be less negatively charged (-0.09 e) due to a charge transfer on the ammonium nitrogen (-0.17 e) on AuNC-4, which is more stabilised due to electron delocalisation. Figure.A.2.3. (d1) and (d2) (from Annexure-2) show the same thing in terms of Frontier Molecular Orbitals. When the d-sp transition bands from the UV-visible absorbance spectra of AuNCs are examined, AuNC-4 with *N*, *N'*, *N''* dimethyl benzene ammonium mercapto ligand AuNCs shows a red shift (i.e., an increase in

wavelength) when compared to **AuNC-1**, **AuNC-2**, or **AuNC-3** with *N*, *N'*, *N''* trialkyl ammonium mercapto ligands. The smaller HOMO-LUMO energy gap of 1.06 eV on the *N*-(5-mercaptopentyl)-*N*, *N'*-dimethyl benzenammonium capped AuNCs, as compared to a considerably higher HOMO-LUMO energy gap of 1.15 eV in the rest, explains the red-shift in **AuNC-4**. The Frontier Molecular Orbitals of *N*, *N'*, *N''*-trialkyl (5-mercaptopentyl) ammonium AuNCs are localised on surface Au-atoms and methylene(-CH₂) units connected directly to thiol ligands, resulting in a greater energy barrier for electronic excitation. Unlike the *N*-(5-mercaptopentyl)-*N*, *N'*-dimethyl benzene ammonium AuNCs with an aromatic substituent on the ammonium nitrogen that shows electron delocalisation in its HOMO as well as HOMO and the electron transfer is mostly guided by the ammonium centre as seen from Mulliken charge analysis. It can be deduced from the computational findings that the dimethyl benzene substituent on the mercapto ligands and Au-surface atoms steer the electronic nature of **AuNC-4** as we have observed from the experiments.

We altered the ammonium head group with different R' groups of thiol ligands in our study while keeping the carbon chain connected to sulphur and ammonium nitrogen as C-11. These quantum clusters are excited to attain the maximum emission maxima in the red wavelength in order to study the fluorescence emission properties of **AuNC-1**, **AuNC-2**, **AuNC-3**, and **AuNC-4**. Table.4A.3. reveals that AuNC-4 has emission maxima at 670nm, which is on the red side of the wavelength spectrum than the other clusters. Except for **AuNC-4** in Table.4A.3, the emission maxima of these nanoclusters follow the particle size trend, i.e., as particle size grows, the emission maxima shift to the red. Because the particle size of **AuNC-4** is lower than that of AuNC-1, AuNC-2, and AuNC-3, the emission should be shifted to the blue side. In the instance of AuNC-4, however, this did not occur. Table.4A.4 shows that, compared to previous AuNCs, the HOMO-LUMO energy gap reduces due to delocalization of electron density from the benzene aromatic ring to the N⁺ of the ammonium head. As a result, a smaller HOMO-LUMO energy gap should result in more emission in the red spectral region, which is consistent with experimental findings.

4A.5. Conclusion

In conclusion, a bottom-up approach was used to create photoluminescent AuNCs with various ligand chain lengths. This study shows that charge transfer between the ligands and Au-surface atoms causes a tuneable photoluminescence emission from 500 to 800 nm on *N*, *N'*, *N''*-trialkyl (11-mercaptoundecyl) capped AuNCs, emphasising the interface chemistry

between gold nanoclusters and capping ligands. The hydrophobicity and bulkiness of the ligands can be used to gain a better understanding of how the thiolate AuNCs self-assemble and vary in particle size. The UV-visible absorption spectra and charge transfer from the ligand to Au-surface atoms using frontier molecular orbital analysis are supported by HOMO-LUMO analysis from DFT studies.

References

- 1 X. Kang and M. Zhu, *Chem. Soc. Rev.*, 2019, **48**, 2422–2457.
- 2 H. Yu, B. Rao, W. Jiang, S. Yang and M. Zhu, *Coord. Chem. Rev.*, 2019, **378**, 595–617.
- 3 Y. Chen, C. Zeng, D. R. Kauffman and R. Jin, *Nano Lett.*, 2015, **15**, 3603–3609.
- 4 Y. Chen, C. Zeng, C. Liu, K. Kirschbaum, C. Gayathri, R. R. Gil, N. L. Rosi and R. Jin, *J. Am. Chem. Soc.*, 2015, **137**, 10076–10079.
- 5 C. Zeng, Y. Chen, K. Kirschbaum, K. Appavoo, M. Y. Sfeir and R. Jin, *Sci. Adv.*, 2015, **1**, 1–7.
- 6 S. Roy, A. Baral, R. Bhattacharjee, B. Jana, A. Datta, S. Ghosh and A. Banerjee, *Nanoscale*, 2015, **7**, 1912–1920.
- 7 J. Zheng, P. R. Nicovich and R. M. Dickson, *Annu. Rev. Phys. Chem.*, 2007, **58**, 409–431.
- 8 H. Dong, L. Liao and Z. Wu, *J. Phys. Chem. Lett.*, 2017, **8**, 5338–5343.
- 9 E. Khatun, A. Ghosh, P. Chakraborty, P. Singh, M. Bodiuzzaman, P. Ganesan, G. Nataranjan, J. Ghosh, S. K. Pal and T. Pradeep, *Nanoscale*, 2018, **10**, 20033–20042.
- 10 A. Kim, C. Zeng, M. Zhou and R. Jin, *Part. Part. Syst. Charact.*, 2017, **34**, 1–6.
- 11 D. Li, Z. Chen and X. Mei, *Adv. Colloid Interface Sci.*, 2017, **250**, 25–39.
- 12 M. I. Halawa, J. Lai and G. Xu, *Mater. Today Nano*, 2018, **3**, 9–27.
- 13 Z. Wu and R. Jin, *Nano Lett.*, 2010, **10**, 2568–2573.
- 14 C. M. Aikens, *Acc. Chem. Res.*, 2018, **51**, 3065–3073.

- 15 K. L. D. M. Weerawardene and C. M. Aikens, *J. Am. Chem. Soc.*, 2016, **138**, 11202–11210.
- 16 Y. Negishi, K. Nobusada and T. Tsukuda, *J. Am. Chem. Soc.*, 2005, **127**, 5261–5270.
- 17 D. E. Mustafa, T. Yang, Z. Xuan, S. Chen, H. Tu and A. Zhang, *Plasmonics*, 2010, **5**, 221–231.

Chapter-4B

**Self-assembly of AuNCs capped with aromatic thiols and
the thermal and solvent effect on its fluorescence**

4B.1. Introduction

As mentioned in previous chapters, metal NCs have less quantum yields (QY) that seldom reach, limiting their use in many optical applications such as biosensing, bioimaging, and solid-state lighting and display.^{1,2,3} Enhancing the emission intensity is imperative for a wider applicability of these materials. Multiple techniques are employed for achieving this as already detailed in other chapters. One such technique, aggregation-induced emission⁴ (AIE) for obtaining high luminescence of metal NCs has recently piqued researchers curiosity⁵. The restriction of intramolecular rotation and vibration of the ligands on the NCs surface following aggregation might be attributed to the AIE origin of metal NCs, promoting radiative energy transfer by restraining ligand-related nonradiative excited state relaxation.^{6,7,8} Cation- and solvent-induced aggregations have been the most prevalent AIE techniques to form NCs so far.^{6,8,9} However, both of these AIE techniques suffer from structural irregularity and inhomogeneity as a result of the random aggregation route, which frequently leads to NC aggregation instability and poor colour purity⁶, limiting their potential practical uses. As a result, new methods for synthesising a more regular or homogenous morphology of NC aggregations are urgently required.

Self-assembly is thought to be capable of guiding metal NCs to form a well-defined architecture as an effective technique for manipulating the spatial arrangement of nanosized building blocks to form specified structures.¹⁰ Although massive building blocks like metal nanoparticles¹¹, proteins¹², and polymers¹³ have had great success in self-assembly, it is more challenging to direct metal NCs to self-assemble into high-ordered structures due to their ultra-small size and distinctive core-shell structure. NCs are unstable in self-assembly due to their high surface energy¹⁴, resulting in recrystallization or fusing into giant nanoparticles. The contacts between metal NCs emanating from the ligand shell on the NC surface, in particular, are rather weak, equivalent to the thermal fluctuation energy of the surroundings, resulting in the detachment of formed NCs and the creation of irregular structures¹⁵. Strengthening the inter-NC association by altering the outer layer of metal NCs, known as capping ligands, is therefore important to the success of metal NC self-assembly. The use of controlling the capping ligands arrangement over the self-assembly of metal NCs has typically been main aspect so far. Here, selection of suitable molecules as metal NC capping ligands in order to direct spontaneous association of NCs under equilibrium conditions into well-defined assemblies connected by covalent or noncovalent bonds, a process known as "induced assembly via capping ligand" is much important. However,

certain fundamental questions about these novel self-assembled emitters, such as their solvatochromic characteristics and the concentration-dependent fluorescence of metal nanoclusters, remain unanswered. Because of the surface plasmon resonance (SPR) absorption, metal nanoparticles have a solvatochromic effect, but these ultrasmall metal nanoclusters (size ≤ 2 nm) lack the constant density of states required to support the SPR band of larger metal nanoparticles.

As a result, there is no compelling evidence that metal nanoclusters have solvatochromic characteristics. In this context, we synthesized water dispersible AuNCs capped with cationic thiol ligand i.e., *N*-(11-mercaptoundecyl)-*N*, *N'*-dimethyl benzenammonium chloride, which form self-assembled structures. These AuNCs are also found to show temperature dependent emission properties as well as solvent dependent fluorescence.

4B.2. Experimental Section

4B.2.1. Synthesis of *N*-(11-mercaptoundecyl)-*N*, *N'*-dimethylbenzenammonium chloride

The synthesis of this ligand is already mentioned in working chapter 4A.

4B.2.2. Synthesis of AuNCs capped with *N*-(11-mercaptoundecyl)-*N*, *N'*-dimethylbenzenammonium chloride

A 20 mL acetonitrile stock solution of HAuCl_4 was combined with an 8.5 mL acetonitrile stock solution of HAuCl_4 (10 mM). This mixture received a dose of thiol (0.593 g, 1.6 mmol) in 2 mL methanol. For 30 min, the material was mixed. Stirring was continued for 45 minutes after adding a NaBH_4 solution (100 μL , 1.58 M) in methanol. The gold nanocluster solution received 30 mL of DI water. In vacuo, acetonitrile was extracted. Aqueous gold nanocluster solution was purified using cellulose membrane dialysis (Aldrich, pore size 12 kDa). After the dialysis the colloidal solution of AuNCs was found to be milky turbid. According to elemental analysis, the final solution had a concentration of ~ 2 mM.

4B.3. Instruments for Characterization

4B.3.1. Transmission electron microscopy

A TF-20 FEI Tecnai transmission electron microscope operating at 200 kV was used to observe Au nanoclusters. Drop casting and air drying the sample solution over a carbon coated mesh 200 grid were used to create the samples.

4B.3.2. High-resolution Transmission electron microscopy

A JEOL JEM-200 high resolution transmission electron microscope operating at 200 kV was used to study the nanoclusters. Sample preparation is similar to TEM.

4B.3.3. X-ray photoelectron spectroscopy (XPS)

X-ray photoelectron spectroscopy (XPS) investigations were carried out using a Thermo Scientific K-alpha+ spectrometer with an energy of 1486.6 eV and micro-focused and monochromatic Al K radiation. After samples were placed onto silicon wafers and dried at room temperature for measurement, binding energies were calibrated to the C 1s peak at 284.8 eV. The XPS peaks profile of individual core amounts of elements were fitted using XPS peak41 software and a Shirley type background.

4B.3.4. Fluorescence Spectroscopy

A Photon Technology International fluorescence spectrophotometer (PTI) with a quartz cell with a 10 mm path length was used to detect steady-state fluorescence (volume 3.5 mL). Throughout the studies, the emission and excitation band widths were kept at 2 nm.

4B.3.5. Microwave Plasma Atomic Emission Spectrometry (MP-AES)

The elemental analysis of nanocluster aqueous solution was carried out on an Agilent 4200 utilising inductively coupled plasma atomic emission spectroscopy (MP-AES). Standard solutions were used for calibration. 1 mL nanocluster aqueous solution was dried at 100°C for 10 minutes and calcined at 350°C for 8 hours to remove the organic ligand. 1 mL aqua regia was used to dissolve the residue, which was then diluted with 15 mL Millipore water. This diluted 15 mL solution was used for further elemental analysis.

4B.4. Results and Discussion

During the synthesis of Au nanoclusters, it was found that after addition of 30 mL DI water and after removing of all solvents the solution became milky white. This solution if dialyzed against DI water the whole colloidal solution became whitish turbid. Under UV light, this dialyzed whitish colloidal solution of AuNCs shows red emission (shown in Fig.4B.1). After centrifugation at ~ 13500 R.P.M., white colloidal AuNCs settled down, which on drying gives a white powder.

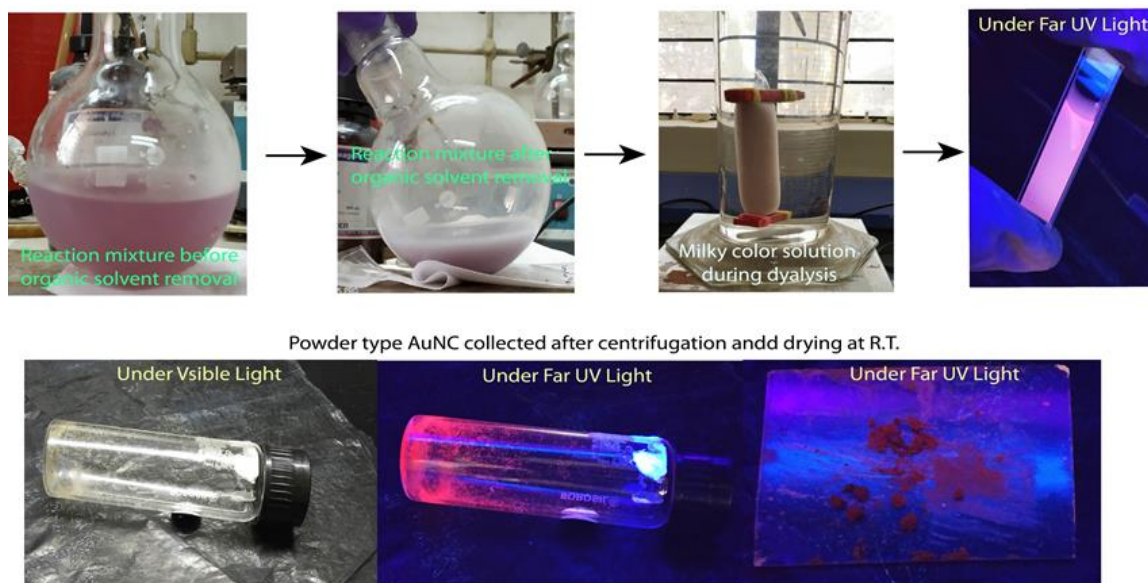


Fig.4B.1. Representative images during and after synthesis of Au nanoclusters capped with *N*-(11-mercaptoundecyl)-*N*, *N'*-dimethylbenzenammonium chloride.

This powder also has very bright red emission under UV light irradiation. The pale white supernatant solution also has red emission albeit comparatively pale, obvious due to less concentration. For convenience, different NCs are named as follows: the dialyzed AuNCs solution as **AuNCs-dialyzed**, the settled down AuNCs solution after centrifugation as **AuNCs-colloidal** and the remained supernatant after centrifugation as **AuNCs-supernatant**.

4B.4.1. Structural Characterization of Au nanoclusters capped with *N*-(11-mercaptoundecyl)-*N*, *N'*-dimethylbenzenammonium chloride

The obtained **AuNCs-dialyzed** solution is then drop casted and air dried on TEM grid for further characterization. From Fig.4B.2, the **AuNCs-dialyzed** solution shows there is a formation of self-assembly which forms small nano level aggregates (marked with yellow arrows). The average diameter for these particles were calculated with the help of around 250 nanoclusters in an image. The average diameter for **AuNCs-dialyzed** were found to be 0.92 ± 0.26 nm. The representative particle distribution curve for **AuNC-dialyzed** also showed in Fig.4B.2. **AuNCs-colloidal** was tried to drop cast over TEM grid, but the problem is that it could not dry properly and stucked to the grid as a thick layer. Thus, the TEM images of **AuNCs-colloidal** could not be taken.

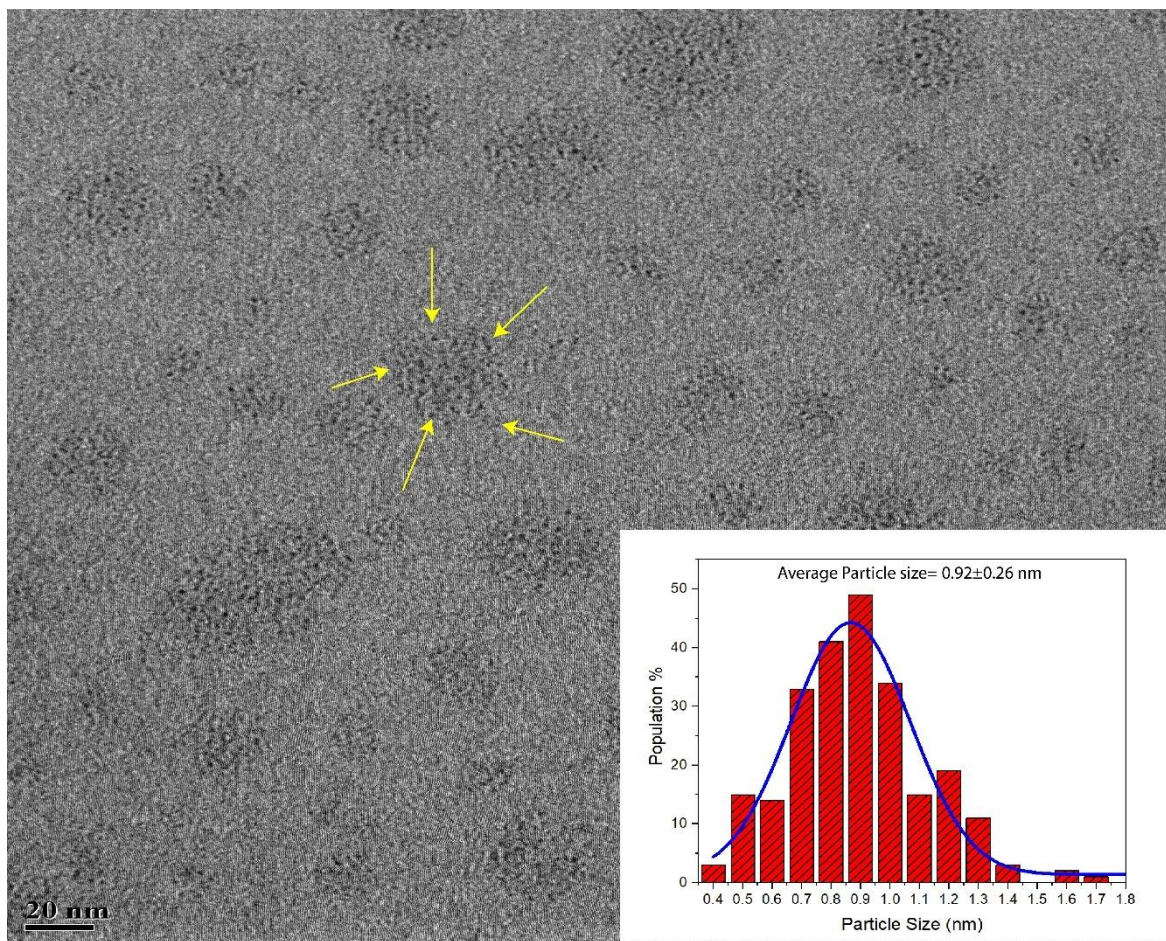


Fig.4B.2. TEM images of The **AuNCs-dialyzed** solution (Resolution~20nm). Yellow arrows around the self-assembled nanoclusters show aggregation effect.

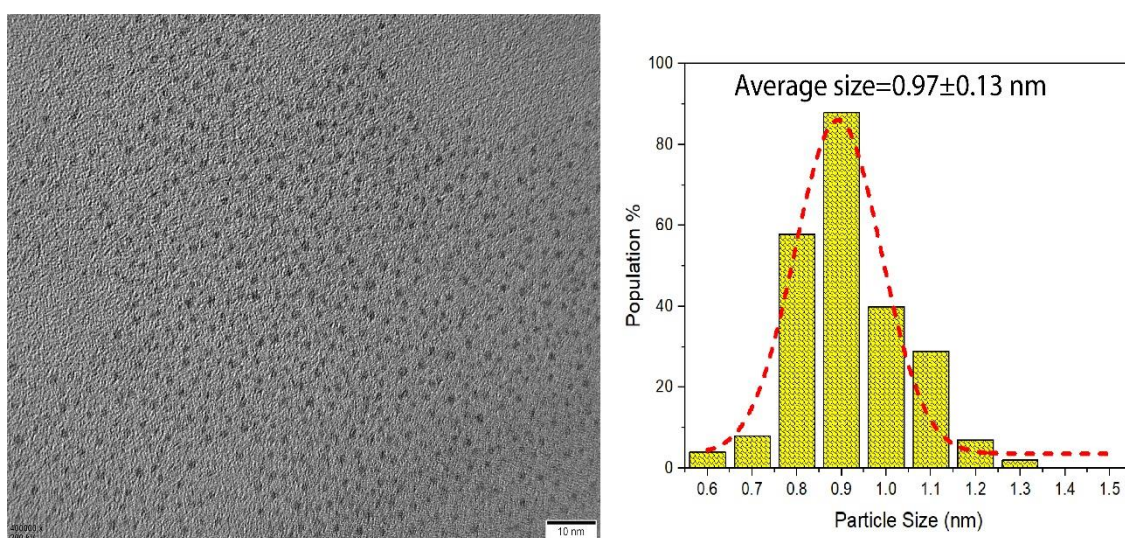


Fig.4B.3. HR-TEM images of **AuNCs-supernatant** solution of AuNCs (Resolution~10nm).

AuNCs-supernatant solution was examined through HR-TEM successfully as shown in Fig.4B.3. The average diameters for these nanoclusters are found to be $\sim 0.97 \pm 0.13$ nm, similar to the particle size of **AuNCs-dialyzed**. These nanoclusters are spherical in nature and not found as aggregates as we see in the case of **AuNCs-dialyzed**.

4B.4.2. X-ray photoelectron spectroscopy (XPS)

X-ray photoelectron spectroscopy was used to determine the oxidation state of Au in **AuNCs-dialyzed** and **AuNCs-supernatant** samples. It was found that both the samples contain Au in its zero-oxidation state. In the case **AuNCs-colloid** the sample preparation is difficult because it forms a thick moist layer over the silicon wafers which is not suitable to run the sample. The $4f_{7/2}$ core binding energies for **AuNCs-dialyzed** and **AuNCs-supernatant** were found at 84.89 eV and 84.71 eV respectively. Similarly, $4f_{5/2}$ core binding energies for **AuNCs-dialyzed** and **AuNCs-supernatant** were found at 85.55 eV and 88.42 eV. Similar to the particle size analysis through TEM, XPS results also indicates similar Au $4f_{7/2}$ binding energies for **AuNCs-dialyzed** and **AuNCs-supernatant**.

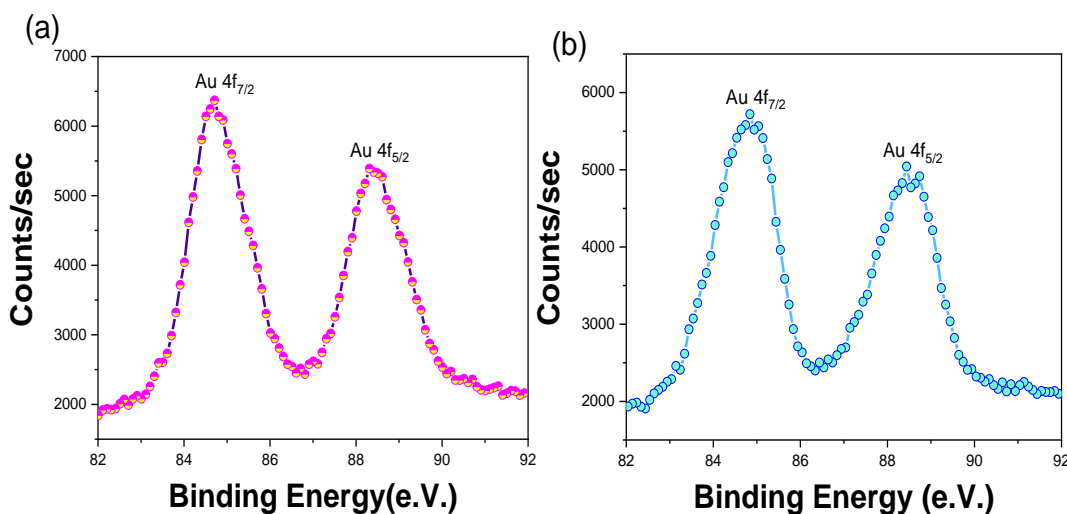


Fig.4B.4. XPS spectrum for (a) **AuNCs-supernatant**, (b) **AuNCs-dialyzed**.

4B.4.3. Optical Characterization for Au nanoclusters capped with *N*-(11-mercaptoundecyl)-*N*, *N'*-dimethylbenzenammonium chloride

4B.4.3.1. UV-visible absorption spectroscopy

AuNCs-dialyzed, **AuNCs-supernatant**, **AuNCs-colloid** all have two absorption bands i.e., at 260 nm and 310 nm corresponds to d-sp and sp-sp transitions. From Fig.4B.5, it was

noted that these above two important transitions for all the three AuNCs appeared on the same wavelength. Such HOMO-LUMO electronic transitions are due to quantum confinement effects indicating that these materials fall in the category of ultra-small nanoclusters.

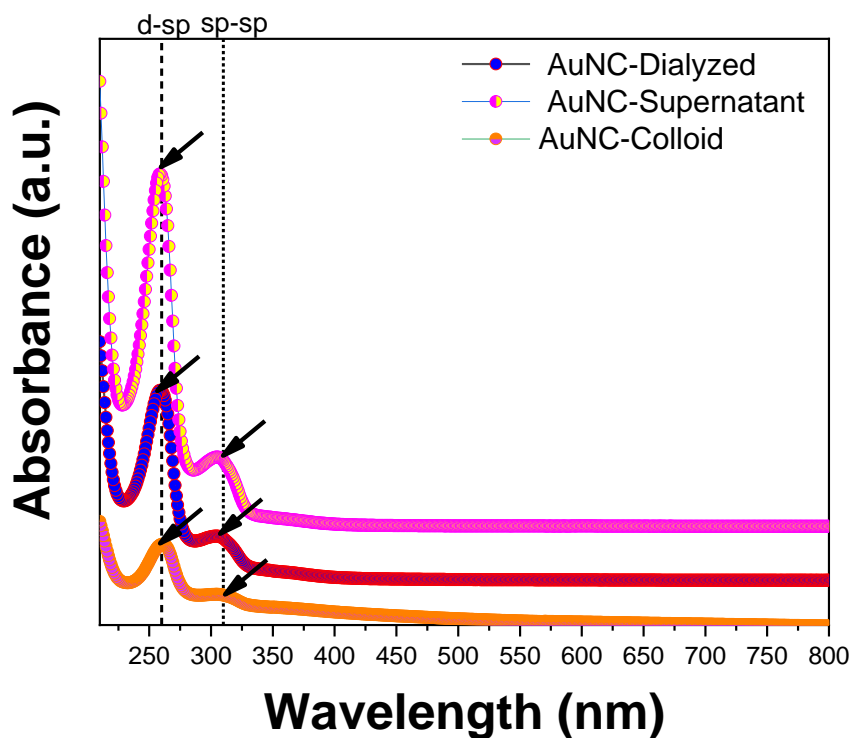


Fig.4B.5. Absorption spectrum for AuNCs-dialyzed, AuNCs-supernatant, AuNCs-colloid.

From Fig.4B.5.,it could be concluded that all these three nanoclusters possess same electronic environment with same absorption characteristics.

4B.4.3.2. Fluorescence spectroscopy

Photoluminescence of ultra-small quantum clusters depends upon quantum confinement effect which is further responsible for the excitation and emission characteristics of upon the particle size and the interface between metal and capping ligand.

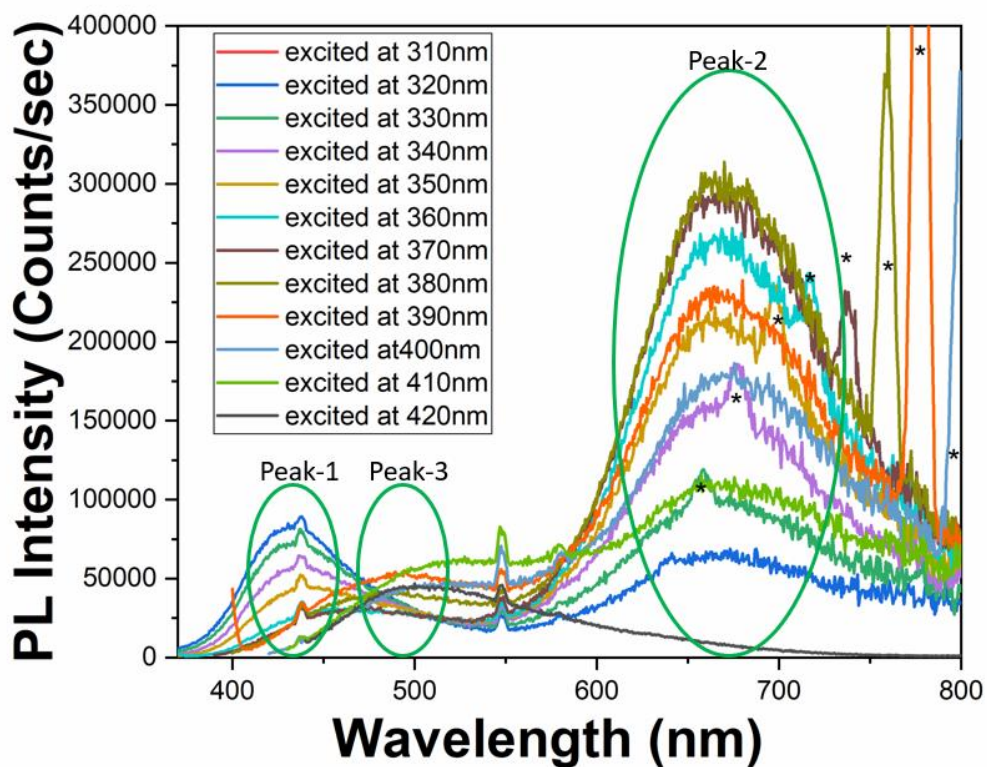
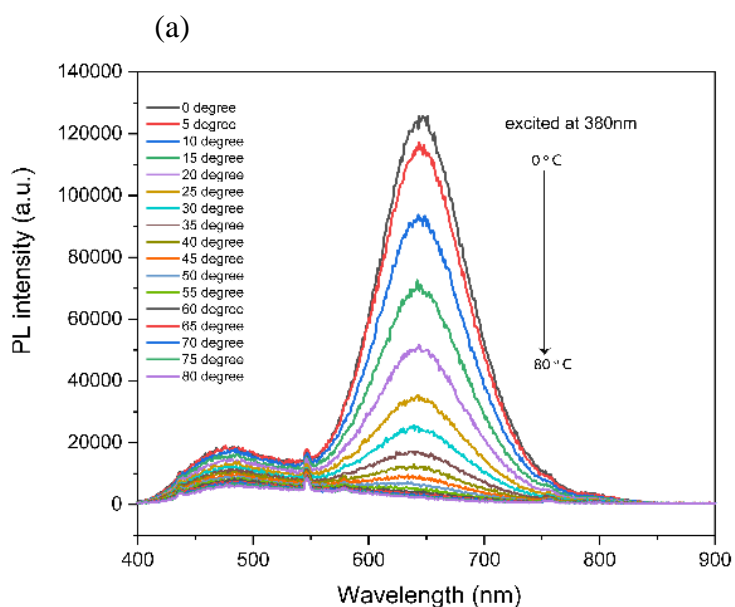


Fig.4B.6. Fluorescence spectra of aqueous solution of AuNCs-dialyzed at various excitation wavelength. * Mark indicates 2 lambda wavelengths.



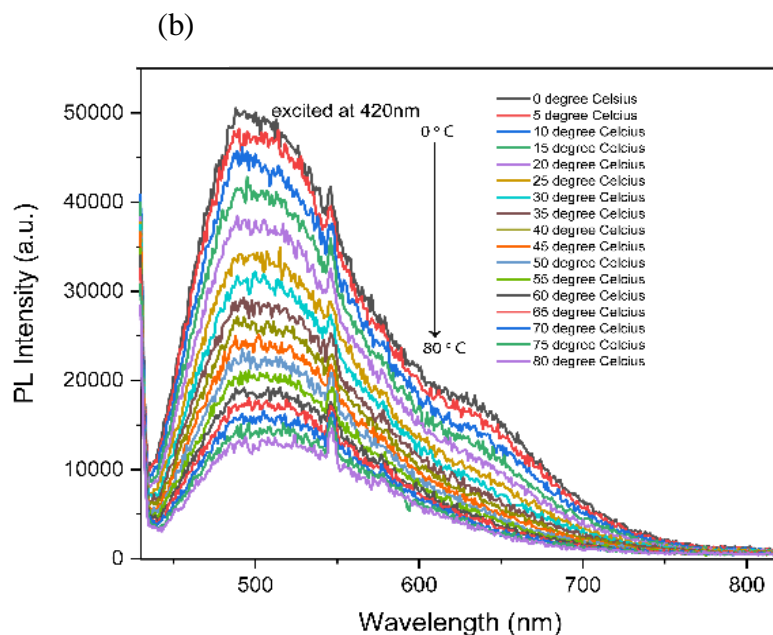


Fig.4B.7. Fluorescence spectra of aqueous solution of **AuNCs-dialyzed** excited at (a) 380 nm and (b) 420 nm at different temperatures.

Fig.4B.6 shows the emission spectrum of **AuNCs-dialyzed** at different excitation wavelength. It was observed that if excited at 310 nm, a small emission peak is observed at 430nm (peak-1). When excitation wavelength was progressively increased from 320 nm to 370 nm, the intensity of emission peak observed around 430 nm goes on decreasing as well as it gets red shifted. Also, a new emission peak observed at 670 nm (peak-2) whose intensity goes on increasing when we start to excites from 320 nm to 370 nm. The intensity of 670 nm (peak-2) emission peak was found to be highest when the excitation wavelength for **AuNC-dialyzed** fixed at 380 nm, and the intensity peak-2 showing red emission for the same sample decreases and goes on decreasing as excitation wavelength increases. Also, the intensity of peak-1 goes on decreasing and red shifted to 500 nm (i.e., peak-3) at 420nm excitation. Peak-2 basically originates from core of Au nanoclusters as we saw in chapter-4A; however, origin of peak-3 and peak-2 are not yet confirmed.

We tested the thermoresponsive property of the as prepared **AuNCs-dialyzed** in aqueous solution to see if they could be used for nano thermometry. As shown in Fig.4B.7, the fluorescence spectra of **AuNCs-dialyzed** sample were measured at temperatures ranging from 0 to 80 °C. If we excite at 380 nm, the peak-1 and peak-2 intensities goes on increasing as temperature decreases from 80°C to 0°C. Similarly, peak-3 intensity also goes on increasing going from 80°C to 0°C when we excited at 420 nm. This property is common in

temperature-sensitive fluorescence materials and is based on Boltzmann distribution statistics.^{16,17} The molecular collision frequency and non-radiative transition rate increase as the temperature rises, while the radiative transition rate remains constant, lowering the intensity of the excited state emission (i.e., fluorescence intensity). Low temperature, on the other hand, is advantageous for increasing the fluorescence intensity of AuNCs. We tried to fit with linear curve calibration (PL intensity vs temperature) for AuNCs, but not possible with linear fit. Also, we found that AuNCs are more sensitive to lower temperatures where PL intensity increases as we go to lower temperatures.

4B.4.3.2. Solvent dependent emission

To check whether the red emission coming from these nanoclusters is same as in water, **AuNCs-dialyzed** was transferred from water to organic solvent and again transferred to water to check the regenerative emission properties of these nanoclusters. For this, first 0.5 mL of **AuNCs-dialyzed** (2 mM solution) was taken in a 2mL centrifuge vial (stage-I) to check its red emission under UV- irradiation. Then centrifugation was done for this solution at 13000 R.P.M to get supernatant (faint white) solution and settled powder. This settled red emissive powder was washed with organic solvent (For e.g., ethanol) 2 to 3 times and fresh 0.5 mL of the same solvent (stage-II) was added again and washed. Red

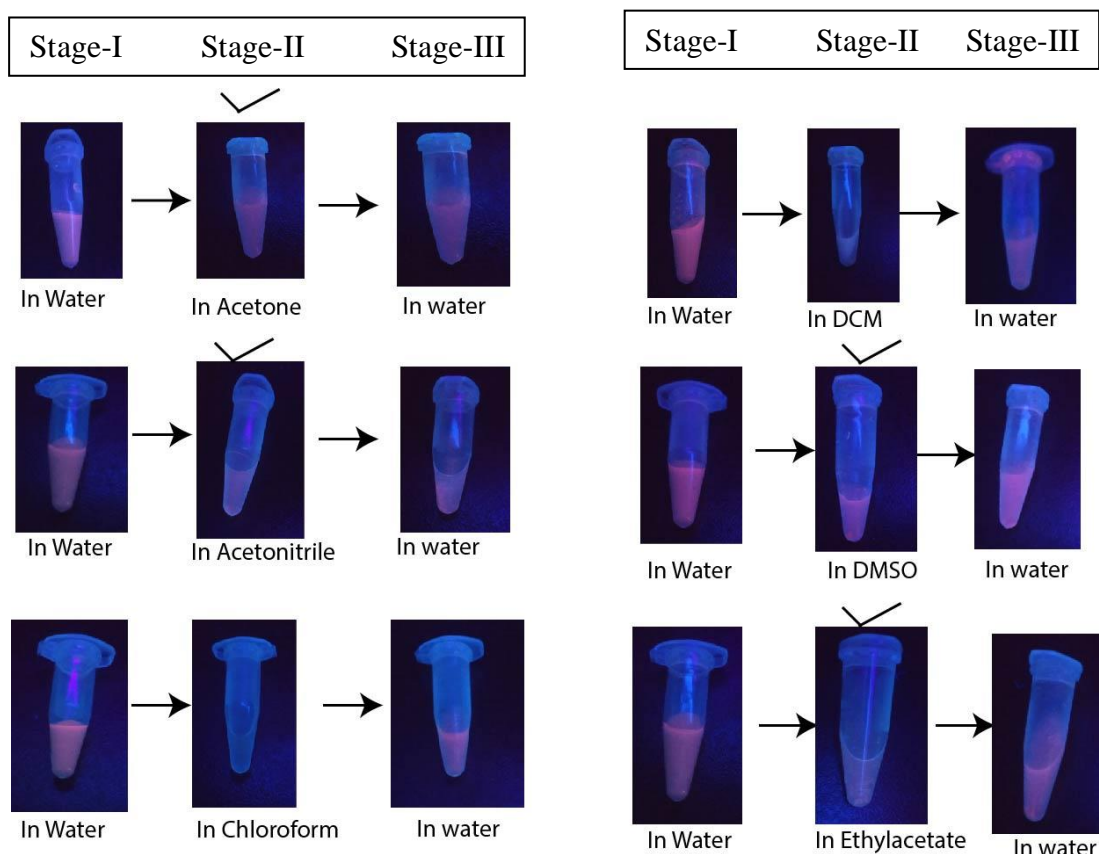


Fig.4B.8. Solvent dependent fluorescence showed for **AuNCs-dialyzed** from stage-I to stage-III to show the regenerative emission characteristics for these nanoclusters. The correct tick label shows that red emission is present after organic solvent addition (stage-II).

emission of this solution was checked under UV lamp for the removal of the organic solvent, centrifugation has been done for the stage-II vial and washing with DI water 2 to 3 times was done. The final volume was made up with 0.5 mL of DI water (stage-III) and its red emission checked under UV-lamp. All these steps are done at Room Temperature (28 °C).

From Fig.4B.8 it was noted that except chloroform and DCM, all the other solvents (i.e., ethanol, acetone, acetonitrile, DMSO and ethyl acetate) in stage-II shows red emission. For chloroform and DCM systems, solvent dependent red emission for **AuNCs-dialyzed** can be categorized as Turn on (stage-I)- Turn off (stage-II)- Turn-on (stage-III). And for the other organic solvents (i.e., ethanol, acetone, acetonitrile, DMSO and ethyl acetate) solvent dependent red emission for **AuNCs-dialyzed** can be considered as Turn on (stage-I)- Turn on (stage-II)- Turn-on (stage-III). The reason behind the quenching of red emission in stage- II for chloroform and DCM systems not understood well yet. Further detailed concentration dependent emission studies are required to sort out this reason.

4B.5. Conclusion

With the use of *N*-(11-mercaptoundecyl)-*N*, *N*'-dimethyl benzenammonium chloride as a capping agent, photoluminescent AuNCs were synthesized. These AuNCs were found to have self-assembly kind of aggregated nanostructures which were confirmed through TEM studies. AuNCs capped *N*-(11-mercaptoundecyl)-*N*, *N*'-dimethyl benzenammonium chloride i.e., **AuNCs-dialyzed** on centrifugation develops two kinds of nanoclusters of similar particle sizes i.e., **AuNCs-colloid** and **AuNCs-supernatant**. From XPS analysis, it was confirmed that Au is fully reduced in all these above nanoclusters. UV-visible absorption spectrum for **AuNCs-dialyzed**, **AuNCs-supernatant**, **AuNCs-colloid** showed no electronic differentiation in all the nanoclusters. To comment on the optical properties for **AuNCs-colloid** and **AuNCs-supernatant** need more fundamental concentration dependent fluorescence studies. The mechanistic aspects behind the ligand based self-assembly formation in **AuNCs-dialyzed** could be studied in future with the help of NMR studies. The NIR fluorescence of **AuNCs-dialyzed** is also responsive to the exterior ecological temperature. Furthermore, this new luminescent nanothermosensor gives a linear

temperature response to the temperature in varied range of 0-80 °C. The NIR fluorescence from **AuNCs-dialyzed** also showed the ability to show sensing properties towards solvent via Turn-on or Turn-off kind of mechanism. To develop as solvent dependent sensor, it requires further fundamental studies with concentration dependent emission for **AuNCs-dialyzed** with different organic solvents.

References

- 1 L. Zhang and E. Wang, *Nano Today*, 2014, **9**, 132–157.
- 2 *J. Am. Chem. Soc.*, 2016, **138**, 390–401.
- 3 P. S. Kuttipillai, Y. Zhao, C. J. Traverse, R. J. Staples, B. G. Levine and R. R. Lunt, *Adv. Mater.*, 2016, **28**, 320–326.
- 4 Y. Hong, W. Y. Lam and B. Zhong, *Chem. Commun.*, 2009, 4332–4353.
- 5 N. Goswami, Q. Yao, Z. Luo, J. Li, T. Chen and J. Xie, *J. Phys. Chem. Lett.*, 2016, **7**, 962–975.
- 6 Z. Luo, X. Yuan, Y. Yu, Q. Zhang, D. T. Leong, J. Y. Lee and J. Xie, *J. Am. Chem. Soc.*, 2012, **134**, 16662–16670.
- 7 J. Mei, Y. Hong, J. W. Y. Lam, A. Qin, Y. Tang and B. Z. Tang, *Adv. Mater.*, 2014, **26**, 5429–5479.
- 8 V. A. Online, J. Liang, Z. Chen, J. Yin, G. Yu and S. H. Liu, *Chem. Commun.*, 2013, **49**, 3567–3569.
- 9 X. Jia, J. Li and E. Wang, *Small*, 2013, **9**, 3873–3879.
- 10 J. A. C. Soc, G. M. Whitesides and B. Grzybowski, *Science (80-.)*, 2002, **295**, 2418–2422.
- 11 M. Grzelczak, J. Vermant, E. M. Furst and L. M. Liz-marza, *ACS Nano*, 2010, **4**, 3591–3605.
- 12 B. O. Okesola, *Chem. Soc. Rev.*, 2018, **47**, 3721–3736.
- 13 L. Chen and H. Yang, *Acc. Chem. Res.*, 2018, **51**, 2699–2710.
- 14 J. Huang, N. Hörmann, E. Oveisi, A. Loiudice, G. L. De Gregorio, O. Andreussi, N.

-
- Marzari and R. Buonsanti, *Nat. Commun.*, 2018, **9**, 3117.
- 15 Z. Wu, C. Dong, Y. Li, H. Hao, H. Zhang and Z. Lu, *angew*, 2013, **123**, 10136–10139.
- 16 Y. Z. and Q. L. Yuanqing Sun, Jiapeng Wu, Chuanxi Wang, *New J. Chem.*, 2017, **41**, 5412–5419.
- 17 P. Yu, X. Wen, Y. Toh and J. Tang, *J. Phys. Chem. C*, 2012, **116**, 6567–6571.

Chapter-5

Conclusion and future perspective

5.1. Conclusion

In conclusion, we found that metal clusters perform excellently in all applications related to biosensing, imaging, and security, owing to their ultra-small size which allows for more large surface area for biomolecules molecule binding. The surface area of QCs also helps them interact with biomolecules and biological systems present inside the cells. The following is a list of chapter-by-chapter conclusions.

Chapter 2 describes development of a red-emitting inorganic fluorescent Au nano-cluster-based sensor to study quorum sensing activity in bacteria. The surface of this inorganic fluorescent probe is covered with acyl homoserine lactones (AHLs) of varying carbon chain lengths. This probe searches for QS molecules binding sites within bacterial cells, instead of the concentration of signal molecules produced, as is currently implemented. After surface functionalization of AHLs over the Au nanocluster surface, the bioactive component of AHL (lactone moiety) remains intact, allowing for natural AHL molecular activity. Because of this trait, these systems are not affected by cell density and can be used before bacteria reach a virulent quorate condition. Fluorescence microscopy studies can also be used to examine the change in selectivity and specificity of AHLs towards their target receptors within different species of bacteria of the same strain. The receptors in *C. sakazakii* are more selective for C-8 AHL than for C-6 or C-12 AHL. *E. coli* receptors have a non-specific interaction with C-6 AHL, C-8 AHL, and C-12 AHL, whereas *P. aeruginosa* receptors had no interaction with any of the three AHLs.

Chapter 3 describes tuning of photophysical and chemical properties of ultra-small nanoclusters and their multifaceted application in biolabeling, bioimaging, and security applications. Anti-galvanic replacement (AGR) in aqueous phase processes has recently been used to control the fluorescence of alloyed AuAg nanoclusters. Traditional capping ligands, such as glutathione, cysteine, and mercaptoundecanoic acid, contain -SH as well as other electron donor groups such as -NH₂, -COOH, -OH, amide, and others, which can result in the formation of a surface Ag⁺-thiolate complex after Ag doping on Au nanoclusters. Aggregate-induced emission is also produced by Ag⁺-thiolate complexes, which increases fluorescence properties already reported. We report a novel structure of AuAg alloyed nanoclusters where Ag incorporation takes over the surface of pristine Au nanoclusters. Also, the Au⁺ are present over these novel AuAg alloyed nanoclusters interacts via metallophillic interaction confirmed

through XPS studies. When compared to pristine AuNCs (Q.Y. ~0.07), this method boosted the red emission quantum yield of AuAgNCs to 9.73, and these AuAgNCs are used in bioimaging and security applications.

Chapter 4 describes synthesis to make photoluminescent AuNCs with different ligand chain lengths with a bottom-up strategy. On *N, N', N''*-trialkyl (11-mercaptoundecyl) capped AuNCs, charge transfer between the ligands and Au-surface atoms induces a tuneable photoluminescence emission from 650 nm to 700 nm, emphasising the interface chemistry between gold nanoclusters and capping ligands. The ligands hydrophobicity and bulkiness can be used to learn more about how the thiolate AuNCs self-assemble and vary in particle size. HOMO-LUMO analysis from DFT research supports the UV-visible absorption spectra and charge transfer from the ligand to Au-surface atoms utilising frontier molecular orbital analysis.

5.2. Future directions

The surface ligand has a big influence on the electrical and optical properties of colloidal systems. Several studies have discovered that ligands can alter the structure and properties. The interactions between NCs and protective ligands, as well as the impact of surface ligands on electrical and optical properties, are still poorly understood. Fluorescence can be generated either from the NC core or the ligand and NC–ligand complex. To properly comprehend such interactions, more research is required. In recent years, NCs have been used for sensing, bioimaging, and chirality determination in a variety of ways. The size, shape, and ligand on the surface of clusters have all been explored as characteristics that influence their intracellular localization (in the cytoplasm, vesicles, or nucleus), uptake process, or even quantitative assessment. Probe's characteristics and multi-efficacy were recently studied and validated in vitro and in vivo experiments. The potential of using NCs for early tumour diagnosis through tumour imaging and targeted therapy was supported by Au/Ag NCs conjugated with a targeting ligand with high targeting specificity and nuclear localization capability, low toxicity of a multi-functional probe with tumour suppressing effect, and the tumour-targeted drug delivery nanocarrier. Doping of various concentration of Ag^+ or Cu^{+2+} over Au nanoclusters could also allow to generate alloyed metallic nanoclusters with anticancer or antibacterial properties. Such properties could also help these nano probes to show dual nature i.e., as a fluorescent probe with antibacterial or anti-cancer properties.

ABSTRACT

Name of the Student: Anurag M. Chahande **Registration No.:10CC15J26002**
Faculty of Study: Chemical Science **Year of Submission: Jan 2022**
AcSIR academic centre/CSIR Lab: **Name of the Supervisor: Dr. R. Nandini Devi**
CSIR-National Chemical Laboratory, Pune
Title of the thesis: "The Optical Properties Of Noble Metal Nanoclusters & Application In Bioimaging and Security"

Au nanoclusters (NCs) with atomic precision have become intriguing fluorescent nanomaterials have aroused a lot of interest in both basic research and practical applications. They have remarkable optical and electronic properties due to improved quantum confinement, outstanding colloidal stability and biocompatibility and so are very promising for a variety of applications, including bioimaging, biosensing, and security. Mostly the optical properties of Au nanoclusters are size dependent, ligand selection and environment required during synthesis. To choose a fluorescent probe in the field of biology, it should have excellent water dispersible properties and selective functional groups for further modification to tag with different biomolecules. In this context in Chapter-2, we developed a water dispersible Au nanoclusters with cationic groups over its surface so that we can surface functionalized with various C-chain length of AHL quorum sensing molecules to sense gram negative bacterial Lux-R homologues of receptors. To enhance Au nanoclusters PL emission and quantum yield in chapter-3, we doped these ultra small nanoclusters with Ag which gives excellent boosted PL emission as well as quantum yield and showed better performance than Au nanoclusters in the field of bioimaging and security. Ligand engineering also found an effective method for tuning the PL emission of such ultra-small nanoclusters. In this context in chapter-4A and 4B, we engineered the cationic thiol capping agent by changing its N⁺ head by adding different alkyl and aryl chains. This will give rise to different hydrophobicity over these engineered Au nanoclusters which shows different particles sizes as well as PL emission.

List of Publications Emanating from the Thesis Work

- (1) **Chahande A.M.**, Lathigara D., Prabhune A.A., Devi R.N., Red fluorescent ultrasmall gold nanoclusters functionalized with signal molecules to probe specificity in quorum sensing receptors in gram - negative bacteria, **Arch. Microbiol.** **2021**,203,4293–4301. <https://doi.org/10.1007/s00203-021-02338-y>.
- (2) **Chahande A.M.**, Singh.S., Devi R.N., Enhanced red emission in water dispersible Au ultra-small nanoclusters by heteroatom doping and their multifaceted applications in imaging (Manuscript communicated)
- (3) **Chahande A.M.**, Maibam.A.,Krishnamurthy S., Devi R.N., Ultra-small Au nanoclusters with tailored photoluminescence properties using modified thiol ligands: a computational and experimental demonstration (Manuscript under preparation)

List of Publications Non-Emanating from the Thesis Work

- (1) Dey.K, Kunjattu H.S., **Chahande A.M.**, Banerjee R.; Nanoparticle Size-Fractionation through Self-Standing Porous Covalent Organic Framework Films, **Angew. Chem.** **2020**,132 (3), 1177-1181

List of Posters Presented in International Conferences with details

- 1) Anurag Chahande, Dr. R. Nandini devi, Ultra-small Au nanoclusters surface functionalized with quorum sensing molecules to target Lux-R receptors in gram-negative bacteria, **ICONSAT-2016, IISER-Pune, India**
- 2) Anurag Chahande, Dr. R. Nandini devi, Bright Au-Ag bimetallic nanoclusters and their enhanced optical properties, **NANOBIOTECK-2017, IISER-TRIVANDRUM, 2017**
- 3) Anurag Chahande, Dr. R. Nandini devi, NIR emitting surface-functionalized gold nanoclusters with signal molecules used for selective imaging to differentiate three different species of gram-negative bacteria (*E. coli*, *C. sakazakii* & *P. aeruginosa*), **Chemo Sensors and Imaging Probes-2019, Gurunank Dev University, Amritsar, India**

List of Posters Presented in National Science Day in NCL with details

- 1) **National Science Day**, held at CSIR-National Chemical Laboratory, Pune on February 2016.
- 2) **National Science Day**, held at CSIR-National Chemical Laboratory, Pune on February 2017.
- 3) **National Science Day**, held at CSIR-National Chemical Laboratory, Pune on February 2018.



Red fluorescent ultra-small gold nanoclusters functionalized with signal molecules to probe specificity in quorum sensing receptors in gram-negative bacteria

Anurag M. Chahande^{1,3} · Disha Lathigara² · Asmita A. Prabhune² · R. Nandini Devi^{1,3}

Received: 9 November 2020 / Revised: 13 April 2021 / Accepted: 17 April 2021

© The Author(s), under exclusive licence to Springer-Verlag GmbH Germany, part of Springer Nature 2021

Abstract

Ultra-small (size < 2 nm) gold nanoclusters (AuNCs) are used as fluorescent probes which have excellent applications in bioimaging and sensing due to their emission in visible and NIR spectral region. Here, this property is exploited for understanding the quorum sensing phenomenon in bacteria which is regulated by signal molecules which are specific to various species. AuNCs are then functionalized with the signal molecules, Acyl Homoserine Lactones (AHL) of varying carbon chain length, C-6, C-8, and C-12 without 3rd C modification, to sense different strains of gram-negative bacteria i.e., *Escherichia coli*, *Cronobacter sakazakii* and *Pseudomonas aeruginosa*. In the concentration employed, selectivity to a limited extent is observed between the three Gram-negative bacteria tested. *E. coli* showed emission with all the AHL conjugates and *P. aeruginosa* did not interact with any of the three conjugates, whereas *C. sakazakii* showed specificity to C-8AHL. This is probably due to selectivity for cognate AHL molecules of appropriate concentrations.

Keywords Quorum sensing · Acyl homoserine lactone · Fluorescence imaging · Selectivity · Receptors · Gold nanoclusters

Introduction

The phenomenon of cell-to-cell communication by means of the exchange of chemical signaling molecules is called quorum sensing (QS). This system is utilized by a variety of bacterial species to synchronize their activities to behave as multi-cellular flora (Waters et al. 2005). Through this mechanism, bacteria can coordinate various activities such as surface attachment, swarming motility, antibiotic resistance or multidrug resistance, sporulation, virulence

or biofilm formation (Boyer et al. 2009; Miller et al. 2001; Rutherford et al. 2012). Such pathogenic traits cannot be expressed by a single bacterium, and are only achieved when the bacterial population density is high enough to devastate the host mechanism. This is controlled by the bacteria by synthesizing and releasing chemical signal molecules called autoinducers (AI). Autoinducers secreted by gram-positive bacteria are oligopeptide molecules and in the case of gram-negative bacteria, quorum sensing is triggered with the help of Acyl Homoserine Lactones (AHL's). These autoinducers are selectively sensed by their complementary receptor proteins and triggers certain cascades which can be detrimental to the host organism.

Most of the gram-negative microflora use transcriptional agents i.e., receptors of Lux-R homologues which can sense acyl homoserine lactone signal molecules (AHLs) synthesized by their cognate Lux-I type synthase homologues. These AHLs usually have a long acyl C chain varying between C4 to C18 attached to the lactone ring and 3 position in the chain is either unmodified or modified with carbonyl or hydroxyl group denoted as oxo or OH. Variation in the structure of AHL is known to impart some level of specificity of detection by the QS systems (Ahmer et al. 2011). Lux-R homologues are proteins which possess two

Communicated by Erko Stackebrandt.

✉ Asmita A. Prabhune
aa.prabhune@ncl.res.in

✉ R. Nandini Devi
nr.devi@ncl.res.in

¹ Catalysis and Inorganic Chemistry Division, CSIR-National Chemical Laboratory, Dr. Homi Bhabha Road, Pune 411008, India

² Biochemical Science Division, CSIR-National Chemical Laboratory, Dr. Homi Bhabha Road, Pune 411008, India

³ Academy of Scientific and Innovative Research (AcSIR), Kamla Nehru Nagar, Ghaziabad 201002, India

functional domains: C-terminal domain for DNA-binding and an N-terminal domain for AHL binding (Galperin 2006). The three tryptophan residues of the polar group from N-terminal interact with the lactone moiety of AHL signal molecule which determines the binding positions (Fuqua et al. 2002; Galperin et al. 2001). The hydrophobic acyl chains of AHL engage in different alignments with the binding pocket: smaller chain length AHLs are elongated and point in the direction of the solvent; whereas, long acyl chain possessing AHLs are bent and point towards the inner leaflet of cell membrane (Li et al. 2012). The most studied quorum sensing system is of *P. aeruginosa* which possess three predominant quorum sensing systems: foremost in the hierarchy is Las-R receptor-Las-I synthase which activates Rhl-R receptor-Rhl-I synthase and PQS (Chen et al. 2019; Kušar et al. 2016). Las-I synthase can synthesize 3-oxo-C-12AHL which selectively binds to its cognate Las-R receptors. This is also associated with phenotypes like motility, iron acquisition, pyocyanin formation. Rhl-I synthase synthesizes *N*-butyryl-L-homoserine lactone which specifically binds with Rhl-R receptors to activate transcriptional factors for the phenotypic expression like exoenzymes production, virulence, biofilm formation etc. Along with these complete systems, an orphan QscR receptor is also present which does not have a cognate synthase. The third system is based on 2-alkyl-4-quinolones which are structurally very different from the cognate signal molecules of the other two (Lee et al. 2015; Papenfort et al. 2016). *Escherichia coli* possess orphan Sdi-A receptors without any AHL synthase and are suggested to interact with a wide variety of AHLs of modified and unmodified acyl chains of C numbers between 4 and 12 (Ahmer et al. 2011; Dyszel et al. 2010). This mechanism is known to regulate bacterial adhesion and biofilm formation in *E. coli*. On the other hand, *C. sakazakii* quorum sensing systems are not well studied yet. Recently, AHLs of various chain lengths i.e., C-11AHL, C-12AHL, C-14AHL, C-15AHL, *N*-(β -ketocaroyl)-L-acyl homoserine lactone, C-8AHL, 3-oxo-C-8AHL and C-18AHL are isolated from biofilm-producing strains of *C. sakazakii* (Singh et al. 2017). However, no information on the specificity or concentration of AHLs is known. Most of the information regarding such binding mechanism arises from biochemical methods by which the signal molecules are isolated from bacterial populations. Very limited studies exist in understanding quorum sensing mechanisms at the early stages using fluorescence imaging. For e.g., recently, a fluorescent labeling agent for quorum sensing receptors (FLAQS) from Rhodamine B and dodecanedioic acid is developed which senses the CepR receptors of wild-type strain *B. cenocepacia* H111 in situ selectively (Gademann 2013). Nonetheless, inorganic fluorescent probes emitting in near infrared spectral region are found to be more advantageous due to less background fluorescence and higher photostability (Mathew

et al. 2014; Tao et al. 2015; Zhang et al. 2014; Zheng et al. 2017). Noble metal (thiolate capped or peptide capped or protein capped) nanoclusters are also used as fluorescence on-off-on (Yan et al. 2018) and fluorescence off (Chan et al. 2012; Ji et al. 2018; Zheng et al. 2018) based sensor for the selective point of care detection of gram-negative and gram-positive bacteria. Recently, we have reported the use of gold nanocluster-based fluorescent probes to distinguish between gram-positive and gram-negative bacteria based on the orphan Sdi-A receptors of *E. coli* (Mukherji et al. 2013). In our quest to further understand the mechanism of quorum sensing, we have focused on the question, whether different strains of gram-negative bacteria have a specific affinity towards a particular AHL molecule. For answering this, we have decorated three AHL signal molecules without 3rd C modification: *N*-hexanoyl-L-homoserine lactone (C-6), *N*-octanoyl-L-homoserine lactone (C-8) and *N*-dodecanoyl-L-homoserine lactone (C-12) over specially designed fluorescent Au nanocluster conjugates and carried out fluorescence imaging studies with *E. coli*, *C. sakazakii* and *P. aeruginosa* statistically comparing the fluorescence intensity in each case. We have observed specificity to a limited extent in the concentration levels of AHL studied. This method is found to be rapid (detection in less than 2 h), with the potential of being able to detect bacteria much prior to the virulent quorate state.

Materials and methods

Synthesis of Au nanoclusters

Synthesis of gold nanoclusters capped with N, N', N''-tripropyl (11-mercaptoundecyl) ammonium chloride is reported from our group elsewhere (Samanta et al. 2012). Briefly, 20 mL of acetonitrile and 0.593 g (1.6 mmol) thiol ligand in 2 mL of methanol was mixed first. 8.5 mL of 10 mM stock solution (in acetonitrile) of HAuCl₄ (99.9%, Aldrich) was added slowly to this mixture and stirred till the solution became colorless. Then, 100 μ L of 1.58 M (stock in MeOH) solution of NaBH₄ was added to this solution under stirring. After addition of NaBH₄ the color of the solution became pale yellow which indicated the formation of Au nanoclusters. All the above reaction steps were carried out at 0 °C. 30 mL of deionized water was then added and acetonitrile was evaporated under vacuum. The Au nanocluster solution is then dialyzed to remove the excess thiol present in the solution and the final Au nanocluster solution is then stored at 4 °C. Through elemental analysis, the final concentration was found to be 2 mM. 0.012 mL of oleic acid stock (0.05 M) in MeOH (0.6 μ moles) was added to 1 mL from the above gold nanocluster solution (2 μ moles) and stirred for 2 h. From 0.2 mM stock of C-6AHL, C-8AHL

and C-12AHL solutions, 14.7 μL of C-6AHL (0.37 μmoles), 17 μL of C-8AHL (0.37 μmoles) and 20.8 μL of C-12AHL (0.36 μmoles) with 500 μL of EtOH were added to the mixture of AuNC@OA solution and stirred again for 2 h to obtain the final conjugate AuNC@OA@AHL. Same concentrations of AuNC and oleic acid were used to synthesis intermediate composites, AuNC@AHL and AuNC@OA.

Transmission electron microscopy

TF-20, FEI Tecnai transmission electron microscope operating at 200 kV was used for observing the clusters and conjugates. Samples were prepared by drop casting the sample solution and air dried over a carbon coated mesh 200 grid. Same method was used to prepare grid of incubated bacteria.

Fluorescence spectroscopy

Fluorescence spectra were collected on a PTI QM-40 fluorescence instrument. For that sample solution was taken in a 3.5 mL quartz cuvette of 10 mm path length.

Fourier-transform IR spectroscopy

FTIR spectra were collected from TENSOR-27 BRUKER instrument. KBr was used as the standard matrix for making samples. Sample solution around 25 μL was placed in 100 mg of KBr powder (99.9%, Aldrich) and grind. This grinded powder was then dried and used to make pellet which then used to take FTIR spectra.

Bacterial cells culture used in quorum sensing studies

Bacterial strains used in this study are (1) *C. sakazakii* ATCC12868, (2) *E. coli* ATCC8739 and (3) *P. aeruginosa* NCIB 6571. Bacteria cells were grown in LB medium at optimum temperature up to log phase i.e., 10^6 cells/mL, harvested and washed with 1X PBS. After that, the cells were resuspended in 1X PBS and incubated with 100 μL AuNC@OA@AHL conjugates for 2 h with gentle shaking. When added to 1 mL of 1X PBS with bacterial cells, Au and AHL concentrations were estimated to be (0.13 μmoles) and (0.024 μmoles) respectively. After incubation, cells were pelleted down, washed with 1X PBS and resuspended in fresh PBS so that any unbound fluorescent clusters would not interfere with the imaging.

Microscopy and image analysis

For imaging, slides were prepared by using 50% glycerol as a mounting medium. The sample solution and the mounting medium were drop casted onto a J. Melvin brand plain glass

slide (size-75 \times 25 mm) and stacked with help of sterilized Sigma-Aldrich cover glasses (size- 22 \times 22 mm). Sample slides were then analysed within 3–4 h of preparation using Zeiss Imager A2 fluorescence microscope using Rhodamine filters (transmission wavelength 660–750 nm) with HXP 120 V (excitation range 350–700 nm) as a source lamp (Carl Zeiss. Inc, Germany). Images were captured and analysed with the help of Zen 2.3 lite software and Image J software respectively.

Results

Our strategy is to exploit AHL-receptor (primarily Lux-R type) interaction for understanding quorum sensing behaviors of different gram-negative bacteria. We have already reported the utilization of fluorescent Au nanocluster-based probes modified with AHL molecules to prove that AHL-Lux-R interaction is independent of the virulent stage and hence can be used in the early stages of bacterial growth (Mukherji et al. 2013). Ultra-small gold nanoclusters (size < 2 nm) showing NIR emission are considered to be better candidates for bioimaging, whereby noise from the endogenous fluorescence of the sample media of interest can be reduced. Such sub 2 nm size nanoclusters possess characteristic quantum confinement effects, which lead to discrete and size-dependent electronic transitions and manifest as photophysical characteristics like fluorescence (Qian et al. 2012; Varnavski et al. 2010). Au nanoclusters (AuNC) capped with N, N', N''-tri propyl(11-mercaptoundecyl) ammonium chloride with broad emission in the red spectral region is synthesized as reported elsewhere (Samanta et al. 2012). This ligand has -SH at one end and a positively charged quaternary ammonium ($^+\text{NR}_4$) head at the other end to promote dispersibility in water, the most useful solvent for biological systems.

We have employed three unmodified AHL molecules consisting of hydrophobic carbon chains with varying lengths, C-6, C-8, and C-12. Figure 1 represents the structures of the three selected AHL molecules in comparison with the cognate signal molecules of the three bacteria (Scheme 1).

Oleic acid is used as a bridging component such that the hydrophobic interaction between its 18-C chain and the acyl C chains of AHLs will assist in forming a stable conjugate (AuNC@OA) (Mukherji et al. 2013). In this way, we anticipate that the head group is free to interact with the receptor proteins as shown in the Suppl. Scheme 1 (see ESM). The conjugate architecture formation at each stage is ascertained by FTIR spectroscopy by studying the interactions between various functional moieties. Electrostatic interaction between the carboxylic functionality and the cationic ammonium head group of AuNC is validated by comparing the C=O stretching frequency of AuNC@OA composite with

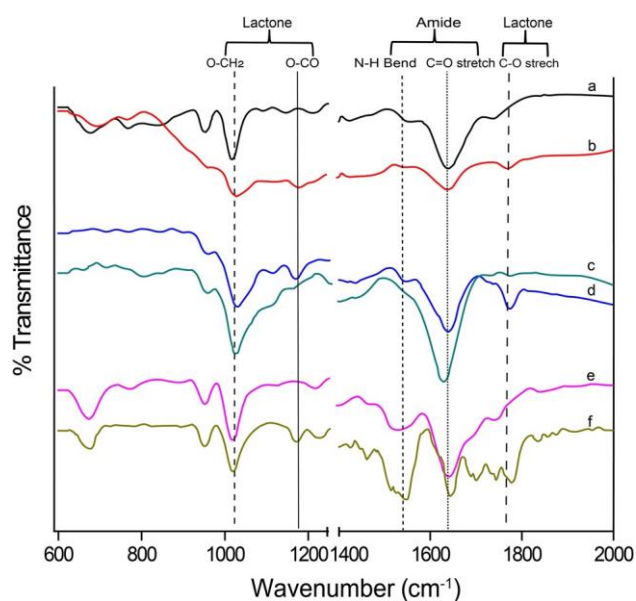


Fig. 1 FTIR spectra of **a** AuNC@OA@C-6AHL, **b** C-6AHL, **c** AuNC@OA@C-8AHL, **d** C-8AHL, **e** AuNC@OA@C-12AHL and **f** C-12AHL

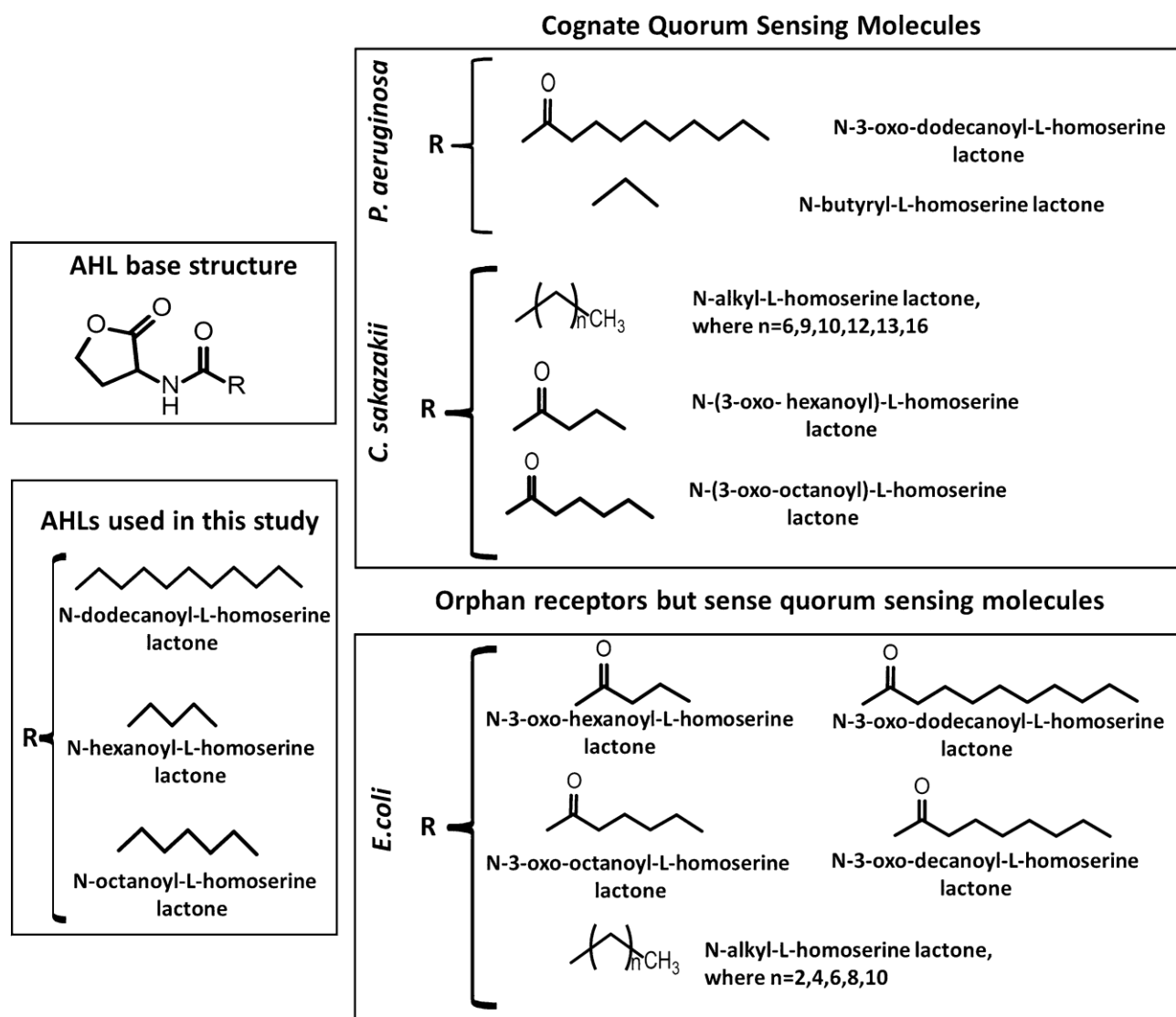
pristine oleic acid. It is already established that carboxylic acid C=O stretch which is observed in 1710 cm^{-1} in pristine sample disappears in bound states with R_4N^+ of the ligand with the appearance of bands near 1640 and 1540 cm^{-1} corresponding to symmetric and asymmetric $-\text{COO}$ vibrations (Nájera et al. 2009; Zhang et al. 2006). A very weak band at 1524 cm^{-1} corresponding to asymmetric $-\text{COO}$ stretch and strong intense band at 1631 cm^{-1} corresponding to symmetric stretch is observed (Full allocation of bands is shown in Suppl. Fig. S.2 in ESM). This implies a desirable configuration, in which R_4N^+ groups of Au nanoclusters interact with $\text{COO}-$ group of oleic acid thereby deploying the hydrophobic carbon chain on the outside. This is also confirmed by taking FTIR of oleic acid at $\text{pH}=7$ and $\text{pH}=9$. At neutral pH, C=O stretch is observed at 1710 cm^{-1} which shows that H^+ of $-\text{COOH}$ is bound. At $\text{pH}=9$, the C=O stretch band appears at 1651 cm^{-1} (symmetric stretch) and 1567 cm^{-1} (asymmetric stretch) (Full allocation of bands is shown in Suppl. Fig. S.3 in ESM). After addition of oleic acid to the AuNC, we recognize an increase in the intensity of asymmetric $-\text{COO}$ stretch (1635 cm^{-1}) indicating the probability of a monodentate interaction. Peak at 1284 cm^{-1} is attributed to C–O stretching vibration of the carboxylic group of oleic acid.

Also peaks at 2888 and 2936 cm^{-1} are the possible symmetric and asymmetric $-\text{CH}_2$ stretching vibrations. The important stretching frequencies for AHLs and AuNC@OA@AHLs are given in Fig. 2. When C-6AHL, C-8AHL, and C-12AHL are added to the AuNC@OA composite solution, the changes in the C=O (strong) stretch, N–H (weak),

lactone C=O stretch, O–CO vibrations and O–CH₂ vibrations are retained (Sheng et al. 2018). From the above FTIR data, we can tentatively conclude that AuNC@OA@AHL composite is of appropriate structure with free lactone head of the AHL present outside the composite and free to interact with the bacterial receptors. TEM images conclude that the average particle size of Au nanoclusters ($0.99 \pm 0.23\text{ nm}$) was not affected after functionalization with AHLs (size of AuNC@OA@C-6AHL = $1.10 \pm 0.23\text{ nm}$, size of AuNC@OA@C-8AHL = $1.04 \pm 0.229\text{ nm}$, size of AuNC@OA@C-12AHL = $1.16 \pm 0.25\text{ nm}$) as shown in Suppl. Fig. S.3 in ESM. The emission spectra for pristine Au nanoclusters ($\lambda_{\text{exc}} = 420\text{ nm}$) and their composites were compared and found to be similar as shown in Suppl. Fig. S.4 in ESM. The emission intensities of the conjugates decrease when compared to pristine clusters as expected.

We selected three representative gram-negative bacteria i.e., *E. coli*, *C. sakazakii* and *P. aeruginosa* for the quorum sensing studies. Bacterial samples were incubated with the conjugates, AuNC@OA@AHLs with all the three AHLs and observed under the fluorescence microscope with $100 \times$ oil immersion lens and at constant exposure time. The concentration of Au nanoclusters, oleic acid, and AHL in all the three AuNC@OA@AHLs remained the same in all the experiments. The experiments were carried out in triplicates to assess the variability. Details of imaging and parameter optimization for all the experiments are given in the Suppl. Figs. S.5–S.9 in ESM. Figure 3 shows representative fluorescence microscopy images of *E. coli*, *C. sakazakii*, and *P. aeruginosa* incubated in conjugates with C-6AHL, C-8AHL, and C-12AHL. *E. coli* shows red emission when incubated with AuNC@OA@AHL composites containing all the three AHL molecules (with a carbon chain length of C-6, C-8, C-12). TEM analysis of the bacteria after incubation with the conjugate indicates the presence of Au particles within the cell wall (Representative images of *E. coli* with C-12AHL are given in Suppl. Fig. S.10 in ESM). Whereas in *C. sakazakii*, fluorescence is observed only with C-8AHL conjugate. However, *P. aeruginosa* when incubated with AuNC@OA@C-6AHL, AuNC@OA@C-8AHL, AuNC@OA@C-12AHL, shows no red emission.

To further examine our assumption of the probe conjugates structure and the mode of interaction, the bacterial cells were stained with intermediate structures like AuNC@AHL, AuNC@OA and AuNCs. AuNCs, AuNC@OA and AuNC@AHL composites were synthesized in such a manner that AuNCs concentration, as well as AHL and oleic acid concentration, were similar as that of the AuNC@OA@AHL conjugates. In the case of AuNC@AHL composite, there may be a chance of electrostatic interaction between the lactone head of AHLs and the quaternary ammonium head of the thiol ligand capped clusters. Here, we anticipate the non-availability of the lactone



Scheme.1 Structures of signal molecules with base Acyl homoserine skeleton. Cognate signal molecules synthesized by *Cronobacter sakazakii* and *Pseudomonas aeruginosa* and those known to be detected by *Escherichia coli* are given along with the ones used in this study

group of AHL for binding to the receptors. In the case of AuNC@OA (hydrophobic due to oleic acid over the surface of AuNC) and pristine AuNC probes without the signal molecule it is possible that fluorescent AuNC and AuNC@OA can randomly access the binding receptor site even without AHL. Surprisingly, no red emission could be seen when *E. coli*, *C. sakazakii* and *P. aeruginosa* were stained with AuNC, AuNC@OA, AuNC@AHL (shown in Suppl. Fig. S5–S7 in ESM) indicating the importance of the proposed probe structure. Hence, from the above studies, it is clear that AuNC@OA@AHL fluorescent probe is the only possible structure which could sense the gram-negative bacterial cells receptors. After the quorum sensing studies, to differentiate the amount of AuNC present in the bacteria and quantify the differential uptake of

the conjugates by the three strains, a statistical analysis of the fluorescence intensities was carried out. Fluorescence intensities from three different zones of the images, containing the same number of cells (average 15 cells per image for an individual experiment), were estimated using Zeiss 2.3 lite software (Details given in Suppl. Fig. S.9 in ESM). For all the three conjugates incubated separately with three different bacteria, we have chosen three images for each strain (average 15–20 bacterial cells per image) to determine the AuNC@OA@AHL conjugate selectivity towards the specific quorum sensing receptors of the pathogen. Statistical analysis was then done to quantify the selectivity and specificity of AuNC@OA@AHL composites towards quorum sensing receptors of pathogens. The data are represented as Mean \pm Standard deviation of three

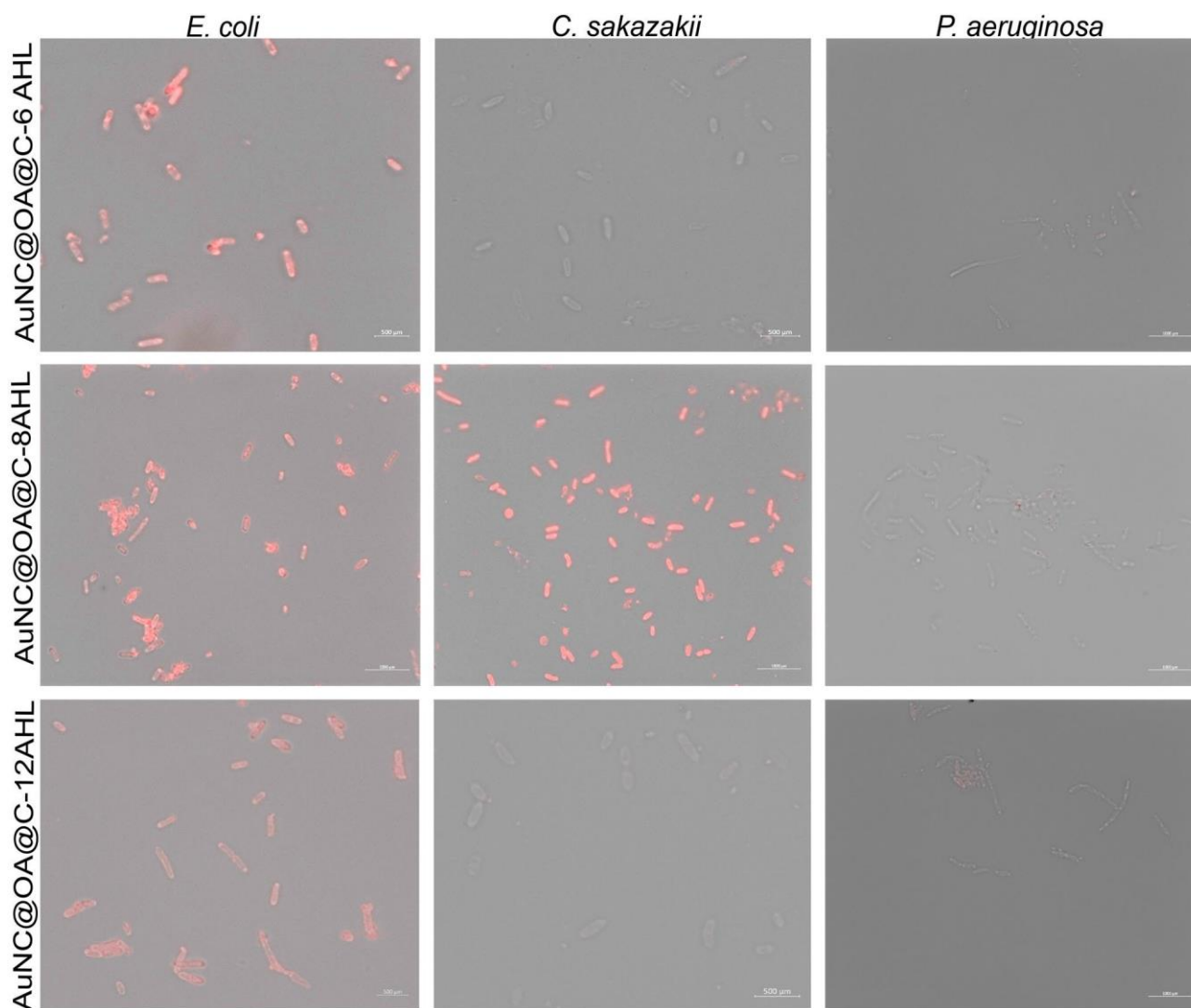


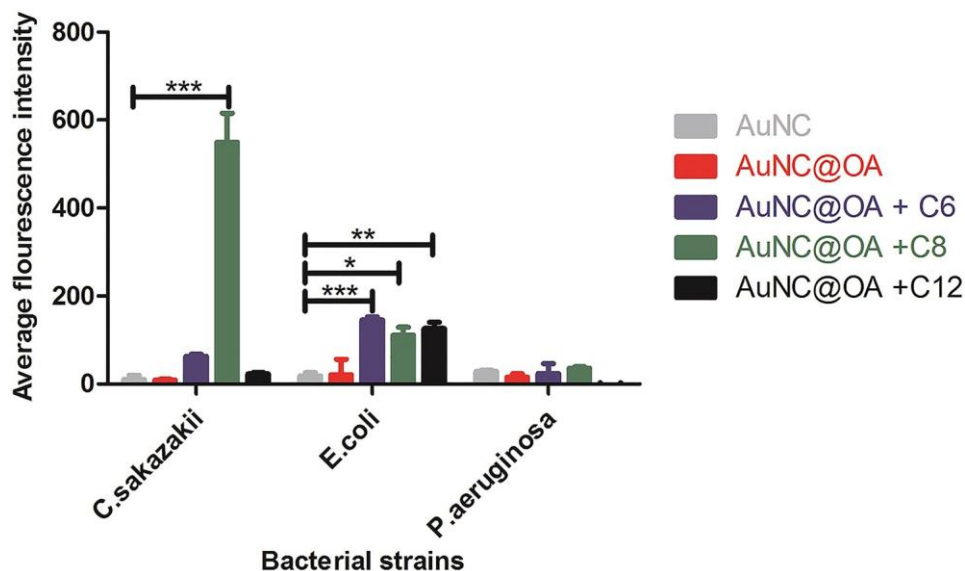
Fig. 2 Fluorescence microscopy images of (left column) *E. coli* incubated with AuNC@OA@C-6AHL (scale bar-500 μm), AuNC@OA@C-8AHL (scale bar-1000 μm), AuNC@OA@C-12AHL (scale bar-500 μm), (middle column) *Cronobacter sakazakii* incubated with AuNC@OA@C-6AHL (scale bar-500 μm), AuNC@OA@C-

8AHL (scale bar-1000 μm), AuNC@OA@C-12AHL (scale bar-500 μm) and (right column) *Pseudomonas aeruginosa* incubated with AuNC@OA@C-6AHL (scale bar-1000 μm), AuNC@OA@C-8AHL (scale bar-1000 μm), AuNC@OA@C-12AHL (scale bar-1000 μm)

independent experiments ($n = 3$). Data sets were compared by performing two-way ANOVA using GraphPad Prism 5. The probability values of $**p < 0.01$ and $***p < 0.001$ were considered to be statistically significant. Here the fluorescence intensity depends upon the concentration of AuNC@OA@AHLs fluorescent probes present in the bacterial cell consequent to their interaction with the Lux-R type receptors. Small variations in emission intensity among the conjugate probes (shown in Suppl. Fig. S.4 in ESM) is not considered since it is within the statistical error. In the case of *C. sakazakii*, AuNC@OA@C-8AHL probe shows red emission with the highest fluorescence

intensity when compared to AuNC@OA@C-6AHL and AuNC@OA@C-12AHL showing specificity to a large extent. However, *E. coli* does not show any preference to any of the conjugates and shows red emission with all the conjugates with similar intensities, albeit lesser than *C. sakazakii*. Hence there is no specific selectivity of AHLs towards Lux-R type receptors of *E. coli*. *Pseudomonas aeruginosa*, on the other hand, does not show much interaction with any of the conjugates under study. Based on the estimation of average intensities, among *E. coli*, *C. sakazakii* and *P. aeruginosa*, the selectivity and specificity of AuNC@OA@C-8AHL are the most pronounced towards *C. sakazakii*.

Fig. 3 Average fluorescence intensity of bacterial cells with different AuNC composites. AuNC was used as negative control (** $p < 0.01$ and *** $p < 0.001$) ($n = 3$)



Discussion

Signal selectivity in quorum sensing is an important phenomenon which may be exploited for target antibacterial activity or bacterial detection. Even though most AHLs have a very similar structural backbone, LuxR receptors have specificity to signal molecules produced by cognate synthases. However, signal promiscuity by LuxR type receptors is also known as in the case of *C. violaceum*, which is suggested to have evolved possibly for inter-species signaling (Hawver et al. 2016). The signal selectivity may be attributed to the variation in interaction of the receptors with AHLs with different structures which is suggested in literature based on crystal structures of the receptors bound to cognate autoinducers (Boursier et al. 2018). It is known that SdiA receptors detect AHLs in nM to μ M concentration levels and both modified and unmodified acyl chain AHLs are detected (Ahmer et al. 2011). We also observe this non-specificity based on C chain length in *E. coli*. However, in the case of *P. aeruginosa*, signaling mechanism is more complex. The predominant AHL is reported to be the LasR cognate modified 3-oxo-C12, which is needed at high concentrations in the absence of las-B promoters. Purified LasR shows excellent binding to 3-oxo-C12 and to a little extent 3-oxo-C10, but no affinity is exhibited for any other AHLs (Lee et al. 2006). Some studies have also established intrinsic structural basis for preference of 3-substituted AHLs as due to H bonding of the polar groups (Bottomley et al. 2007). Orphan QscR is more relaxed in signal selectivity apparently due to larger ligand-binding site and different H bonding pattern than LasR (Ha et al. 2012). However, since it is suggested that QscR is activated later than LasR, its activity may not be apparent in early stages (Oinuma et al. 2011). Hence, it is probable that unmodified AHLs at the

concentration used are not detected by the bacteria. Lack of such detailed studies in case of *C. sakazakii* prevents us from commenting further on the intrinsic structural features which may have resulted in the selectivity to C-8AHL. However, this study may point to a possibility of signal selectivity in *C. sakazakii* which needs further mechanistic insights.

Conclusions

In summary, a red-emitting inorganic fluorescent Au nanocluster-based probe is developed for studying quorum sensing behavior of bacteria. This inorganic fluorescent probe is made up of gold nanoclusters which are decorated on the surface with acyl homoserine lactones (AHLs) of different carbon chain lengths. During surface functionalization of AHLs over the Au nanocluster surface, the bioactive part of AHL (lactone moiety) remains intact to show natural activity as pristine AHL molecule. This property makes the surface-functionalized Au nanoclusters more capable to detect bacterial quorum sensing receptors before they achieve the havoc quorum state. This method is advantageous over the biosensor targeting method because of its simplicity. Also, with the fluorescence microscopy studies, we can study the variation in selectivity as well as specificity of AHLs towards their target receptors inside different species of bacteria of the same strain. The specificity of the receptors of *C. sakazakii* for C-8 AHL is more than C-6 AHL and C-12 AHL. And the receptors of *E. coli* non-specifically interact with C-6 AHL, C-8 AHL and C-12 AHL, whereas, *P. aeruginosa* does not interact with any of the three AHLs. Further studies into the development of this method will allow us to detect selectively the pathogenic bacteria and understand their quorum sensing mechanism before or at early quorate state.

Supplementary Information The online version contains supplementary material available at <https://doi.org/10.1007/s00203-021-02338-y>.

Acknowledgements AMC acknowledges a fellowship from University Grants Commission, Govt. of India, Dr. Kiran A. Kulkarni from CSIR-NCL, Pune for help with data interpretation and Center for Material Characterizations division of CSIR-NCL, Pune for the TEM measurements.

Author's contributions AAP and RND contributed to the conceptualization and design of experiments and data interpretation. AMC contributed to synthesis and DL to biochemical experiments.

Funding This work was supported by the Department of Biotechnology, Govt. of India, Sanction No. BT/PR10847/NNT/28/736/2014.

Data availability All data is given in Supplementary data.

Declarations

Conflict of interest The authors declare that they have no conflict of interest or competing interests.

Ethical approval This article does not contain any studies with human participants or animals performed by any of the authors.

Consent for publication. All authors give consent for publication.

References

- Ahmer BMM, Soares JA (2011) Detection of acyl-homoserine lactones by *Escherichia* and *Salmonella*. *Curr Opin Microbiol* 14:188–193
- Bottomley MJ, Muraglia E, Bazzo R, Carfi A (2007) Molecular insights into quorum sensing in the human pathogen *Pseudomonas aeruginosa* from the structure of the virulence regulator LasR bound to its autoinducer. *J Biol Chem* 282:13592–13600
- Boursier ME, Manson DE, Combs JB, Blackwell HE (2018) A comparative study of non-native *N*-acyl L-homoserine lactone analogs in two *Pseudomonas aeruginosa* quorum sensing receptors that share a common native ligand yet inversely regulate virulence. *Bioorg Med Chem* 26:5336–5342
- Boyer M, Florence WD (2009) Cell-cell signalling in bacteria: not simply a matter of quorum. *FEMS Microbiol Ecol* 70:1–19
- Chan PH, Chen YC (2012) Human serum albumin stabilized gold nanoclusters as selective luminescent probes for *Staphylococcus aureus* and methicillin-resistant *Staphylococcus aureus*. *Anal Chem* 84:8952–8956
- Chen R, Deziel E, Groleau MC, Schaefer AL, Greenberg EP (2019) Social cheating in a *Pseudomonas aeruginosa* quorum-sensing variant. *Proc Natl Acad Sci USA* 116:7021–7026
- Dyszal JL, Soares JA, Swearingen MC, Lindsay A, Smith JN, Ahmer BMM (2010) *E. coli* K-12 and EHEC genes regulated by SdiA. *PLoS One* 5:1–15
- Fuqua C, Greenberg EP (2002) Listening in on bacteria: acyl-homoserine lactone signalling. *Nat Rev Mol Cell Biol* 3:685–695
- Gademann K (2013) Fluorescent labeling agents for quorum-sensing receptors (FLAQS) in live cells. *Chem Eur J* 19:9766–9770
- Galperin MY (2006) Structural classification of bacterial response regulators : diversity of output domains and domain combinations structural classification of bacterial response regulators : diversity of output domains and domain combinations. *J Bacteriol* 188:4169–4182
- Galperin MY, Nikolskaya AN, Koonin EV (2001) Novel domains of the prokaryotic two-component signal transduction systems. *FEMS Microbiol Lett* 203:11–21
- Ha C, Park SJ, Im SJ, Park SJ, Lee JH (2012) Interspecies signaling through QscR, a quorum receptor of *Pseudomonas aeruginosa*. *Mol Cells* 33:53–59
- Hawver LA, Jung SA, Ng WL (2016) Specificity and complexity in bacterial quorum-sensing systems. *FEMS Microbiol Rev* 40:738–752
- Ji H, Wu L, Pu F, Ren J, Qu X (2018) Point-of-care identification of bacteria using protein-encapsulated gold nanoclusters. *Adv Healthc Mater* 7:1–6
- Kušar D, Srimpf K, Isaković P, Kalšek L, Hosseini J, Zdovc I, Kotnik T, Vengušt MS, Tavčar-Kalcher G (2016) Determination of *N*-acylhomoserine lactones of *Pseudomonas aeruginosa* in clinical samples from dogs with otitis externa. *BMC Vet Res* 12:1–11
- Lee J, Zhang L (2015) The hierarchy quorum sensing network in *Pseudomonas aeruginosa*. *Protein Cell* 6:26–41
- Lee J, Lequette Y, Greenberg EP (2006) Activity of purified QscR, a *Pseudomonas aeruginosa* orphan quorum-sensing transcription factor. *Mol Microbiol* 59:602–609
- Li Z, Nair SK (2012) Quorum sensing : how bacteria can coordinate activity and synchronize their response to external signals ? *Protein Sci* 21:1403–1417
- Mathew A, Pradeep T (2014) Noble metal clusters: applications in energy, environment, and biology. *Part Part Syst Charact* 31:1017–1053
- Miller MB, Bassler BL (2001) Quorum sensing in bacteria. *Annu Rev Microbiol* 55:165–199
- Mukherji R, Samanta A, Illathvalappil R, Chowdhury S, Prabhune AA, Devi RN (2013) Selective imaging of quorum sensing receptors in bacteria using fluorescent Au nanocluster probes surface functionalized with signal molecules. *ACS Appl Mater Interfaces* 5:13076–13081
- Nájera JJ, Horn AB (2009) Infrared spectroscopic study of the effect of oleic acid on the deliquescence behaviour of ammonium sulfate aerosol particles. *Phys Chem Chem Phys* 11:483–494
- Oinuma KI, Greenberg EP (2011) Acyl-homoserine lactone binding to and stability of the orphan *Pseudomonas aeruginosa* quorum-sensing signal receptor qscR. *J Bacteriol* 193:421–428
- Papenfort K, Bassler BL (2016) Quorum sensing signal-response systems in gram-negative bacteria. *Nat Rev Microbiol* 14:576–588
- Qian H, Zhu M, Wu Z, Jin R (2012) Quantum sized gold nanoclusters with atomic precision. *Acc Chem Res* 45:1470–1479
- Rutherford ST, Bassler BL (2012) Bacterial quorum sensing: its role in virulence and possibilities for its control. *Cold Spring Harb Perspect Med* 2:1–25
- Samanta A, Dhar BB, Devi RN (2012) Ultrasmall gold cluster arrays encapsulated in silica nanospheres : applications in fluorescence imaging and catalysis. *J Phys Chem C* 116:1748–1754
- Sheng H, Wang F, Gu C, Stedtfeld R, Bian Y, Liu G, Wu W, Jiang X (2018) Sorption characteristics of: *N*-acyl homoserine lactones as signal molecules in natural soils based on the analysis of kinetics and isotherms. *RSC Adv* 8:9364–9374
- Singh N, Patil A, Prabhune AA, Raghav M (2017) Diverse profiles of *N*-acyl-homoserine lactones in biofilm forming strains of *Cronobacter sakazakii*. *Virulence* 8:275–281
- Tao Y, Li M, Ren J, Qu X (2015) Metal nanoclusters: novel probes for diagnostic and therapeutic applications. *Chem Soc Rev* 44:8636–8663
- Varnavski O, Ramakrishna G, Kim J, Lee D, Goodson T (2010) Critical size for the observation of quantum confinement in optically excited gold clusters. *J Am Chem Soc* 132:16–17

- Waters CM, Bassler BL (2005) Quorum sensing : communication in bacteria. *Annu Rev Cell Dev Biol* 1:319–346
- Yan R, Shou Z, Chen J, Wu H, Zhao Y, Qiu L, Jiang P, Mou XZ, Wang J, Li YQ (2018) On-off-on gold nanocluster-based fluorescent probe for rapid *Escherichia coli* differentiation, detection and bactericide screening. *ACS Sustain Chem Eng* 6:4504–4509
- Zhang L, Wang E (2014) Metal nanoclusters: New fluorescent probes for sensors and bioimaging. *Nano Today* 1:132–157
- Zhang L, He R, Gu H (2006) Oleic acid coating on the monodisperse magnetite nanoparticles. *Appl Surf Sci* 5:2611–2617
- Zheng Y, Lai L, Liu W, Jiang H, Wang X (2017) Recent advances in biomedical applications of fluorescent gold nanoclusters. *Adv Colloid Interface Sci* 242:1–16
- Zheng Y, Wang X, Jiang H (2018) Label-free detection of *Acinetobacter baumannii* through the induced fluorescence quenching of thiolated AuAg nanoclusters. *Sens Actuat B Chem* 277:388–393

Publisher's Note Springer Nature remains neutral with regard to jurisdictional claims in published maps and institutional affiliations.

Appendix 1

Physicochemical Characterizations

The characterisation of AuNCs, AuAgNCs, organic thiol molecules and AuNCs composites with various carbon chain AHLs can be done using a variety of physicochemical approaches. The fundamentals of the procedures utilised in this investigation, such as powder, TEM, NMR, IR Spectroscopy, Zeta-potential, Photoluminescence, UV-visible Spectroscopy, Life time measurements.

1. Transmission Electron Microscopy (TEM)

A TEM functions similarly to a slide projector. A projector shines a beam of light through (transmits) the slide, which is influenced by the structures and objects on the slide as it travels through. As a result of these processes, only a portion of the light beam is passed through particular areas of the slide. The picture of the slide is subsequently projected onto the viewing screen using the transmitted beam. The only difference is that a beam of electrons (like light) is shone through the specimen in a TEM (slide). Any transmitted information is projected onto a phosphor screen.

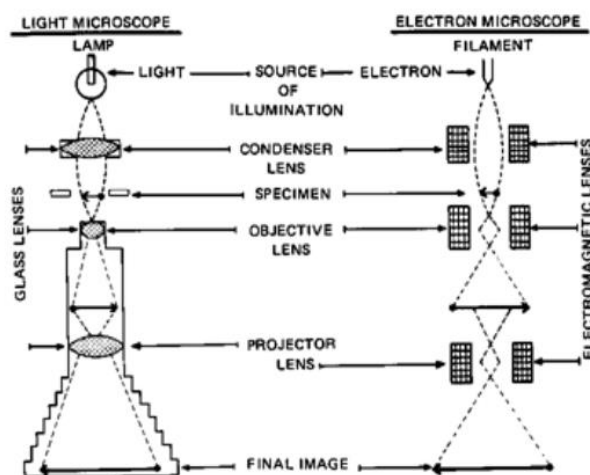


Figure 1. Principle of TEM

A "light source" at the microscope's top releases electrons that flow through vacuum in the microscope's column. Electrons are focused into a very tiny beam using electromagnetic lenses in the TEM. After that, the electron beam passes through the specimen. Some electrons are dispersed and lost from the beam depending on the density of the substance.

The un-scattered electrons hit a fluorescent screen at the bottom of the microscope, creating a shadow image of the specimen with its various components displayed in varying degrees of darkness depending on their density. The image can be examined in real time by the operator or recorded using a camera. The areas of the picture that are brighter represent those areas of the sample where more electrons were transported (they are denser). The areas of the sample that are lighter in colour signify those areas of the sample that are more important electrons were sent through the (they are thinner or less dense)

2. NMR Spectroscopy

A Bruker AV 400 MHz NMR spectrometer with a 9.4 Tesla superconducting magnet was used for all of the NMR measurements. At this magnetic field, ^1H has a resonance frequency of 400 MHz. The proton NMR spectra were obtained using a typical one-pulse experiment with a 30° flip angle and a 1 second relaxation time. Data was collected using 32 to 64 scans and 32K data points. The frequency domain spectrum is created by Fourier Transforming the raw data obtained without the use of any window function. A typical ZGPG30 pulse approach was used to accomplish proton decoupling. The solvent peak's chemical changes are discovered at 7.28ppm (^1H , d- CDCl_3).

4. IR SPECTROSCOPY (Infra-red Spectroscopy)

Infrared energy is transmitted through a sample in IR Spectroscopy. The sample absorbs some of the infrared light and transmits the rest. The resulting spectrum depicts the sample's molecule absorption and transmission, resulting in a molecular fingerprint. It represents the absorption peaks' fingerprint, which corresponds to the frequency of vibrations between the bonds of the atoms that make up the material. Because each material is made up of a particular set of atoms, no two compounds have the same infrared spectrum. As a result, infrared spectroscopy may be used to positively identify (qualitatively) any type of material. Furthermore, the size of peaks in the spectrum is a direct reflection of the amount of material present. Many people refer to FT-IR spectrometers as FT-IRs. FT-IR is a technique for getting infrared spectra that involves employing an interferometer can gather an Interferogram of a sample signal and then applying a Fourier transform to the Interferogram to acquire the spectrum. The Interferogram is collected and digitalized by an FT-IR spectrometer, which then performs the FT function and displays the spectrum. Bonds and groups of bonds vibrate at specific frequencies, which is how the process works. Whenever a molecule is exposed to infrared rays, it absorbs the energy at frequencies that are specific

to that molecule. The transmittance and reflectance of infrared light at various frequencies on the specimen are translated into an IR absorption plot with reversal peaks. The FT-IR spectral pattern that result is examined and compared to known signatures of identified items in the FT-IR library. A modulated IR light is directed to a point on the specimen during FT-IR examination. The principle that almost all molecules absorb infrared light underlies the operation of FT-IR spectroscopy. Molecules absorb exclusively at the frequencies where the infrared light influences the molecule's dipolar moment. Infrared photons interact with a molecule with a dipolar potential, causing excitation to higher vibrational states. As previously stated, infrared light is absorbed by practically all molecules, and each molecule absorbs IR light at different frequencies. This attribute gives each molecule an own character.

It allows to determine the molecular type (qualitative analysis) as well as the amount of the molecule in the sample (quantitative analysis). Because each type of molecule absorbs at specific frequencies, the absorption spectral pattern or fingerprint is unique over the whole IR spectrum. FT-IR is a kind of infrared spectroscopy that identifies a molecule's vibrational transitions. FT-IR has an advantage over conventional infrared spectroscopy in that it uses a Michelson interferometer to measure all wave numbers at once.

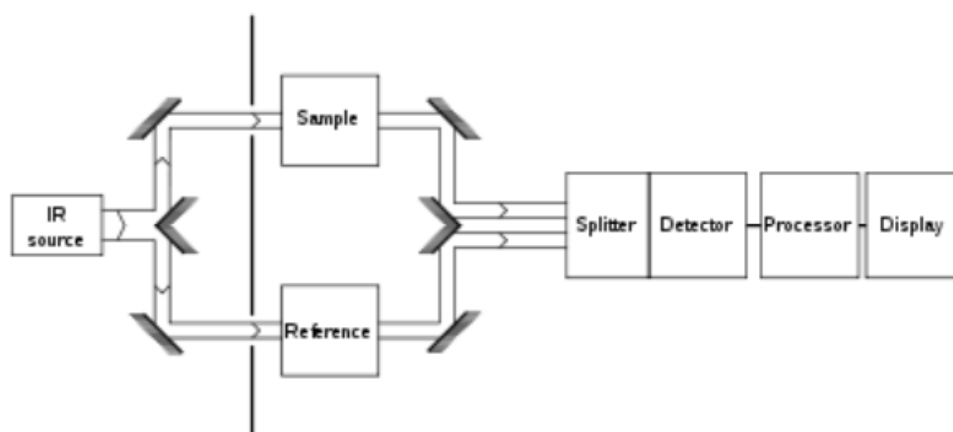


Figure 2. Schematic diagram of Infrared Spectroscopy

3. Dynamic Light Scattering and Zeta Potential

The random changes in the intensity of light scattered from a suspension or solution could be used to measure particle size. Dynamic light scattering (DLS) is the most common name for this technique, although it's also known as photon correlation spectroscopy (PCS) and quasielastic light scattering (QELS). The technique of dynamic light scattering begins with

the phenomenon under investigation (particle motion, not particle size). After that, the measurement's nature and data interpretation are explained. Finally, some closing remarks are made. A sample's zeta potential is frequently employed as a measure of dispersion stability. Large zeta potentials indicate that the dispersion will be more stable. With the SZ-100, you can get a better knowledge of aggregation and flocculation in samples and speed up the process of generating stable formulations, whether they're dispersions, emulsions, or suspensions. The zeta potential, or electrostatic attraction / repulsion, is significant in a variety of industries, including pharmaceuticals, mineral processing, water treatment, and electronics additives. The SZ-100 allows for zeta potential measurement that is quick, accurate, and repeatable.

7. UV-visible Spectroscopy

The spectroscopy of photons in the UV-visible region is known as UV-Vis spectroscopy. This implies it makes advantage of the light that is visible and nearby (near UV and near IR ranges). The colour of the compounds involved is directly impacted by absorption in the visible spectrum. Electronic transitions take place in the electromagnetic spectrum region. For two reasons, UV spectroscopy is a useful analytical tool. It has two applications: first, it may be used to identify functional groups in molecules, and second, it can be used to perform assays. This second job, determining a substance's content and strength, is particularly useful. When valence (outer) electrons absorb photons, either ultraviolet or visible, they are promoted from their normal (ground) states to higher energy (excited) states. The energy of the orbitals involved in the electronic transition are constant. Because energy is quantized, it appears that the absorption peaks in the UV Spectrum will be sharp. This is, however, a rare occurrence. The spectrum, on the other hand, contains large peaks. This is because absorbent materials can also absorb vibrational and rotational energy levels.

According to Beer-law, Lambert's a solution's absorbance is proportional to the concentration of absorbing species in the solution and the route length.

$$A = \log(I_0/I) = \epsilon l c$$

I_0 = Intensity of incident radiation

I = Intensity of transmitted radiation

l = Path length through the sample

c = Concentration of absorbing species

ϵ = Molar absorption coefficient

UV spectrophotometer is the instrument used in UV spectroscopy. It compares the intensity of light before it passes through the sample (I) to the intensity of light after it passes through the sample (I_0). Transmittance is the ratio (I/I_0) that is usually stated as a percentage (% T). The Transmittance is used to calculate the absorbance(A).

$$A = -\log(\%T)$$

A light source, a sample holder, a diffraction grating or a monochromator to separate the different wavelengths of light, and a detector are the main components of a spectrophotometer. Tungsten filaments, continuous deuterium arc lamps, and, more recently, light emitting diodes and xenon arc lamps for visible wavelengths have all been used as radiation sources. A photodiode or CCD is commonly used as the detector. Single-beam or double-beam spectrophotometers are available. All of the light in a single beam instrument travels through the sample cell. Before reaching the sample, light is split into two beams in a double beam instrument. One beam serves as a reference, while the other travels through the sample. The sample and reference beams are measured at the same time in some detectors with two detectors (photodiodes). The two beams pass through a beam chopper in other devices, which blocks one beam at a time. The sample beam and the reference beam are alternately measured by the detector. In the ultraviolet or visible spectrum, a UV Spectrum is essentially a graph of absorbance vs wavelength.

8. Photoluminescence Spectroscopy

Photoluminescence refers to a variety of phenomena such as fluorescence, phosphorescence, and Raman scattering. Photoluminescence spectroscopy is a non-destructive, contactless way of exploring a material's electrical structure. In a process known as photo-excitation, light is directed onto a sample, where it is absorbed and imparts surplus energy into the substance. The sample can discharge this surplus energy by emitting light, which is known as luminescence. This luminescence is known as photoluminescence in the case of photo-excitation. Electrons within a material shift into acceptable excited states as a result of photo-excitation. The excess energy is released when these electrons return to their equilibrium states, which may or may not entail the emission of light (a radiative process) (a nonradiative process). The difference in energy levels between the two electron states involved in the transition between the excited state and the equilibrium state determines the energy of the emitted light (photoluminescence). The relative contribution of the radiative process is related to the quantity of radiated light. Fluorescence is the consequence of a three-step

process that occurs in fluorophores or fluorescent dyes, which are molecules that emit light. A fluorescence probe is a fluorophore that is designed to respond to a specific stimulation or to locate inside a specific region of a biological material. A Jablonski diagram depicts the process responsible for the fluorescence of fluorescent probes and other fluorophores. Excitation is the first stage. An external source, such as an incandescent lamp or a laser, emits a photon that is absorbed by the fluorophore, resulting in an excited electronic singlet state (S_1'). This technique distinguishes fluorescence from chemiluminescence, which involves a chemical reaction populating the excited state. Excited-State Lifetime is the second stage. For a limited amount of time (usually 1–10 nanoseconds), the excited state exists. The fluorophore undergoes structural changes and is exposed to a variety of possible interactions with its molecular surroundings throughout this time. These processes have two major ramifications. First, the energy of S_1' is largely dissipated, resulting in a relaxed singlet excited state (S_1), which is the source of fluorescence emission. Second, through fluorescence emission, not all molecules that were stimulated by absorption (Stage 1) return to the ground state (S_0). Other processes that reduce the population S_1 include collisional quenching, fluorescence resonance energy transfer (FRET), and intersystem crossover (see below).

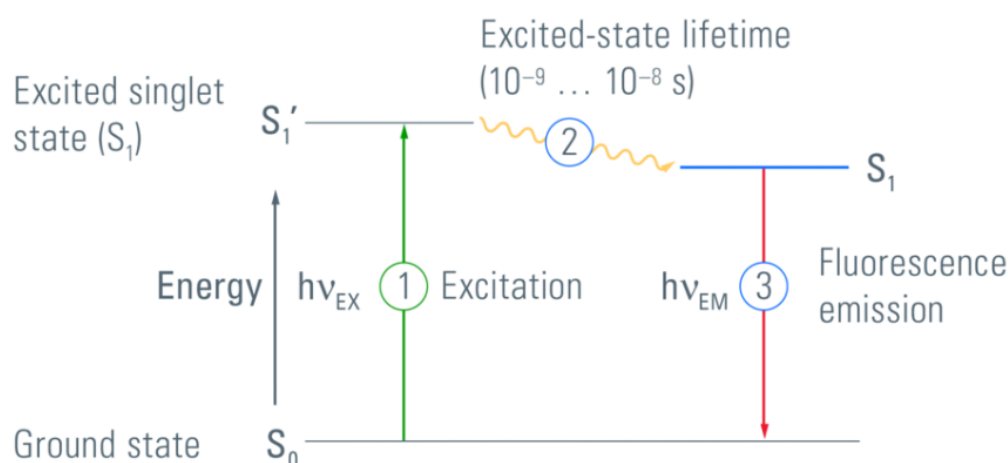


Figure 5. Jablonski Diagram

Other processes that reduce the population S_1 include collisional quenching, fluorescence resonance energy transfer (FRET), and intersystem crossover (see below). The ratio of the number of fluorescence photons emitted (Stage 3) to the number of photons received is the fluorescence quantum yield (Stage 1). Fluorescence Emission is the third stage. The

fluorophore is returned to its ground state S_0 by emitting a photon of energy. The energy of this photon is lower, and so has a longer wavelength, than the excitation photon, due to energy dissipation during the excited-state lifespan. The Stokes shift is the difference in energy or wavelength between the absorbed and released photons. Because it permits emission photons to be detected against a low background while being separated from excitation photons, the Stokes shift is critical to the sensitivity of fluorescence techniques. Absorption spectrophotometry, on the other hand, necessitates the measurement of transmitted light in relation to high incident light levels at the same wavelength.

Appendix 2

Computational Details

Chapter-4A

DFT investigations on a model of ultra-small cluster, $\text{Au}_{25}(\text{SR})_{18}$ were used to investigate the effect of the ligand on the luminescence shown by all of these Au nanoclusters.

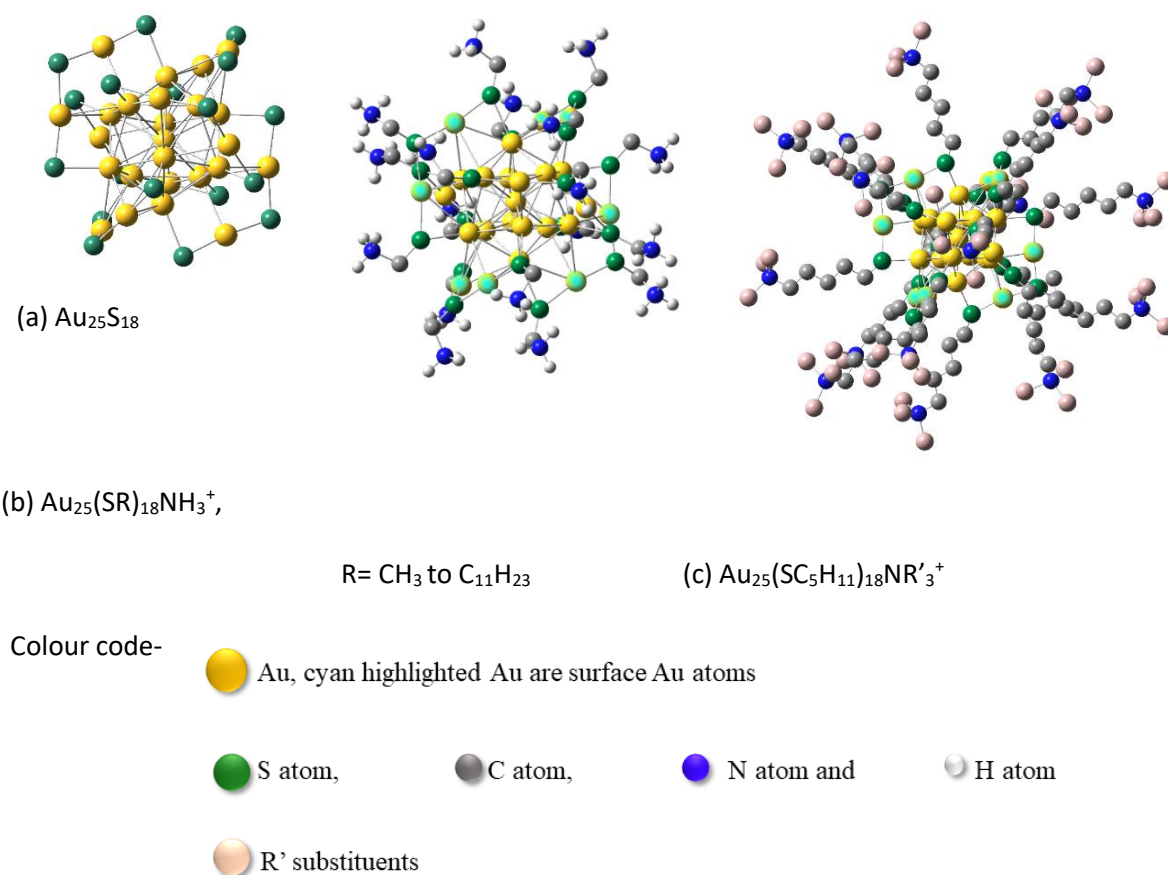


Figure.A.2.1. (a) Model $\text{Au}_{25}\text{S}_{18}$ nanocluster (b) Thiol ligand with quaternary ammonium head on $\text{Au}_{25}(\text{SR})_{18}$ nanocluster model (c) Alkylated thiol ligand with quaternary ammonium head on $\text{Au}_{25}(\text{SC}_5\text{H}_{11})_{18}$ nanocluster.

As illustrated in Figure A.2.1.(a), the $\text{Au}_{25}\text{S}_{18}$ nanocluster is made up of core 13-Au atoms, the smallest building unit of a bulk gold FCC lattice. Because most of the electron density on Au-S nanoclusters is localised on the periphery Au atoms, as shown in Figure.A.2.1. (a), the Au-13 core with 12 Au surface atoms can appropriately match the observed electronic features. With

an average Mulliken charge of +0.99, the atoms in the Au₁₃ core of Au₂₅S₁₈ are electron deficient. The surface Au atoms, on the other hand, are negatively charged (-1.22) and connected to the positively charged (+0.09) S-atom of the thiol ligand.

There is a charge transfer from the core Au atoms to the peripheral Au atoms in most AuS nanoclusters, and most of the electronic features are intrinsic to the peripheral Au atoms and S-atom of thiol ligands.

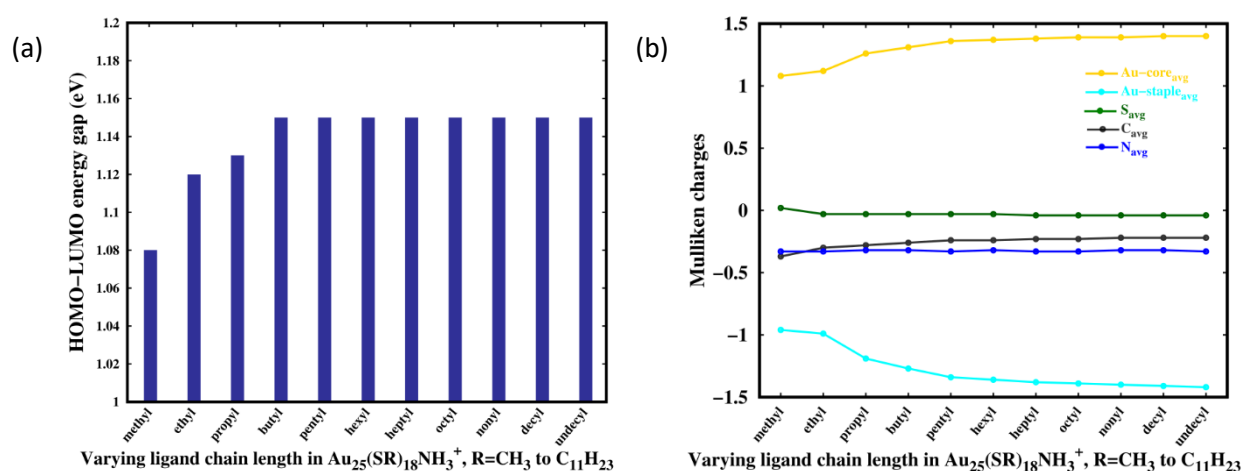
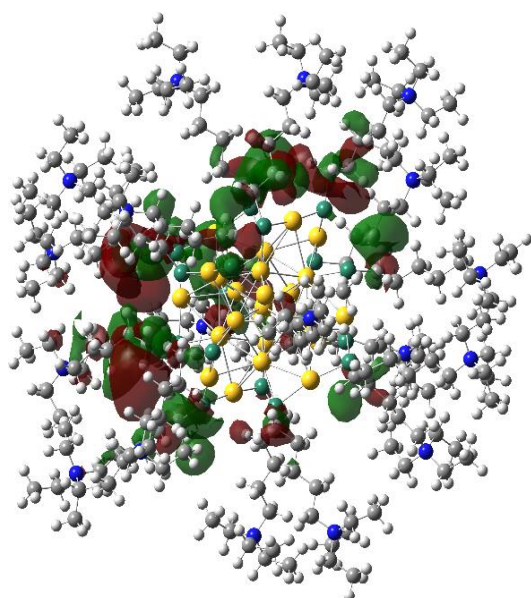


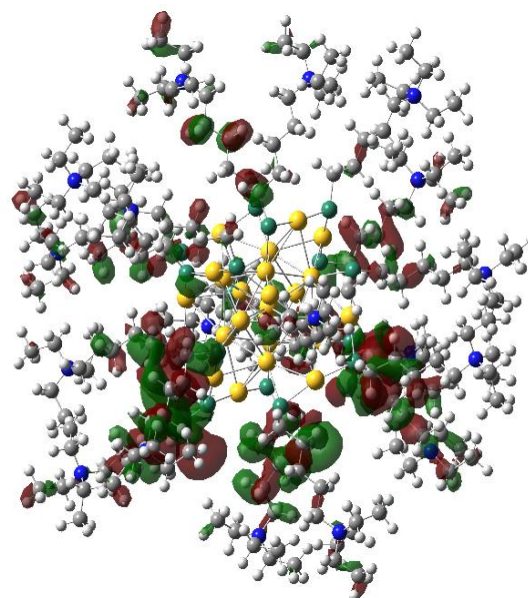
Figure.A.2.2 (a) HOMO-LUMO energy gaps of Au₂₅(SR)₁₈NH₃⁺ nanoclusters for varying alkyl, R chain length (b) Average Mulliken charges on different atoms of Au₂₅(SR)₁₈NH₃⁺ nanoclusters for varying alkyl chain (R) length.

As a result, how the electrical characteristics of AuNCs vary as the alkyl group of the thiol ligand with quaternary ammonium head changes from methyl to undecyl was investigated. With a quaternary ammonium head coupled to the Au₂₅ nanocluster, various alkyl units were introduced to the thiol ligand and the intrinsic and electronic changes observed as the alkyl chain length increases. The Au₂₅(SR)₁₈NH₃⁺ nanoclusters HOMO-LUMO energy gaps are estimated and shown as Figure.A.2.2 (a). The HOMO-LUMO gap increases as the length of the alkyl chain increases from methyl to propyl, but it remains constant at 1.15 eV from butyl ammonium to undecyl ammonium. When the average Mulliken charges of the Au-core, surface

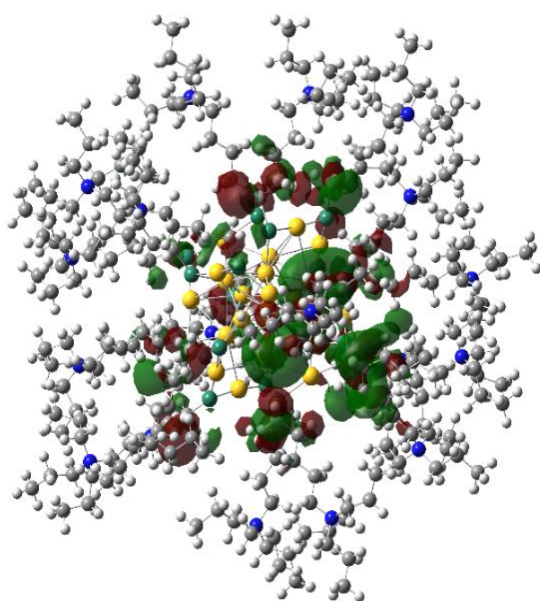
Au-atoms, S-atoms, C atoms of the hydrocarbon chain, and N of the ammonium head are depicted in Figure A.2.2. (b). However, the charge transfer from pentyl ammonium to undecyl ammonium ligands stays constant and unaffected by the length of the hydrocarbon chain. In summary, thiol ligands with quaternary ammonium heads affect the electronic properties of AuNCs and cause a greater charge transfer from Au-core to surface Au-atom only for ligands with lower alkyl groups. The charge transfer from Au-core to Au-surface remains stable as the alkyl group chain length increases, with $\Delta q_{\text{avg}} = +0.40$ in Au-core and $\Delta q_{\text{avg}} = -0.17$ in Au-surface. As a result, mercaptopentyl moiety in between thiol and ammonium heads was considered for computational research on these AuNCs to lower the computational cost.



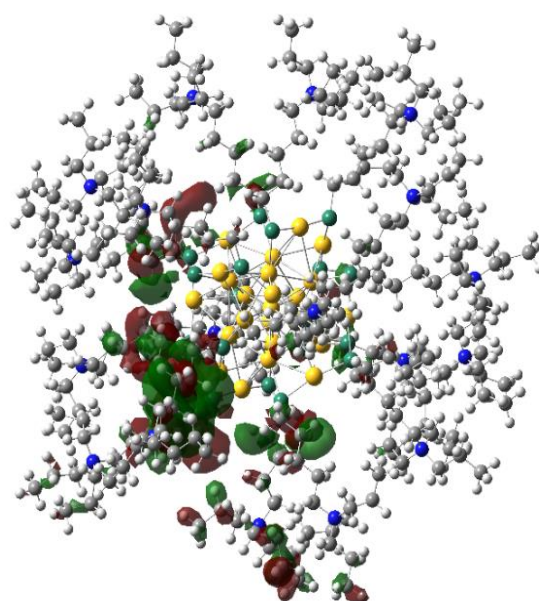
(a1) HOMO of *N, N', N''*-triethyl (5-mercaptopentyl) ammonium capped AuNC



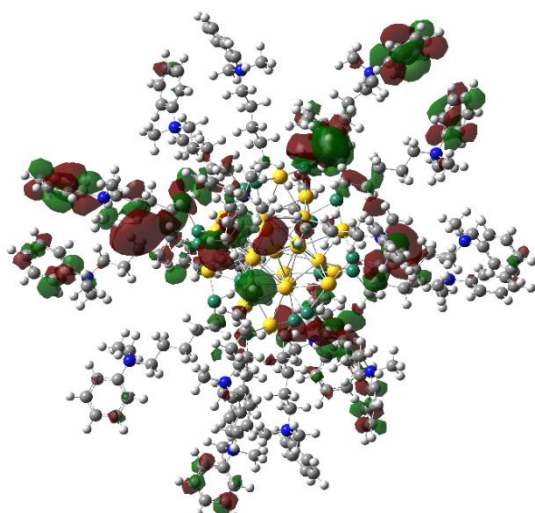
(a2) LUMO of *N, N', N''*-triethyl (5-mercaptopentyl) ammonium capped AuNC



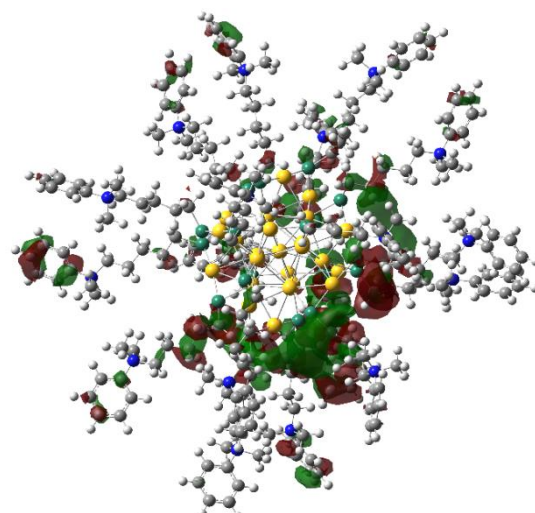
(b1) HOMO of N, N', N'' -tripropyl (5-mercaptopentyl) ammonium capped AuNC



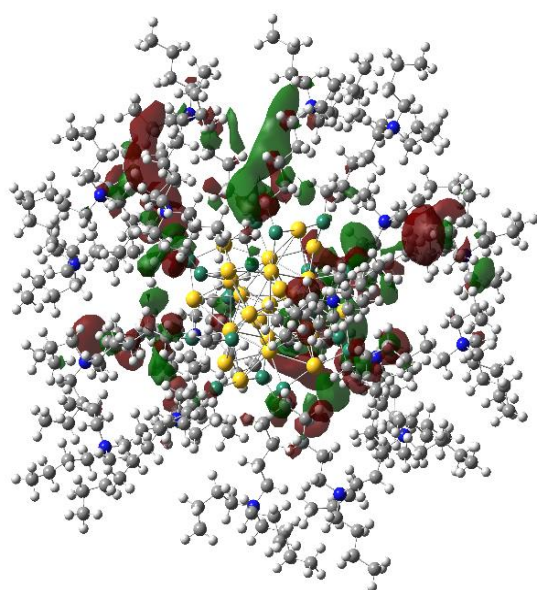
(b2) LUMO of N, N', N'' -tripropyl (5-mercaptopentyl) ammonium capped AuNC



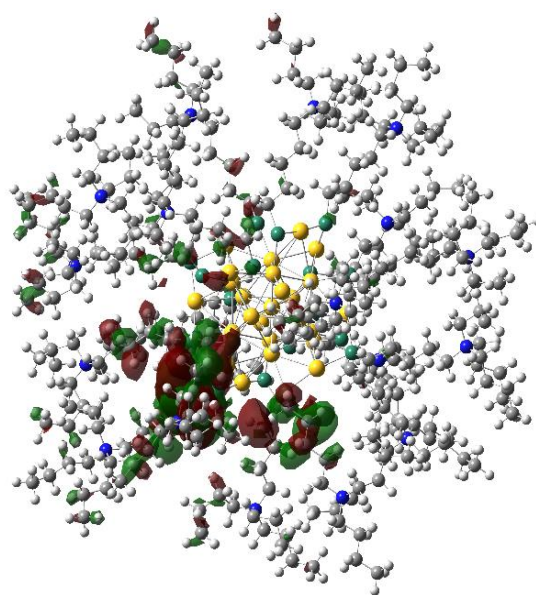
(c1) HOMO of N, N', N'' -tributyl (5-mercaptopentyl) ammonium capped AuNC



(c2) LUMO of N, N', N'' -tributyl (5-mercaptopentyl) ammonium capped AuNC



(d1) HOMO of *N*-(5-mercaptopentyl)-*N*, *N'*-dimethyl benzenammonium capped AuNC



(d2) LUMO of *N*-(5-mercaptopentyl)-*N*, *N'*-dimethyl benzenammonium capped AuNC

Figure.A.2.3. Frontier Molecular Orbitals (FMOs) of the *N*, *N'*, *N''*-trialkyl substituted (5-mercaptopentyl)-ammonium capped AuNCs.

Erratum